Design and Characterization of InGaN/GaN Dot-in-Nanowire Heterostructures for High Efficiency Solar Cells

ROSS CHERITON

uOttawa

A Doctoral Thesis submitted to the Department of Physics at the University of Ottawa

Doctor of Philosophy in the subject of Physics
Department of Physics
Faculty of Science
University of Ottawa

July 2018 – version 1.0

Dedicated to my wife Trista.

ABSTRACT

Light from the sun is an attractive source of energy for its renewability, supply, scalability, and cost. Silicon solar cells are the dominant technology of choice for harnessing solar energy in the form of electricity, but the designs are approaching their practical efficiency limits. New multijunction designs which use the tunable properties of the more expensive III-V semiconductors have historically been relegated to space applications where absolute power conversion efficiency, resilience to radiation, and weight are more important considerations than cost. Some of the more recent developments in the field of semiconductor materials are the so-called III-nitride materials which mainly use either indium, aluminum or gallium in combination with nitrogen. Indium gallium nitride (InGaN) is one of these III-nitride semiconductor alloys that can be tailored to span the vast majority of the solar spectrum. While InGaN growth traditionally requires expensive substrate materials such as sapphire, three-dimensional nanowire growth modes enable high quality lattice mismatched growth of InGaN directly on silicon without a metamorphic buffer layer. The absorption and electronic properties of InGaN can also be tuned by incorporating it into quantum confined regions in a GaN host material. This opens up a route towards cost-effective, high efficiency devices such as light emitted diodes and solar cells which can operate over a large range of wavelengths. The combination of the two material systems of InGaN/GaN and silicon can marry the low cost of silicon wafers with the desirable optoelectronic properties of III-nitride semiconductors. This thesis investigates the potential for highly nanostructured InGaN/GaN based devices using quantum-dot-in-nanowire designs as novel solar cells which can enable intermediate band absorption effects and multiple junctions within a single nanowire to absorb more of the solar spectrum and operating more efficiently. Such semiconductor nanostructures can in principle reach power conversion efficiencies of over 40% on silicon, with a cost closer to conventional silicon solar cells as opposed to methods which use non-silicon substrates.

In the primary strategy, the nanowires contain InGaN quantum dots which act as photon absorption/carrier generation centres to sequentially excite photons within the large band gap semiconductor. By using this intermediate band of states, large operating voltages between contacts can be maintained without sacrificing the collection of long wavelength solar photons. In this work, we characterize the properties of such nanowires and experimentally demonstrate sub-bandgap current generation in a large area InGaN/GaN dot-in-nanowire solar cell.

Experimental characterization of InGaN / GaN quantum dots in nanowires as both LEDs and solar cells is performed to determine the nanowire material parameters to understand how they relate to the

nanowire device performance. Multiple microscopy techniques are performed to determine the nanowire morphology and contact effectiveness. Optical characterization of bare and fabricated nanowires is used to determine the anti-reflection properties of nanowire arrays. Photoluminescence and electroluminescence spectroscopy are performed. Illuminated current-voltage characteristics and quantum efficiencies are determined. Specular and diffuse reflectivities are measured as a function of wavelength.

Technology computer-aided design (TCAD) software is used to simulate the performance of the overall nanowire device. The contribution from quantum dots or quantum wells is simulated by solving for the carrier wavefunctions and density of states with the quantum structures. The discretized density of states from the quantum dots is modelled and used in a complete drift-diffusion device simulation to reproduce electroluminescence results. The carrier transport properties are modified to demonstrate effects on the overall device performance.

An alternate design is also proposed which uses an InGaN nanowire subcell on top of a silicon bottom subcell. The dual-junction design allows a broader absorption of the solar spectrum, increasing the operating voltage through monolithically grown series-connected, current-matched subcells. The performance of such a cell is simulated through drift-diffusion simulations of a dual-junction InGaN/Si solar cell. The effects of switching to a nanowire subcell based on the nanowires studied in this thesis is discussed.

Symbol	Variable
A	Area
A_k	Unit area in reciprocal space
A_{state}	Unit area per state
a	Strained lateral lattice constant
$a_{c\parallel}$	Conduction band deformation potentials $\parallel$ to c-place
$a_{c\perp}$	Conduction band deformation potential $\perp$ c-plane
a_0	Unstrained lateral lattice constant
A_0	Absorption parameter
A_1	Wurtzite material parameter
A_2	Wurtzite material parameter
A_3	Wurtzite material parameter
A_4	Wurtzite material parameter
A_5	Wurtzite material parameter
A_6	Wurtzite material parameter
A_7	Wurtzite material parameter
$\vec{a}_1, \vec{a}_2, \vec{a}_3$	Real space lattice vectors
$\vec{b}_1, \vec{b}_2, \vec{b}_3$	Reciprocal lattice vectors
c_0	Unstrained perpendicular lattice constant
c	Speed of light in vacuum
$C_{n,au}$	Auger coefficient for electrons
$C_{p,au}$	Auger coefficient for holes
C_{13}	Elastic constant
C_{33}	Elastic constant
c_{nj}	Electron capture coefficient
c_{pj}	Hole capture coefficient
$D_{3D,e}$	Bulk density of states
D_v	Bulk density of states as a function of k
$D_{2D,e}$	2D density of states
D_a	2D density of states as a function of k
$D_{1D,e}$	1D density of states
D_l	1D density of states as a function of k
$D_{0D,e}$	0D density of states
D_l	Wurtzite band parameter

Symbol	Variable
D_2	Wurtzite band parameter
D_3	Wurtzite band parameter
D_4	Wurtzite band parameter
D_n	Electron diffusion coefficient
D_p	Hole diffusion coefficient
$d_{AM,\theta}$	Effective atmosphere thickness at incident angle θ
$d_{AM,\perp}$	Atmosphere thickness
$\hat{e}$	Polarization vector
e_{31}	Piezoelectric constant
e_{33}	Piezoelectric constant
E	Energy
EQE	External quantum efficiency
E_{offset}	Energy band offset parameter with no strain
$E_{offset,s}$	Energy band offset parameter under strain
ΔE_c	Conduction band offset
ΔE_v	Valence band offset
$E_p^{\parallel}$	III-nitride band parameter
$E_p^{\perp}$	III-nitride band parameter
E_i	Energy level at state i
E_f	Electric field
E_g	Bandgap
E_c^0	Unstrained conduction band edge energy
E_{g0}	Unstrained bandgap
$E_{g,s}$	Strained bandgap
E_C	Conduction band energy
E_V	Valence band energy
E_{fn}	Electron quasi-Fermi level
E_{fp}	Hole quasi-Fermi level
FF	Fill factor
F	Electric field
F_v^j	Minimization function for Poisson's equation
F_n^j	Minimization function for electron current continuity equation
F_p^j	Minimization function for hole current continuity equation
$F_{1/2}$	Fermi integral of order one-half
F	Electric field
F_w	Wurtzite band parameter
f_c	Fermi function for electrons
f_v	Fermi function for holes
f	Photon frequency

Symbol	Variable
f_g	Photon frequency for bandgap transition
g_p^j	Hole wavefunctions in quantum well
G_{opt}	Optical generation rate
G_{therm}	Thermionic generation rate
h	Planck's constant
$\hbar$	Planck's reduced constant
H_{ij}	Hamiltonian matrix element
H_t	Hamiltonian matrix element for wurtzite materials
$H_s(x)$	Heaviside step function
I_s	Irradiance
I_m	Current at maximum power point
I_{sc}	Short circuit current
I_{ph}	Photocurrent
G_b	Gaussian broadening parameter
J_{dark}	Current without illumination
J_{light}	Current without illumination
J_o	Reverse saturation current
J_{sc}	Short circuit current density
$\vec{J}_n$	Electron current density
$\vec{J}_{n,drift}$	Electron drift current density
$\vec{J}_{n,diff}$	Electron diffusion current density
$\vec{J}_p$	Hole current density
$\vec{J}_{p,drift}$	Hole drift current density
$\vec{J}_{p,diff}$	Hole diffusion current density
k	Extinction coefficient
k_B	Boltzmann constant
K_t	Hamiltonian matrix element for wurtzite materials
$\vec{k}$	Wave vector in reciprocal space
$\vec{k}_x$	Reciprocal wave vector along $\vec{x}$
$\vec{k}_y$	Reciprocal wave vector along $\vec{y}$
k_x	Wavevector magnitude along $\vec{x}$
k_y	Wavevector magnitude along$\vec{y}$
k_1	Coefficient for first lattice wavevector along $\vec{b_1}$
k_2	Coefficient for second lattice wavevector along $\vec{b_2}$
k_3	Coefficient for third lattice wavevector along $\vec{b_3}$
$\vec{k}_\parallel$	Momentum operator $\parallel$ to c-plane
$\vec{k}_\perp$	Momentum operator $\perp$ to c-plane
L_x	One dimensional potential well width
L_y	One dimensional potential well length
L_z	One dimensional potential well height
m	Particle mass
m_0	Electron rest mass

Symbol	Variable
m_e	Mass of electron
m_r	Reduced mass
m_e^*	Effective electron mass
m_h^*	Effective hole mass
$m_h^\perp$	Effective hole mass in perpendicular to c-plane
$m_h^\parallel$	Effective hole mass parallel to c-plane
M_b	Bulk matrix element for optical gain in quantum dots
MMF_{spec}	Solar cell mismatch factor
MMF_{ref}	Solar spectrum mismatch factor
n_1	Coefficient for first lattice direction in real space along $\vec{a_1}$
n_2	Coefficient for second lattice direction in real space along $\vec{a_2}$
n_3	Coefficient for third lattice direction in real space along $\vec{a_3}$
n_r	Real part of refractive index.
Δn	Excess electron concentration
n	Electron concentration
n_0	Electron concentration at equilibrium
n_p	Minority carrier concentration in *n*-type material
n_{2D}	2D carrier concentration in quantum well
n_{QD}	Areal quantum dot density
N_C	Effective density of states in the conduction band
N_V	Effective density of states in the valence band
n_i	Intrinsic carrier concentration
N_d	Donor concentration
N_a	Acceptor concentration
N_d^-	Ionized donor concentration
N_a^+	Ionized acceptor concentration
N_{tj}	Number of electrons in trap j
N_1	Number of non-degenerate states
N_2	Number of states including spin degeneracy
n_{id}	Ideality factor
P_s	Irradiance from the sun
p	Hole concentration
p_0	Hole concentration at equilibrium
$\vec{\mathbf{p}}_{cv}$	Photon momentum operator
p_n	Minority carrier concentration in *p*-type material
Δp	Excess hole concentration
P_s	Photon flux from the sun
P_{in}	Power incident on a solar cell
P_m	Maximum power density point
$P_{c\epsilon}$	Conduction band hydrostatic energy shift

Symbol	Variable
P_{PZ}	Piezoelectric polarization component
P_{SP}	Spontaneous polarization generated by a solar cell
P_t	Maximum power of the solar cell
P_{out}	Power generated by a solar cell
q	Elementary charge
Q	Total charge
Q_n	Total charge in *n*-type side of depletion region
Q_p	Total charge in *p*-type depletion region
Q_s	Photon flux above bandgap incident on a solar cell
$\vec{\mathbf{R}}$	Real space lattice vector
r_{QD}	Quantum dot to wetting layer gain ratio
r_{QD}^{sp}	Spontaneous emission rate in quantum dot and wetting layer
R_n	Electron recombination rate
R_p	Hole recombination rate
R_{srh}	Shockley-Read-Hall recombination
R_{sp}	Spontaneous emission rate
R_{au}	Auger recombination rate
$R_{n,rad}$	Electron radiative recombination rate
$R_{p,rad}$	Hole radiative recombination rate
U	Potential
S_f	Electron flux density
SR	Spectral responsivity
t_{ij}	Transfer matrix coefficient for quantum well and barrier
t_{au}	Auger recombination time
t_b	Broadening lifetime parameter
t_{QD}	Quantum dot thickness
T	Temperature
T_s	Temperature of sun
T_{cell}	Temperature of sun
u	Anion-cation bond length ratio
V_0	Potential inside well
$V(r)$	Potential
V_k	Volume in reciprocal space
V_{state}	Volume of single k state in reciprocal space
V_{oc}	Open circuit voltage
V_m	Voltage at maximum power point

Symbol	Variable
V	Voltage
V_a	Applied bias
V_k	Volume in k space
w	Total energy of electron
x_d	Depletion width
x_n	Extent of depletion region on *n*-type side
x_p	Extent of depletion region on *p*-type side
α	Absorption coefficient
β_s	Spectral photon flux emitted per unit solid angle
β_c	Spectral photon flux incident per unit solid angle
Γ	Energy level broadening parameter
δ_{ij}	Kronecker delta function
Δ_{so}	Spin-orbit splitting of the valence band energy
Δ_1	Wurtzite crystal-field split energy
Δ_2	Wurtzite spin-orbit band parameter
Δ_2	Wurtzite spin-orbit band parameter
ϵ	Permittivity of free space
ϵ_r	Relative permittivity
ϵ_s	Semiconductor permittivity
ϵ_{strain}	Strain
ϵ_{ij}	Strain tensor elements for dimensions $i, j \in \{x, y, z\}$
η_{AM}	Air mass
η	Solar cell efficiency
θ_w	Wurtzite band parameter
θ_k	Wurtzite band parameter
θ_ϵ	Wurtzite band parameter
$\theta_{1/2,sun}$	Half angle subtense of the sun from Earth
θ	Zenith (vertical) angle
λ	Photon wavelength
λ_k	Wurtzite band parameter
λ_ϵ	Wurtzite band parameter
μ_n	Electron mobility
μ_p	Hole mobility
μ	Chemical potential
μ_1	Chemical potential for first intermediate band transition
μ_2	Chemical potential for second intermediate band transition
ν_{drift}	Figure of merit for drift-dominated intermediate band solar cells

Symbol	Variable
$\bar{\nu}_n$	Average thermal velocity of electrons
$\bar{\nu}_p$	Average thermal velocity of holes
∇	Three dimensional partial spatial derivative
ρ	Charge density
σ_{nj}	Electron capture cross section
σ_{pj}	Hole capture cross section
τ	Carrier lifetime
τ_w	Hot electron relaxation time
$\tau_{n,srh}$	Electron SRH lifetime
$\tau_{p,srh}$	Hole SRH lifetime
τ_{nj}	Electron lifetime at trap j
τ_{pj}	Hole lifetime at trap j
τ_{hc}	Relaxation time for hot carriers
Φ_s	Solar spectrum
Φ_m	Measured source spectrum
Φ_{bi}	Built-in voltage
$\Phi_{\lambda,ph}$	Spectral photon flow
ϕ	Azimuthal (horizontal) angle
Ψ	Carrier wavefunction
Ω_s	Solid angle
ω	Angular photon frequency

"If I have seen further it is by standing on the shoulders of Giants."

—Isaac Newton

ACKNOWLEDGEMENTS

There were many who helped in my journey through the PhD program that I would like to thank.

To my lovely wife Trista, who worked on her PhD thesis the same time I was working on mine, you are always there to support me as we navigated our doctoral studies. You helped me every step of the way and inspired me to always strive to do my best in all aspects of life. I couldn't imagine doing it without you!

Thanks to my mom and dad for being the best parents I could have ever asked for! Thanks to my sisters Noor and Sherry, and my in-laws Terrilynne and William for always supporting me. I owe so much to how much love we have in the family!

A very big thank you to my thesis supervisor and mentor Dr. Karin Hinzer for accepting me as her student when I couldn't continue my previous PhD project. Completing a PhD in physics was my major life goal and you made it possible despite life's uncertainties! The opportunities and experiences I had to pleasure of having throughout my PhD (thanks to your hard work!) were rich and numerous beyond what I could have imagined, and you've inspired me to see the opportunities everywhere to do great things.

I am grateful to Dr. Zetian Mi, who is now at the University of Michigan, for the collaboration and for the excellent growth and fabrication experience and capability of his team. The GaN nanowires on silicon your group produces are state-of-the-art and it is clear that your team has worked very hard to make such high quality devices despite a highly sophisticated design! Thanks to Dr. Ashfiqua Connie for the very useful discussion and collaborations. I would like to thank Dr. Sharif Sadaf the useful discussions, walking me through the fabrication process and for his supplementary LED samples provided for study. His expertise in the growth, fabrication and design of the nanowire on silicon samples has aided tremendously in the results of this thesis. Even when the project funding was over, he took the time to collaborate. Thank you so much.

I would also like to thank the students and researchers of the SUNLAB. The collaborative atmosphere fostered by Dr. Karin Hinzer, Dr. Henry Schriemer, and Dr. Jacob Krich is one that has made it a pleasure to call myself a SUNLAB member. Thanks to my other committee members, Dr. Serge Desgeniers and Dr. Stephen O'Leary for their expert advice and comments that helped shape this thesis for the better.

Thanks to CMC Microsystems for the design tools and equipment that are **absolutely** crucial to this thesis work, Ontario Graduate Scholarships for ensuring I can afford to live, Natural Sciences and Engineering Research Council for the research project funding and travel,

Ontario Centres for Excellence for the funding and internships, Canadian Foundation for Innovations for the world-class equipment, and the University of Ottawa for the new building/lab/training.

Finally, I would like to thank all Canadians! Research isn't free, and I always strive to be conscious that it is virtually all funded by taxpayers through government agencies. You have all had a hand in this research and it my best hope you get value from it through the improved scientific knowledge, future commercial ventures to create jobs, improve the environment and well-being for the next generation, and training for the new scientific minds of tomorrow.

CONTENTS

LIST OF FIGURES

LIST OF TABLES

CROSSLIGHT APSYS SCRIPTS

ACRONYMS

AM Air mass

CCD Charge-coupled device

DSSC Dye sensitized solar cell

EDS Energy dispersive X-ray spectroscopy

EL Electroluminescence

IR Infrared

IV Current-voltage

LED Light emitting diode

LDA Local density approximation

MBE Molecular beam epitaxy

MQW Multiple quantum well

PL Photoluminescence

NA Numerical aperture

MP Megapixel

SRH Shockley-Read-Hall

SEM Scanning electron microscopy

STEM Scanning transmission electron microscopy

TEM Transmission electron microscopy

UV Ultraviolet

Part I

INTRODUCTION

Part one of this thesis comprises an introduction to the solar resource, general overview of solar cell development, novel III-nitride materials and the physics of the nanostructuring strategies which bring numerous advantages for building intermediate band and multijunction solar cells.

1 INTRODUCTION

"A star is drawing on some vast reservoir of energy by means unknown to us. This reservoir can scarcely be other than the subatomic energy which, it is known exists abundantly in all matter; we sometimes dream that man will one day learn how to release it and use it for his service. The store is well nigh inexhaustible, if only it could be tapped. There is sufficient in the Sun to maintain its output of heat for 15 billion years. "

— Sir Arthur Stanley Eddington, 1920

The sun is the cause for the existence of virtually all life on Earth. The heat and light from the sun is what has sparked the very first organic life on Earth, followed by billions of years of evolution. The sun has since remained a consistent input of energy for the Earth. The existence of life itself has led to organisms themselves becoming a future source of chemical energy upon death in the form of hydrocarbons that our civilization has come to rely on as our primary source of energy[1]. The convenience, low cost, and high energy density of coal, oil, and gas are the primary reasons for their prevalence in modern world's energy consumption. It is this convenience in combination with the world's growing need for energy to drive economic progress which has led to serious projected economic and environmental issues such as climate change[2]. Not only are these "fossil fuels" a limited resource, there are many negative and largely unforeseen consequences associated with their heavy usage. The pollution from burning hydrocarbons is a major detriment to human health[3] and the environment[4]. The quantity of carbon dioxide being released in a very short time is far from insignificant, unprecedented in history[5], and its effect on the Earth's climate is global and extremely difficult to control and predict[6].

Hence, the search for alternate sources of energy is an environmental and economic priority. Ideally, a source of energy and its conversion process should have no negative impact on the environment, be predictable, reliable, virtually renewable, affordable, occupy minimal volume, have a high energy density and be easy to store. Light from the sun can satisfy most of these desired traits. The photovoltaic effect in particular is a physical process in which the light matter interaction with special materials can produce renewable electrical power that is available whenever the sun is shining. It is also fortunate that the amount of energy in the form of light that reaches Earth is far beyond our current energy requirements, is completely renewable for billions of years and produces no harmful by-products during operation.

Semiconductor materials are the fundamental ingredient in modern electronic devices, including solar cells. They remain at the forefront of technological research and development due to their unique

electronic structures, and hence highly controllable conductivities that are relatively constant in insulators and metals. Light from the sun can produce free charge carriers in semiconductors that can flow as a current at certain electrical potential difference to perform electrical work. However, not all semiconductors are ideal for this purpose. As a hot black body emitter, light emitted by the sun comes in a spectrum of wavelengths, ranging from X-rays to radio waves. The vast majority of the light from the sun falls in the visible to near-infrared spectral range of light, which can either be transmitted, reflected, or absorbed by materials. Semiconductors with large gaps in their electronic structure can provide higher voltage electrical power at the expense of lower current by restricting their absorption to short wavelength photons and transmitting a significant fraction of light. Those with smaller gaps in their electronic structure have the opposite problem, where high current is achieved at the cost of losing the majority of photon energy to heat, yielding low operating voltages by allowing longer wavelength photons to be absorbed.

The optimization of electrical power via the photovoltaic effect requires a judicious choice of bandgap for moderate voltage and current. This trade-off leads to what is known as the *Shockley-Quiesser limit* of power conversion efficiency[7]. The maximum of this limit using the solar spectrum leads to an ideal semiconductor bandgap of around 1.2-1.3 eV, with a peak efficiency of a single cell of around 30% under typical sunlight conditions on earth, and about 40% at the absolute limit of concentrated sunlight.

The seemingly unavoidable losses arise from the thermalization of excited carriers excited by photons with energies over 1.2-1.3 eV and the transmission of photons with energies less than 1.2-1.3 eV. Additional losses are introduced from thermodynamic considerations of the sun and the solar cell. The non-zero temperature of solar cells and re-emitted light also play a role in reducing the efficiency[8]. The thermalization of carriers is very difficult to avoid as relaxation and thermalization times in semiconductors are typically measured in the picoseconds and femtoseconds, respectively [9–11], releasing energy through phonon interactions from higher conduction band states.

By combining semiconductors of different bandgaps, however, the solar spectrum can be split among separate cells, providing a route to higher efficiency solar cells[12, 13]. The spectrum can be split by optical means, where the portions of the solar spectrum are spatially divided onto various distinct cells using lenses or filters. However, the most common approach is to grow a higher bandgap subcell on top of a lower bandgap solar cell, with thin highly conducting, transparent regions between them to conduct current from one cell to another. The idea is to use the long wavelength transparency of high bandgap materials to sequentially filter the spectrum. This strategy has led to the development of multijunction solar cells, and record high power conversion efficiencies in excess of 46%[14] with recent developments towards six different active subcells[15]. Record solar cell efficiencies are monitored by the National Renewable Energy Laboratory over time[16], and are shown in Figure 1.

The main drawback of the multijunction approach is the cost. As all commercial multijunction designs do not use silicon as the substrate (by far the cheapest crystalline semiconductor substrate), the cost is inherently significantly higher. In addition, the number of exotic semiconductor layers adds to the growth time and material cost. While multijunction cell designs on silicon have been investigated[17–22], there are significant unresolved material quality deficiencies which arise from the lattice mismatch of the bulk silicon/III-V semiconductor interface. These defects can propagate throughout the material, drastically affecting performance[23]. In order to enable these designs monolithically, alternative growth techniques are required to produce quality III-V material on silicon.

Strategies to mitigate the need for lattice matched growth include metamorphic growth[24], porous intermediate layers[19, 25], wafer bonding[26, 27], mechanical stacking[28, 29], and nanowire growth[30]. The latter strategy is a promising method for enabling growth on silicon. Precise control over the growth conditions enables nanowires to form as opposed to the traditional bulk layer-by-layer growth of traditional devices. The finite width of the nanowire base on the substrate prevents the build-up of the strain sufficient to cause lattice dislocations[31]. Nanowires also improve on the ability to absorb broadband incident light[32], use less material[33], and can host aligned quantum dots[34, 35]. As a result, a large amount of nanowire growth occurs on silicon to provide a low-cost template for future devices.

With the growth material restrictions alleviated, new solar cells can be grown directly on silicon using a greater variety of semiconductor materials. One of the most promising new materials is the $In_xGa_{1-x}N$ alloy, which has one of the largest band gap ranges of all semiconductor alloys, varying from 3.4 eV for GaN to 0.7 eV for InN. This range of possible bandgaps spans more than 90% of the solar irradiance through control of the relative fraction of indium and gallium atoms. Indium gallium nitride is now used for virtually all "white light" LEDs for residential and commercial lighting to provide blue light and the source for phosphorescence across the rest of the visible spectrum. One of the major challenges to $In_xGa_{1-x}N$ growth involves the incorporation of high indium fractions due to the high vapour pressure of InN. Using nanostructured growth, higher indium fractions in wurtzite InGaN can be directly grown on silicon wafers with high material quality[36]. This has tremendous promise for new solar cells designs, where large bandgap tunability and the use of low cost substrates can be achieved in a single solar cell.

Multijunction structures using nanowires can allow for high conversion efficiencies along with all previously stated advantages, however, going beyond two junctions introduces difficulties in fabricating tunnel junctions due to the difficulty in achieving activated *p*-type doping for improving the hole mobility[37, 38]. Increasing the height of nanowires beyond a few microns places greater difficulty in maintaining nanowire uniformity, where the height uniformity of nanowires improves the overall device performance[39]. An elegant alternative for attaining high efficiency solar cells is to form an intermediate

band of accessible states within a large band gap material. This allow the absorption of low energy photons via this intermediate state, while maintaining the large operating voltage of the large bandgap material[40]. In principle, this effect has the potential to increase the conversion efficiency to 63% for a single intermediate band[40], and up to 80% for multiple intermediate bands[41] under full concentration.

For wide bandgap materials such as GaN and the alloy InGaN, there is an even greater potential with intermediate band designs[41, 42]. An intermediate band in GaN can be realized using InGaN quantum dots/wells within a GaN host material[43]. By pairing quantum dot growth with nanowire growth, the density and alignment of quantum dots per nanowire can be precisely controlled. Nanowires can also restrict the dimensions of the quantum dots for increased control over the confined states[44, 45].

The growth of such nanowires as LEDs and solar cells has successfully been achieved by the group of Dr. Mi at McGill University (now at the University of Michigan)[36, 46, 47]. We intend to investigate the potential and propose design modifications to such LEDS as a next generation solar cell platform through the characterization and simulation of the potential sub-bandgap and tandem optoelectronic properties of the InGaN/GaN quantum-dot-in-nanowire devices. The quantum dots are quite large in lateral size in comparison to typical quantum dots and can be considered quantum discs which approach intermediate characteristics between quantum wells and quantum dots. In this thesis, we label the quantum discs quantum dots with this context under consideration. The electrical and optical characteristics of such nanowire solar cells are assessed experimentally and compared with the simulated performance of device models to determine an optimized solar cell design based on this novel InGaN on silicon platform.

1.1 OVERVIEW

This thesis aims to study the characteristics of InGaN/GaN quantum-dot-in-nanowire solar cells using quantum dots to increase the absorption into the visible region and determine optimized designs for higher power conversion efficiencies under the standard AM1.5G solar spectrum. The quantum-dot-in-nanowire platform is investigated towards its potential for intermediate band solar cells and multijunction solar cells on silicon.

Chapter 2 provides insight and background on the development of semiconductor materials and optoelectronic devices, including InGaN/GaN solar cells. The current status and remaining challenges of solar cells technologies are presented. The basics of semiconductor physics in bulk and nanostructured materials are described. The chapter ends with a discussion of intermediate band solar cells and the suitability of its implementation using the InGaN/GaN material system.

Chapter 3 introduces the theory of semiconductor devices and details the operation principles and various aspects of solar cells. The chapter also includes sections on the simulation techniques used in this thesis for capturing quantum mechanical effects in nanostructured light-sensitive devices.

Chapter 4 comprises a discussion of the numerous types of characterization and growth techniques for materials and devices and their connection to solar cell design. The chapter contains experimental results of this thesis, which has a primary focus on characterization of the optoelectronic properties of the individual nanowires and the fabricated solar cells. A wide range of microscopic/nanoscopic imaging techniques are used assess nanowire properties and the effects of the solar cell fabrication methods on cell performance.

Chapter 5 contains the modelling and simulation results pertaining to nanowire solar cells on silicon. The performance metrics of InGaN/GaN quantum well solar cells and InGaN/GaN quantum dot LEDs are calculated based on various modelling approaches to identify desirable design modifications. The requirements of an InGaN/-GaN quantum well solar cell to become a true intermediate band solar cell is discussed. The limitations and potential research avenues to these simulations are presented.

Chapter 6 focuses on the simulation of a bulk InGaN/Si dual-junction solar cell without any sub-bandgap current generation processes. A realistic silicon subcell is designed for current matching with a bulk InGaN based on the interpolation of experimentally determined absorption coefficients. Consequences and opportunities for a nanowire-on-silicon dual-junction solar cell are discussed.

Chapter 7 is the conclusion of the thesis which investigates the implications of the results, and future work related to realizing an intermediate band solar cell using InGaN/GaN nanowires with dots/wells, as well as other promising avenues and application for solar cells based on nanostructured large-bandgap material.

1.2 MOTIVATION AND CONTRIBUTION

This thesis aims to both characterize and simulated the performance and properties of InGaN/GaN quantum dot-in-nanowire solar cells on silicon. The cost-effectiveness of using a silicon substrate with highly tunable III-nitride semiconductors would allow the efficiency of silicon-based solar cells to include other high efficiency features such as multijunction stacks, intermediate bands, and light trapping through nanostructures. The characterization and simulation work in this thesis is made possible with a collaboration with McGill through the Natural Sciences and Engineering Research Council (NSERC) Photovoltaic Innovation Network (PVIN) Project 11. All growth and fabrication processes are undertaken at McGill University under Dr. Zetian Mi. An organizational chart detailed the contributions and collaborations to the best of my knowledge is shown in Figure 2.

The contributions of this thesis to the field of semiconductor device physics are as follows:

- High resolution electron microscopy, helium-ion, and atomic force microscopy of InGaN/GaN nanowires
- Characterization of the luminescence properties of InGaN/GaN nanowires
- Characterization of reflective properties of densely-packed, randomly distributed InGaN/GaN nanowire ensembles and solar cells
- Characterization of the electrical performance of InGaN/GaN quantum-dot-in-nanowire solar cells
- Low temperature luminescence characteristics of InGaN/GaN nanowire solar cells and LEDs
- Spatially-resolved single nanowire micro-electroluminescence
- Simulation of InGaN/GaN quantum-dot-in-nanowire LEDs
- Simulation of a realistic dual-junction InGaN/Si solar cell
- Demonstration of deep sub-bandgap current generation in InGaN/GaN nanowires
- Insight into carrier transport dynamics in InGaN/GaN quantum dots under various incident photon wavelengths
- Design considerations for realizing intermediate band solar cells from InGaN/GaN quantum well solar cells

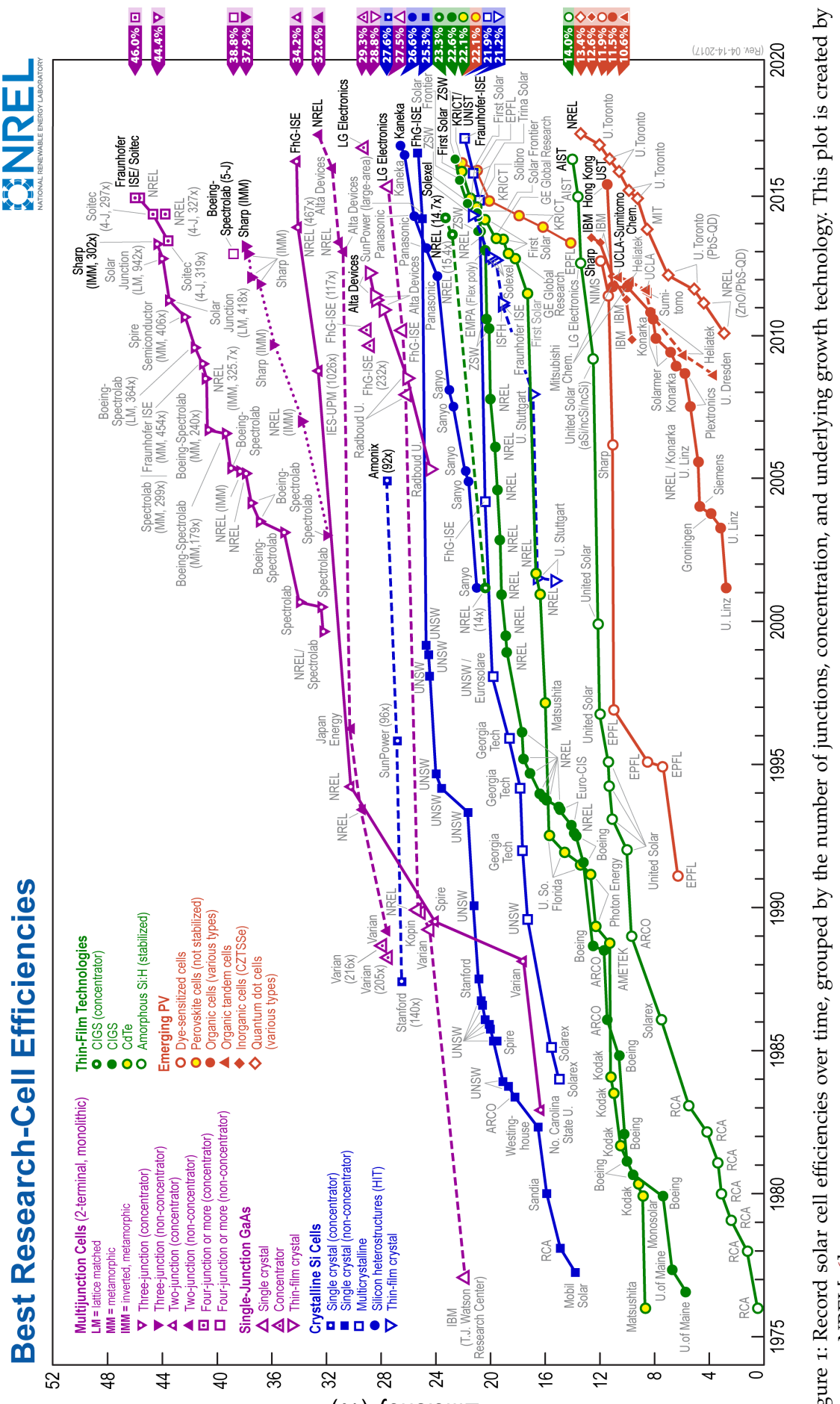

Figure 1: Record solar cell efficiencies over time, grouped by the number of junctions, concentration, and underlying growth technology. This plot is created by NREL[16].

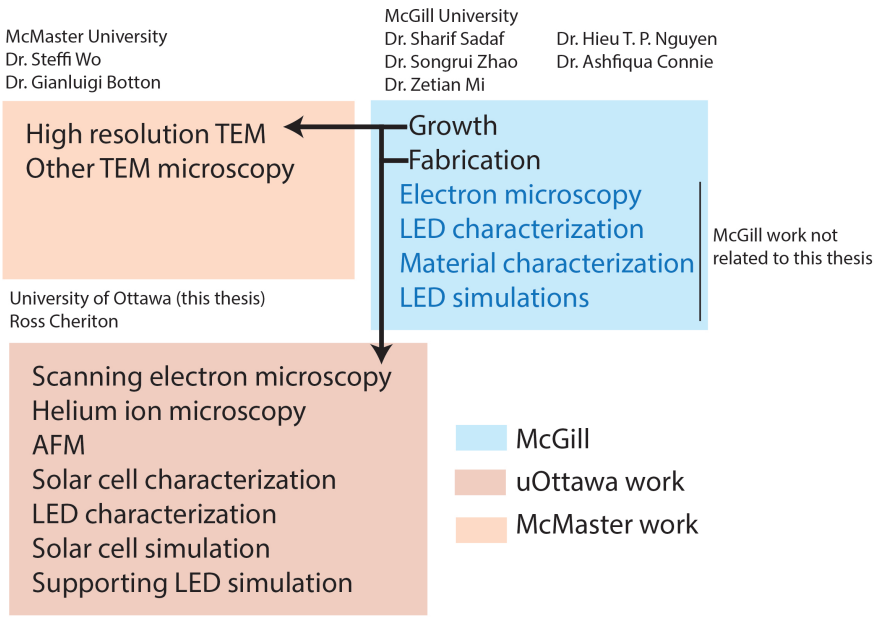

Figure 2: Organizational diagram highlighting the contributions and collaborations involving this thesis. The box in red summarizes the characterization and device simulation work done by the thesis author using samples grown and fabricated at McGill University. Simulation work is largely based on designs of the as-grown nanowire devices.

2

PHYSICS OF SEMICONDUCTORS

"In the late 1960s, red and the low green LEDs and the infrared semiconductor lasers had already been developed, but there was no prospect of practical blue light emitters, even in the '70s."

— Isamu Akasaki, 2014

2.1 BACKGROUND

This section outlines the historical timeline of semiconductor device development, based on papers by Jenkins[48] and Łukasiak[49],The study of semiconductors began in the nineteenth century where the conductivity of materials was mainly of interest. In 1833, Michael Faraday studied silver sulphide, which exhibited the anomalous effect of increasing its conductivity with temperature[50], being the first discovery of a semiconductor property. Just a few years later in 1839, Henri Becquerel found that when platinum electrodes coated in silver chloride were placed in an electrolytic solution of nitric acid, a voltage was produced between the electrodes under illumination by sunlight. This was the first demonstration of the photovoltaic effect[51], the physical process in which solar cells operate. Several decades later in 1873, Willoughby Smith found that the conductivity of selenium (which was considered a metal at the time) varied with the amount of light incident on its surface[52], an effect not seen in other types of metals. These series of discoveries implied that a new group of materials exists, one which is distinct from traditional metals or insulators. In 1874, rectification was demonstrated in various metal-oxide combinations by Carl Ferdinand Braun[53]. This is recognized as the first semiconductor diode and spawned the idea that electronic devices with unique properties can be fabricated using a combination of semiconductor and metal. In 1883, Charles Fritts produced what is now considered the first photovoltaic cell[54]. The cell was created using a thin layer of molten selenium poured onto a metal surface, which was then covered with gold leaf. The gold leaf was sufficiently thin to allow for some light to pass through and be absorbed by the selenium layer.

Despite the accomplishment, the theory behind the light-matter interaction with semiconductors and solar cells was not well understood and further progress was hindered. The lack of applications for semiconductors also slowed the development of semiconductor devices prior to the twentieth century. A promising route towards semiconductor usage emerged through radio from the discovery and detection of radio waves in 1887[55]. At the turn of the century, both Braun and Sir J. C. Bose aimed to use semiconductor rectifiers as part of radio frequency detection devices. Between 1902 and 1906,

Greenleaf Whittier Pickard worked on testing a variety of materials for rectification properties. Working for AT&T, he apparently tested tens of thousands of materials, of which fused silicon was the most promising in its stability of rectification[56]. However, with the arrival of three terminal devices in vacuum tubes as amplifiers around the same time, the interest in the semiconductor diode waned.

The improvement to semiconductor diodes and photocells came with larger area copper oxide and selenium devices that could operate at higher currents and were suitable for battery charging and light sensors. The dominance of the vacuum tube continued until radar required increasingly higher frequencies, where semiconductor diodes demonstrated lower capacitances necessary in high frequency devices.

The development of more advanced semiconductors required a more fundamental understanding of materials and their conductivity. In 1931, Alan Wilson described the conductivity of semiconductor in terms of energy gaps between electron states[57]. This allowed for traditional semiconductor physics to explain how doping affects the conductivity of a material, as well as how the conductivity changes with temperature.

Radar still required more reliable and higher quality semiconductor materials to improve in performance. Hence in 1935, R. S. Ohl worked on improving the purity of silicon by the melting and resolidification of an ingot of relatively pure silicon. The separation of impurities (namely aluminum, boron and phosphorus) in this process allowed for silicon as pure as 99.999% to be achieved. Not only did such silicon make a better diode, but a very strong photovoltaic effect was observed[58, 59]. This method is not dissimilar from today's method of diffusing dopants to form a *p*-*n* junction. Indeed, it just so happens that the very impurities that plagued device performance in earlier diodes such a boron and phosphorus are *p*-type and *n*-type dopants used in solar cells today!

By 1942, germanium *p*-*n* junctions were being made with relative ease as a result of the purification of germanium[60]. These germanium diodes demonstrated excellent performance for the time and were considered for a solid-state version of the vacuum tube-based triode. This device would become known as the transistor, which has revolutionized our entire society and become the fundamental component in electronic devices in use today. William Shockley and others would go on to drive the development of the transistor based on a gate voltage that would dynamically modify the effective conductivity of the device[61, 62].

Various iterations of the transistor were developed with the goal of handling increasingly larger currents with increased stability. The use of the Czochralski method[63] developed back in 1918 allowed germanium of sufficient quality to be grown and compete with the vacuum tube. With germanium semiconductor devices successfully being produced, the last major innovation came with the switch to silicon. The larger bandgap of silicon prevented the significant generation of thermally excited free carriers, leading to even more sensitive

devices that can operate at higher temperatures. This switch would occur with the development of the floating zone technique[64] which led to impurity levels of less than 10^{10} cm^{-3} in silicon ingots.

The development of integrated circuits would continue in parallel with the development of photovoltaic cells. In 1954, Daryl Chapin, Calvin Fuller and Gerald Pearson at Bell Laboratories created the first photovoltaic cell that could produce significant power[65]. Over time and through multiple advances in material quality and design, the efficiency of silicon solar cells would improve to reach 26.3%[66] as of the publication date of this thesis. The development of cheaper thin film solar cells would keep pace with cells exhibiting about 5% absolute efficiencies lower than silicon and steadily improve to a present day record of about 23% for copper indium selenide cells[67], and about 22% for a perovskite solar cell[68].

The gateway to higher efficiencies was through the development of multijunction solar cells in the late 1970's. The first multijunction solar cell was fabricated by Bedair *et al*. using an AlGaAs/GaAs dual junction design[69]. A second dual-junction design was made using InGaP/GaAs and used for deployment in spacecraft for its radiation hardness and high efficiency[70]. The first triple junction solar cell for space applications was formed in the late 1990's by combining InGaP, InGaAs and germanium[71]. The thinner and hence lighter weight of germanium substrates as opposed to gallium arsenide substrates, along with the higher efficiencies was the major appeal for space-based solar power. With these high efficiencies and the knowledge of significantly improved efficiencies with concentration, interest in modifying germanium-based triple junction solar cells for terrestrial applications increased. The record of 41.6% based on lattice-matching with germanium was subsequently matched with different designs which allowed for improved current matching between subcells[72].

For higher numbers of junctions, the efficiency is projected to increase to 50% in realistic designs[73]. However, the increasing complexity of multijunction solar cells coupled with their exotic materials leads to a significant areal cost. A parallel, yet fundamentally different approach lies in the development of cost-effective solar cells. Thin-film solar cell materials types such as copper indium gallium selenide (CIGS), organic, perovskites, and amorphous silicon aim for cost reductions at moderate efficiencies to gain commercial viability.

In contrast, no commercial InGaN solar cells current exist due to uneconomical growth and insufficient material quality in faster growth methods such as molecular beam epitaxy (MOCVD). Nonetheless, InGaN solar cells have been proposed a result of their exceptional radiation hardness[74], large bandgap tunability, high electron mobilities[75], drift velocity[76, 77], thermal conductivity[78], and high temperature operation[79]. The recent interest in InGaN solar cells came as a result of the revision of the InN bandgap at 0.7 eV[80–87], which was previously thought to be around 2 eV[88, 89].

2.2 SEMICONDUCTORS

The interaction between light and matter has always been an important field of study in physics. While reflection, transmission, and absorption of light incident upon a material are basic properties that are evident upon experiment, they are dictated by the interaction of the atomic energy levels with the electric field of the photon. In solid materials, individual atoms are densely packed such that their discrete electronic energy levels overlap with one another, hybridizing on a large scale to form a continuous band of energy levels. The structure of these bands, known as the **band structure**, as a function of energy and electron momentum, controls the reflection, transmission and absorption that are unique to each material.

The configuration of the band structure relative to the energy level at which electrons have a 50% chance of occupying, known as the **Fermi level**, has led to the classification of three distinct regimes of materials which we know as metals, semiconductors and insulators. When a photon is incident on a material, absorption can occur if the photon energy is approximately equal or greater to the energy difference between occupied and unoccupied bands.

In all materials, there are accessible bands of states which are delocalized across the crystal lattice. These collections of states are referred to as **conduction band** states as they permit the movement of electrons throughout the material. This is contrasted to electrons in the **valence band**, which are highly localized around the atoms in the crystal as there are no empty states at similar energies for charge transport to occur. The difference between the lowest energy of the conduction band and the highest energy of the valence is the **bandgap** of the material.

For metals, the conduction band states are populated even without external excitation, resulting in free electrons within the material. This can be interpreted as a zero or negative bandgap, depending on the metal. These free electrons will respond to the electric field of photons by oscillating such that the incident field inside the metal remains zero, creating an identical field being produced in the reverse direction, which we perceive as reflection.

Insulators are materials which have such a large energy gap between the valence and conduction band states, that there will be only be a negligible number of carriers in the conduction band under typical conditions. Insulators require high energy photons or electrons incident upon them to produce free carriers since the bandgap is so large.

For semiconductors in equilibrium, the Fermi level lies in the center of the bandgap. This results in electrons completely occupying the valence band states, and a virtually empty conduction band. Incident photons with energy greater than the band gap of the semiconductor can be absorbed, while the material is transparent to lower energy photons. In the lack of light or heat, most pure semiconductors at room temperature are highly insulating as few electrons have sufficient thermal energy to occupy the conduction band. It turns out that

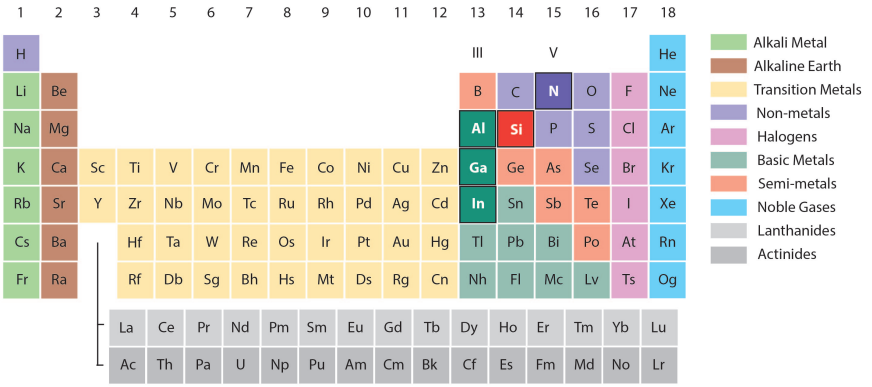

Figure 3: Periodic table of the elements. The elemental components which make up the III-V nitrides are indium, gallium, aluminum and nitrogen. Silicon is also highlighted as it is the substrate used this thesis.

semiconductors are naturally suited for direct solar energy power conversion as a result of this bandgap.

The periodic table of the elements contains elements which are semiconducting in their pure form, with many more resulting from a combination of two of more elements. The elements that are semiconducting in their pure form are highlighted in Figure 3. Not all semiconductors can be used for high efficiency solar cells either since their bandgap value places limits on the maximum possible solar cell efficiency. A bandgap that is too large would result in few photons being absorbed despite a high operating voltage. On the contrary, a small bandgap absorbs much more photons, but results in a low operating voltage.

The group IV materials can form semiconductors from a single atomic species with diamond-type cubic lattices. Silicon and germanium both form semiconductors with moderate band gaps of 1.11 eV and 0.67 eV, respectively, which correspond to the solar spectrum. The bandgap of carbon depends on which of the many allotropes it has formed, where it can be either insulating or metallic. The properties of carbon are highly dependent on the allotrope, where it can be a semi-metal (graphite), a semiconductor(graphene on SiC)[90] or an insulator (diamond). Silicon is by far the most common semiconductor material, owning to its abundance, moderate bandgap, low cost, and mature fabrication technologies. The indirect bandgap of silicon, however, makes it a poor absorber at longer wavelengths and a poor light emitter, both of which are not ideal in photovoltaic materials.

There are numerous semiconductors that can be formed through the combination of group III and group V elements, as well as group II and group VI elements. These combinations usually result in compound semiconductors, which are charge neutral solid materials that demonstrate a range of bandgaps which are roughly inversely proportional to the size of the atomic species and unit cell lattice constant. Figure 4 illustrates the bandgap variation with lateral lattice constant for a variety of different semiconductors with a focus on InGaN.

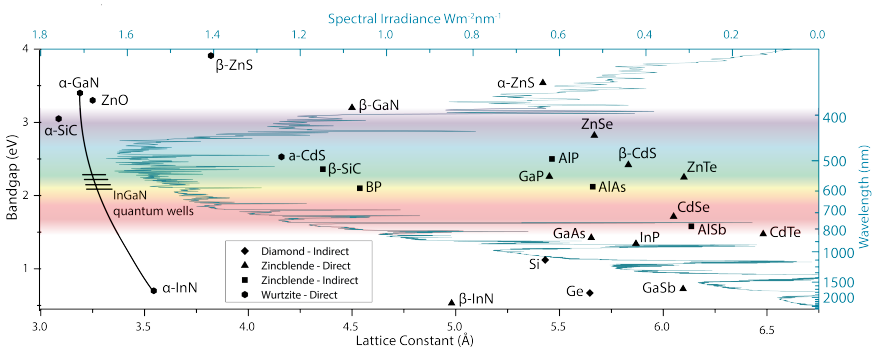

Figure 4: Band gap versus lattice constant for the most common semiconductors. The $In_xGa_{1-x}N$ band gap variation is drawn with a line. The AM1.5G solar spectrum is overlaid in turquoise. Data is obtained from http://www.matprop.ru/semicond[91], and http://www.semiconductors.co.uk/[92].

For the III-V compound semiconductors, combinations of three elements can demonstrate materials with tunable properties. This enables the tailoring of semiconductor bandgaps and lattice constants for high quality growth of a variety of semiconductors on a few different binary semiconductor compound substrates. Extending the alloy to four or more compounds can lead to independent control over the lattice constant and bandgap.

2.2.1 *Gallium Nitride*

Gallium nitride is a large bandgap semiconductor that is transparent to visible light. The lattice structure is typically of the wurtzite configuration and has a hexagonal Bravais lattice with a Ga-N basis. Zincblende GaN is not energetically favoured under most growth conditions and is less common as a result. The nanowires discussed in this thesis possess the wurtzite crystal structure. For wurtztite GaN, the gallium and nitrogen atoms are arranged in alternating layers of interpenetrating 2D hexagonal lattices. Figure 5 illustrates the crystal structure in both real-space and reciprocal space.

The development of GaN devices was spurred by research into blue light emitting diodes (LEDs). The growth of single crystal GaN had been achieved in 1968[93], followed quickly by the demonstration of blue LEDs grown using halide vapour phase epitaxy (HVPE)[94]. Despite these initial breakthroughs, the efficiency and colour control of such devices were quite poor. The production of commercially viable GaN devices would have to wait until the problems of impurity contamination and crystal quality improved, as well as the ability to create sufficient quality *p*-type GaN.

Once the technique of metal organic chemical vapour deposition (MOCVD) had been sufficiently developed, significant progress began to occur towards realizing high quality GaN crystals. This included cooling the reactor walls and removing the need for requiring

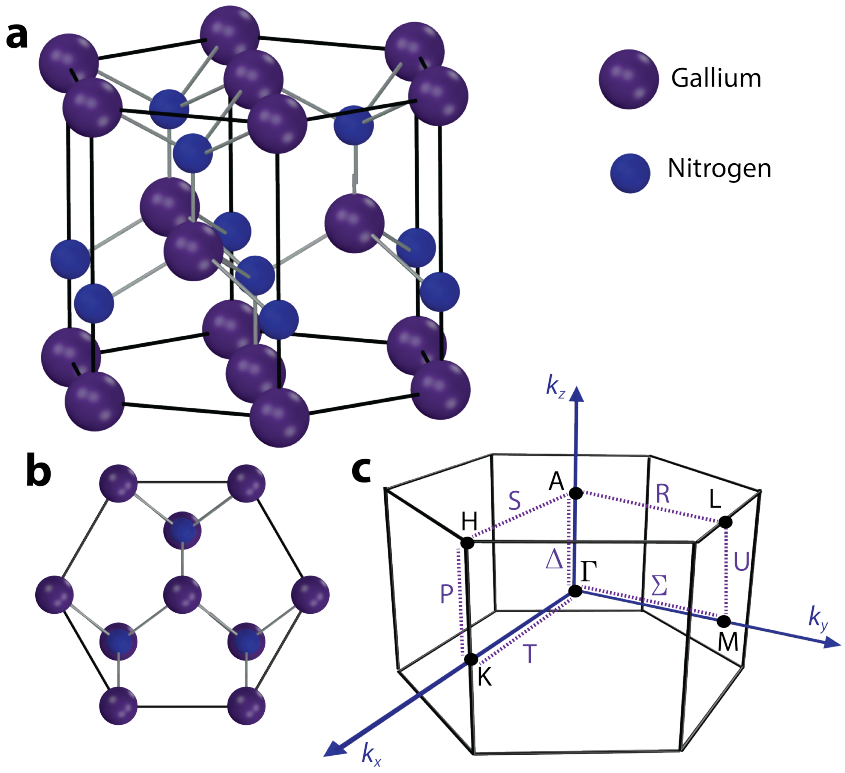

Figure 5: Crystal structure of wurtzite GaN from (a) an angled view (b) and plan view in the [0001] direction. (c) Brillouin zone in k-space of wurtzite-GaN showing high symmetry points and vectors. Asymmetry found in relaxation of real GaN crystals is not shown.

hydrogen chloride, which was the primary source of oxygen contamination from water which was difficult to remove.

The GaN devices at the time emitted blue light as a result of the intentional but unactivated magnesium dopants which remained bonded to a hydrogen atom. Impact ionization of an electron creates a free electron that can recombine with the hole left from the magnesium-hydrogen pair, followed by another recombination with another magnesium dopant. The move towards true band-to-band recombination of carriers would require the alloying of indium to lower the bandgap to correspond with visible light.

In 1995-1996, the first high brightness InGaN/GaN LEDs and lasers were grown with a quantum well structure on sapphire which removed the need for doping in the recombination region[95]. Upon these developments that were deemed worthy of a Nobel prize, the InGaN/GaN quantum well system has been the template for developing commercial optoelectronic devices which operate at the UV and visible wavelength region of visible light.

It is also possible (although extremely difficult) to form bulk GaN (>100 μm dimensions) using gallium and ammonia powders [96], chemical vapour transport techniques[97], and ammonothermal seeds with semi-bulk GaN growth using halide vapour phase epitaxy HVPE[98]. Crystal quality, growth rates, and cost are still existing issues such that heteroepitaxy is currently the dominant growth method for gallium nitride.

2.2.2 *Indium Gallium Nitride*

Prior to 2002, interest in InGaN as a semiconductor was quite low. The established bandgap for pure InN was around 2 eV, which means its optoelectronic operating range would be decidedly from the near ultraviolet to the colour red. Despite the initial attractiveness of this wavelength range, producing high quality InGaN material with a high indium molar fraction proved too great a challenge for current growth techniques. This initial bandgap estimation was supported by absorption sputtered and metalorganic vapor-phase epitaxy grown indium nitride films. Such materials demonstrated a vanishing absorption coefficient around 1.9 eV[99] with theoretical work supporting[100, 101] from a lack of growth and accurate physical parameters of indium nitride. However, with increasing indium nitride film quality, annealing, and lower doping concentrations, absorption deep into the near-infrared began to emerge.

In 2002, numerous groups (Wu *et al.*, Davydov *et al.*, Matusoka *et al.*, Hori *et al.* and Inushima *et al.*) began to report photoluminescence, X-ray diffraction, and density functional theory calculations which pointed to an InN bandgap of 0.6-1.0 eV[80–87, 102], as opposed to the previous accepted value of 2 eV. Additional theory work suggested the error was a result of the reliance on the so-called *band-gap-commoncation rule* and explained the reasons for the anomaly[103].

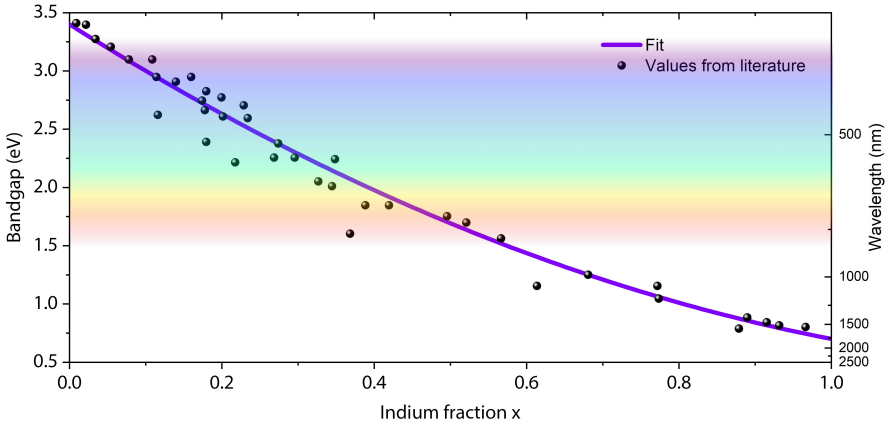

Figure 6: Experimentally determined values of the bandgap as a function of indium composition for InGaN[81, 105–115]. A curve with bowing parameter of 1.4 eV is drawn that corresponds to strained InGaN.

The result was the redefinition of the bandgap of InN and a renewed interest in the InGaN material system. InGaN was now a material that could be used for laser diodes and photodiodes in fiber-optic communications. Over the following decade, the bandgap for InN was re-established at 0.7 eV.

While the bandgaps of InN and GaN were quickly agreed upon by various groups, the bowing parameter for alloys in between were less understood. It is proposed that photoluminescence and cathodoluminescence experiments underestimate the bandgap[104] as optical transitions can involve states below the bandgap. The bandgap can be described by a modified version of Vegard's law for semiconductor bandgaps,

$$E_{InGaN} = xE_{InN} + (1-x)E_{GaN} - bx(1-x), \tag{1}$$

where in the case of InGaN b is approximately 1.4 eV according to experimental data[81, 105–115]. The bowing parameter used in this thesis is 1.4 eV, as opposed to the larger bowing parameter of about 2.8 eV expected for completely relaxed InGaN[116]. Since the InGaN quantum dots are within a GaN matrix, strain in the quantum dots is expected to exist. Figure 6 shows the change in bandgap of InGaN with indium fraction.

The newly discovered bandgap range is also very desirable for solar cell applications. As the optimal power conversion efficiency from the solar spectrum is found by using a semiconductor with a 1.2 eV bandgap, an InGaN solar cell can in principle have a more desirable bandgap than either silicon or GaAs.

Unfortunately, the growth of InGaN films with high indium fractions is quite challenging for multiple reasons. Firstly, the spacing between indium and nitrogen atoms in InN is quite different from that of gallium and nitrogen in GaN. This leads to dislocations in the crystal lattice. Secondly, InN has a very high vapour pressure when compared to GaN, resulting in the preferential incorporation of gallium over indium in InGaN alloys. Thirdly, there is a significant

Spontaneous Polarization Calculation	GaN	AlN	InN
P_{SP} (LDA-DFT)	-32	-99	-41
P_{SP} (GGA-DFT)	-34	-90	-42

Table 1: Spontaneous polarization parameters calculated via LDA Bernardini[118] for the III-nitride materials in units of mC/m^2.

difference in the formation enthalpies between InN and GaN which causes indium to segregate into clusters.

The growth quality of InGaN is heavily dependent on a variety of factors as the sub-optimal conditions leads to either high indium segregation into clusters which accelerate the accumulation of indium as they grow larger, or a lack of indium being present in the epitaxial layers. The challenge of integrating indium into the film while maintaining homogeneity has spurred a heavy focus on optimizing growth conditions. Successful growth of high indium InGaN are typically achieved only with very thin layers.

2.3 POLARIZATION IN III-NITRIDE MATERIALS

One of the benefits to using III-V semiconductors is the possibility to combine materials with very different optical properties monolithically into a single device if the lattice strain is managed. The interface between two different III-V semiconductors, however, can give rise to charge accumulation at the interface that affect carrier transport depending on the material combination. There are two types of polarization effects that can arise for materials: spontaneous polarization and piezoelectric polarization where the non-centrosymmetric crystal structure of the III-nitrides leads to a non-isotropic polarization field.

The total polarization is a simple sum of the two polarization components:

$$P = P_{PZ} + P_{SP}, \tag{2}$$

In zincblende III-V semiconductors, there is no spontaneous polarization as all bonds are intrinsically symmetric. In III-nitride structures, which are usually wurtzite in crystal structure, there is an intrinsic asymmetry that can heavily influence the transport of carriers, especially in multiple quantum well structures. The relevant spontaneous polarization parameters are shown in Table 1 for different III-nitride materials as obtained from Bernadini *et al*. using Berry-phase polarization theory. The calculation uses a generalized gradient approximation in density functional theory (GGA-DFT)[117] after refinements to the results obtained from the initial local density approximation (LDA) approach in density functional theory (DFT)[118].

Piezoelectric polarization parameters	GaN	AlN	InN
Lattice constant a (Å)	3.197	3.108	4.580
Lattice constant c (Å)	5.210	4.983	5.792
Piezoelectric constant e_{13} (mC/m^2)	-37	-62	-45
Piezoelectric constant e_{33} (mC/m^2)	67	150	81
Elastic constant C_{13} (GPa)	68	94	70
Elastic constant C_{33} (GPa)	354	377	205

Table 2: Piezoelectric polarization parameters for the III-nitride materials as obtained from Berandini *et al.*[117].

For alloys, such as $In_xGa_{1-x}N$, the spontaneous polarization is a linear interpolation of the spontaneous polarizations the binary alloy parameters which is calculated using the formula below:

$$P_{SP} = P_{SP,GaN} + P_{SP,InN}(1-x). \tag{3}$$

The piezoelectric polarization in GaN, AlN or InN is caused from compressive and tensile strain between different lattice constants of the two materials and is calculated from

$$P_{PZ} = 2\frac{a-a_0}{a_0}\left(e_{31} - e_{33}\left(\frac{C_{13}}{C_{33}}\right)\right), \tag{4}$$

where a and a_0 are the strained and unstrained lattice constants for the material. This formula does not take into account any relaxation of lattice. The piezoelectric polarization parameters are shown in Table 2. The simulation of realistic III-nitride devices, especially those which use InAlN, requires the treatment of the polarization charge at the interface. In the case of recent device designs, the polarization effects can actually be leveraged for improved performance either as increased transport through tunnel junctions[119, 120], superlattices[121, 122] or carrier localization for LED applications[123, 124]. The total polarization charge at the interface as a function of molar fractions for various alloys is shown in Figure 7.

2.4 BLOCH WAVES IN SEMICONDUCTORS

When atoms condense into solid matter, the discrete atomic states overlap to form hybridized or molecular states. In the limit of macroscopic crystals, the states form a band that we typically associate with bulk semiconductors. We can determine the density of these states by starting with a sphere in reciprocal *k*-space. In perfect crystals, the orderly arrangement of an incredibly large number of atoms sets up a periodic boundary condition of the potential. This potential U must be the same at every point in the **Bravais lattice**, or infinite periodic arrangement of unit cells. Mathematically, this is described as

$$U(\vec{r}+\vec{R}) = U(\vec{r}), \tag{5}$$

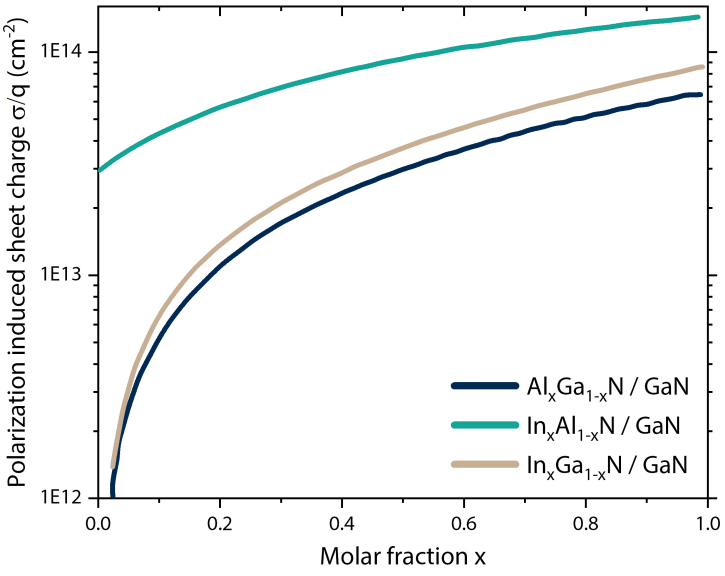

Figure 7: Polarization charge at the interface of various III-V semiconductors with GaN.

where $\vec{\mathbf{R}}$ is a lattice vector in real space

$$\vec{\mathbf{R}} = n_1\vec{a_1} + n_2\vec{a_2} + n_3\vec{a_3}, \tag{6}$$

and n_i are the linear combination coefficients of the real space primitive lattice vectors.

Electrons are the active elements of the lattice which allow the atoms to participate in bonding, and they are described by their wavefunctions. The electron wavefunctions are solved by the Schrödinger equation

$$H\psi(\vec{r}) = \left(-\frac{\hbar^2}{2m}\nabla^2 + U(\vec{r})\right)\psi(\vec{r}) = E\psi(\vec{r}). \tag{7}$$

These otherwise free electrons wavefunctions are modified by the function $u(\vec{r})$ which is periodic with the crystal lattice so their wavefunctions are of the form

$$\psi(\vec{r}) = e^{i\vec{k}\cdot\vec{r}}u_{n\vec{k}}(\vec{r}). \tag{8}$$

The function $u_{nk}(\vec{r})$ is periodic such that

$$u_{n\vec{k}}(\vec{r}+\vec{\mathbf{R}}) = u_{n\vec{k}}(\vec{r}), \tag{9}$$

where n is the index of independent eigenstates at each k, and $\mathbf{k}$ is the wavevector in reciprocal space. Equations 8 and 9 form what is known as Bloch's theorem.

In real crystals, the wavefunction is also periodic in three dimensions so that

$$\psi\left(\vec{r}+\left(n_1\vec{a_1}+n_2\vec{a_2}+n_3\vec{a_3}\right)\right)=\psi(\vec{r}), \tag{10}$$

where n_1, n_2, and n_3 are integers indicating primitive cells of the crystal in each direction $\vec{a}_1$, $\vec{a}_2$ and $\vec{a}_3$, which are the lattice vectors of the unit cell in real-space.

The wavevector can be written in terms of a continuous linear combination of its reciprocal lattice vectors $\vec{b}_1, \vec{b}_2, \vec{b}_3$ with coefficients k_i:

$$\vec{k}=k_1\vec{b}_1+k_2\vec{b}_2+k_3\vec{b}_3, \tag{11}$$

where $k \in \mathbb{N}$.

The scalar product of $\vec{k}$ and $\vec{r}$ in the plane wave wavefunction results in a factor of 2π from the relations between $\vec{a}$ and $\vec{b}$ vectors:

$$\vec{b}_1=2\pi\frac{\vec{a}_2\times\vec{a}_3}{\vec{a}_1\cdot((\vec{a_2}\times\vec{a_3})}, \tag{12}$$

$$\vec{b}_2=2\pi\frac{\vec{a}_3\times\vec{a}_1}{\vec{a}_1\cdot((\vec{a_2}\times\vec{a_3})}, \tag{13}$$

and

$$\vec{b}_3=2\pi\frac{\vec{a}_1\times\vec{a}_2}{\vec{a}_1\cdot((\vec{a}_2\times\vec{a}_3)}. \tag{14}$$

The dot product between the two vectors is calculated by

$$\vec{b}_i\cdot\vec{a}_j=2\pi\delta_{ij}. \tag{15}$$

The exponential in the Bloch function becomes

$$e^{i2\pi(n_1k_1+n_2k_2+n_3k_3)}=1, \tag{16}$$

as a result of the required periodicity. The allowed coefficients for the block vector are thus

$$\vec{k}=\sum_{i=1}^{3}\frac{m_i}{N_i}\vec{b}_i, \tag{17}$$

where $m \in \mathbb{N}$, N_i are the number of primitive cells in the crystal in each dimension $i = 1, 2, 3$. This is known as the Born-von Karman boundary condition.

2.5 PARTICLE IN A BOX

The Schrödinger equation allows us to solve for the wavefunctions of particles given a potential,

$$-\frac{\hbar}{2m}\nabla^2\psi(\vec{r}) + V(\vec{r})\psi(\vec{r}) = E'\psi(\vec{r}), \tag{18}$$

where E' is the state energy, V is the potential, and ψ is the particle wavefunction. In the case where the potential is an infinite well, we have

$$V(x,y,z) = \begin{cases} V_0 = \text{const} & \text{if } 0 \geqslant x,y,z \geqslant L \\ \infty & \text{otherwise} \end{cases} \tag{19}$$

We can combine the potential and energy terms within the well in a single parameter E

$$E = V_0 - E'. \tag{20}$$

The Schrödinger equation becomes

$$-\frac{\hbar}{2m}\nabla^2\psi(\vec{r}) = E\psi(\vec{r}). \tag{21}$$

The infinite potential outside the region of interest forbids particles from leaving. This implies boundary conditions where the wavefunction must be zero at the boundaries of the region. More explicitly,

$$\psi_x(0) = 0 \qquad \psi_x(L) = 0 \tag{22}$$
$$\psi_y(0) = 0 \qquad \psi_y(L) = 0 \tag{23}$$
$$\psi_z(0) = 0 \qquad \psi_z(L) = 0. \tag{24}$$

Our particle must be somewhere in the box, giving the probability of finding the particle in the box to be 1. The probability is expressed as

$$\int_{box} \mathbf{d}\vec{r}\, \psi^*(r)\psi(r) = 1. \tag{25}$$

The wavefunction that satisfies these conditions is the sinusoidal periodic function which is its own negative second derivative. In a cubic box of side length L, the boundary condition leaves us with the solution in the form of

$$\psi(\vec{r}) = \left(\frac{2}{L}\right)^{3/2} \sin(k_x x)\sin(k_y y)\sin(k_z z). \tag{26}$$

This solution allows us to solve for the energy states in the box, E, which are calculated using

$$E = \frac{\hbar^2}{2m}\left(k_x^2 + k_y^2 + k_z^2\right). \tag{27}$$

The only case where the $\sin(k_x x)$ functions are zero is when $k_x x$ is equal to some integer multiple of π. The solution can be generalized to all three dimensions for k_x and k_y and k_z:

$$k_x x = n_x \pi, \tag{28}$$
$$k_y y = n_y \pi, \tag{29}$$
$$k_z z = n_z \pi, \tag{30}$$

where n_x, n_y and $n_z \in \mathbb{N}_{\geqslant 1}$.

The quantum states can now be classified by the quantum numbers (n_x, n_y, n_z) and (k_x, k_y, k_z) where the energies are constant for each quantum number combination, according to

$$E = \frac{\hbar^2 k^2}{2m}. \tag{31}$$

2.6 DENSITY OF STATES

The density of allowed states as a function of energy determines the absorption properties, carrier dynamics, and recombination in a semiconductor. The dimensionality of the semiconductor as a result of confinement has a profound effect on the density of states.

2.6.1 *Three-dimensional Density of States*

To calculate the density of states, which is the number of states per unit volume, we can begin with a spherical volume in $\vec{k}$-space.

The volume of such a sphere can be expressed by

$$V_k = \frac{4}{3}\pi k^3. \tag{32}$$

The k is the radius of the sphere and its magnitude is

$$k^2 = k_x^2 + k_y^2 + k_z^2. \tag{33}$$

The allowed k states can be written down from the boundary conditions of a particle in a three-dimensional box:

$$k_x = \frac{2\pi n_x}{L_x} \tag{34}$$
$$k_y = \frac{2\pi n_x}{L_y} \tag{35}$$
$$k_z = \frac{2\pi n_x}{L_z}, \tag{36}$$

where $n \in \mathbb{Z}_{\geqslant 0}$.

The smallest non-trivial volume in k-space is when $n = 1$, which we can define as

$$V_{state} = k_x k_y k_z. \tag{37}$$

Substituting k_x, k_y and k_z into Equation 37, we have

$$V_{state} = \frac{\pi^3}{L_x L_y L_z}, \tag{38}$$

with the real space volume as $L_x L_y L_z$.

If we define the total number of states in the region as $N_{1,3D}$, we have then this spherical volume in k-space V_k over the smallest non-trivial k-space volume element V_{state}:

$$N_{1,3D} = \frac{V_k}{V_{state}} = \frac{4}{3}\pi \frac{k^3}{k_x k_y k_z} = \frac{k^3}{6\pi} L_x L_y L_z. \tag{39}$$

Taking into account the spin degeneracy, we have

$$N_{2,3D} = 2N_{1,3D} = \frac{k^3}{3\pi^2} L_x L_y L_z. \tag{40}$$

The density of states per real space volume unit is

$$D_\nu = \frac{N_{2,3D}}{L_x L_y L_z}. \tag{41}$$

So we then have

$$D_\nu = \frac{k^3}{3\pi^2}, \tag{42}$$

where from equation 31, k in terms of energy is

$$k = \sqrt{\frac{2m^* E}{\hbar^2}}. \tag{43}$$

.

We wish to obtain the density of states as function of energy, so we differentiate D_ν with respect to energy using

$$D_{3D} = \frac{dD_\nu}{dE}. \tag{44}$$

The density of states is therefore

$$D_{3D}(E) = \frac{1}{3\pi^2} \frac{d}{dE} \left(\frac{2m^* E}{\hbar^2} \right)^{\frac{3}{2}}. \tag{45}$$

We can evaluate the previous equation to obtain:

$$D_{3D}(E) = \frac{1}{2\pi^2} \left(\frac{2m^*}{\hbar^2} \right)^{\frac{3}{2}} \sqrt{E}. \tag{46}$$

2.6.2 *Quantum Well Density of States*

Quantum wells can be prepared by restricting carriers to two dimensions, resulting in a different density of states distribution. In such a case, the magnitude of the k vector is obtained by only two components where

$$k = \sqrt{\widetilde{k_x}^2 + \widetilde{k_y}^2}. \tag{47}$$

The area traced out by a radius of k is

$$A_k = \pi k^2. \tag{48}$$

The smallest values of k_x and k_y are the same as before in the previous section with periodic boundary conditions $k_x = 2\pi/L_x$ and $k_y = 2\pi/L_y$.

The area per k state is

$$A_{state} = k_x k_y = \frac{(2\pi)^2}{L_x L_y}. \tag{49}$$

To get the number of states in the area traced out by the circle of radius k, we divide Equation 48 by Equation 49, and define $N_{1,2D}$

$$N_{1,2D} = \frac{A_k}{A_{state}} = \frac{k^2}{4\pi} L_x L_y, \tag{50}$$

where doubling this accounts for the spin degeneracy to give

$$N_{2,2D} = \frac{k^2}{2\pi} L_x L_y. \tag{51}$$

The areal density of these states is the number of states in the area A_{state} divided by $L_x L_y$

$$D_a = \frac{N_{2,2D}}{L_x L_y} = \frac{k^2}{2\pi}. \tag{52}$$

Substituting Equation 43 into Equation 52 gives us

$$D_a = \frac{m^* E}{\pi \hbar^2}. \tag{53}$$

The density of these states per energy is

$$D_{2D,a} = \frac{\partial D_a}{\partial E} = \frac{m^*}{\pi \hbar^2}, \tag{54}$$

which is constant with respect to energy. Therefore, the density of states in the x and y directions is constant within each discrete k_z

subband. The total density of states is zero at energies lower than the discrete k_z subband energy, giving

$$D_{2D}(E) = \frac{m^*}{\pi\hbar^2}\left(\sum_{n_z}\mathcal{H}_\int(E - E_{n_z})\right), \tag{55}$$

where $\mathcal{H}_\int$ is the Heaviside function, n_z is the state that corresponds to confinement in the z direction (normal to the plane of the quantum well).

This density of states is what is expected for InGaN/GaN quantum wells, and can be used for quantum dots which are weakly confined in the lateral dimensions, but strongly confined in the vertical direction.

2.6.3 *Quantum Wire Density of States*

In the case of nanowires, the dimensionality is further reduced so that carriers are only free in one dimension. The treatment is similar to that of the quantum well. To find the density of states for a quantum wire, we shall suppose a line segment in k space that spans from $-k$ to k. The length of this line is expressed as

$$L_k = |2k|. \tag{56}$$

Each segment has a "radius" of k, corresponding to the length each state occupies, so

$$L_{state} = k. \tag{57}$$

If the free direction is parallel to the axis of the quantum wire, the reciprocal space length of the wire is

$$k = \frac{2\pi n_z}{L_z} \quad \text{with } n_z = \mathbb{Z}. \tag{58}$$

The ratio of L_k to L_{state} is the number of states in L_k and is called $N_{1,1D}$:

$$N_{1,1D} = \frac{L_k}{L_{state}} = \frac{k}{\pi}L_z. \tag{59}$$

With spin degeneracy, this doubles to

$$N_{2,1D} = \frac{L_k}{L_{state}} = 2\frac{k}{\pi}L_z. \tag{60}$$

The number of states per L_z length is defined as D_l, and expressed as

$$D_l = \frac{N_{2,1D}}{L_z} = \frac{2k}{\pi} = \frac{2}{\pi}\sqrt{\frac{2mE}{\hbar^2}}. \tag{61}$$

The density of states is then $D_{1D} = \frac{\partial \lambda}{\partial E}$, which is

$$D_{1D}(E) = \frac{2}{\pi}\left(\frac{\partial k}{\partial E}\right), \tag{62}$$

since $k = \sqrt{\frac{2m^* E}{\hbar}}$.

The one-dimensional density of states in terms of energy is then

$$D_{1D}(E) = \frac{1}{\pi}\sqrt{\frac{2m^*}{E\pi^2\hbar^2}}. \tag{63}$$

Accounting for the other dimensions k_x and k_y, we have

$$D_{1D} = \frac{1}{\pi}\sqrt{\frac{2m^*}{\pi^2\hbar^2}} \sum_{n_x,n_y} \frac{1}{\sqrt{E - E_{n_x,n_y}}} \mathcal{H}(E - E_{n_x,n_y}), \tag{64}$$

as the density of states in the k_x and k_y dimensions are discrete. An inverse square root dependence on the energy is apparent in this expression, which is specific to wire-like confinement.

2.6.4 *Quantum Dot Density of States*

The final case of the density of states is one where carriers are confined in all three dimensions. The dimensionality is essentially zero. States are completely absent at all energies, except where there is the correct combination of allowed k values.

The density of unique states is therefore

$$D_{0D}(E) = \delta(E - E_{n_x,n_y,n_z}). \tag{65}$$

The double degeneracy of the states at zero field adds a factor of 2 to make the expression

$$D_{0D}(E) = 2\delta(E - E_{n_x,n_y,n_z}). \tag{66}$$

The number of combinations increases as a function of energy, so the density of states can be expressed as

$$D_{0D}(E) = 2 \sum_{n_x,n_y,n_z} \delta(E - E_{n_x,n_y,n_z}). \tag{67}$$

2.7 INTERMEDIATE BAND SOLAR CELLS

Converting sunlight to electrical power is an inefficient process even with the best solar cells. While multijunction solar cells hold all the efficiency records with high sunlight concentration, designs which manage to set new records are increasingly more complex in design,

material alloys and numbers of layers. In contrast, intermediate band solar cells can be physically simpler, where light of various wavelengths can be absorbed through intermediate transitions via states present the previously forbidden optical bandgap, as shown in Figure 8.

This extension beyond a normal solar cell is not limited by the Shockley-Queisser limit, where the fundamental assumption is the transmission of photons below the band gap of the cell. With intermediate band solar cells, previously unabsorbed photons can be absorbed into intermediate states and then subsequently into conduction band states upon a secondary absorption event. The absorption of low energy photons contributes to the total current generated in the device. While in traditional solar cells this absorption would lead to a reduction in maximum operating voltage, there is ideally no voltage drop for intermediate band of states. Transport from intermediate states to the conduction and valence band contacts is necessarily forbidden, forcing either recombination or excitation into higher energy states instead of conduction. When carriers are collected, the voltage is related to the quasi-Fermi levels of the large band gap host material. This leads to potentially high efficiency according to detailed balance calculations.

In practice, however, intermediate band solar cells are difficult to realize. The very states which form the intermediate band solar cell provide recombination pathways for excited carriers. This is especially true when the intermediate band is formed through impurity atoms where the non-radiative recombination rate is likely to overshadow sequential absorption processes. The reality is that any intermediate band solar must have excellent material properties in order to achieve significant current generation improvements from sub-bandgap photons without losing operating voltage.

In a typical solar cell with a well-defined valence and conduction band, the carrier populations in each band are electrically decoupled from each other. This can be interpreted as the difference in the quasi-Fermi levels of each band and results in an electrochemical potential difference μ between the electron population in each band. In an intermediate band solar cell, the intermediate band complicates the situation as the overall potential difference is a sum of the two potential differences between the valence band and the intermediate band, and the intermediate band and the conduction band. The total chemical potential is expressed as

$$\mu = \mu_2 + \mu_3. \tag{68}$$

The voltage of the intermediate band solar cell is then given by μ. For a black body of 6000 K, roughly resembling the spectrum of the sun, the intermediate band solar cell efficiency has been shown to have a maximum possible efficiency of 63.1% with optimal bandgaps[40]. With a more accurate terrestrial solar spectrum, the limiting efficiency is increased to 65.1% under a slightly different band position choice. It is important to note that these efficiencies are calculated based on

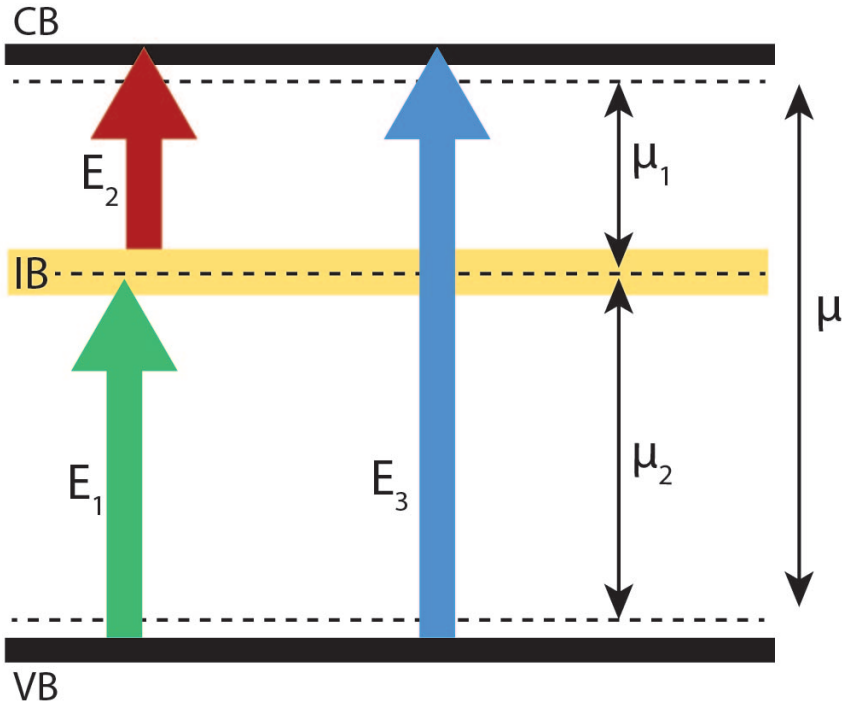

Figure 8: Schematic of the operating principle of the intermediate band solar cell. The coloured arrows indicated different photon energies. The intermediate band is drawn in yellow. The dashed lines indicate the quasi-Fermi level of each band.

the maximum possible concentration from the sun at approximately 46,200 suns[125]. At 1-sun, the maximum possible efficiency drops to about 48%[126].

There are numerous strategies that have been proposed to realize an intermediate band within a semiconductor band gap as proposed by Martí *et al.*[40]. In silicon, a proposed approach involved the hyperdoping silicon with deep trap such as titanium[127] and sulfur[128] atoms. In principle, this creates a nearly degenerate band of states within the bandgap to support sequential absorption events. Another route is through the use of highly mismatched alloys, which are semiconductors that have large differences in their constituent atoms in terms of electronegativity and ionicity. Examples of these such alloys are GaNAs and ZnTeO[129]. In these alloys, the band structure deviates from the traditional semiconductor as function of alloy composition since the top two conduction bands become so decoupled where the lower conduction band can be considered an intermediate band. Indeed, a GaNAs-based intermediate band solar cell has been demonstrated using samples with and without an electron blocking layer that can control the coupling of the intermediate band with the conduction band on the *n*-doped side of the solar cell[130].

One of the more promising intermediate band strategies is one which was proposed by Martí and Luque, who themselves investigated the use of quantum dots or wells to form such an intermediate band within the absorber region of a *p-i-n* junction[43]. The use of quantum dots/wells is advantageous for their more mature growth

techniques, as the growth has developed sufficiently to demonstrate nearly routine high material quality. Quantum dot intermediate band solar cells have been realized by InAs quantum dots in various host materials such as GaAs[131] and AlGaAs[132], GaNAs[133]. InAs/GaAs-based quantum dot systems are used for their more mature quantum dot growth processes. This limits the potential efficiency due to the less than ideal bandgap. In InGaN-based quantum dot systems, the indium composition in the dot and host material can be controlled to correspond to the ideal theoretical power conversion efficiency. A similar sequential absorption effect of sub-bandgap photons has been observed in manganese dopants in GaN with re-emission through InGaN quantum wells[134]. This has been investigated theoretically as a means for producing an intermediate band if the manganese dopant concentration is sufficient to create a band of states for a maximum efficiency of 53.4% operation[135]. To date, an InGaN-based intermediate band solar cell effects has been demonstrated[136]. This work by Sang *et al*. has shown sub-bandgap current generation from $In_{0.4}Ga_{0.6}N$ quantum dots grown in a GaN host material on AlN/s-apphire substrates. The quantum dots are formed through indium segregation in InGaN quantum well layers in up to 30 layers. There is significantly more work on the simulation of InGaN-based intermediate band solar cells[137–140], which focus on the limiting efficiency using InGaN quantum dots within various assumptions, achieving efficiencies over 60% in theory.

The density of quantum dots and concentration of sunlight can be considered crucial for providing any chance of an intermediate band solar cell to perform efficiently. From detailed balance simulations, the restriction to the typical 1-sun concentration of sunlight lowers the potential optimal efficiency by up to 13% absolute[141]. The presence of this detrimental effect is somewhat contingent on the density of intermediate states. For self-assembled quantum dots, the density is usually on the order of 10^{10} cm^{-2}, with the highest densities approaching 10^{12} cm^{-2}[142, 143], with InGaN quantum dots in particular reaching 3 x 10^{11} cm^{-2}[144]. Work by Sakamoto *et al*. has shown that at least 10^{13} quantum dots per cm^2 is required to produce an efficient device at 1000 suns, and a density of at least 10^{14} cm^{-2} to have access the peak theoretical efficiency at 100 suns. At 1-sun, quantum dot densities approach quite unrealistic levels of at least 10^{17} cm^{-2}[145]. Increasing the number of quantum dots via stacking is not a simple solution to increase sub-band absorption in bulk devices due to the general decrease in material quality and reduced carrier transport. Stacking of quantum dots also leads to a thicker intrinsic absorber layer that lowers the three-dimensional spatial density of intermediate states.

In semiconductor epitaxy, lattice-matched growth generally leads to much higher quality material. When lattice mismatched materials are required for high efficiency designs, the difficulty increases significantly as a function of the difference between the two lattice constants. The dislocations and reduced material quality associated with mismatched growth can be addressed through nanowire designs, where

the nanoscale footprint of the nanowire on the substrate does not build up sufficient strain to cause lattice defects. Therefore, nanowire designs largely avoid the performance degradation due to defects from lattice mismatch.

Another beneficial effect of nanowire devices is the optical focusing effects from sub-wavelength features. With judicious design, the photogeneration rate inside the quantum dots can be modified by the nanowire-induced spatial variation of the electric field component of incident light[146]. With GaAs nanowires, it has been shown that the light absorption can be increased by over an order of magnitude[147]. The nanowire morphology and quantum dot position can be adjusted to optimize this effect. The combination of quantum dot stacking and sub-wavelength optical design using nanowires can provide the effective generation rate that intermediate band solar cell concept relies on.

2.7.1 *Intermediate Band Potential of InGaN/GaN Nanostructures*

To realize the benefits of an intermediate band solar cell, an intermediate band must be able to absorb sufficient photons, support a long carrier lifetime in that band, and be able to transport carriers from the intermediate band to the higher conduction band regions of the device. These desirable properties can be expressed as a figure of merit which can provide a sense of the potential of the material system in a convenient form described by Sullivan *et al.*[148] and [149]. The figure of merit for drift-dominated transport devices is expressed as

$$\nu_{drift} = \frac{E_g}{q}\alpha_{min}^2(\mu\tau)_{min}, \tag{69}$$

where ν_{drift} is the figure of merit in a solar driven by drift current, E_g is the band gap of the host material, μ is the mobility of the limiting carrier species, q is the elementary charge, $(\mu\tau)_{min}$ is the mobility-lifetime product of the shortest-lived carrier species, and α_{min} is the lowest absorption coefficient between the two transitions.

This figure of merit can be calculated for the InGaN/GaN material system using published values of these material parameters to date to determine its potential for an intermediate band solar cell. In the case of InGaN and GaN, the mobility of holes is around two orders of magnitude smaller than the electron mobility due to the large effective masses of the heavy hole states (1.7 m_0 for GaN and 1.6 m_0 for InN[150]). The generation of drift current from the intermediate band is therefore dictated by the facilitation of hole transport through the device. From earlier studies of InGaN films, the hole mobility was found to be around 1.1[151] and 2[152] $cm^2/V{\cdot}s$. More recent studies on actual superlattice structures demonstrated hole mobilities as high as 18.2 $cm^2/V{\cdot}s$[153], suggesting that superlattice structures can improve the hole mobility, especially with doping. It is important to note that the indium composition fractions in these superlattices were all in the range of 15-20% for these samples. Higher indium

compositions are expected to have similar or lower mobilities, but the superlattice structures may have to be re-designed to enable efficient transport through the higher barriers.

The high mobility of electrons and low mobility of holes leads to many electrons throughout the superlattice, but few holes in all but the very closest wells to the *p*-type bulk material. The lifetimes of the holes must be sufficiently long so that they may reach the *n*-type side of the solar cell despite their low mobility. In particular, the non-radiative lifetimes are of interest as any radiative recombination has a reasonable chance of re-absorption in a relatively thick intermediate band and is not as detrimental. In early work, the nonradiative lifetimes have been estimated to be about 130 ps[154]. Subsequent devices began to demonstrate nonradiative lifetimes of 1.97 ns[155], total lifetimes of 6 ns in a device dominated by non-radiative recombination[156], 18 ns[157], and most recently 100 ns[158] in yellow emitting quantum wells. This last result is especially promising as it is a significant increase in the non-radiative lifetime over previous work and contains quantum-dot like accumulations of indium like the ones found in the nanowires in this thesis.

The bandgap of the GaN system is quite large in comparison to most proposed intermediate band systems. Whereas the ideal bandgap combination for intermediate band solar cells under concentration is about 1.9 eV[148] for the conduction to valence band energy difference, and 0.7 eV for the intermediate band position, a larger band gap generally benefits from less nonradiative recombination between the three bands. The host material can in principle be an indium-rich (40%) InGaN alloy along with a nearly pure InN quantum dot intermediate band to suit the ideal design. Nevertheless, the value of 3.4 eV will be used to calculate the figure of merit for an InGaN/GaN quantum well-based intermediate band solar cell as it corresponds to the samples in this thesis.

The final piece of the figure of merit equation is the absorption of the intermediate band region. A high absorption coefficient in the intermediate band region allows the region to be made thinner. This is highly advantageous as it increases the electric field across the intermediate band region so that carriers have less distance to travel in a stronger field. In addition, a thinner intermediate band region allows for improved absorption at the rear of the device and interferes less with the traditional photovoltaic effect of the overall *p*-*n* junction. Fortunately, the absorption coefficient of InGaN quantum wells can be exceptionally high. Recent modelling has shown that coupled quantum-dot based InGaN/GaN systems can reach absorption coefficients over 20,000 cm^{-1}[159] at certain wavelengths, and experimental results demonstrating absorption coefficients of over 10,000 cm^{-1} only 0.3 eV above the bandgap[160], and 60,000 cm^{-1} only 0.2 eV above the bandgap[161].

The figure of merit is not a fixed parameter for a particular material system as it can vary widely depending on the material quality and dimensionality-dependent absorption where the intermediate band material exists. Another factor is the wavelength-dependence on the

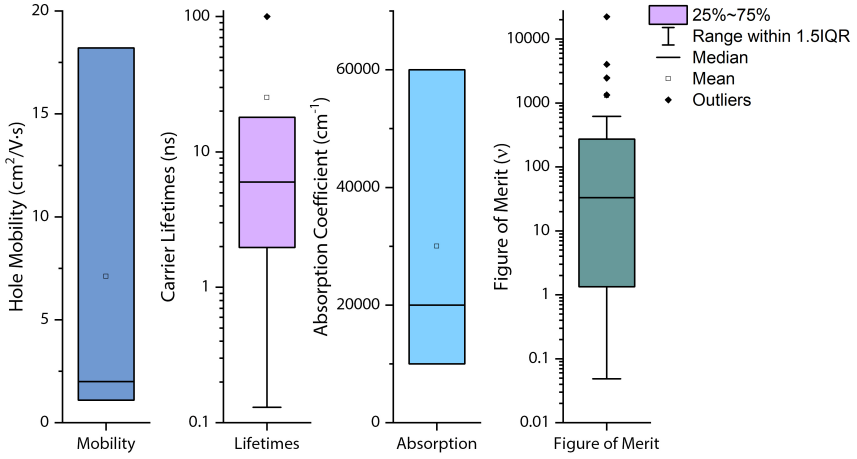

Figure 9: Material parameters obtained from the literature. All unique combinations of the material parameters were chosen to determine the approximate figure of merit for a potential intermediate band solar cell based on InGaN/GaN quantum wells. IQR indicates the interquartile range or middle 50% of the data (first quartile minus the third quartile).

absorption coefficient. The variation is considered using a statistical approach which aggregates parameters that affect the figure of merit from many InGaN/GaN multiple quantum well structures. An approximate range of figure of merit for InGaN/GaN quantum well-based intermediate band can be estimated based on measured (and in some cases calculated) material parameters established to date. It is important to note that the absorptivities are those of the valence band to intermediate states, and not of the usually more limiting intermediate band to conduction band absorptivity. This likely presents an inflated figure of merit, but nevertheless can provide a rough estimate. Using the various combinations of carrier lifetimes, mobilities, and absorption coefficients obtained from various sources, an ensemble of figures of merit were generated as shown in Figure 9. The values ranged from 0.04 to over 20,000. The mean value was 1304, and the median value was 33. The highest values were statistical outliers, as they corresponded to high absorption coefficients that may not be applicable to most photons of wavelengths that would be absorbed. We expect our InGaN/GaN quantum dots in nanowires, which have up to 100 ns non-radiative lifetimes, mobilities up to 10 $cm^2/V{\cdot}s$, host bandgaps of 3.4 eV, and absorption coefficients likely at least 10,000 cm^{-1}, to have a figure of merit of at least 340. Figure of merits over 100 can push enable efficiency improvements of over 20% absolute over traditional solar cells[148]. This suggests the InGaN/GaN material system is very promising as an intermediate band material system and worthy of future investigation.

2.7.2 *Quantum Confined Intermediate Bands*

One of the most promising strategies used in forming an intermediate band in a semiconductor is to form quantum dots or quantum wells. There are two types of quantum wells: type 1 and type 2. The former type are quasi-two-dimensional regions of lower bandgap semiconductor sandwiched between larger bandgap semiconductors, where both the electron and holes are confined in the space physical region. The latter type occurs when the electron and hole confinement are mutually exclusive in space, such that the electron quantum well states are physically separate from the hole quantum well states. The resulting spatially-dependent band diagram contains a square well with quantum confined energy levels which can form the intermediate band. Quantum wells have been successfully used in semiconductors devices for decades, leading to many advances such as lasers with lowered threshold currents[162], blue light emitting diodes[94] and lasers[95], infrared photodetectors[163], and high mobility transistors[164].

This confinement and energy state discretization becomes increasingly significant as the thickness of the quantum well is reduced. Multiple quantum wells can be stacked on top of each other, forming a superlattice of thin, alternating semiconductor regions. In bulk semiconductors, the thickness of these layers must be controlled precisely to balance the strain resulting from changes in the lattice constants. The maximum quantum well thickness allowed prior to lattice deformations is called the critical thickness. In nanowire-based structures, the strain can be relieved at the outside nanowire surface leading to significantly reduced constraints on quantum well dimensions and compositions.

A natural progression from quantum well is quantum dots. As the confinement along the growth axis has given rise to quantum wells, the further confinement in lateral dimensions leads to the formation of quantum dots. In practice, this lateral confinement is weaker than the vertical confinement as a corollary of the Stranski-Krastanov[165] or Volmer-Weber[166] growth modes. These growth strategies typically lead to quantum dots which have disc or dome shapes.

In nanowires, quantum dots are naturally formed as a result of the limited lateral area on the nanowire for epitaxy. The lateral dimensions of some nanowires can be relatively large in comparison to the vertical quantum confinement, so the lateral confinement is again dictated by the strain formed between the two semiconductor materials. In many cases, the lateral confinement is weak enough such that the quantum dots closely resemble quantum well states in the density of states distribution. This has been demonstrated in InGaN/GaN nanoposts where diameters past 40 nm were shown to have a negligible effect on the bandgap[167]. This is the case for the quantum dots formed in the nanowire solar cells described in this thesis which have diameters of about 40 nm.

Carrier transport through multiple quantum well regions is dictated by band gap differences between the two semiconductors and

the barrier and well thicknesses. In cases where the quantum wells separation is significant, tunneling through the large bandgap barrier material is negligible. In this case, confined electrons (holes) can either escape thermionically or through secondary absorption to the conduction (valence band). If the barriers are thin and the bandgap difference is low, carriers have a high probability of tunneling through the barriers, facilitating conduction. In the limit of this regime, the individual quantum well states hybridize to form a miniband and transport through the multiple quantum well region is very efficient. Many quantum well superlattices support carrier transport in between these two regimes, where carrier transport occurs through a quantum mechanical tunneling process.

3 SOLAR CELL THEORY

"The fundamental laws necessary for the mathematical treatment of a large part of physics and the whole of chemistry are thus completely known, and the difficulty lies only in the fact that application of these laws leads to equations that are too complex to be solved. "

— Paul Dirac, 1929

3.1 INTRODUCTION

The primary measure of a solar cell is its power conversion efficiency. In most photovoltaic applications, the optical power is the solar spectrum filtered to some degree by the atmosphere. In this chapter, the origin and properties of the solar spectrum are discussed. The physics behind solar cells, the photovoltaic effect that drives their operation, and the sources of loss are outlined. The maximum theoretical performance as dictates by a black body spectrum using thermodynamic considerations are calculated. The subsequent section is focused on the performance metrics that are used to characterize the output of solar cells. The second half of the chapter contains the theoretical approach of the modelling techniques and that will be implemented in Chapter 5 for modelling the effect of quantum well and quantum dot nanostructures in the nanowire solar cells.

3.2 SOLAR SPECTRUM

In the quest to harness the maximum amount energy of the sun, its critical to understand the spectrum of photon energies produced. The nuclear fusion process within the sun releases an enormous amount of energy in the form of heat light and heat. Every second, roughly 3.7 x 10^{38} protons are fused into helium nuclei, producing 3.846 x 10^{26} W of power. A fraction of this power is radiated as heat in the form of a nearly black body spectrum of light with an effective temperature of 5777 K, corresponding to the temperature of the surface of the sun where the light is emitted into vacuum. The ideal black body spectrum of an object is described by Planck's law,

$$I_s(f,T) = \frac{2hf^3}{c^2}\frac{1}{e^{\frac{hf}{k_B T}} - 1}, \tag{70}$$

where h is Planck's constant, c is the speed of light, f is the frequency of light, k_B is Boltzmann's constant, T is temperature, and I is the spectral radiance of the object. Minor changes to the spectrum of sunlight are neglected here, but are apparent through the absorption lines in the gases (mostly helium and hydrogen) that make up the

sun. According to Equation 70, photons are emitted from any object that has a non-zero temperature. The spectral photon flux emitted from such an object β_s like the sun is expressed as

$$\beta_s(E, s, \theta, \phi) ds d\Omega_s dE = \frac{2}{h^2 c^2} \left(\frac{E^2}{e^{\frac{E}{k_B T_s}} - 1} \right) d\Omega_s ds dE, \tag{71}$$

where T_s is the temperature of the sun, E is energy, s is a point with a surface area ds surrounding it, Ω_s is the solid angle, and θ and ϕ are the polar and azimuthal angles, respectively.

When the spectral photon flux is incident to the surface dS and integrated over solid angle element $d\sigma$, the integration to obtain the flux does not occur over the entire angular range since the light is not incoming from all directions. If one is on the surface of the black body, the angular range is from 0 to π. Farther from the black body, the total solid angle is less than π. In the case of the sun, the 93 million km distance gives the sun a mere 0.53°of subtense.

$$\beta_c(E, s) = \int_\Omega \beta_s(E, s\theta\phi) \cos\theta d\sigma dS dE, \tag{72}$$

where β_c is the spectral photon flux on the cell. The integral evaluates to:

$$\beta_c(E, s) dS dE = \frac{2\pi \sin^2 \theta_{1/2,sun}}{h^2 c^2} \left(\frac{E^2}{e^{\frac{E}{k_B T_s}} - 1} \right) dS dE. \tag{73}$$

The light from the sun is emitted isotropically and is roughly the same temperature at any point on the surface, which allows us to simplify Equation 73 to obtain

$$\beta_c(E) = \frac{2\pi \sin^2 \theta_{1/2,sun}}{h^2 c^2} \left(\frac{E^2}{e^{\frac{E}{k_B T_s}} - 1} \right). \tag{74}$$

The irradiance I of the sun is related to the photon flux density through

$$I_s(E) = E\beta_c(E). \tag{75}$$

The earth receives about a third of a billionth of the photon flux density at the sun's surface. This adds up to a total power 1.22 x 10^{17} W incident on the earth, averaging to 1353 W/m^2 on a plane normal to the sun at the top of the atmosphere[168]. This black body spectrum has the highest irradiance in the wavelength range of 400-700 nm. On top of this blackbody spectrum, the atmosphere of Earth attenuates a significant amount of the ultraviolet light from molecular oxygen, nitrogen, and ozone, and numerous bands within the infrared spectrum are absorbed by water vapour and carbon dioxide.

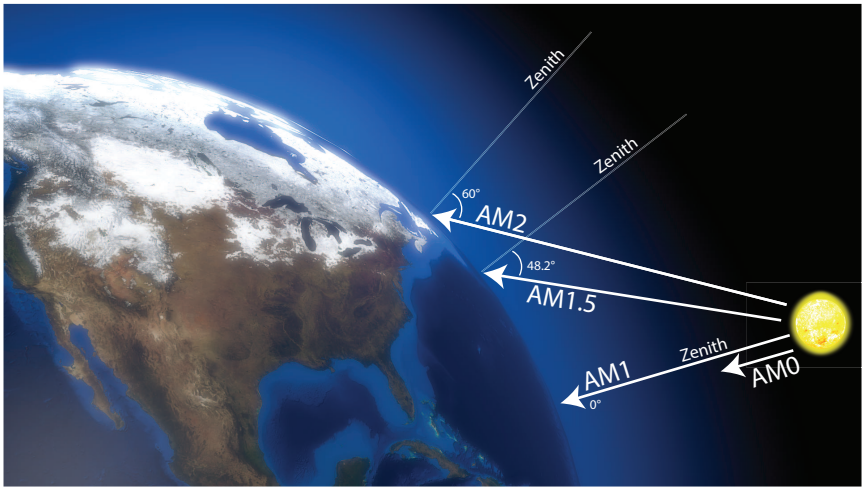

Figure 10: Air mass and associated angle of incident on the surface of the Earth. The air mass AM0 indicates the solar spectrum without any modification from the atmosphere of the Earth.

The absorption is a function of the effective thickness of the atmosphere, which changes as a result of the angle the sunlight makes with the atmosphere.

The **air mass** is a parameter that indicates the amount of attenuation from the atmosphere and is a function of the optical path of the sunlight. It is defined as

$$\eta_{AM} = \frac{d_{AM,\theta}}{d_{AM,\perp}}, \tag{76}$$

where $d_{AM,\theta}$ and $d_{AM,\perp}$ are the optical paths through the atmosphere at a given time and the optical path length through at the atmosphere when directly overhead. This parameter can thus vary from 1 to ∞ depending on the time of day and geographical latitude.

The air mass can also be expressed as a zenith angle of the sun, θ by

$$\eta_{AM} = \frac{1}{\cos(\theta)}. \tag{77}$$

In the case of the AM1.5G spectral standard, the spectrum corresponds to light from the entire hemisphere of the sky on a clear day when the sun is at a zenith angle of 48.2°from the vertical. The "G" suffix indicates the global source. The AM1.5D is a similar spectrum of just the sun, neglecting the surround blue sky, focusing on just direct rays from the sun and the circumsolar region which is used by concentrator solar cells. The different reference solar spectra are shown in Figure 11. The air mass concept is illustrated in Figure 10. It is this solar spectrum that solar cells are designed for as it corresponds to a solar spectrum accessible to any place on Earth with an absolute latitude less than 71.6°, therefore applicable for almost all human settlements on Earth for at least part of the year.

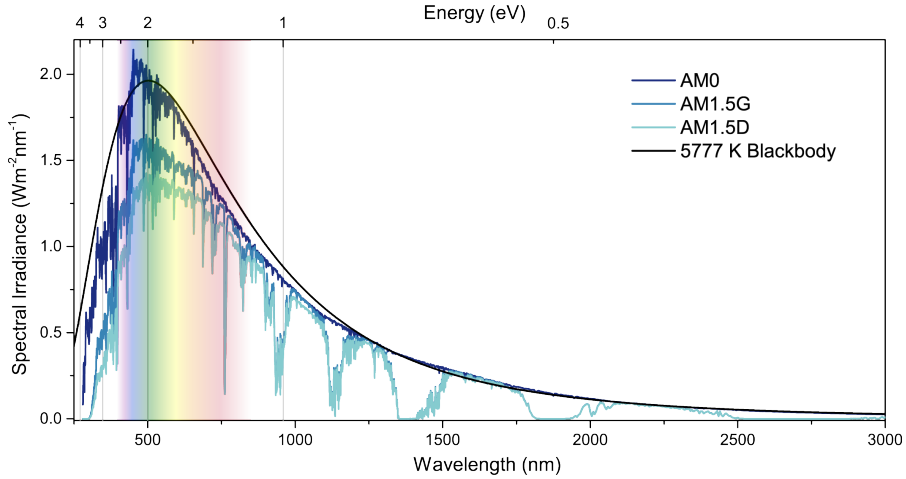

Figure 11: Reference solar spectra at various air masses on Earth. A perfect blackbody radiation spectrum at 5777 K is shown in black.

3.3 THE p-n JUNCTION

The band gap of semiconductors creates possibilities for variable conductivity through the addition of different atomic species within the crystal known as **impurities** or **dopants**. In small quantities, judicious choices of dopants can create localized states within the band gap as well modify the total number of electrons available in the material. Dopants which tend to release an excess electron once incorporated into the host crystal lattice, are called **donors** and contribute to a higher electron concentration. In contrast, dopants which tend to accept electrons from the lattice are called **acceptors**. Semiconductors with an excess and lack of donors are called ***n*-type** and ***p*-type** semiconductors, respectively. Within the band structure picture, a lack of an electron can be interpreted as a **hole** with an equal and opposite charge. Where n-type materials create free electrons in a lattice, p-type materials create free holes. For the fabrication of devices, semiconductors can tolerate various levels of doping, which is highly desirable as the concentration and species of dopants within the crystal structure significantly affects the carrier concentrations in the conduction and valence bands, hence the conductivity. In addition, after the dopant electrons are released, the nuclei of the dopant atomic species carry excess charge and influence carrier transport through the electric field they create.

If a p-type and n-type semiconductor are brought together, donor electrons from the n-type material are drawn to the acceptor ions on the p-type material and vice versa. The result is a depletion of charge carriers at the p-n interface. The p-type region around the interface becomes negatively charged as its acceptor atoms accept the excess electrons from the n-type side. The n-type region on the other side of the interface becomes positively charged as electrons move to the p-type side. This charge difference forms an electric field across the interface called a p-n junction. The process is illustrated in figure 12.

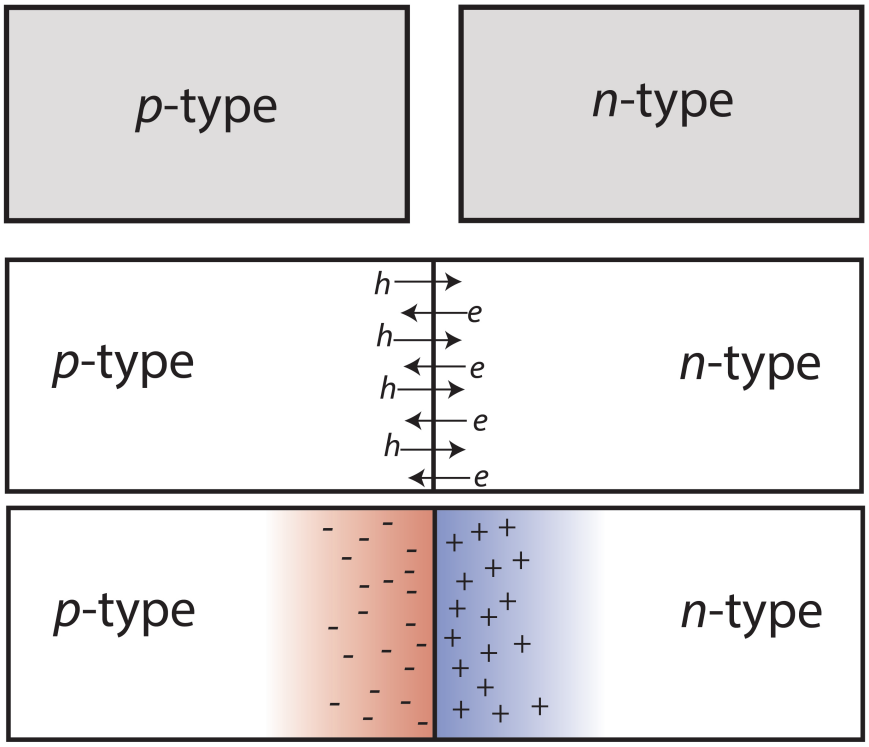

Figure 12: The formation of the electric field in a *p-n* junction arising from mobile electrons and holes from *n*-type and *p*-type semiconductors.

This technology forms the basis of the entire microelectronics industry today, providing revolutionary technologies such as digital camera sensors, photodiodes, computer chips, memory, solar cells, lasers, light emitting diodes (LEDs), fluid-free heating and cooling, numerous sensors and more. In solar cells, the *p-n* junction creates the conditions for efficient charge separation.

3.3.1 *Photovoltaic Effect*

The electric field created in a *p-n* junction is naturally suited for the separation of charge. The electric field prevents the flow of electrons, and hence electric current, in one direction. This is the defining characteristic of a diode. In forward bias, the drift current begins to increase as the drift current weakens. In a semiconductor, excess free electrons and holes can arise from light or heat. In the case of an incident photon within sufficient energy upon a semiconductor, an electron can be excited into the conduction band, leaving a hole in the valence band. The two carriers carry opposite charge in a region of high electric field that can overcome the usually small binding energy between the electron and hole, causing them to separate. By maintaining a population of excited carriers, the chemical potential difference between the conduction and valence bands of the material is increased and measured as a voltage. This is the **photovoltaic effect**. In a solar cell, the charges are separated before recombination

through the *p-n* junction resulting in current flow. The charge separation process can be driven by a combination of carrier diffusion and carrier drift under electric field. In a perfect material, increasing the incident light leads to an asymptotic increase of the open circuit voltage that approaches the band gap of the semiconductor divided by the elementary charge:

$$V_{oc} \xrightarrow{light} \frac{E_g}{q}, \tag{78}$$

where E_g is the band gap of the junction material. This limit is theoretically reached when the entire electron population is in the conduction band. Since all photogenerated electrons thermalize to the conduction band edge, the maximum energy per extracted electron would be E_g. In practice, the voltage is always at least 0.3 V less than the $\frac{E_g}{q}$ ratio due to recombination mechanisms.

3.3.2 *Photocurrent*

With increasing incident light, the photocurrent usually increases linearly. The total photocurrent of a solar cell can be determined by integrating the quantum efficiency across the solar spectrum using

$$J_{sc} = q \int \Phi_s(E) EQE(E) dE, \tag{79}$$

where Φ_s is the solar photon spectrum, EQE is the quantum efficiency, and q is the elementary charge.

Even with the creation of a single free electron with every absorbed photon, the amount of current produced as a function of photon wavelength is not generally the same. Photons with shorter wavelengths are absorbed closer to the front surface of the solar cell and farther away from the ideal *p-n* junction location. This leads to increased recombination from the surface or bulk. Longer wavelength photons are absorbed deeper in the semiconductor and face a similar issue. These factors contribute to poorer performance of solar cells in these spectral regions. The measure of this spectral performance is called the quantum efficiency. It measures the average number of electrons collected per incident photon. The quantum efficiency can be calculated from the photocurrent through the equation:

$$EQE(\lambda) = \frac{I_{ph}}{q\Phi_{\lambda,ph}(\lambda)}, \tag{80}$$

where $\Phi_{\lambda,ph}$ is the spectral photon flow (typically in units of $s^{-1}nm^{-1}$, q is the elementary charge, and I_{ph} is the photocurrent. The quantum efficiency across all wavelengths is less than 100% in solar cells, with the possible exception of multi-exciton generation which occurs with

UV light. The quantum efficiency is related to the spectral responsivity by

$$SR_\lambda = \left(\frac{\lambda q}{hc}\right) EQE(\lambda), \tag{81}$$

which measures the current as a function of optical power.

3.3.3 *Ideal Diode*

Solar cells have the same basic p-n semiconductor layer structure as typical diodes, and thus follow the ideal diode equation as a result. The current density through a diode without illumination is described by the exponential relation

$$J_{dark} = J_o \left(e^{n_{id}\frac{qV}{k_B T}} - 1\right), \tag{82}$$

where q is the elementary charge, T is the cell temperature in Kelvin, k_B is the Boltzmann constant, n_{id} is the ideality factor, V is the applied voltage bias, and J_o is the reverse saturation current for the solar cell. The dark saturation current is related to the leakage current through the diode under reverse bias conditions. Low bandgap solar cells generally have a smaller dark saturation current than high bandgap solar cells since the thermal generation is more prominent. The ideality factor is a dimensionless parameter that characterizes how close the solar cell follows the ideal diode equation. The ideality factor can indicate the type of recombination within the junction or resistivity of the contacts. Under illumination, the solar cell produces current proportional to the incoming light intensity. At 0 V bias, the photocurrent is called the short-circuit current J_{sc}. The total current under illumination (J_{light}) is simply the difference between the short circuit current under illumination and the dark current (without illumination):

$$J_{light}(V) = J_{sc} - J_{dark}. \tag{83}$$

The open circuit voltage as a function of current can be written from Equation 82 when the total current through the device is zero, taking the form

$$V_{oc} = \frac{k_B T}{q} \ln\left(\frac{J_{sc}}{J_o} + 1\right). \tag{84}$$

3.3.4 *Current-Voltage Characteristics*

The primary characterization technique for solar cells involves measuring the current-voltage characteristics. This allows for the direct

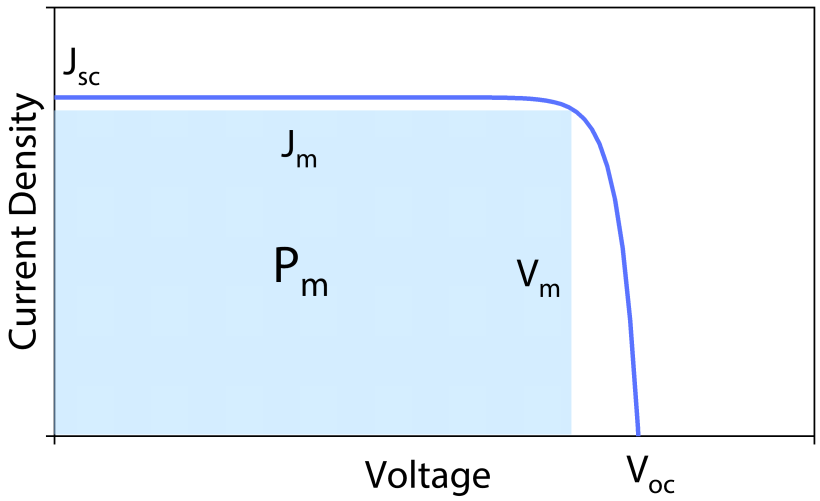

Figure 13: Current-voltage characteristic of a solar cell highlighting the performance metrics of a solar cell.

determination of the shunt and series resistances, short-circuit current, open-circuit voltage, fill factor, dark current, power conversion efficiency and operating voltage of a solar cell. The technique involves measuring the current flowing through a solar cell as a function of voltage. In the dark, a solar cell demonstrates the characteristic of a typical diode with a turn-on voltage corresponding to the built-in voltage of the junction. Under illumination, current is produced and adds a vertical shift to the curve. A current-voltage characteristic can be plotted as shown in Figure 13. In solar cell literature, the convention is to flip the curve over the x axis such that the curve lies in the first quadrant of the plot and the current is positive.

The largest rectangular area contained within the current-voltage characteristic is the maximum power density produced by the solar cell (P_m). The efficiency is calculated from the ratio of the output power density P_m to the input optical power density P_{in}. The fill factor is a measure of the quality of the solar cell accounting for its potential. It can be visualized as the ratio of the area of the largest rectangle inside the J-V curve to the $J_sc \cdot V_{oc}$ product. It is defined by

$$FF = \frac{J_m V_m}{J_{sc} V_{oc}}, \tag{85}$$

where J_m is the current density at the maximum power point, J_{sc} is the current density at zero voltage bias, V_{oc} is the open-circuit voltage, and V_m is the voltage at the maximum power point. Expressing the current and power as current and power densities J_m and P_m allow for direct comparison of solar cell performance regardless of the solar cell area.

To harness the maximum amount of power from the solar cell, the cell should be operating at the voltage that corresponds to the maximum power density. The maximum power density P_m lies at the

point where the product of the voltage and current of the cell is maximized:

$$P_m = J_m V_m. \tag{86}$$

When the total power P_t is desired, the voltage at the maximum power point is multiplied by the current at the maximum power point I_m, with the similar relation

$$P_t = I_m V_m. \tag{87}$$

3.4 ULTIMATE EFFICIENCY LIMIT

Solar cells have thermodynamically-defined fundamental limits on their efficiency from the black body spectrum of the sun and the cell temperature itself. For an approximate calculation, the sun can be treated as a black body emitter, where radiated light is dictated by the Stefan-Boltzmann law as a function of temperature. This is coupled with the limits of the solar cell band gap, where absorption is only allowed at energies above the bandgap, while lower energy photons simply pass through the material or are reflected.

In 1961, Shockley and Queisser developed the theory for the ultimate efficiency limit for a single junction solar cell on Earth based on these limitations[7]. The derivation of the ultimate efficiency limit is outlined below.

If we define a function Q_s as the number of photons with energy above the bandgap per unit time at a black body temperature of T_s incident on the solar cell, we have the integral

$$Q_s(E_g, T_s) = \frac{2\pi}{c^2} \int_{f_g}^{\infty} \frac{1}{\left(e^{hf/k_B T_s} - 1\right)} f^2 \, df, \tag{88}$$

where f is the photon frequency, f_g is the photon frequency that corresponds to the bandgap, T_s is the temperature of the sun, c is the speed of light, h is Planck's constant, and k_B is the Boltzmann constant.

This can be simplified by introducing the parameter x such that $x = hf/(k_B T_s) = E/(k_B T_s)$, and in the special case of the bandgap, we can also set $x_g = hf_g/(k_B T_s)$ to obtain

$$Q_s(E_g, T_s) = \frac{2\pi (k_B T_s)^3)}{h^3 c^2} \int_{x_g}^{\infty} \frac{x^2}{e^x - 1} \, dx. \tag{89}$$

The total power per unit area from a black body emitter at temperature T_s is described by the integral of Planck's law over photon frequency,

$$P_s = \frac{2\pi h}{c^2} \int_0^{\infty} \frac{f^3}{e^{hf/k_B T_s} - 1} \, df. \tag{90}$$

By substituting for x, we arrive at

$$P_s = \frac{2\pi(k_B T_s)^4}{h^3 c^2} \int_0^\infty \frac{x^3}{e^x - 1} dx. \tag{91}$$

The integral can be solved directly to obtain the total power incident on a unit area from this black body emitter:

$$P_s = \frac{2\pi(k_B T_s)^4}{h^3 c^2} \left(\frac{\pi^4}{15}\right) dx. \tag{92}$$

Through complete radiative recombination in the solar cell, the cell can achieve its ultimate efficiency under the detailed balance limit. Each photon outputted by this ideal solar cell is the wavelength corresponding to the bandgap of the material. The emitted photon energy of hf_g is multiplied by the photon flux per unit time to get the output power per unit area

$$P_{out} = hf_g Q_s, \tag{93}$$

where hf_g is the bandgap energy of the cell.

The incident power per unit area from the sun is simply $P_{in} = P_s$. The ratio of these power densities provides the limiting single junction cell efficiency

$$\eta(x_g) = \frac{P_{out}}{P_{in}} = hf_g \left(\frac{Q_s}{P_s}\right), \tag{94}$$

which becomes

$$\eta(x_g) = x_g \left(\frac{\int_{x_g}^\infty \frac{x^2}{e^x - 1} dx}{\int_0^\infty \frac{x^3}{e^x - 1} dx} \right). \tag{95}$$

Realistic single junction solar cells will never reach these high efficiencies due to some level of recombination that not only prevents a few carriers from being collected, but increases the temperature of the solar cell, further decreasing the performance. The model is then further expanded to include the geometric solid angle of the sun, the actual solar spectrum, and radiative recombination (from entropy considerations) to obtain a more realistic limit for solar cell efficiencies known as the Shockley-Queisser or detailed balance limit. Accurate simulations of realistic solar cells require the modelling of the carrier transport, defects, reflection, and other loss processes that are not captured in the ultimate efficiency model.

The ultimate efficiency for black body emitter and the detailed balance limit for our sun's spectrum are plotted as function of single junction bandgap in Figure 14. The ideal band gap choice is ~1.2 eV

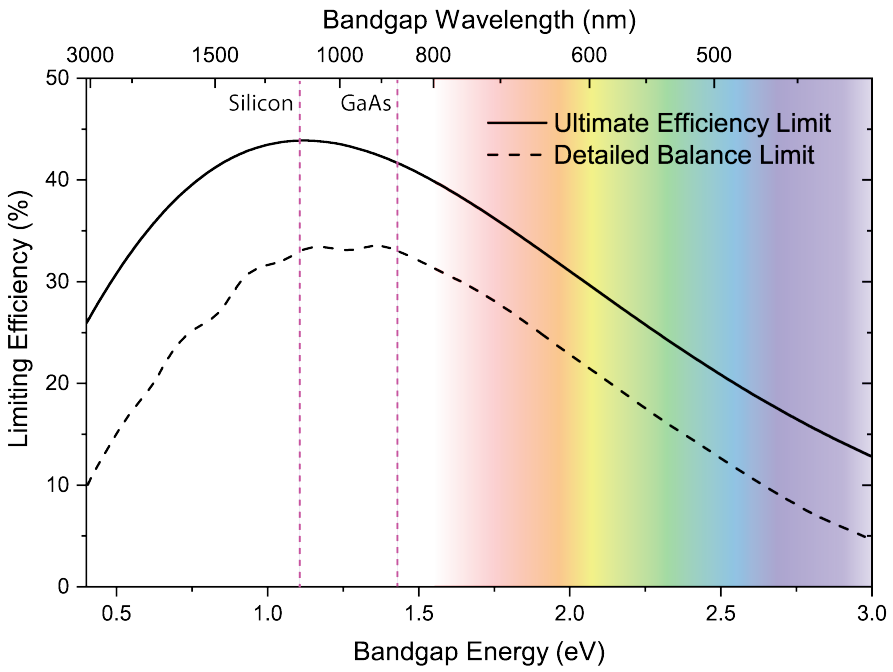

Figure 14: Ultimate and detailed balance solar cell efficiency limits as a function of bandgap overlaid with the bandgaps of silicon and gallium arsenide.

under the ultimate limit, which shifts to higher energies of ~1.3eV under the detailed balance limit. The maximum efficiency is over 40% in the single junction case, while the best single junction solar cells today at have efficiencies under 28.8%[169] for one sun and[170] of 29.3% under concentrated light.

3.4.1 *Semiconductor Device Equations*

To simulate and predict the performance of solar cells based on realistic materials, models which rely on the transport of charge distributions across an electric field profile are used. This involves solving for the semiconductor charge densities, electrostatic potentials, and electric fields caused by the semiconductor *p-n* junction. The fundamental equation for dealing with this type of physics was developed by Siméon Denis Poisson in 1813[171, 172], who generalized the Laplace's second order differential equation to obtain

$$\nabla^2 \cdot \phi(x, y, z) = -\frac{\rho(x, y, z)}{\epsilon}, \tag{96}$$

where $\phi(x, y, z)$ is the three-dimensional potential profile, ϵ is the permittivity and $\rho(x, y, z)$ is the charge density distribution.

This equation can be adapted for semiconductors where the charge distribution is caused by ionized donors and acceptors in the *p-n* junction and their released electrons and holes, and the permittivity is that of the semiconductor.

In this case, we have Poisson's equation tailored for the semiconductor junction:

$$\nabla^2 \cdot \phi(x,y,z) = -\frac{\rho}{\epsilon_0 \epsilon_r} \times \left(-n(x,y,z) + p(x,y,z) + N_D^+(x,y,z) - N_A^-(x,y,z)\right), \quad (97)$$

where ϵ_0 is the permittivity of free space, ϵ_r is the relative permittivity of the semiconductor, N_D^+ is the ionized donor concentration, N_A^- is the ionized acceptor concentration, n is the electron concentration, and p is the hole concentration.

This equation can be used to solve for the potential and electric fields across semiconductor junctions. However, these equations do not capture the effect of recombination and generation of carriers from heat or light. For this, we require *continuity equations* which account for the incoming and outgoing flux of charge through the device coupled with the generation and recombination rates in steady state conditions.

The carrier flux along direction normal to the junction can be described by

$$\frac{\partial n}{\partial t}(x,t) A dx = \left(\frac{J_n(x+dx) - J_n(x)}{q}\right) + (G(x,t) - R(x,t))\, A dx, \quad (98)$$

where J_n is the charge flux (current) density, G_n is the electron generation rate, and R_n is the overall electron recombination rate, t is time, A is the area, q is the elementary charge and dx is an infinitesimal displacement along the junction. The term $J_n(x+dx)$ can be approximated to be

$$J_n(x) + \frac{\partial J_n(x)}{\partial x} dx \quad (99)$$

by a Taylor series expansion. Once the area from Equation 98 is cancelled out, and the Taylor series is substituted in, the result is

$$\frac{\partial n}{\partial t}(x,t) = \frac{1}{q}\left(\frac{d}{dx} J_n(x,t)\right) + G_n(x,t) - R_n(x,t). \quad (100)$$

The formulation is similar for holes, giving

$$\frac{\partial p}{\partial t}(x,t) = -\frac{1}{q}\left(\frac{d}{dx} J_p(x,t)\right) + G_p(x,t) - R_p(x,t). \quad (101)$$

In general, these are three-dimensional equations yielding

$$\frac{\partial n}{\partial t}(x,y,z,t) = \frac{1}{q}\left(\nabla J_n(x,y,z,t)\right) + G_n(x,y,z,t) - R_n(x,y,z,t), \quad (102)$$

and

$$\frac{\partial p}{\partial t}(x,y,z,t) = -\frac{1}{q}\left(\nabla J_p(x,y,z,t)\right) + G_p(x,y,z,t) - R_p(x,y,z,t), \quad (103)$$

where ∇ indicates the gradient.

These equations ensure that the number of carriers is conserved throughout the system. The drift-diffusion equations along with the continuity equation and Poisson's equation can be solved self-consistently to obtain the parameters that define the operation of the *p-n* junction at every point in the device. To be more specific, the recombination terms can include Auger, Shockley-Read-Hall, and radiative recombination contributions, while the generation term can be divided into heat and light terms.

The current density can also be defined more explicitly in terms of drift or diffusion terms. The built-in electric field of the *p-n* junction can to the drift current where the electric field is high. The non-uniform distribution of carriers across the device also gives rise to a diffusion current where the natural diffusion of charge moves the carriers across the device. Adding these into Equations 102 and 103, we obtain

$$\begin{aligned}\frac{\partial n}{\partial t}(x,y,z,t) = \frac{1}{q}\left(\nabla J_{n,drift}(x,y,z,t) + \nabla J_{n,diff}(x,y,z,t)\right) \\ + G_{n,therm}(x,y,z,t) + G_{n,opt}(x,y,z,t) \\ - R_{n,rad}(x,y,z,t) - R_{n,srh}(x,y,z,t) - R_{n,aug}(x,y,z,t),\end{aligned} \tag{104}$$

and

$$\begin{aligned}\frac{\partial p}{\partial t}(x,y,z,t) = -\frac{1}{q}\left(\nabla J_{p,drift}(x,y,z,t) + \nabla J_{p,diff}(x,y,z,t)\right) \\ + G_{p,therm}(x,y,z,t) + G_{p,opt}(x,y,z,t) \\ - R_{p,rad}(x,y,z,t) - R_{p,srh}(x,y,z,t) - R_{p,aug}(x,y,z,t).\end{aligned} \tag{105}$$

3.4.1.1 *Minority Carrier Diffusion Equations*

In semiconductors, *majority carriers* are defined as the type of carriers which are more abundant. Minority carriers are simply the other type. In *p*-type semiconductors, the minority carriers are electrons, while in *n*-type semiconductors, holes are the minority carriers.

In the case of minority carriers, which exist in regions of nearly zero electric field since they are far from the junction, there is no drift component of the current. The diffusion current in this case is expressed as

$$J_n = J_{n,diff} = qD_n\nabla n, \tag{106}$$

and

$$J_p = J_{p,diff} = qD_p\nabla p, \tag{107}$$

where $D_n = \frac{kT}{q}\mu_n$ is the diffusion coefficient of electrons, $D_p = \frac{k_B T}{q}\mu_p$ is the diffusion coefficient of electrons with μ_n and μ_p being the electron and hole mobilities, respectively.

Assuming we have low-level injection ($\Delta n \ll p_o$, and similarly for holes), and the generation is only through optical processes, we arrive at the minority carrier diffusion equations which are used in solar cell simulations in this thesis where the electric field is low (away from the junction):

$$\frac{\partial \Delta n_p}{\partial t} = D_n \nabla^2 n_p - \frac{\Delta n_p}{\tau_n} + G_{opt}, \tag{108}$$

and

$$\frac{\partial \Delta p_n}{\partial t} = D_p \nabla^2 p_n - \frac{\Delta p_n}{\tau_p} + G_{opt}. \tag{109}$$

The parameters τ_n and τ_p are the electron and hole lifetimes, respectively, Δn_p is the excess electron concentration in the *p*-type material, and Δp_n is the excess hole concentration in the *n*-type material.

The excess carrier concentrations are

$$\Delta p_n = p - p_0, \tag{110}$$

and

$$\Delta n_p = n - n_0. \tag{111}$$

3.4.1.2 *Drift Current Equations*

In the case of drift current, free electrons and holes are influenced by the electric field of the junction. The drift current densities for electrons and holes are expressed as a function of the quasi-Fermi levels:

$$\vec{J}_n = qn\mu_n \vec{F}, \tag{112}$$

and

$$\vec{J}_p = qp\mu_p \vec{F}, \tag{113}$$

where $\vec{F}$ is the electric field.

The drift current is especially important when the electric fields are strong, and the drift current density equations are used extensively in the InGaN/GaN solar cell simulations in this thesis. An extension to this model includes the hydrodynamic model, where hot electron

effects are taken into account[173]. These effects use the following equation:

$$\nabla \cdot S + R_n w - \nabla E_c \cdot J_n + \frac{n(w - w_0)}{\tau_w} + \frac{\partial (nw)}{\partial t} = 0, \tag{114}$$

where w is the total energy of the electron and $w_0 = \frac{3}{2} k_B T$ is the energy of the electron at equilibrium, and τ_w is the relaxation time. The electron energy flux density S for hot carriers is described by

$$S = -\frac{5}{3} J_n w - \frac{10}{9} \mu_n n w \nabla w. \tag{115}$$

The equations for holes is analogous. This generalized current density is used in the drift-diffusion simulations with the Crosslight® APSYS simulation package [173].

3.4.2 *Recombination*

Semiconductor crystals are never perfect. Crystal lattices possess defects such as elemental impurities, which can replace lattice atoms or occupy spaces between atoms, distorting carrier transport locally. Defects can also arise from dislocations in the lattice organization which break the symmetry of the lattice over an extended region of the semiconductor. Both instances can create states within the bandgap that are accessible to free electrons and holes. Defects act as traps for excited carriers to recombine and release their energy. If the traps are within the bandgap and cause an electron and hole to meet in the same trap, the recombination is labelled as Shockley-Read-Hall (SRH) recombination which follows

$$R_{srh} = \frac{np - n_i^2}{\tau_{p,srh}(n + n_1) + \tau_{n,srh}(p + p_1)} \tag{116}$$

in the simple single level approximation where

$$n_1 = N_c e^{\frac{-E_c + E_t}{k_B T}} \tag{117}$$

and

$$p_1 = N_v e^{\frac{-E_t + E_v}{k_B T}}. \tag{118}$$

In Crosslight® APSYS, the SRH recombination rate is calculated for multiple traps using

$$R_{n,tj} = c_{nj} n N_{tj} (1 - f_{tj}) - c_{nj} n_{1j} N_{tj} f_{tf} \tag{119}$$

and

$$R_{p,tj} = c_{pj} p N_{tj} f_{tj} - c_{pj} p_{1j} N_{tj} (1 - f_{tj}), \tag{120}$$

where n_{1j} is the electron concentration when the quasi-Fermi level is at the energy of the j^{th} trap (E_{tj}), f_{tj} is the trap occupancy of trap j, N_{tj} is the number of traps, and c_{nj} and c_{pj} are the electron and hole capture coefficients of trap j. Since recombination must involve both electrons and holes in the trap, the carrier density is related to the electron and hole recombination rates as a function of time by

$$N_{tj}\frac{\partial f_{tj}}{\partial t} = R_{n,tj} - R_{p,tj}. \tag{121}$$

The variables c_{nj} and c_{pj} are the capture coefficients for electrons and holes, respectively, and control the lifetime of the carriers by

$$\frac{1}{\tau_{nj}} = c_{nj}N_{tj}, \tag{122}$$

and

$$\frac{1}{\tau_{pj}} = c_{pj}N_{tj}. \tag{123}$$

In terms of more basic parameters, the capture coefficients are described by

$$c_{nj} = \sigma_{nj}\bar{v}_n = \sigma_{nj}\sqrt{\frac{8kT}{\pi m_e^*}}, \tag{124}$$

and

$$c_{pj} = \sigma_{pj}\bar{v}_p = \sigma_{pj}\sqrt{\frac{8kT}{\pi m_h^*}}, \tag{125}$$

where $\bar{v}_n$ $\bar{v}_p$ are the average thermal velocities of the electron and holes, σ_{nj} and σ_{pj} are the capture cross sections of electrons and holes, and m_e^* and m_h^* are the bulk electron and hole effective masses.

Auger recombination is described by

$$R_{au} = \left(C_{n,au}n + C_{p,au}p\right)\left(np - n_i^2\right), \tag{126}$$

where $C_{n,au}$ and $C_{p,au}$ are the Auger coefficients, and n_i is the intrinsic carrier concentration.

3.4.2.1 *Carrier Concentrations*

Carrier concentrations across semiconductor bands follow the Fermi distribution function from the bottom of the conduction band and higher. For holes, the distribution begins at the top of the valence

band. In the conduction and valence bands, the electron and hole concentrations are described by

$$n = N_C F_{n,\frac{1}{2}}\left(\frac{E_{Fn} - E_C}{kT}\right), \tag{127}$$

and

$$p = N_V F_{p,\frac{1}{2}}\left(\frac{E_V - E_{Fp}}{kT}\right), \tag{128}$$

respectively, where N_C and N_V are the effective density of states for the conduction band and valence band respectively. The Fermi integral of order $\frac{1}{2}$ ($F_{\frac{1}{2}}$) can be expressed for electrons and holes and is

$$F_{\frac{1}{2}}(\eta) = \int_0^\infty \frac{\xi^{\frac{1}{2}}}{1 + e^{\xi - \eta}} d\xi, \tag{129}$$

where η can be defined for either the conduction band or valence band:

$$\eta_C = \frac{(E_F - E_C)}{k_B T} \tag{130}$$

and

$$\eta_V = \frac{(E_V - E_F)}{k_B T}. \tag{131}$$

In the limit of low carrier concentrations, the expressions can be approximated by

$$n = N_C e^{\frac{E_{Fn} - E_C}{k_B T}} \tag{132}$$

and

$$p = N_V e^{\frac{E_V - E_{Fp}}{k_B T}}. \tag{133}$$

Throughout the simulations in this thesis, the more general form of the carrier concentrations is used for the device simulations in this thesis.

3.5 ANALYSIS OF THE p-n JUNCTION

Virtually all modern solar cells use a semiconductor p-n homojunction design to separate carriers by charge to opposite metal contacts.

The potential, electric field and the carrier concentrations in these solar cells can be determined in most junction designs. The potential is related to the carrier concentration through the differential equation:

$$\frac{\partial^2 \phi}{\partial x^2} = \frac{\rho}{\epsilon_s} = \frac{q}{\epsilon_s}(p - n + N_d^+ - N_a^-), \tag{134}$$

where the ϕ is the electrostatic potential, x is the position along the direction normal to the junction axis, ρ is the charge density, ϵ_s is the permittivity, p and n are the carrier concentrations, respectively, and N_d^+ and N_a^- are the ionized donor and acceptor densities, respectively. A useful approximation can be made to simplify the calculations. The edges of the depleted region are assumed to be abrupt, where the transition from the depletion region to the quasi-neutral regions on both sides of the junction are assumed to be equally abrupt. This is known as the ***full-depletion approximation***.

The width of this well-defined depletion region can be written as

$$x_d = |x_n| + |x_p|, \tag{135}$$

where x_d is the depletion width, x_n and x_p are the extents of the junction on both sides. We can also write out the total charge density function in each region of the junction as

$$\rho(x) = q(p(x) - n(x) + N_d^+(x) - N_a^-(x)). \tag{136}$$

We can also assume that virtually all donors and acceptors are ionized and there are few carriers inside the depletion region, giving us

$$\rho \cong q(N_d^+ - N_a^-). \tag{137}$$

Under the full-depletion approximation, the charge density in the quasi-neutral regions is by definition zero, and the charge density in the p-type side of the depletion region (n-type depletion region) is the density of acceptors (donors) multiplied by the elementary charge. For our charge densities, we have

$$\rho(x < -x_p) = 0 \tag{138}$$
$$\rho(-x_p < x < 0) = -qN_a^- \tag{139}$$
$$\rho(0 < x < x_n) = qN_d^+ \tag{140}$$
$$\rho(x > x_n) = 0. \tag{141}$$

The total charge on both sides of the junction Q_n and Q_p are obtained by multiplying the charge density in a region by the width of that region and the ionized dopant charge:

$$Q_p = -qN_a^- x_p \tag{142}$$
$$Q_n = qN_d^+ x_n. \tag{143}$$

The electric field gradient is described by Gauss' law

$$\frac{\partial E}{\partial x} = \frac{\rho(x)}{\epsilon_s} = \frac{q}{\epsilon_s}(p - n + N_d^+ - N_a^-), \tag{144}$$

where E is the electric field, ϵ_s is the semiconductor permittivity and is applicable in the depletion region ($-x_p < 0 < x_n$). In the quasi-neutral regions, the electric field is zero. This gives us electric fields of

$$E(x < -x_p) = 0 \tag{145}$$
$$E(-x_p < x < 0) = -\frac{qN_a^-(x + x_p)}{\epsilon_s} \tag{146}$$
$$E(0 < x < x_n) = \frac{qN_d^+(x - x_n)}{\epsilon_s} \tag{147}$$
$$E(x > x_n) = 0. \tag{148}$$

The maximum field is found exactly at the semiconductor *p-n* junction interface and calculated by

$$E(x = 0) = E_{max} = \frac{qN_a^- x_p}{\epsilon_s} = \frac{qN_d^+ x_n}{\epsilon_s}. \tag{149}$$

This equation simplifies to a relation between the doping levels and depletion widths on each side of the junction, which is

$$N_d^+ x_n = N_a^- x_p. \tag{150}$$

This relation makes sense as the total amount of positive charge has to match the negative charge on the other side. The potential across the junction is related to the electric field by

$$\frac{\partial \phi(x)}{\partial x} = -E(x). \tag{151}$$

The potential is obtained through integrating both sides of the equation 151. In the case of the *p-n* junction, we obtain

$$\phi_{bi} - V_a = \frac{qN_d x_n^2}{\epsilon_s} + \frac{qN_a x_p^2}{\epsilon_s}, \tag{152}$$

where ϕ_{bi} is the built-in voltage.

Calculating the depletion width is obtained by stating x_p and x_n in terms of the doping and the depletion width:

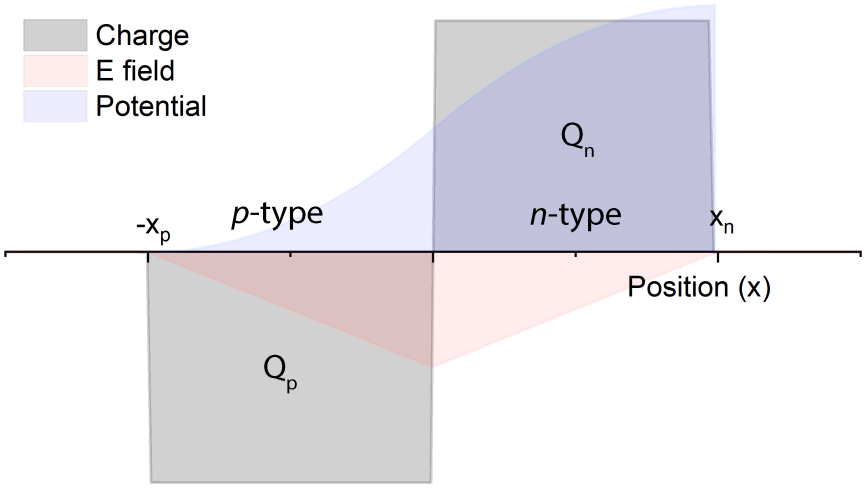

Figure 15: Illustration of the charge profile, electric field, and potential of an ideal p-n junction with equal n and p doping.

$$x_n = x_d \frac{N_a^-}{N_a^- + N_d^+} \tag{153}$$

$$x_p = x_d \frac{N_d^+}{N_a^- + N_d^+}, \tag{154}$$

and substituting them into equation 152 to get

$$x_d = \sqrt{\frac{2\epsilon_s}{q}\left(\frac{1}{N_a^-}\frac{1}{N_d^+}\right)(\phi - V_a)}. \tag{155}$$

These can also be separated into the widths for the n and p sides of the depletion region to get

$$x_n = \sqrt{\frac{2\epsilon_s}{q}\left(\frac{N_a^-}{N_d^+}\right)\frac{1}{N_a^- + N_d^+}(\phi - V_a)} \tag{156}$$

and

$$x_p = \sqrt{\frac{2\epsilon_s}{q}\left(\frac{N_d^+}{N_a^-}\right)\frac{1}{N_a^- + N_d^+}(\phi - V_a)}. \tag{157}$$

An illustration with the depletion region charge, electric field, and potential of a junction with equal n and p doping is shown in Figure 15.

3.5.1 *Analysis of the p-i-n Junction*

The nanowire solar cells proposed in this thesis have *p-i-n* junction designs to increase the electric field across the absorption region with the quantum dots. This design is used in fast photodiodes, where

the higher electric field increases the speed at which the carriers are swept out of the junction[174]. In materials with poor carrier lifetimes, the increased field can compensate for the lower diffusion lengths where carriers are accelerated out of the low quality material faster than the recombination rate[175]. The *p-i-n* junction can be solved similarly to the *p-n* junction where the potential across in the intrinsic region must also be accounted for. The potential is related to the applied bias with

$$\phi_b + \phi_p + \phi_i = \phi_i - V_a, \tag{158}$$

where the potentials in the *n*-type, *p*-type and intrinsic regions are

$$\phi_n = \frac{qN_d^+ x_n^2}{2\epsilon_s}, \tag{159}$$

$$\phi_p = \frac{qN_a^- x_n^2}{2\epsilon_s}, \tag{160}$$

and

$$\phi_i = \frac{qN_a^- x_i d}{\epsilon_s}, \tag{161}$$

respectively. The width of the intrinsic region is d. The total charge must be similarly balanced on both sides of the *p-i-n* junction. If the doping is higher on one side of the junction, the depletion region is pushed more into the opposite region to balance the charge.

$$Q = N_a^- x_p = qN_d^+ x_n. \tag{162}$$

The width of the depletion region on both sides of the junction can thus be solved for and we obtain

$$x_n = \frac{\sqrt{d^2 + \frac{2\epsilon}{q}\frac{(N_a^- + N_d^+)}{N_a^- N_d^+}(\phi_i - V_a)} - d}{1 + \frac{N_d}{N_a}} \tag{163}$$

and

$$x_p = \frac{\sqrt{d^2 + \frac{2\epsilon}{q}\frac{(N_a^- + N_d^+)}{N_a^- N_d^+}(\phi_i - V_a)} - d}{1 + \frac{N_a}{N_d}}. \tag{164}$$

The width of the depletion region can also be expressed as

$$x_d = x_n + x_p = \sqrt{d^2 + \frac{2\epsilon}{q}\frac{(N_a^- + N_d^+)}{N_a^- N_d^+}(\phi_i - V_a)}. \tag{165}$$

The potentials are calculated using the same methods as the *p-n* junction once the edges of the depletion region are known. Solving for the potential in each of the three *p-i-n* regions, the potential is

$$\phi(x) = \begin{cases} -\frac{qN_d}{2\epsilon_s}(x + x_n)^2 & -x_n < x < 0 \\ -\phi_n - \frac{qN_d x_n}{\epsilon_s}x^2 & 0 < x_p < d \\ -(\phi_i - V_a) + \frac{qN_a}{2\epsilon_s}(x - d - x_p)^2 & d < x < d + x_p \end{cases} \tag{166}$$

3.6 QUANTUM WELLS

The discovery and characterization of quantum wells in the 1970's led to the realization that the density of states, carrier transport and the resulting absorption properties of semiconductors can be tuned. In quantum well superlattice structures, the carrier transport depends highly on the thickness and bandgap of the barrier and well materials. The transport types can be divided into three regimes:

- Miniband conduction
- Wannier-Stark hopping
- Tunneling

The three transport mechanisms are illustrated in Figure 16. The first type of quantum well heterostructure is a miniband superlattice which happens in sufficiently thin wells. The quantum well states extend throughout the superlattice, so transport depends on the effective mobility of superlattice similarly to bulk transport. Carriers are free to move across the entire region as the states hybridize completely to form a miniband within the superlattice. Under sufficiently high electric fields, the miniband can break down due to the large energy differences across the wells.

The second type of conduction occurs when the barriers are sufficiently thick or high to isolate quantum well states from each other. Each confined carrier must tunnel through a barrier to arrive at the neighbouring well. This results in a slower, more inefficient type of transport.

The third type of superlattice structure uses Wannier-Stark hopping for carrier transport. In this regime, electric fields enable the carriers to hop from one well to the next due to sufficiently thin barriers and drop down to the lower energy states in the neighbouring well. The carriers repeat this process to move from one side of the superlattice to another, but only in one direction.

3.6.1 *Miniband Transport Model*

In the miniband transport model, the model assumes that confined wavefunctions are hybridized into a single band. In this regime, carrier transport is fluid throughout the quantum well region, For the

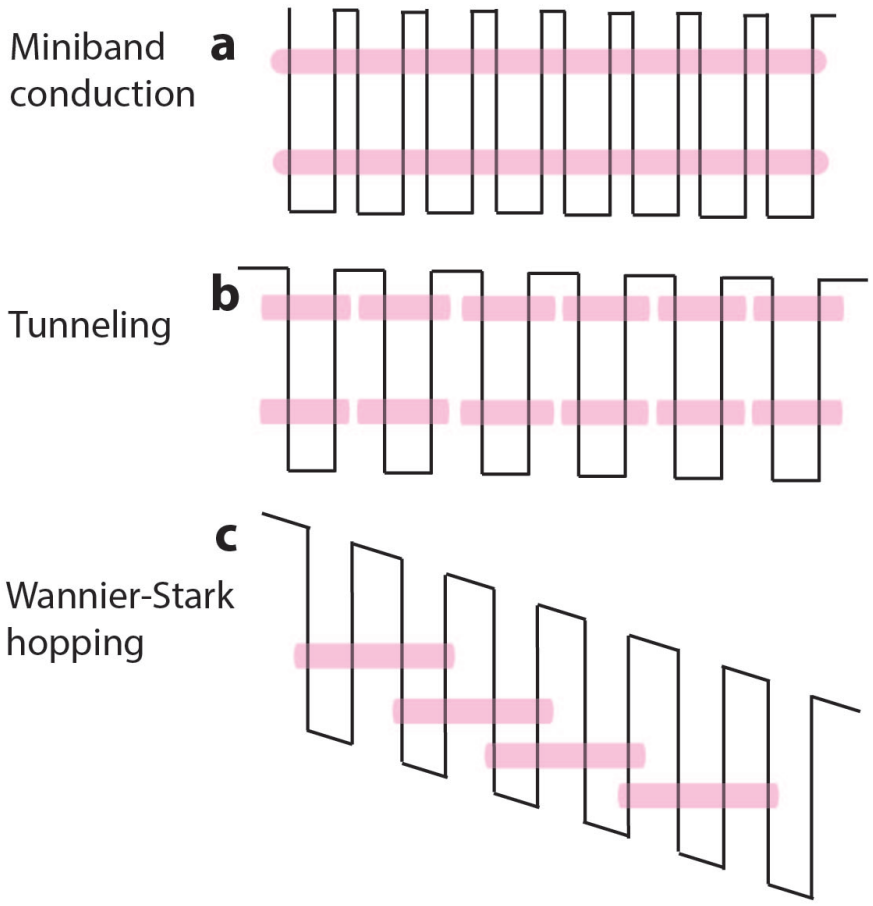

Figure 16: Three distinct quantum well transport types. (a) Miniband transport occurs when the quantum well barriers are thin enough that quantum well subbands hybridize into a single band of states. (b) Tunneling occurs through carrier wavefunctions overlapping and with neighbouring wells and possess non-zero probabilities of transferring into them. (c) Wannier-Stark hopping occurs when quantum well states span across an adjacent quantum well with an electric field across the quantum well region causing carriers to relax into a lower state of the adjacent well.

finite element simulations of nanowire performed in this thesis, the formalism of Nakamura[176] is used.

The approach involves solving the Schrödinger equation for the total envelope function in the multiple quantum well region with the effective mass approximation.

For the time-independent Schrödinger equation

$$\left(-\frac{\hbar^2}{2}\frac{d}{dz}m_e^*(z)\frac{d}{dz}+V(z)\right)\psi(z)=E\psi(z), \tag{167}$$

where E is the electron energy, V is the spatially dependent potential, $\hbar$ is the reduced Planck's constant, m_e^* is the electron effective mass, and z is the direction normal to the quantum well plane.

In a periodic potential, the potential follows

$$V(z+d)=U(z), \tag{168}$$

where d is the period of the superlattice, the Schrödinger equation must also be periodic in the form of

$$\psi(z+d)=C\psi(z). \tag{169}$$

The absolute value of the constant, C, must be equal to 1. At the boundaries of the potentials, $z=d$ and $z=0$, the wavefunction must satisfy

$$\psi(d)=e^{-ik_z d}\psi(0) \tag{170}$$

and

$$\psi'(d)=e^{-ik_z d}\psi'(0), \tag{171}$$

where k_z is the wavevector in the z direction and

$$\Psi'(z)\equiv\frac{d\Psi(z)}{dz}. \tag{172}$$

The boundary condition at the well/barrier interface has been generalized in the PhD thesis of S. Mori[177] and his subsequent publication[178] in the form of

$$\begin{bmatrix}\psi_B(z_i)\\ \frac{d}{dz}\psi_B(z_i)\end{bmatrix}=\begin{bmatrix}t_{11} & t_{12}\\ t_{21} & t_{22}\end{bmatrix}\begin{bmatrix}\psi_A(z_i)\\ a\frac{d}{dz}\psi_A(z_i)\end{bmatrix}, \tag{173}$$

where ψ_A and ψ_B are the envelope functions for the well and barrier sides of the interface, t_{ij} is the interface(or transfer) matrix for the well and barrier materials. The w indicates the well material, b indicates the barrier material, and a is the lattice constant.

This formalism had been modified for finite element analysis by Wacker[179] and Nakamura et al.[180] such that superlattice devices can be modelled with computer simulation software such as Crosslight® APSYS and is the fundamental theory behind miniband solar cell calculations in the thesis.

3.6.2 *Coupled Well Transport Model*

When the barriers between quantum wells are significant, transport in the quantum well region can occur through tunneling, thermionic escape, or photonic escape. Each quantum well has its own states which only extend into the barriers to some extent. In Crosslight® APSYS, quantum well superlattices which do not form a miniband can be simulated using a variety of approximations. The most basic model for quantum wells treats each well separately, assuming a symmetric, square barrier and flat potential well. Any interactions between wells are neglected. This effectively removes tunneling between wells and significantly reduces the transport of carriers across the quantum well region.

For relatively flat quantum wells (small electric field), the electron concentration inside the well can be approximated as being restricted to just the well and only dependent on the Fermi level and confined state levels. Inside the quantum well, the carrier concentrations follow the relation:

$$n_{2D}(x,y) = \sum_j \rho^0_{2Dj} k_B T \ln\left(1 + \exp\left[\frac{E_{fn}(x,y) - E_j(x,y)}{k_B T}\right]\right), \quad (174)$$

where j is the confined state index, and ρ^0_{2Dj} is the density of states in two dimensions at state j. The Fermi level and the confined state(s) are allowed to vary throughout the well in the case of finite wells. In the case of solar cells with no or small applied biases, the *p-n* or *p-i-n* junction may cause a significant tilt in the band profile but may become much flatter near the maximum power point.

There may also be significant localized electric fields due to piezoelectric or strain effects. This is particularly true in the nanowire structures studied in this thesis as they have InGaN/GaN quantum wells that are aligned along the (0001) growth plane. In this case, the symmetric/flat well assumption may not be valid and affects the coupling between adjacent wells. This level of simulation allows for sloped potentials inside the wells which are affected by the carrier concentration and other charges. These simulations couple the charge profile with the potential self-consistently such that both are solved sequentially until suitable solutions for the carrier concentrations and potential are found. The idea is to solve for the carrier concentrations followed by the potential profile to account for their effects on each other.

The self-consistent method consists of a similar carrier density expression inside the well, which has the form

$$n_{2D,sc}(x,y) = \sum_j g^j_n(y) \rho^0_{2Dj} k_B T \ln\left(1 + \exp\left[\frac{E_{fn}(x,y) - E_j}{k_B T}\right]\right), \quad (175)$$

where $g^j_n(y)$ is the electronic wavefunction of each state j and only varies as a function of the growth direction y. The confined states E_j

are now spatially independent and are updated as the electric field changes. The self-consistent simulation process is as follows:

Step 1:
Solve for the potential profile and carrier concentrations at equilibrium assuming a flat band profile according to Equation 174.
Step 2:
Use the band profile from Step 1 and calculate an updated carrier concentration and potential profile according to the self-consistent model described in Equation 175.
Step 3:
Continue to run Step 2 until the carrier concentration and potential profile do not change significantly.
Step 4:
Once self-consistency is obtained, the bias is updated and Steps 2 and 3 are repeated.

The valence bands can be quite close to each other in energy, leading to a mixing between the bands near the Γ-point of the band structure. The mixing can lead to a non-parabolic condition of the bands. In this case, a more accurate picture of the hole concentrations can be calculated from the integral over the valence band energies.

$$p = \sum_j g_p^j(y) \frac{1}{2\pi} \int_{-\infty}^{E_k(0)} \left(1 - f_v\left(E_j(k), E_{fp}\right)\right) dk^2, \tag{176}$$

where f_v is the Fermi distribution of holes in the valence band, g_p^j are the hole wavefunctions, and $E_k(0)$ is the highest energy hole state at the Γ ($k = 0$) point.

3.6.3 *Interband Absorption in Electric Fields*

The absorption in semiconductors is dictated by the incident photon energy, carrier populations in each band, and the band energies. In an electric field, bands are tilted in energy and absorption characteristics change. The quantum mechanical nature of the carriers allows their wavefunction to cover a finite spatial volume throughout which the band is not flat. This allows for the absorption of photons at lower energies than would otherwise be possible, and a general modification to the absorption spectrum. This is the fundamental property of electro-optic modulators and is called the Franz-Keldysh Effect or photo-assisted Zener tunneling.

If an electron is expressed as single charge in a uniform, time-independent electric field along the semiconductor growth direction (z), one can write the Schrödinger equation as

$$\left(-\frac{\hbar^2}{2m_r}\nabla^2 + qF \cdot r\right) \Phi(r) = E\Phi(r), \tag{177}$$

where F is the electric field, and the reduced effective mass m_r can be expressed as

$$m_r = \frac{m_e m_h}{m_e + m_h}. \tag{178}$$

The solution to Equation 177 is of the general form

$$\Phi(r) = \frac{1}{\sqrt{A}} e^{ik_x + ik_y} \Phi(z), \tag{179}$$

where $\Phi(z)$ remains the z-component of the single electron wavefunction in the electric field without an explicit form. We can use the Schrödinger equation again for this component,

$$\left(-\frac{\hbar^2}{2m_r} \frac{d^2}{dz^2} + qFz \right) \Phi(z) = E_z \Phi(z). \tag{180}$$

Since the field is parallel to the $\vec{z}$ direction, the dot product becomes scalar multiplication.

The energy level E is thus

$$E = -\frac{\hbar^2}{2m_r} \left(k_x^2 + k_y^2 \right) + E_z. \tag{181}$$

Rearranging Equation 180, we have

$$\frac{\hbar^2}{2m_r} \frac{d^2}{dz^2} - (qFz - E_z) \Phi(z) = 0, \tag{182}$$

allowing for a quick comparison to the Airy equation:

$$\frac{d^2}{dx^2} y - xy = 0. \tag{183}$$

The form of the solution is that of Airy functions $Ai(Z)$, where Z is the modified variable

$$Z = \sqrt[3]{\frac{2m_r qF}{\hbar^2}} \times \left(z - \frac{E_z}{qF} \right). \tag{184}$$

Therefore, the electron wavefunction can be expressed by k_x, k_y, and E_z in a $\vec{z}$-oriented electric field. The holes states are expressed in a similar way with the opposite charge of q.

3.6.4 *Absorption*

The general absorption spectrum of photons across the bandgap can be expressed by

$$\alpha(\hbar\omega) = A_0 \sum_n |\phi_n(0)|^2 \delta(E_n + E_g - \hbar\omega), \tag{185}$$

where $\phi_n(0)$ are states at the gamma point, E_g is the bandgap, $\hbar\omega$ is the photon energy, n are the states indices, and E_n is state energy. The factor A_0 is

$$A_0 = \frac{\pi q^2 |\hat{e} \cdot \vec{p}_{cv}|^2}{n_r c \epsilon_0 \omega m_0^2}, \tag{186}$$

where $\vec{p}_{cv}$ is a matrix element of the momentum operator, $\hat{e}$ is the polarization vector, n_r is the refractive index, c is the speed of light, q is the elementary charge, ϵ_0 is the permittivity of free space, ω is the photon angular frequency, and m_0 is the electron rest mass.

With an electric field along the z direction, the states are of the form in Equation 179. In a bulk material, we also have a continuum of states, so the sum becomes an integral leading to the absorption as a function of photon wavelength:

$$\alpha(\hbar\omega) = 2A_0 \times \sum_{k_x,k_y} \int_0^\infty dE_z |\phi(0)|^2 \delta\left(\frac{\hbar^2}{2m_r}\left(k_x^2 + k_y^2\right) + E_z + E_g - \hbar\omega\right). \tag{187}$$

In this thesis, Crosslight® APSYS calculates the absorption spectrum using this equation for the quantum well regions of the semiconductor and uses experimentally determined absorption coefficients for the bulk materials.

3.6.5 *Optical Transitions in Quantum Dots*

For a device with quantum dots, the simulations in this thesis express the carrier concentration as a sum of the quantum well and quantum dot carrier concentrations

$$n_{2D} = n_{QW} + n_{QW}, \tag{188}$$

since it generalized the system to include quantum dots embedded in a wetting layer. The areal electron concentration in the quantum dots is dependent on the energy distribution of electron and the density of quantum dots

$$n_{QD} = 2\sum_i \rho_{QD} f_c(E_i), \tag{189}$$

where f_c is the Fermi function

$$f_c(E_i) = \frac{1}{1 + \exp\frac{E_i - E_{fn}}{kT}}, \tag{190}$$

where E_i is the energy level at state i. The factor of 2 in Equation 189 arises due to spin-degeneracy of states at zero field. A similar formulation is followed for holes.

The quantum dot density is a parameter determined by experiment, and the energy levels of the quantum dot can be solved in 3D via the effective mass approximation. In this thesis, quantum dot hole states are not solved by a $\vec{k} \cdot \vec{p}$ Hamiltonian with valence mixing, and only uses a simple single band effective mass approximation similarly to the treatment applied to conduction bands. This means the calculated hole state energies are only approximate, but sufficient for use in determining the approximate density of states for device modelling. Therefore, the ordering, precise energies, and the character (light hole, heavy hole, or split-off hole) of the hole states are not guaranteed to be correct. Simulations with a full 6x6 $\vec{k} \cdot \vec{p}$ treatment are performed in this thesis for quantum wells structures.

The optical gain (or absorption if negative) in the quantum dots is calculated by the following formula:

$$g_{QD}(E) = \sum_i \sum_j \frac{\pi q^2 \hbar M_b^2 n_{QD}}{F \epsilon_0 c m_0^2 n_r t_{QD}} | < \psi_i | \psi_j > |^2 G_b(E - E_{ij})(f_c - f_v), \tag{191}$$

where t_{QD} is the quantum dot/well thickness, n_r is the refractive index, i and j are state indices, F is the electric field, M_b is the matrix element for the bulk surrounding material. The process of exciting an electron to the conduction band from intermediate quantum dot states is accomplished using a similar formalism. If dots are close enough to couple quantum mechanically, an additional factor of 2 is added to account for their sharing of energy levels. The term G_b is a Gaussian broadening parameter that covers inhomogeneous broadening and recombination from higher conduction band states and is described as

$$G_b(E) = \frac{1}{\sqrt{2\pi}} \exp - \frac{(E - E_i j)^2}{s\Delta^2}, \tag{192}$$

where

$$\Delta = \frac{\hbar}{\tau_b}, \tag{193}$$

τ_b being the broadening lifetime. The effect of broadening time constant is demonstrated in Figure 17. Similar to the carrier concentrations, the gain can be described by a sum of the quantum well (wetting layer) and quantum dot gains as in

$$g_{2D} = r_{QW} g_{QW} + g_{QD}, \tag{194}$$

where r_{QW} is a parameter that describes the quantum well contribution to the gain as the wetting layer thickness and presence depends

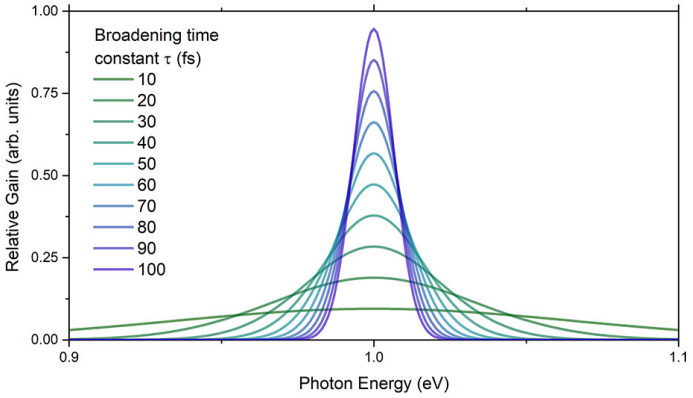

Figure 17: Relative gain broadening function for simulating the natural and inhomogeneous broadening of the gain spectrum in quantum dots.

on the choice of quantum dot system. The spontaneous emission rate in the quantum dot is written as

$$r_{QD}^{sp}(E) = \frac{q^2 n_r F M_b^2}{\pi \epsilon_0 m_0^2 \hbar^2 c_0^3} | < \psi_i | \psi_j > |^2 \frac{G_b(E - E_{ij}) \rho_{QD}}{t_{QD} f_c (1 - F_v)}. \tag{195}$$

The spontaneous emission rate in the well is added to that of the quantum dot in the form of

$$r_{2D}^{sp} = r_{QW} r_{QW}^{sp} + r_{QD}^{sp}. \tag{196}$$

The radiative recombination rate in the quantum dot is the sum of the spontaneous emission rates for all wavelengths of light,

$$R_{sp} = \int r_{2D}^{sp}(E) dE. \tag{197}$$

This methodology is followed for simulating the radiative emission from quantum dots inside the InGaN/GaN nanowire structures in forward bias. The state configuration for multiple dot geometries, sizes and compositions can be solved for separately by 3D effective mass models and combined in a single simulation of a device with an ensemble of quantum dots of various sizes. This can be complementary to the gain broadening term and provides a relatively more accurate way to approach the inhomogeneous broadening of the spontaneous emission and absorption in quantum dots.

3.6.6 *Modelling of Strained Wurtzite Quantum Wells*

In devices with heterointerfaces, strain effects can be captured to simulate more realistic semiconductor device performance characteristics. Strain arising between the InGaN and GaN crystal lattices can cause a shift in the bandgap alignment between the two materials. In

a quantum well, the well material usually has larger lattice constant which results in a compressive strain in the well. This is the case for InGaN surrounded by GaN. For the conduction band, the band offset without strain is defined as a fraction of the total change in band energies,

$$E_{offset,s} = \frac{\Delta E_c}{\Delta E_c + \Delta E_v}. \tag{198}$$

Once strain is present, there is a shift in the light hole, heavy hole and crystal field split-off bands where the highest valence band may not remain the same as the unstrained material. Therefore, the expression for strained materials explicitly specifies the lowest conduction band and the energy of the strain conduction band such that

$$E_{offset} = \frac{\Delta E_c^{min}}{\Delta E_c^{min} + \Delta E_v^{max}}, \tag{199}$$

where

$$\Delta E_v^{max} = E_v^{highest,InGaN} - E_v^{GaN}, \tag{200}$$

which means the valence band offset is defined by the difference in position between the highest energy valence band in GaN and the highest valence band in the InGaN.

The strain tensor for two crystal lattices interacting can be described by the following components:

$$\epsilon_{xx} = \epsilon_{yy} = \frac{a_0 - a}{a} \tag{201}$$

$$\epsilon_{zz} = -2\frac{C_{13}}{C_{33}}\epsilon_{xx} \tag{202}$$

$$\epsilon_{xy} = \epsilon_{yz} = \epsilon_{zx}, \tag{203}$$

where C_{13} and C_{33} are strain parameters, and a_0 and a are the unstrained and strained lattice, respectively.

For the conduction band, the strain is modelled as a modification to the effective mass for both the transverse and perpendicular directions under the parabolic band model according to Chuang[181].

The Hamiltonian is described by

$$H_c(\vec{k}_{\|}, \vec{k}_{\perp}) = \frac{\hbar^2}{2}\left(\frac{\vec{k}_{\|}^2}{m_e^{\|}} + \frac{\vec{k}_{\perp}^2}{m_e^{\perp}}\right) + E_c^0(z) + P_{c\epsilon}(z), \tag{204}$$

where $P_{c\epsilon}$ is the conduction band hydrostatic energy shift, $m_e^{\|}$ is the transverse effective mass, $m_e^{\perp}$ is the effective mass parallel to the growth direction,E_c^0 is the unstrained conduction band edge, $k_{\|}$ and $k_{\perp}$ are the momentum operators $-i\nabla_{\|}$ and $-i\nabla_{\perp}$ in the transverse and growth directions, respectively.

The conduction band hydrostatic energy shift is described by

$$P_{c\epsilon} = a_{c\perp}\epsilon_{zz} + a_{c\parallel}\left(\epsilon_{xx} + \epsilon_{yy}\right), \tag{205}$$

where a_{cz} and a_{ct} the conduction band deformation potentials parallel and perpendicular to the [0001] direction.

The valence band structure is more involved due to the three types of hole bands close in energy. A $\vec{k}\cdot\vec{p}$ Hamiltonian for strained wurtzite materials has been derived in[182], which is

$$H^{v}_{6x6}(k) = \begin{bmatrix} H^{U}_{3x3}(k) & 0 \\ 0 & H^{L}_{3x3}(k) \end{bmatrix} \tag{206}$$

$$H^{U}(k) = \begin{bmatrix} F_w & K_t & -iH_t \\ K_t & G & \Delta - iH_t \\ iH_t & \Delta + iH_t & \lambda \end{bmatrix} \tag{207}$$

$$H^{U}(k) = \begin{bmatrix} F_w & K_t & iH_t \\ K_t & G & \Delta + iH_t \\ -iH_t & \Delta - iH_t & \lambda \end{bmatrix}. \tag{208}$$

The matrix elements of the Hamiltonian are:

$$F_w = \Delta_1 + \Delta_2 + \lambda + \theta \tag{209}$$
$$G = \Delta_1 - \Delta_2 + \lambda + \theta \tag{210}$$
$$K_t = \frac{\hbar^2}{2m_0} A_5 k_t^2 \tag{211}$$
$$H_t = \frac{\hbar^2}{2m_0} A_6 k_t k_z \tag{212}$$
$$\lambda = \lambda_k + \lambda_\epsilon \tag{213}$$
$$\lambda_k = \frac{\hbar^2}{2m_0}\left(A_1 k_z^2 + A_2 k_t^2\right) \tag{214}$$
$$\lambda_\epsilon = D_1\epsilon_{zz} + D_2\left(\epsilon_{xx} + \epsilon_{yy}\right) \tag{215}$$
$$\theta_w = \theta_k + \theta_\epsilon \tag{216}$$
$$\theta_k = \frac{\hbar^2}{2m_0}\left(A_3 k_z^2 + A_4 k_t^2\right) \tag{217}$$
$$\theta_\epsilon = D_3\epsilon_{zz} + D_4\left(\epsilon_{xx} + \epsilon_{yy}\right) \tag{218}$$
$$\Delta = \sqrt{2}\Delta_3. \tag{219}$$

The valence band is described in reference to the conduction band level by

$$E_v^0 = E_c^0 - E_g + \Delta_1 + \Delta_2, \tag{220}$$

where Δ_1 is the crystal-field split energy and Δ_2 and Δ_3 are spin-orbit interaction parameters.

The confined states in simple quantum wells can be solved at the Γ, L, and X points, where the states are either electron, light hole, heavy hole, or split-off states, through the formalism of Chuang [182, 183]. With the application of a potential difference, the resulting external field spatially changes the quasi-Fermi level. However, in this approximation, the density of states and energy levels are assumed to remain unchanged from equilibrium.

The energy levels inside the wells are still calculated based on the carrier concentration. The model treats the heavy and light hole states as parabolic and assumes no coupling between the two types. The calculations are as simplified by setting the effective masses in the plane of the quantum well to be identical.

In most quantum well structures, the heavy and light hole states do not exhibit a parabolic dispersion. A deviation from parabolicity can arise due to strain. These deviations can modelled by treating the states as anisotropically parabolic as opposed to the more general non-parabolic shape. This treatment can be different between zincblende and wurtzite quantum wells.

For wurtzite InGaN, the heavy and light hole bands are not parabolic and also anisotropic. Having an approximate analytical effective mass model for accurate and fast numerical simulation is desirable. Crosslight® APSYS uses the effective masses obtained from bulk wurtzite materials and a combination of effective mass models for lightly and heavily populated hole bands. When the bands are lightly populated (small $\vec{k}$ vectors), the effective masses are:

$$\frac{m_0}{m_{hh}^{\perp}} = -(A_1 + A_3) \tag{221}$$

$$\frac{m_0}{m_{lh}^{\perp}} = -\left(A_1 + \frac{E_2^0 - \lambda_\epsilon}{E_2^0 - E_3^0} A_3\right) \tag{222}$$

$$\frac{m_0}{m_{ch}^{\perp}} = -\left(A_1 + \frac{E_3^0 - \lambda_\epsilon}{E_3^0 - E_2^0} A_3\right) \tag{223}$$

$$\frac{m_0}{m_{hh}^{\parallel}} = -(A_2 + A_4) \tag{224}$$

$$\frac{m_0}{m_{lh}^{\parallel}} = -\left(A_2 + \frac{E_2^0 - \lambda_\epsilon}{E_2^0 - E_3^0} A_4\right) \tag{225}$$

$$\frac{m_0}{m_{ch}^{\parallel}} = -\left(A_2 + \frac{E_3^0 - \lambda_\epsilon}{E_3^0 - E_2^0} A_4\right), \tag{226}$$

where $E_i^0 (i = 1, 2, 3)$ are the edges of the valence bands at the Γ point, and m_{lh}, m_{hh} and m_{ch} are the effective masses for light holes, heavy holes, and split-off hole bands in either parallel or perpendicular to the c-plane.

In the case of heavy populations (or large $\vec{k}$ vectors), the effective masses are

Material	a_0(Å)	c_0 (Å)	c_0/a_0	u
wz-AlN	3.110	4.980	1.6013	0.382
wz-GaN	3.190	5.189	1.6266	0.377
wz-InN	3.540	5.706	1.6120	0.380

Table 3: Experimental lattice parameters of III-nitride materials as obtained from Rinke *et al.* [184]

$$\frac{m_0}{m_{hh}^{\perp}} = -(A_1 + A_3) \tag{227}$$
$$\frac{m_0}{m_{lh}^{\perp}} = -(A_1 + A_3) \tag{228}$$
$$\frac{m_0}{m_{ch}^{\perp}} = -A_1 \tag{229}$$
$$\frac{m_0}{m_{hh}^{\parallel}} = -(A_2 + A_4 - A_5) \tag{230}$$
$$\frac{m_0}{m_{lh}^{\parallel}} = -(A_2 + A_4 + A_5) \tag{231}$$
$$\frac{m_0}{m_{ch}^{\parallel}} = -A_2, \tag{232}$$

where A_i are the valence band effective mass parameters.

In this thesis, and average of the small k and large k treatments is used in simulations.

The III-nitride lattice parameters used in this thesis were obtained from a variety of experimental growth papers summarized by Rinke *et al.*[184] and can be viewed in Table 3, where a_0 is the lattice constant in the hexagonal lattice plane, c_0 is the lattice constant in the [0001] direction, u is ratio of the anion-cation bond length in the (0001) plane to the c_0 lattice constant. The material and band parameters are obtained from the same paper, where the experimental parameters are favoured over the calculated ones if they are available. The material and band parameters used in this thesis are listed in Table 4.

3.7 DEVICE SIMULATION

Virtually all modern semiconductor device designs rely on technology computer-aided design (TCAD) to simulate their operation and performance, where the standard differential semiconductor equations are solved. The calculations involved in complex two-and three-dimensional devices are either prohibitively tedious or impossible to solve analytically, leading to the computation of numerically derived solutions. For the multiple quantum dot-in-nanowire solar cells discussed in this thesis, Crosslight® APSYS, a commercially available semiconductor device simulation software was used to simulate the optoelectronic properties of the fabricated devices.

Parameter	AlN	GaN	InN
E_g (eV)	6.15	3.5	0.69
$m_e^{\parallel}$	0.322	0.186	0.065
$m_e^{\perp}$	0.329	0.209	0.068
A_1	-3.991	-5.947	-15.803
A_2	-0.311	-0.528	-0.497
A_3	3.671	5.414	15.251
A_4	-1.147	-2.512	-7.151
A_5	-1.329	-2.510	-7.060
A_6	-1.952	-3.202	-10.078
A_7(eV Å)	0.026	0.046	0.175
$E_P^{\parallel}$ (eV)	16.972	17.292	8.742
$E_P^{\perp}$(eV)	18.165	16.265	8.809

Table 4: Band parameters for III-nitride materials.

Crosslight® software contains a group of software packages that solve the drift-diffusion equations which correspond to the generation, recombination and transport of carriers through the semiconductor device under equilibrium and non-equilibrium conditions. In particular, APSYS is the general drift-diffusion solver that includes the option of modelling advanced physical effects such as thermionic emission, ray tracing, heat transport, quantum confinement, relaxation and hot carrier effects, high frequency modulation, and much more. The device simulation process for solar cells is outlined in this section and is used for all the simulation results presented in this thesis.

The initial step involves preparing a *.layer* file which indicates the physical dimensions of the device, materials, layer thicknesses, contact positions, stress, mesh density, any quantum confinement approximations and doping levels. The layer file is processed, creating three files: a *.geo* file, a *.doping* file and a *.mat* file, that are designed to be interpreted by the computer. The mesh density defined in the *.layer* file is used to create the *.geo* file that lists the mesh parameters for each layer. The *.mat* file contains the material parameters of each layer and the contact types. The *.geo* file is then processed into a verbose *.msh* file, which is used for finite element analysis of the device.

An optional *.gain* file can be created from the material file that reveals the gain characteristics and other optical properties that are doping and mesh independent.

The *.sol* file is created by the user to define all the parameters which are to be used in the simulation of the device. This includes but is not limited to the carrier mobilities, carrier lifetimes, temperature, numerical optimization parameters, electrical and optical biases, step sizes, reflectivities, illumination spectrum and the enabling of advanced

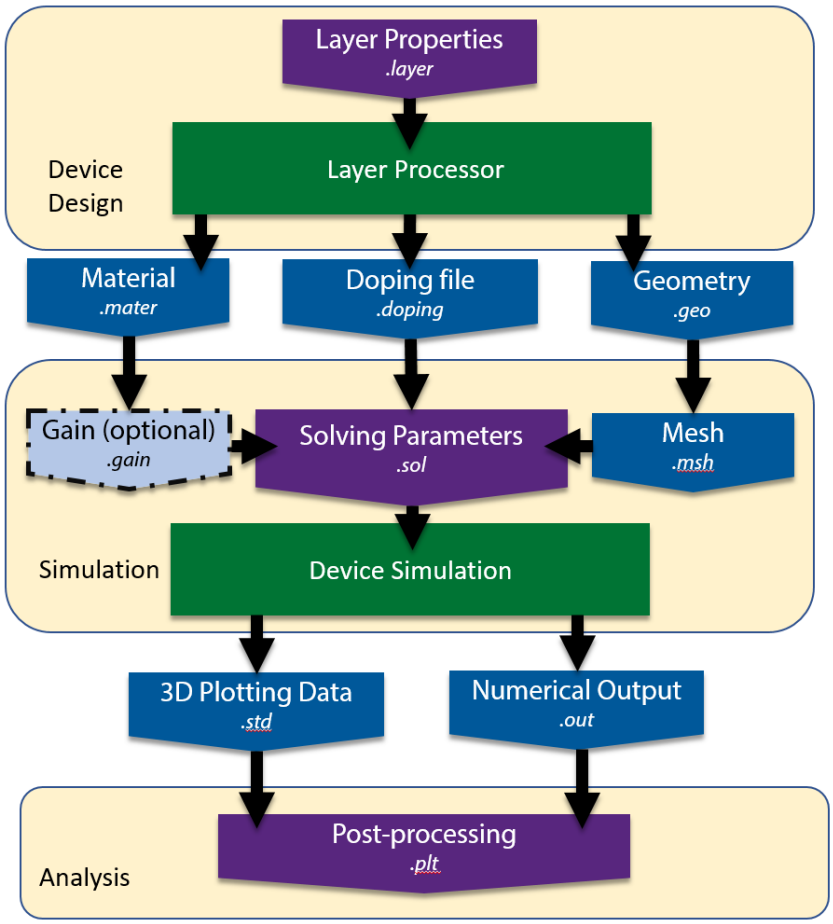

Figure 18: Device simulation process for Crosslight® APSYS.

physical models. The *.sol* file reads the *.msh*, *.doping*, *.mat* files (and optionally the *.gain* file) to perform the desired simulations.

The output of the simulation is contained in two files: an *.out* file and a *.std* file. The *.out* files include the actual numerical results of the simulation and the *.std* file includes numerical data in a form that enables 3D plotting of the results. The numerical results from the *.out* and *.std* files must be processed using *.plt* files to obtain graphical plots and organized data that be readily interpreted by the user. Plots can be printed as postscript files or saved as tab-delimited ASCII data files. All plots in this thesis were outputted to ASCII data files, and plotting using OriginLab® Origin® 8.0. A flowchart for the simulation is shown in Figure 18.

The drift-diffusion solver approaches the differential equations by dividing up the device into finite elements. The differential equations become vectors which are solved for single values of the potential, carrier concentration, and carrier energy values at each node. This is in contrast to determining the continuous potential, carrier concentration, and carrier energy functions directly. The finite elements are solved based on the box method[185], where the equations are integrated in 2D(3D) over a small area(volume) around each node and sets the flux into a particular node area(volume) equal to any source

and/or sink inside. The integration problem is treated as a summation as in traditional numerical integration techniques.

The solution is not straightforward in the case of realistic devices since the semiconductor equations are coupled and also non-linear. Crosslight® APSYS follows the Newton-Raphson method of iterative solving where the solution is approached iteratively starting with an initial guess. The solver makes a guess to the solution and then examines how well the guess matches with the drift-diffusion equations. If the new guess matches the differential equations better than the previous guess, it is kept as the new guess. Otherwise, a new guess is made. The generalized algorithm is as follows

$$F_v^j(V^{j1}, E_{fn}^{j1}, E_{fp}^{j1}) = 0 \tag{233}$$

$$F_n^j(V^{j1}, E_{fn}^{j1}, E_{fp}^{j1}) = 0 \tag{234}$$

$$F_p^j(V^{j1}, E_{fn}^{j1}, E_{fp}^{j1}) = 0, \tag{235}$$

where j is an index from 1 to N (the number of mesh points), j1 is the mesh point and its nearest neighbour mesh points, fn and fp are the electron and hole quasi-Fermi levels. There are 3N of these equations (three for each mesh point) that represent the discretized form of the drift-diffusion equations. Equations 235 are solved through a linear solver after being linearized using the Jacobian matrix. The Richardson iteration scheme improves upon the basic Newton's method by only requiring one or two refactorizations of the Jacobian matrix at each bias point, leading to much faster computation.

3.8 SUMMARY

In summary, this chapter discusses the operation of solar cells built from semiconducting materials and the theory behind their operation with the introduction of nanostructures. The analysis of simple *p-n* and *p-i-n* junctions was performed and coupled with the standard semiconductor equations provide the framework in which the performance of solar cells in general can be simulated. With the addition of quantum dots and quantum wells, the accurate simulation of carrier concentrations and their transport in a solar cell device becomes more challenging. The modelling approach for the carrier transport is dependent on the superlattice characteristics. The parameters used in the device simulations with Crosslight® APSYS are described. This concludes the introductory material of this thesis, leading into the experimental and simulation work in Part II.

Part II

RESULTS AND DISCUSSION

Part two of this thesis comprises the two main chapters on the study of InGaN/GaN quantum-dot-in-nanowire solar cells and LEDs. Chapter 4 includes the detailed presentation of the growth, fabrication and experimental characterization results and methods of the InGaN/GaN quantum-dot-in-nanowire solar cells. Chapter 5 discusses the modelling and simulation of the InGaN/GaN quantum-wells solar cells and InGaN/GaN quantum-dot LEDs to illustrate the operation of the deep sub-bandgap current generation strategy and carrier transport regimes for optimal power conversion performance in the quantum dot region. Chapter 6 investigates the InGaN/Si dual junction solar cell design using experimental absorption coefficients and the possibility of a nanowire-based InGaN top subcell.

4

EXPERIMENTAL CHARACTERIZATION OF INGAN/GAN DOT-IN WIRE SOLAR CELLS

"...great difficulties are felt at first and these cannot be overcome except by starting from experiments ... and then be conceiving certain hypotheses ... But even so, very much hard work remains to be done and one needs not only great perspicacity but often a degree of good fortune."

—Christiaan Huygens, 1687

4.1 OVERVIEW

The experimental characterization of the InGaN nanowire solar cell and LEDs is the central effort of this thesis. To determine the characteristics of the nanowire devices and how their properties change based on device variations, experiments are used to elucidate details on the physical processes and design considerations in more efficient InGaN/GaN on silicon nanowire solar cells. The work in this thesis does not include the growth and fabrication of the devices being characterized. Fabricated and unfabricated samples were provided by McGill University's III-nitride nanowire research group with and without design modifications proposed by the University of Ottawa. Samples were characterized using a wide range of tools and techniques to improve the understanding of the material system and device configuration of the InGaN/GaN nanowires. The research undertaken in this chapter comprises the following imaging techniques:

- Optical microscopy
- Laser scanning confocal microscopy
- Scanning electron microscopy (SEM)
- Microelectroluminescence microscopy
- Height profile by atomic force microscopy (AFM)
- Energy dispersive X-ray spectroscopy mapping

In addition to the aforementioned microscopy techniques, atomic resolution scanning transmission electron microscopy (STEM) of similar nanowire devices were previously performed by Dr. Steffi Wo at McMaster University[36]. Spectroscopy was performed using a system completely rebuilt for InGaN nanowire spectroscopy as well as a multitude of other semiconductor types. The work in constructing this system has enabled the research presented in this chapter and provided the SUNLAB core facility with the following capabilities:

- Liquid nitrogen temperature microphotoluminescence spectroscopy

- High resolution, large area photoluminescence mapping
- Liquid nitrogen temperature electroluminescence spectroscopy
- Simultaneous spectroscopy and high resolution optical microscopy
- Polarization-resolved spectroscopy
- Simultaneous multiple laser/broadband illumination of sample

The nanowire solar cells were measured as LEDs as well to infer the material and optical parameters of the nanowires themselves for operation as solar cells. Electrical properties of the InGaN/GaN nanowire solar cells were investigated using

- Dark and illuminated current-voltage characteristics
- External quantum efficiency

Optical properties of the nanowires were assessed through the specular and diffuse reflectivity of bare and fabricated nanowire samples over a wide range of optical wavelengths.

4.2 MOLECULAR BEAM EPITAXY

To obtain the highest quality semiconductor nanostructure growth, strict control over the layer thicknesses and material composition is required. Molecular beam epitaxy (MBE) is the most used epitaxial technique for the growth of quantum well and quantum dot structures, where the lattice defects and variances in growth must be kept to a minimum.

MBE is the deposition of elemental sources from solid sources under ultra-high vacuum. Sources of high purity elements, such as gallium and indium, are evaporated by effusion, radio-frequency plasma, cracking, or electron beams in separate cells. The pressure is kept at extremely low pressures ($< 10^{-8}$ mbar) so that mean free path of the evaporated elements is longer than any of physical dimensions of the growth chamber. The trajectories of the evaporated elements are represented by an unobstructed beam from the source to the substrate. When the molecular beam arrives at the substrate, atoms bond to the surface and proceed to react chemically with the substrate atoms, adding to the existing crystal lattice. The temperature of the source primarily dictates the growth rate. Due to the layer-by-layer growth process, molecular beam epitaxy can be very slow, with growth rates on the order of a micron per hour or less.

The introduction of dopants is achieved from either solid or gas sources and introduced in small quantities alongside the host materials. The temperature of the substrate is also controlled to optimize the adhesion of elemental sources, material quality, and control diffusion of atoms on the epilayer. In many cases, it is common for some of the molecular beam to reflect off the substrate, desorb, re-adhere or reorganize on the substrate during growth. In a successful growth,

the temperatures, pressures, and elements are set to facilitate the minimization of the Gibbs free energy of the film.

Regardless of epitaxial process, different combinations of atoms form crystals with their unique lattice constants. The matching of the substrate and epitaxial layer lattice constants is a critical factor in the quality of the epilayer from the growth. If there is a mismatch of the lattice constants between the two crystals, strain builds in the epilayer. Above a certain layer thickness, the strain is sufficient to introduce undesirable defects and dislocations in the epitaxial layer as it reorganizes to minimize the strain energy. Since virtually all grown semiconductor materials require low defect densities to realize high performance optoelectronic devices, the choice of semiconductor materials has traditionally been limited to substrates which share the same or similar lattice constants and crystal symmetry as the epitaxial material.

The growth of one semiconductor material on another can proceed via one of the three growth modes. The most common mode is Frank–van der Merwe growth, where the epitaxy proceeds in a layer-by-layer addition of atoms arranges in a continuation of the substrate lattice. The growth of subsequent layers occur only once the previous layer is completed as atoms prefer to attach themselves to the surface as opposed to other adatoms. This growth mode is utilized in the vast majority of semiconductor devices as it leads to high quality material with few lattice defects. The Frank-van der Merwe growth mode limits the device design to stacks of two-dimensional slabs and occurs in homoepitaxy and in lattice-matched heteroepitaxy.

The Stranski-Krastanov growth mode occurs when the lattice mismatch between two semiconductor lattices leads to a few layers of strained two-dimensional growth followed by clustered growth around segregated islands on top. The initial monolayers are known as the wetting layer with the clusters of growth occurring once the growth surpasses what is known as the critical thickness. This critical thickness varies between different semiconductor combinations and is a function of their lattice mismatches. The clusters of material on top of this wetting layer can form three dimensional confinement structures that are analogous to dot-like (zero-dimensional) dimensions found in atoms. If growth continues, larger and larger clusters form until individual clusters meet and form lattice defects at their interfaces. In this mode, the growth is typically stopped prior to cluster coagulation. An additional epitaxial layer of the same material as the substrate is usually grown on top to return to layer-by-layer growth. Multiple layers of quantum dots may then be grown on a substrate. The Stranski-Krastanov growth mode has led to the development of telecommunication wavelength lasers[186], solar cells[187, 188], and full colour LEDs[189] due to the additional confinement and tunability of the quantum dot density of states.

With Volmer-Weber growth, the lattice mismatch between the two different semiconductor materials is sufficiently large that any epitaxial material accumulates immediately in clusters without an intermediate wetting layer. The higher surface energy of the substrate versus

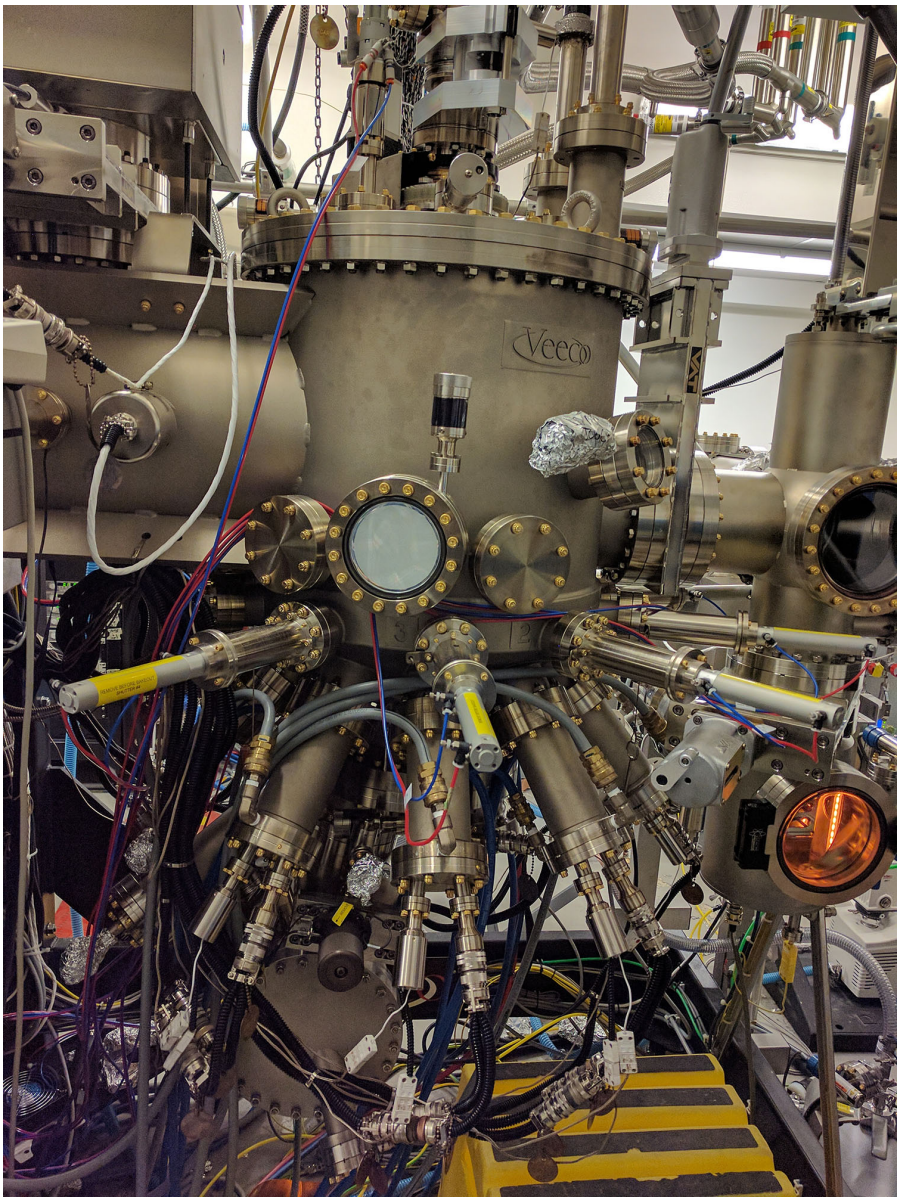

Figure 19: Photograph of the Veeco® molecular beam epitaxy chamber at McGill University used to grow the nanowires.

the lower surface energy of the initial adatom clusters leads to cluster formation. The growth proceeds with the formation of larger and larger clusters as in Stranski-Krastanov growth modes. The Volmer-Weber epitaxial layers will eventually form defected multi-layer films if allowed to continue without returning to strain-balancing material.

4.2.1 *InGaN/GaN Dot-in-Nanowire Growth*

The samples in this thesis were all grown and fabricated at McGill University by students and researchers in Dr. Zetian Mi's group, specifically Dr. Ashfiqua Connie, Dr. Sharif Sadaf, and Dr. Songrui Zhao, and Dr. Hieu Pham Trung Nguyen. The fabrication process for nanowire solar cells is nominally similar to the fabrication process for nanowire LEDs, which were are also characterized in this thesis. The nanowires

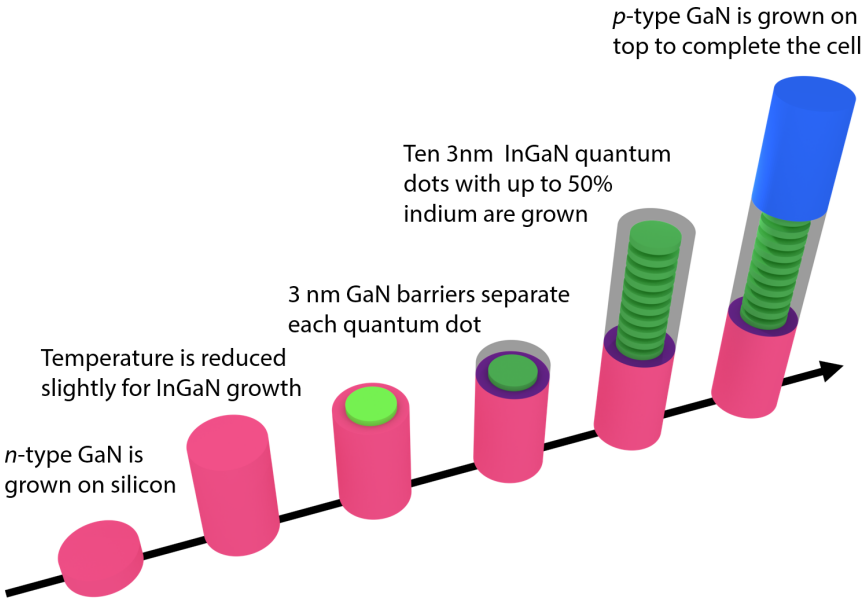

Figure 20: Growth process for InGaN quantum dots in a GaN nanowire. The fuchsia base is *n*-type GaN and the blue top is the *p*-type GaN. The GaN material between the dots is not intentionally doped.

were grown in a Veeco Gen II reactor via radio frequency plasma-assisted molecular beam epitaxy on 2-inch diameter *n*++-silicon (111) wafers without a catalyst. Vertically-oriented GaN nanowires spontaneously begin to form on the silicon (111) at a growth temperature of 770°C. The silicon wafers have a resistivity of 10^{-5} Ω. The bottom of the nanowire is a 270 nm Si-doped *n*-GaN, forming the base of the cell. The intrinsically-doped InGaN/GaN quantum dot region is then formed by alternating between 3 nm of GaN and 3 nm of $In_{0.4}Ga_{0.6}N$ at 640°C. The growth temperature of the quantum dots directly affects the indium incorporation of the quantum dots, where higher temperatures correspond to lower indium concentrations. The top of the cell is formed by a 200-300 nm thick *p*+-GaN region, followed by an optional 10 nm AlGaN electron-blocking layer. Silicon was used as the *n*-type dopant at a concentration of 10^{19} cm^{-3} with magnesium being the *p*-type dopant at a concentration of $5x10^{18}$ cm^{-3}. The lattice of the nanowire is vertically aligned in the energetically preferred wurtzite configuration. From previous scanning transmission electron microscopy of similar nanowires, the polarity of the nanowires was determined to be N-face polar[36]. In the case of core-shell nanowires, AlGaN growth in the nanowires is formed by a roughly 50-100 nm thick shell of $Al_{0.2}Ga_{0.8}N$. The resulting sample morphology consists of densely packed forest of nanowires with an areal nanowire density of approximately 1-1.5 x 10^{10} cm^{-2}. The diameters of the completed nanowires are about 90 nm. The growth process is illustrated in Figure 20.

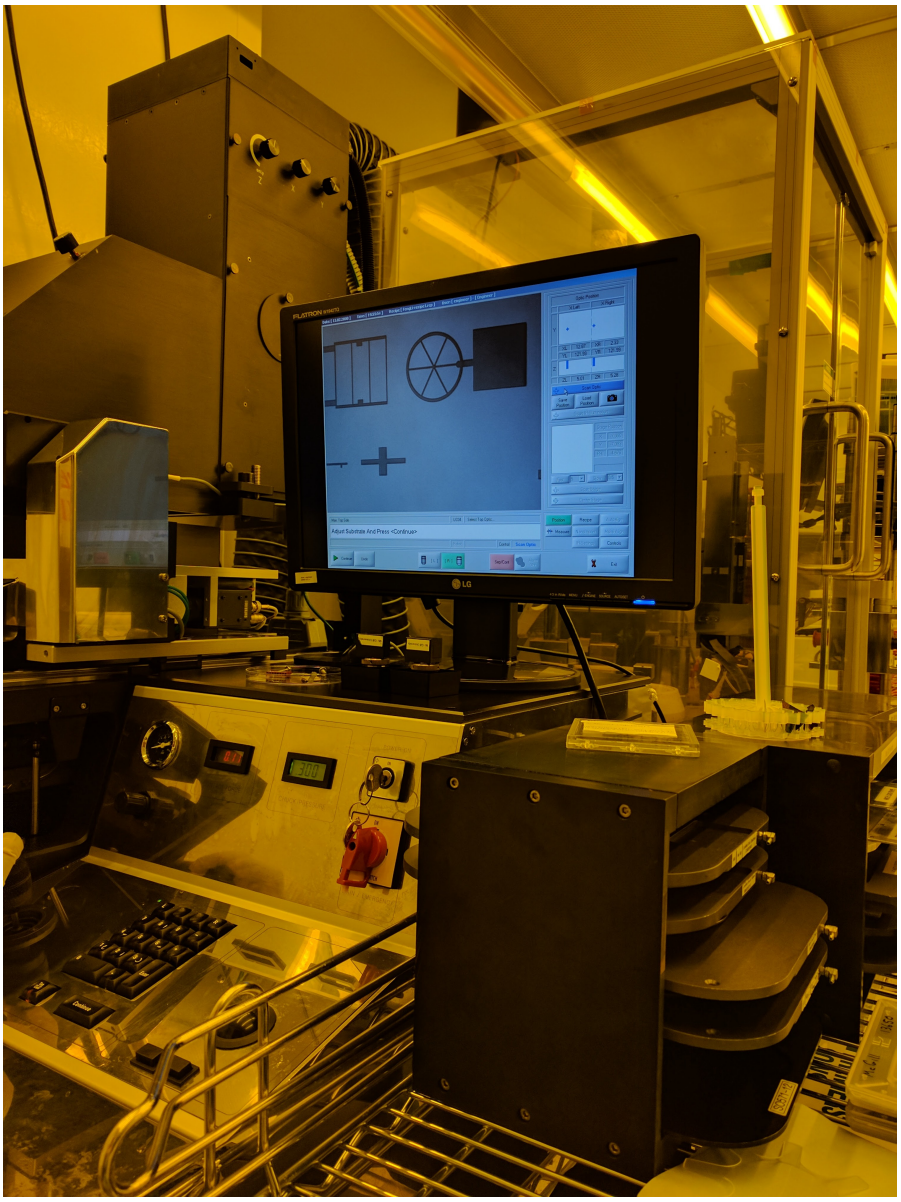

Figure 21: UV lithography stepper at McGill University used for exposing resist for patterning device contacts.

4.2.2 *Cell Fabrication*

The nanowires must be then fabricated into solar cells. The wafers are first cleaved in six triangular slices. The initial step includes spin-coating a polyimide resist, filling in the gaps between the nanowires to provide additional passivation of the surface and for planarization. The polyimide is dry-etched to reveal the tops of the nanowires. The initial top contact pattern is formed by a Nexdep® electron beam deposition system, providing 7.5 nm of titanium and 9 nm of gold. A transparent contact is formed by the sputtering of indium tin oxide (ITO) as a top contact covering the entire surface. The ITO is then etched to isolate the nanowire cells. The Ti/Au contacts are annealed at 550°C under a nitrogen atmosphere followed by the annealing of the ITO under 7 mbar of air.

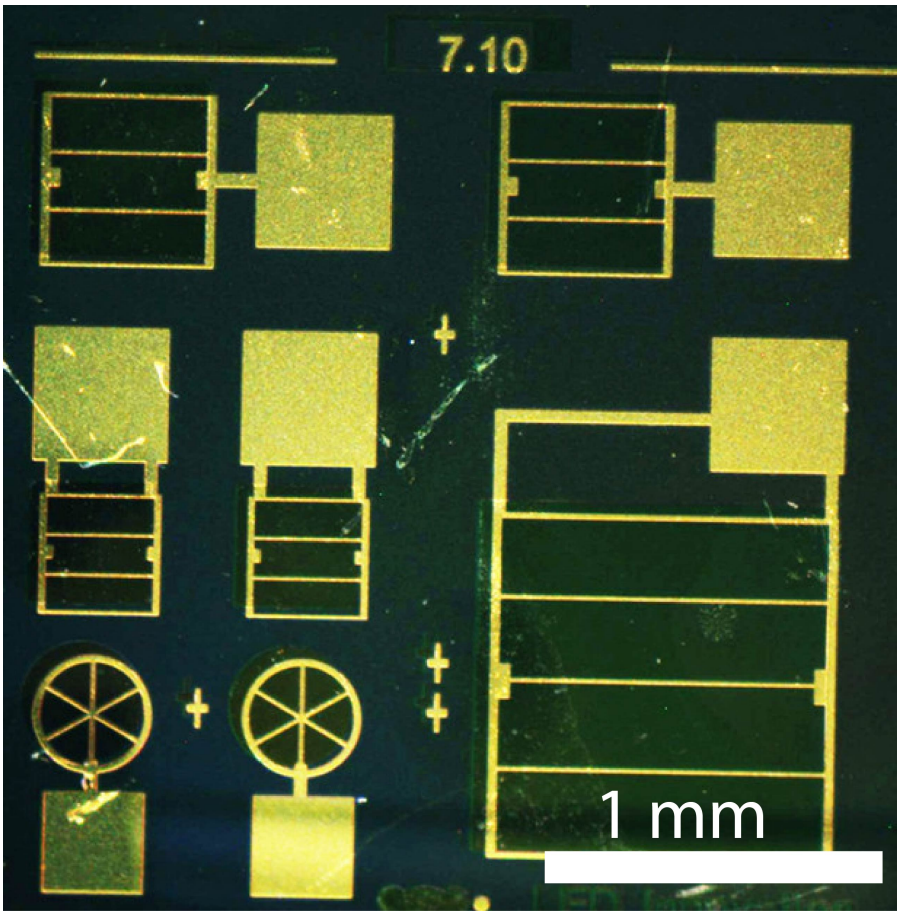

Figure 22: Solar cell mask with bonding pads. Seven cells of four different sizes are shown.

Silicon dioxide is then deposited by plasma-enhanced chemical vapour deposition (PECVD) to define the solar cell areas, which are then selectively exposed by etching with 6:1 hydrofluoric acid to water solution. The lift-off was done using MF319 and stepper lithography. The stepper lithography system is pictured in Figure 21. The final top contact pads were then deposited by electron beam deposition of titanium and gold again. Microposit® remover 1165 was used for Ti/Au/ITO lift-off, isolating the solar cells. The back contact was formed by a single Ti/Au layer covering the entire area back of the silicon wafer.

A mask is used to produce a pattern of four different sizes of solar cells with gold pads for contacts. From largest to smallest, the square cells are sized 1 mm x 1 mm, 500 µm x 500 µm, and 350 µm x 350 µm, while the smallest circular cell is 350 µm in diameter. The top Ti/Au contact pads were 400 µm x 400 µm in size with 40 µm traces connecting the pads to the cells, as shown in Figure 22. Some misalignment during the lithography manifests itself as an offset between the darker cell areas and the top gold contacts.

Each cell has finger contacts deposited on the indium tin oxide (ITO) to reduce resistive losses in the contacts. Each finger is 10 µm in width to reduce reflection losses. A schematic of the fabricated sample is shown in Figure 23.

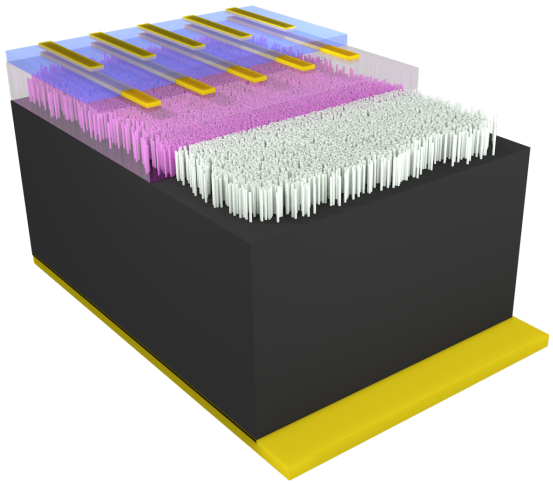

Figure 23: 3D schematic cut-away of fabricated nanowire solar cell on Si (111). The polyimide is illustrated in pink, silicon in dark grey, nanowires in white, and contacts in gold. Schematic is not to scale.

4.3 SAMPLES

The samples described in this thesis were of various designs to form different device types. Some were designed for solar cells, while others were made exclusively as single or multijunction LEDs. The nanowire designs varied with the number of quantum dots, the inclusion of an electron blocking layer, the number of junctions, as well having AlGaN/GaN core-shell structures. Some samples were left unfabricated to enable the characterization of the nanowires on silicon themselves prior to the polyimide and ITO layers. Not all device types were investigated in this thesis. The potential of multijunction nanowire solar cells on silicon is also discussed from six junction designs. An overview of the samples and their design properties is shown in Table 5.

Designation	Fabricated?	QDs per junction?	Number of junctions	Doped?	Electron Blocking Layer?	AlGaN shell?	Device configuration
MN647	No	1	1	No	No	No	*p-i-n*
MN656	No	6	1	Yes	No	No	*p-i-n*
MN698	Yes	10	1	Yes	No	No	*p-i-n*
MN797	Yes	10	1	Yes	Yes	Yes	*p-i-n*
MN1246	No	5	6	Yes	No	Yes	*n-p-n* LED
MN1325	Yes	10	1	Yes	No	Yes	*n-p-n* LED
MN1359	Yes	5	3	Yes	No	Yes	*n-p-n* LED
MN1418	Yes	5	3	Yes	No	Yes	*n-p-n* LED
MN1482	Yes	10	1	Yes	No	Yes	*p-i-n*
MN1672	No	0	1	Yes	No	Yes	*p-i-n*
MN1673	No	10	1	Yes	No	Yes	*p-i-n*

Table 5: InGaN/GaN quantum-dot-in-nanowire sample list with design characteristics.

4.4 MICROSCOPY

4.4.1 *Optical Microscopy*

Basic characterization of the nanowires was performed by optical microscopy with a Nikon® Eclipse LV150NL microscope with 5X, 50X and 100X objectives. Images at 100X of a variety of samples are shown in Figure 24. The variety of colours between samples is representative of the varying nanowire heights with different junction configurations. Localized changes in colour arise from the sub-wavelength dimensions of the nanowire array where the electric field of photons of various wavelengths from the illumination lamp interferes constructively and destructively with the nanowire-covered surface. The single junction cells are green in appearance as a result of interference effects in the nanowire layer, which acts as an effective medium between the ITO/air and silicon substrate.

In certain samples, a distinct spotted pattern is observed in optical microscope which is attributed to nanowires that grow significantly higher than the surrounding nanowires. The required contrast and resolution to identify taller nanowires in optical images necessitated imaging by laser scanning confocal microscopy. Confocal microscopy was performed using a laser scanning microscope with 488 nm, 532 nm and 650 nm lasers, and a 20X Mitutoyo® objective with a 0.35 numerical aperture. A 488 nm laser was used to achieve the best possible resolution. Despite the sub-micron sizes of the nanowires, the confocal microscope was able to identify spots on the surface which corresponded to the infrequent occurrence of tall nanowires that have been identified by scanning electron microscopy and atomic force microscopy. The speckled pattern is visible in Figure 25.

4.4.2 *Scanning Electron Microscopy*

Nanowire morphology is an important property of a nanowire solar cells. The diameter of the nanowires influences the spectral reflectivity of incident light, as well as the transport and recombination of carriers in the nanowires. The height of the nanowires also affects the amount of incident light absorption and greatly controls the transport properties through the nanowire. A convenient and powerful method of imaging the overall morphology of the nanowires is by scanning electron microscopy (SEM). This technique uses the scattering of electrons with a surface to produce imaging contrast only fundamentally limited by the *de Broglie* wavelength of the accelerated electrons and, more practically, the interaction volume of electrons with the surface being imaged. Prior to imaging, samples were mounted on sample mounts covered in adhesive carbon tape. The vacuum chamber of a Zeiss® GeminiSEM® 500, which is pumped to a vacuum of $<10^{-5}$ Torr. Imaging is done at a variety of voltages ranging from 2 kV to 20 kV. Individual nanowires are resolved with an imaging resolution of approximately a few nanometres. The diameters of the nanowires

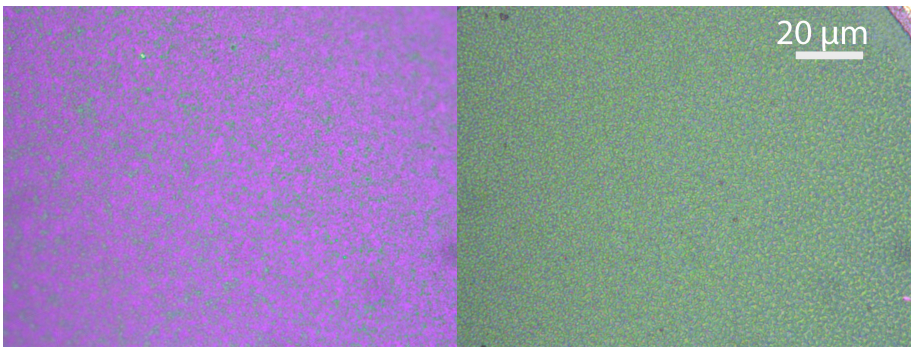

(a) 1J *p-i-n* MN698 (unfabricated) (b) 1J *p-i-n* MN797

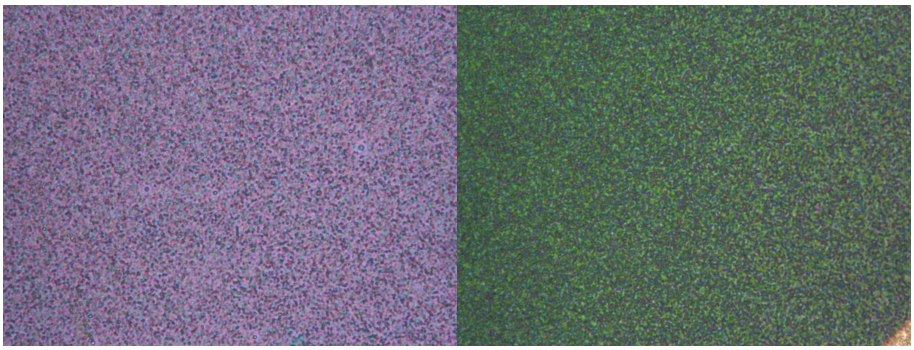

(c) 1J *n-p-n* MN1325 (d) 1J *p-i-n* MN1482

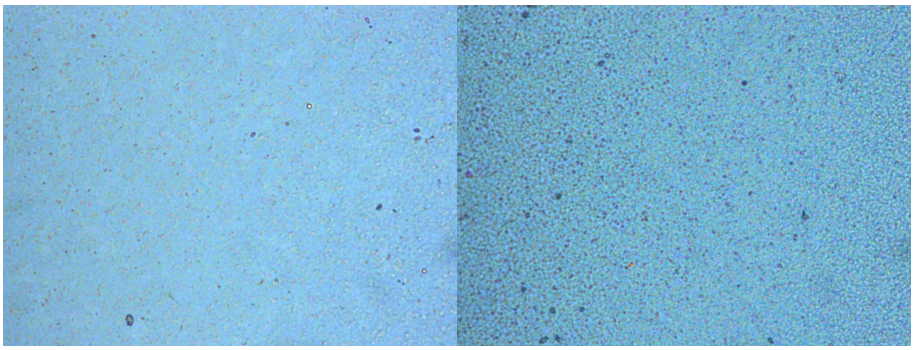

(e) 3J *n-p-n* MN1359 (f) 3J *n-p-n* MN1418

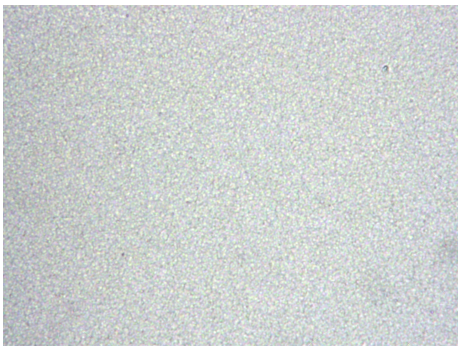

(g) 6J *n-p-n* MN1246

Figure 24: Optical micrographs at 100X magnification of various grown InGaN/GaN nanowire samples on silicon

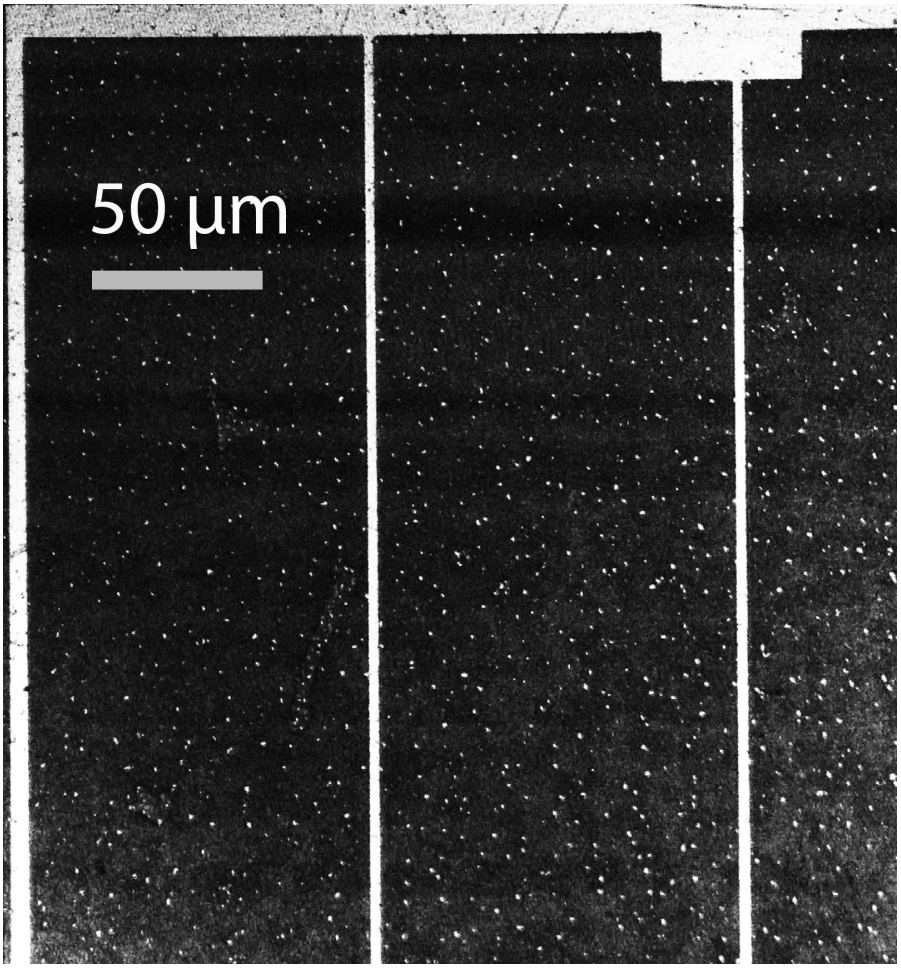

Figure 25: Confocal microscope image of a fabricated nanowire sample. White dots on the surface are indicative of tall nanowires which have continued to grow higher as the majority begin to coalesce during growth.

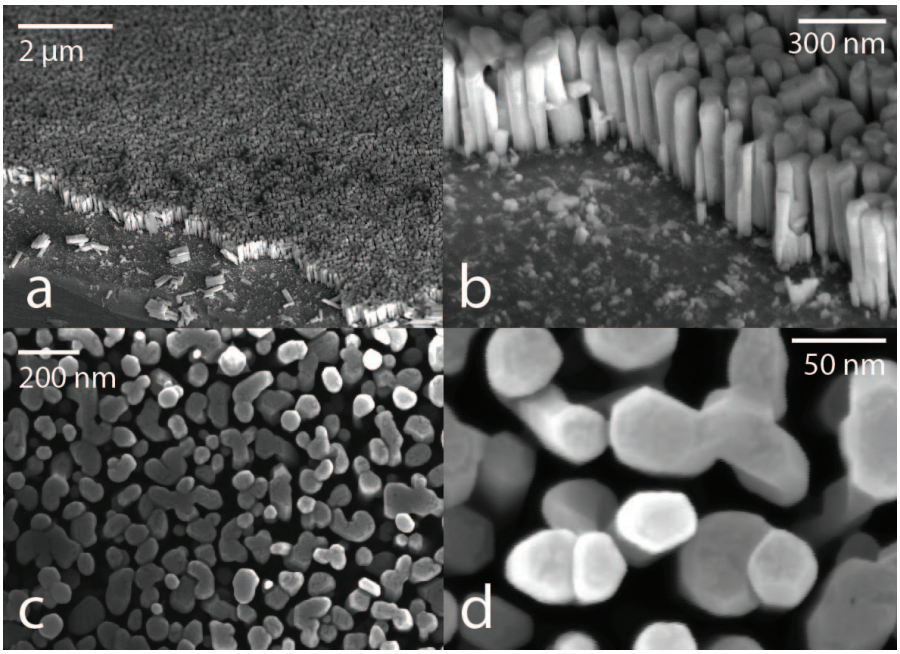

Figure 26: Scanning electron microscopy of unfabricated InGaN/GaN nanowires on silicon. (a) 45° view of the nanowire ensemble at the edge of the cleaved wafer. (b) Close-up 45° view of nanowires with a section of nanowires removed to show the density of nanowire nucleation. (c) Plan view of the nanowire ensemble to illustrate the nanowire density. (d) High resolution plan view of nanowires demonstrating hexagon geometries.

was analyzed statistically from plan-view images displaying over 100 nanowires.

For bare, unfabricated nanowire samples, scanning electron microscopy of the samples enables us to determine the areal density of nanowires. From high resolution scanning electron microscope images such as in Figure 26 of the nanowires, the packing factor, diameter and density of the nanowires was determined.

The plan view image in Figure 26c was converted to binary using a basic threshold algorithm so that the binary image closely resembled the original image. The number of 1s vs 0s in the binary file were summed and compared to produce a factor of approximately 70% nanowire material coverage at the top surface. From Figure 26c, the number of nanowires were counted within a region. The density was found to be approximately 105 nanowires per square micron, or 1.05 x 10^{10} nanowires per cm^2. This corresponds well to nanowire LED samples previously fabricated, which had a density of about 10^{10} nanowires per cm^2. The number of unique nanowires measured by SEM may underestimate the quantum dot density since many nanowires fuse together during growth.

The diameters of 70 nanowires were measured and the distribution is plotted in Figure 27. The diameters of nanowires were found to be around 90 nm, with a variation roughly corresponding to a Gamma distribution, as shown in Figure 27. The space between nanowires is

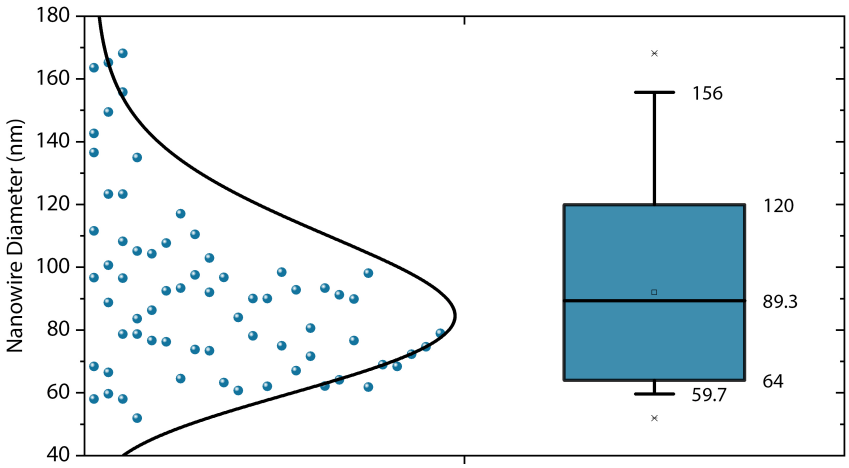

Figure 27: Histogram and box plot of bare nanowire diameter distributions. The box illustrates the standard deviation of the ensemble and the error bounds indicates the 5-95 percentile range.

approximately 50 nm which decreases significantly with an AlGaN shell which was not applied to the nanowires shown in Fig 26.

Shorter, incomplete nanowires can be seen in between the larger nanowires in the cross-sectional SEM image (Figure 28) which is visible at the cleaved plane of an unfabricated sample. Due to their reduced height, they are not expected to participate in current generation since they lack the required electrical contact to the ITO and they are expected to contain significant InGaN quantum dot regions. The heights of the nanowires are determined to be about 500-600 nm with orientations of up 20° from the vertical. Angular orientations of nanowires measured near the edge of the wafer are from SEM imaging are a result of damage from the cleaving process.

Once fabricated into a device, the polyimide and ITO cover the nanowires. In Figure 29, the ITO is highlighted in blue with the nanowires highlighted in purple. It is clear that some nanowires make better contact with the ITO layer, while other nanowires may not be contacted properly to the top. This is expected to result in a highly nonuniform current production for nanowire solar cells or luminescence in nanowire LEDs.

4.4.3 *Other Microscopy*

The nanowire samples were also studied using a Zeiss® ORION® NanoFab® scanning helium ion microscope. A helium ion microscope operates similarly to an electron microscope but uses helium nuclei (two bound protons) instead of an electron as the accelerated particle. An extremely sharp tip which has only three atoms at the apex (called a trimer) under field ionization can emit a beam of helium atoms. The shorter *de Broglie* wavelength of the helium particle is achieved via its

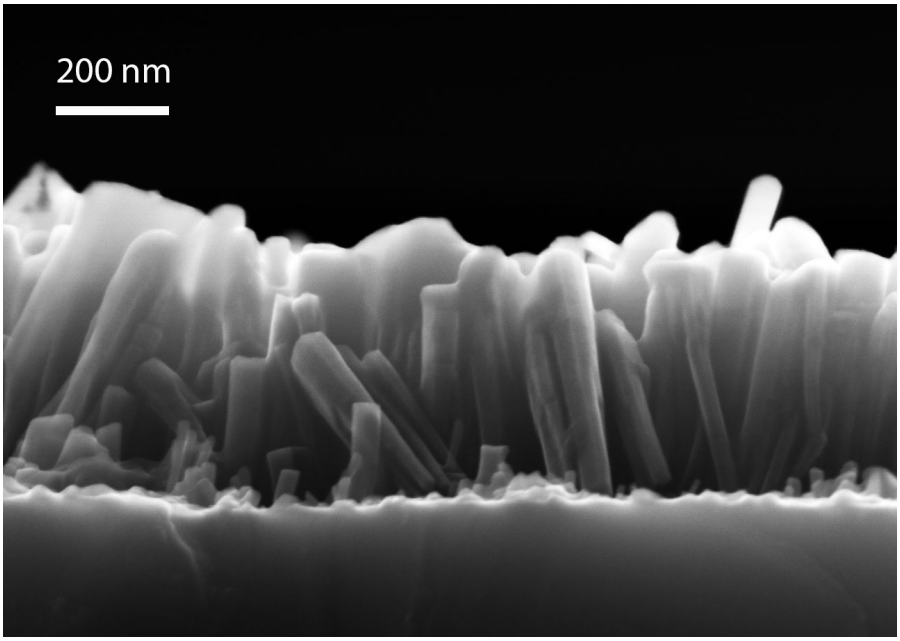

Figure 28: Cross-sectional SEM image of InGaN nanowire on the silicon substrate. The sample is unfabricated.

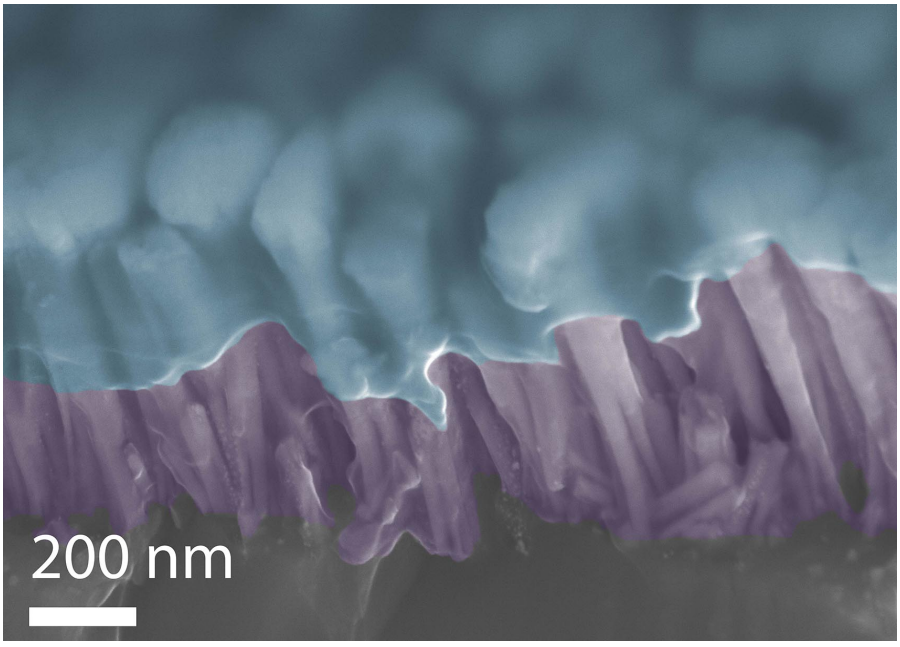

Figure 29: False-colour high incidence angle scanning electron micrograph of a cleaved, fabricated nanowire solar cell. In this cross-section, the ITO is coloured blue, nanowires are coloured in purple and the silicon substrate is in grey.

much heavier mass when compared to an electron, providing higher imaging resolution. The source of the helium beam is also confined to one of the atoms of the trimer, leading to a point source size of less than an Angstrom with high brightness. Another important difference is the interaction volume of the helium ions is very small since they do not penetrate and scatter with a volume like electrons do. The technique is therefore superior to electron microscopy for surface details and can obtain sub-nanometre resolution. Scanning helium ion microscope images were taken by the Zeiss ORION Nanofab at the University of Ottawa as shown in Figure 30.

Images were taken with the as-grown nanowires and on nanowires that were intentionally broken off the surface and scattered onto a substrate for imaging along the growth axis. In some samples, tall, well-formed nanowires were found with heights over 100 nm taller than the surrounding nanowire ensemble. Other samples demonstrate very few (or none) tall nanowires suggesting subtle changes in growth conditions can control the presence of these tall nanowires. It is possible that during growth, the preferential growth in the vertical direction as opposed to the radial direction growth leads to slightly taller nanowires (which begin to growth first) to accumulate more gallium and nitrogen atoms and become much taller. The nanowires tend to become wider near the top during growth and tend to join with one or two adjacent nanowires to form irregularly shaped nanowires. The uniformity of the nanowire height is essential to optimizing the device performance as it ensures that all nanowires can form ohmic contacts to the top electrodes. If the *n*-type base of a tall nanowire is electrically connected to a *p*-type emitter of an adjacent nanowire, the connection acts like a *p*-*n*-*p* LED and transport is hindered in that nanowire.

From previous high-resolution scanning transmission electron microscopy work by Dr. Zetian Mi's group at McGill University[47] and Dr. Steffi Wo at McMaster University[36], the InGaN quantum dots have been revealed to vary in shape from disk-shaped to lens-shaped within the nanowire heterostructure, as shown in Figures 31. Using high-angle annular dark-field mode of scanning transmission electron microscopy (HAADF-STEM), the atomic ordering can be resolved in columns. The small diameter of the nanowires allows the InGaN quantum dots to be resolved without cross-sectional milling. The microscopy of nanowires has helped to determine the dot and barrier geometries and dimensions for finite element computer simulations of the devices in Chapter 5.

4.4.4 *Energy Dispersive X-ray Spectroscopy*

A useful tool that is typically coupled with scanning electron microscopes is energy dispersive X-ray spectroscopy (EDS or EDX). This technique relies on using the scanning electron beam as source of high energy electrons incident on the atomic species of the sample under study. The high energy of the electron has a certain probabil-

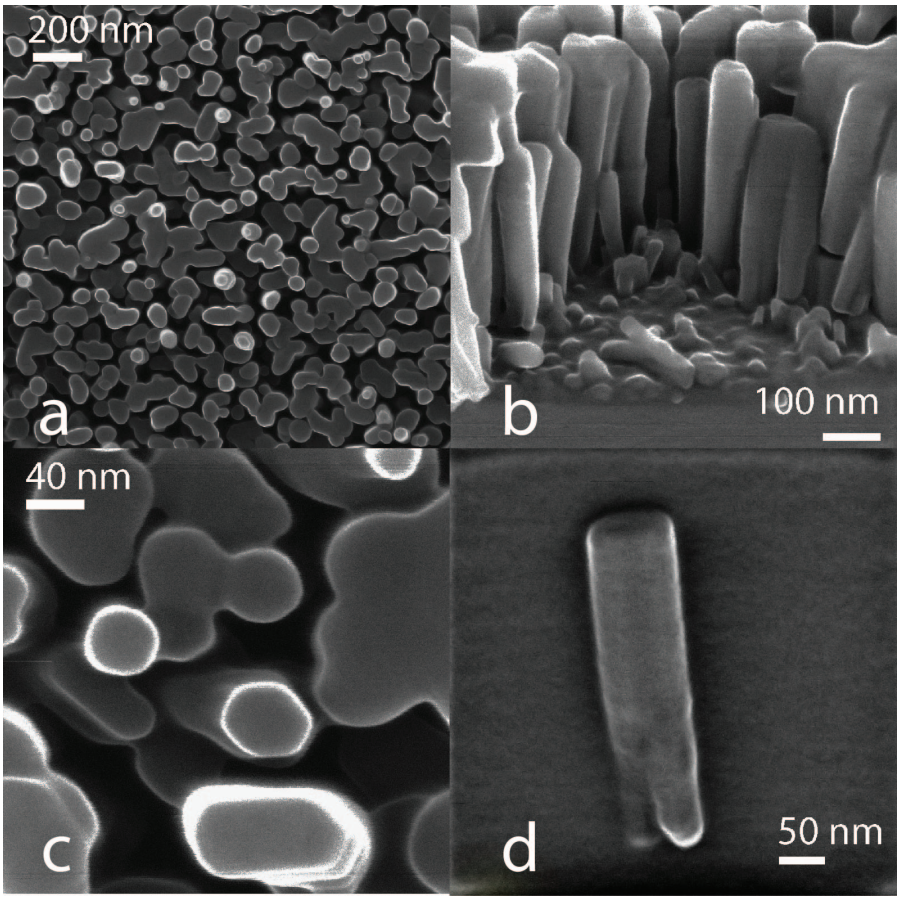

Figure 30: Scanning helium-ion microscope images of as-grown InGaN/-GaN nanowires. The images show (a) a plan-view of the nanowire array, (b) 55°view of nanowires at the edge of a cleaved sample, (c) high resolution of plan-view of the nanowires showing hexagon shapes in single narrow nanowires, (d) two fused nanowires broken off from the substrate.

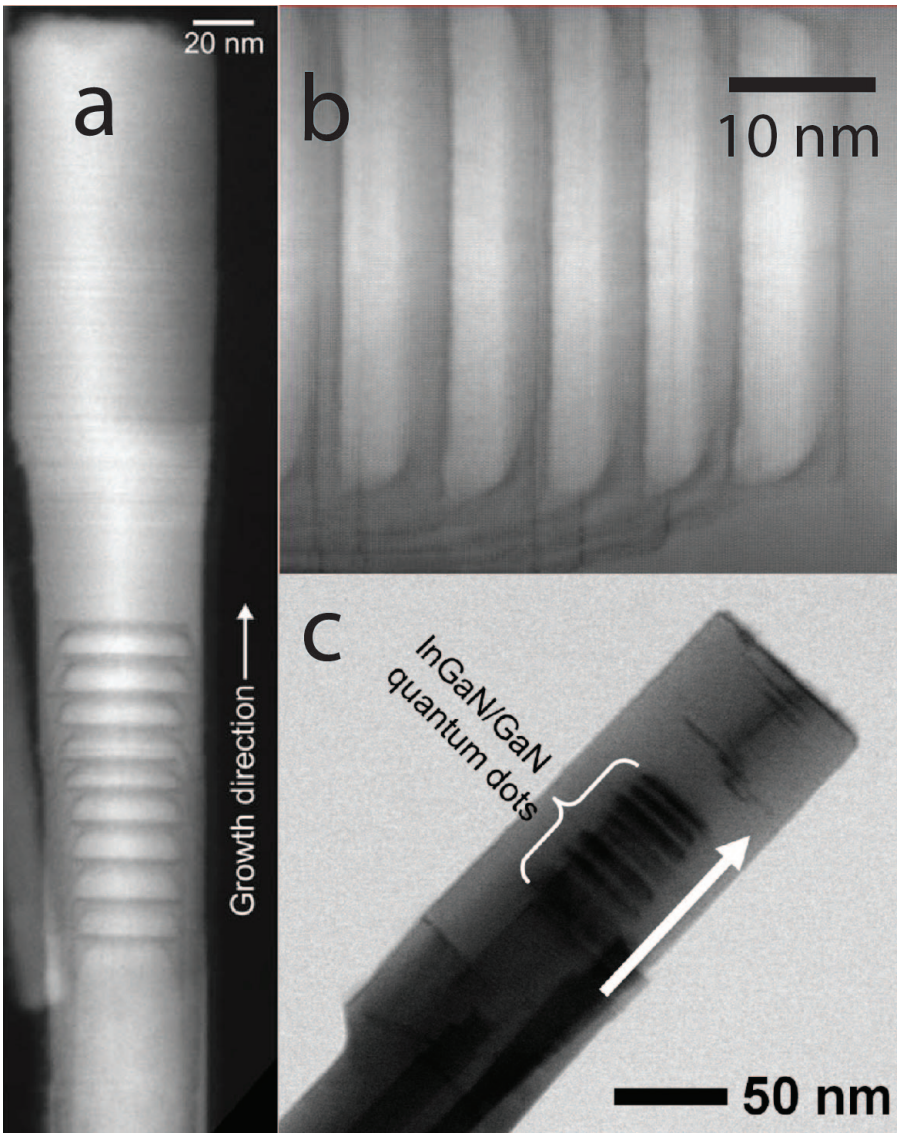

Figure 31: Scanning transmission electron microscope images of similar InGaN/GaN nanowires from previous publications by researchers at McGill University and McMaster University. Figures (a) and (b) are from Nguyen *et al.* (2015)[47] and (c) is from[36].

ity to excite a bound electron from an atom and leave a hole that is quickly filled by a higher energy bound electron. This drop in energy releases an X-ray with a characteristic energy that corresponds to the difference between the temporarily empty state and the higher energy state. Since these energy differences are unique to each atom, the atomic species can be determined.

The energy of the electron beam was adjusted to be higher than the largest primary transition energy of either nitrogen, indium, gallium, and silicon. The sample was cleaved to reveal a cross-sectional view of the sample. A Zeiss® GeminiSEM® 500 was used for the imaging and electron source. An XFlash 6 silicon drift detector was used to measure emitted X-ray photons. The acceleration voltage was set at 10 kV to provide sufficient energy for the indium atom transitions. The atomic elements of nitrogen, indium, gallium, carbon, oxygen and silicon were identified.

The composition of the nanowires was verified by scanning the electron beam over a cross-sectional view of the nanowire as seen in Figure 28. Strong silicon, gallium, nitrogen peaks were identified as shown in Figure 32. Small peaks from oxygen and carbon were identified and attributed to contamination of the nanowire surface or microscope chamber. A weak indium peak was identified from the quantum dots. The peak intensities are not calibrated to correspond to fractional composition.

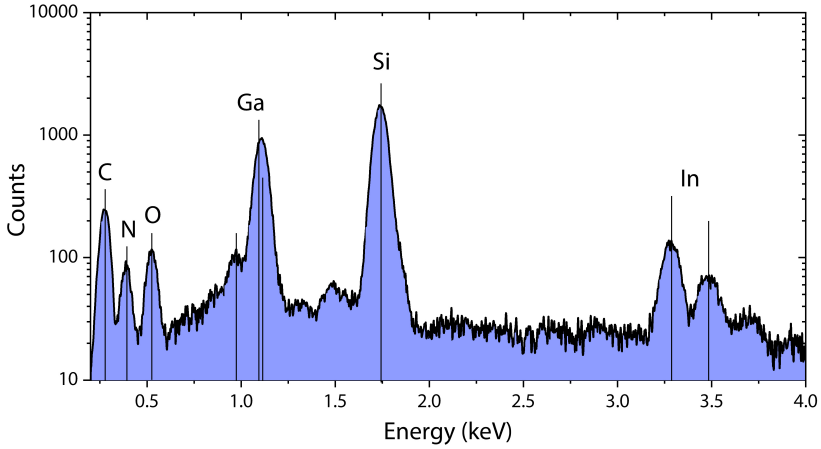

Figure 32: Energy dispersive X-ray spectrum of the GaN nanowires with InGaN quantum dots. The peaks for oxygen and carbon are attributed sample contamination and SEM chamber contamination.

A two-dimensional EDS map was performed that can spatially identify atomic species in an SEM image. The EDS signal was overlaid with a side-view SEM image as shown in Figure 33 An even distribution of gallium and nitrogen is seen throughout the nanowires. A weak indium signal was detected in the middle of the nanowire structures as expected but was insufficient in resolving the ten individual dots themselves.

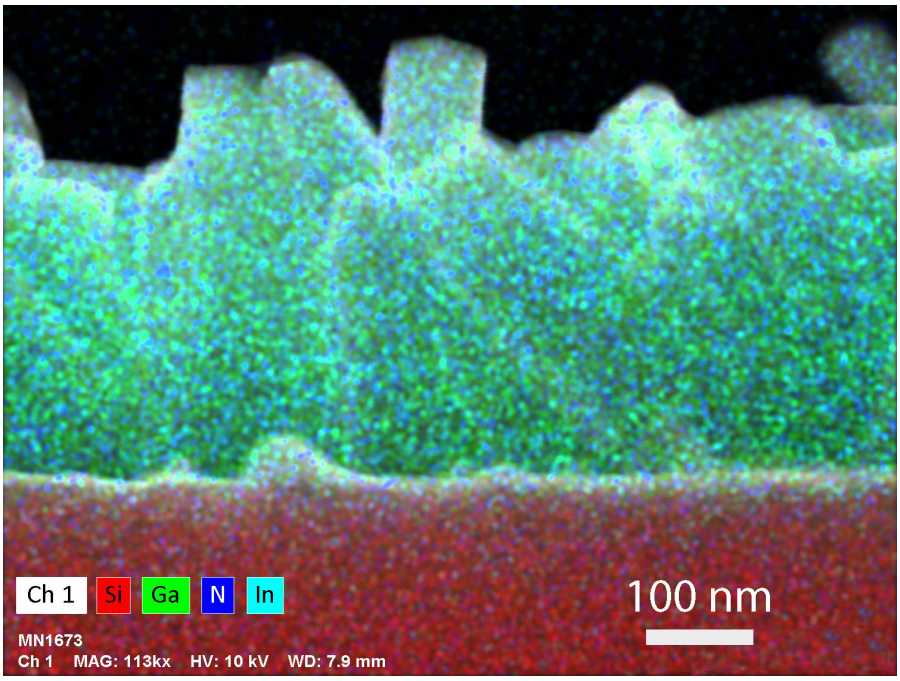

Figure 33: Energy dispersive X-ray spectroscopic map (colours) overlaid on a cross-sectional scanning electron micrograph (white). Different colours correspond to counts from different atomic species.

The EDS spectroscopy mapping confirms the chemical composition of the nanowires and the approximate position of the quantum dots. The technique however is not as effective as high angle angular scanning transmission electron microscopy (HAADF-STEM) with electron energy loss spectroscopy (EELS) or EDS spectroscopy which can determine the indium composition of individual dots as has been demonstrated in work by H.P.T. Nguyen *et al.*[190]. However, EDS using SEM is simpler to perform since less sample preparation is required and the technique could determine the relative amounts of indium in the nanowires, and quantified if compared to a reference sample.

4.4.5 *Atomic Force Microscopy*

More detailed imaging of the top surface of the nanowires was achieved using atomic force microscopy (AFM). This technique can produce very high resolution maps of the surface morphology by scanning an extremely sharp silicon tip across a surface. The small tip dimensions (a few nanometres) enables nearly atomic resolution imaging of surfaces laterally and is especially good at resolving height variations on a surface. Height variations are detected using a laser reflecting off the cantilevered tip, and the beam deflection is resolved using a quadrant photodiode. As the tip scans across the sample, deviations from the expected tip position are interpreted as height differences. A scanning electron microscope image of an AFM tip is shown in Figure 34.

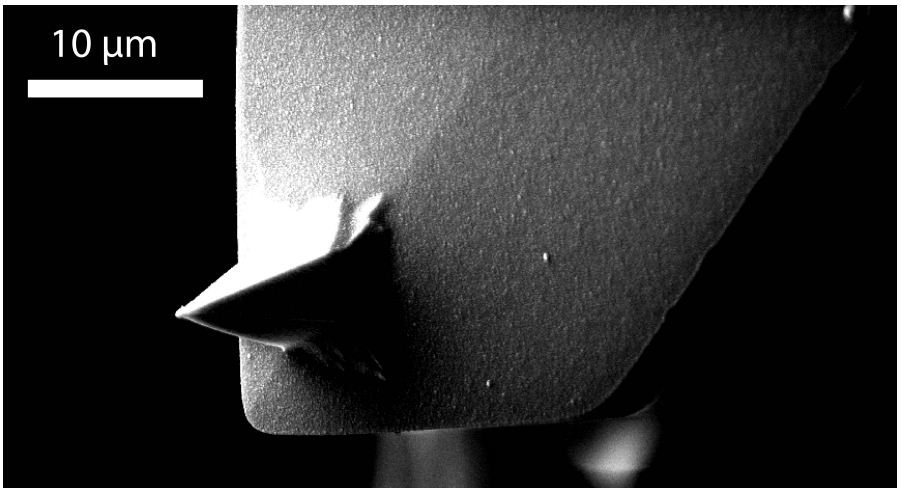

Figure 34: An atomic force microscope tip shown for reference. This tip in particular is conductive and can be used for electrical measurements as well as surface morphology.

AFM was performed using a Bruker® Dimension Icon® system with ScanAsyst® probes in tapping mode. Forward and backward traces were used to produce images through the height sensor. Cleaved unfabricated nanowire-on-silicon samples were placed on a stabilized vacuum stage. Probe tip quality was assessed via SEM microscopy prior to its use for atomic force microscopy scans. The surface morphology of the top nanowire surface was mapped over a region 5 µm x 5 µm for wide scans to 300 nm x 300 nm for high spatial resolution scans.

Shown in Figure 35, AFM revealed a non-uniformity in nanowire height and size which corresponds well to SEM images. Most nanowires had heights within 50 nm of each other, with a small minority of single nanowires growing up to 150 nm higher. During the scan, the high aspect ratio of the nanowires presented a challenge for producing accurate images. The AFM tip geometry is asymmetric along the scan direction, which can produce an asymmetry in the forward and backward traces and a trailing signal on one side of the anomalously tall nanowires when the scan speed is high. To accommodate for this, the scan speed was reduced from 1000 ns/s 100 nm/s as well as adjusting the tapping mode parameters. Most nanowires demonstrated a roughly rounded hexagonal shape, owing to the wurtzite lattice structure of GaN. The tops of the nanowires were slightly rounded, which may indicate the presence of slightly lens-shaped InGaN quantum dots as found in the work by Steffi Wo *et al*. on similar GaN-nanowire-on-silicon devices[36].

Nanowires which were sufficiently separated in height from neighbouring nanowires could be imaged as a single entity, as shown in Figure 36a. The vertical scale is exaggerated to illustrate the texture of the top surface. Figure 36b is a plan-view AFM image of the top of the same nanowire, where the rounded hexagonal shape is apparent. The rounded shape is used to infer the approximate geometry of the embedded InGaN quantum dots.

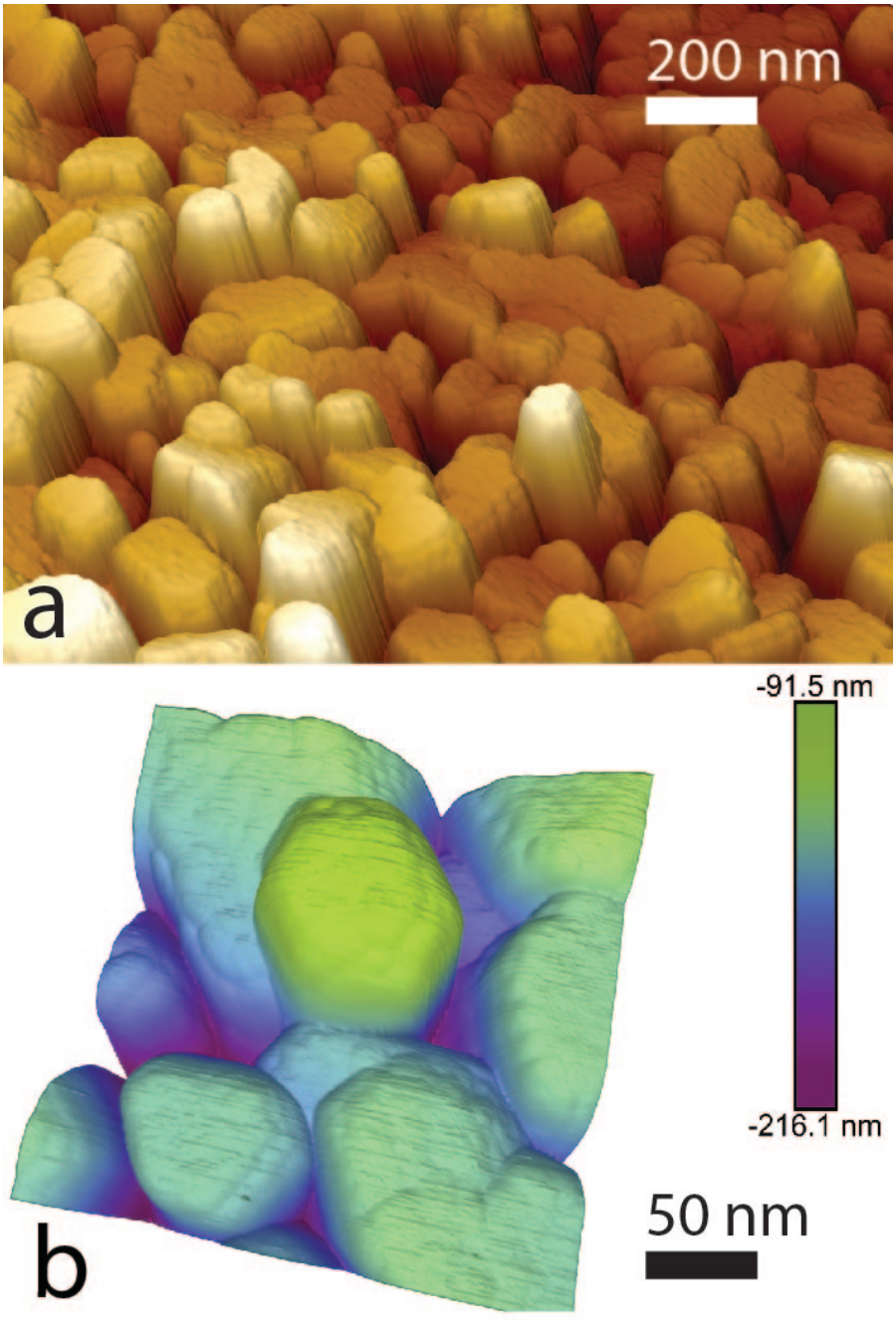

Figure 35: Atomic force microscopy of bare InGaN nanowires on silicon. (a) Large area AFM scan of many nanowires. The gradual colour gradient is attributed to a slight tilt of the sample relative to the stage. (b) High resolution AFM scan of a few nanowires demonstrating the rounded edges of the nanowires and the joining of nanowires near the top.

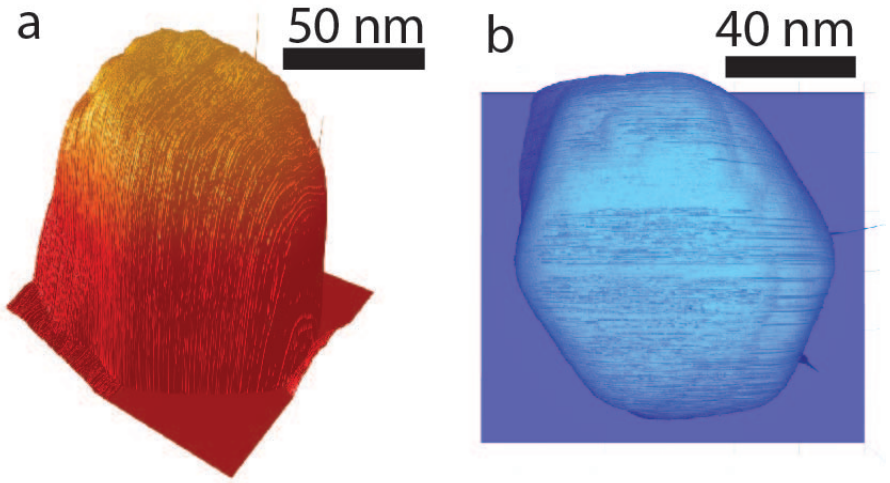

Figure 36: Atomic force microscopy of single, bare InGaN nanowires on silicon demonstrating the hexagonal shape and rounded top profile.

4.5 QUANTUM EFFICIENCY

An important metric for optoelectronic devices is the measured of quantum efficiency, which is the probability to generate an electron for each incident photon on the device (for solar cells), or the probability to generate a photon for every injected electron (for LEDs or lasers). In the case of a solar cells, an ideal device would have a quantum efficiency that is ideally 100% across the entire solar spectrum. A typical quantum efficiency measurement consists of a white light beam that enters a monochromator to separate the beam by wavelength. A slit selects a monochromatic beam of light and direct it onto the solar cell being tested. The current generated by the solar cell is measured as a function of wavelength. The system is depicted in Figure 37.

To eliminate the effect of stray light increasing the current measured, many quantum efficiency measurement systems incorporate a lock-in technique and multiple measurements to establish very reliable and consistent measurements. The quantum efficiencies (QE) as a function of wavelength were measured using a Newport® IQE-200 quantum efficiency measurement system, shown in Figure 38. The system is designed to allow for simultaneous EQE and IQE measurements on a temperature-controlled stage. The beam is divided by a beam splitter and focused on the sample to provide monochromatic illumination. Data is collected through two, three or four channels simultaneously, depending on the measurement type. The first channel is used for measuring the intensity of the incident beam of light and is mounted after the beam splitter. The second channel is used to measure the current generated in a photo-sensitive device with light reflected by the beam splitter. The third channel is used to measure the specular reflection off the sample and is mounted above the beam splitter. The fourth channel is used to measure the remaining diffusely reflected light and is coupled to a separate integrating sphere

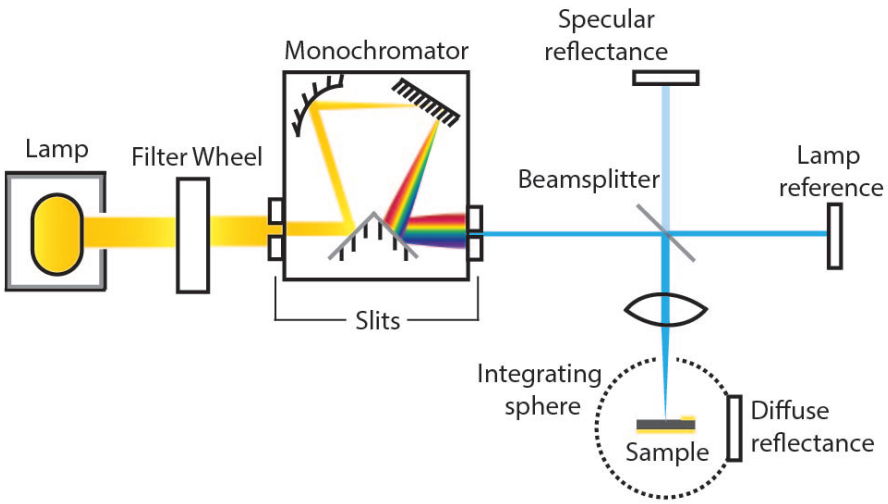

Figure 37: Illustration of the quantum efficiency measurement setup. The integrating sphere is only used for diffuse reflectivity measurements.

module. The first, third and fourth channels each consist of a silicon/germanium photodiode connected to a Merlin® 70101 lock-in amplifier. The single channel lock-in amplifier rotates between each channel at each wavelength step. The lock-in amplifier is synchronized with an optical chopper at 87 Hz.

The light source is a filtered 300 W Xenon arc lamp that enables quantum efficiencies to be measured from 300 nm to 1800 nm. Wavelength selectivity is obtained through an Oriel® CS130 monochromator system which outputs a minimum spectral full width at half maximum of 5 nm from the Xenon lamp. The spectral width was verified using an ASD® Fieldspec® spectroradiometer. For simple external quantum efficiency (EQE) measurements, channels 1 and 2 are used. To account for the specular reflectivity of the sample, the internal quantum efficiency (IQE) can be measured using channels 1, 2 and 3. In rougher surfaces that do not contain an anti-reflection coating, the fourth channel must be used to measure the diffuse reflectivity and thus the true IQE of the device.

Quantum efficiency measurements were performed on samples with 10 quantum dots in each nanowire. The beam emitted by the monochromator was modified to produce a smaller beam aperture from the monochromator to ensure the beam on the cell was incident on the active area of the small cell. The quantum efficiency was measured as a function of beam intensity which was controlled by the entry slits from the monochromator. Internal and external quantum efficiencies are measured from 300 nm to 900 nm. Longer wavelengths are expected to be either absorbed in the silicon substrate (<1150 nm) or reflected off the back of the substrate (>1150 nm).

As expected, there was a peak in the quantum efficiency around 375 nm. This corresponds to absorption in the GaN region of the nanowire. The production of current in the nanowires extended beyond the bandgap of GaN with a significant tail into the visible spec-

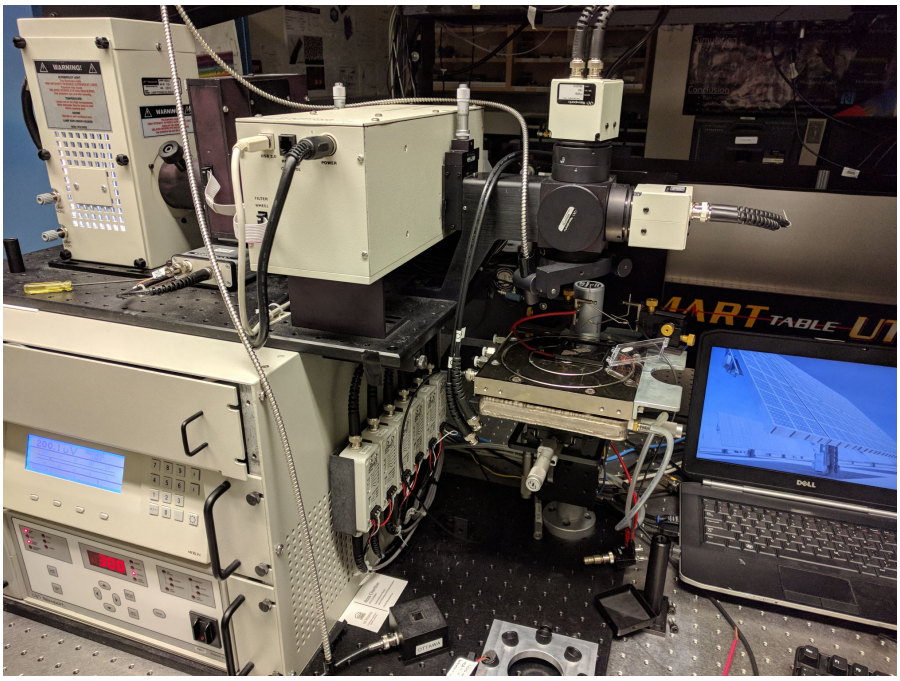

Figure 38: Newport® IQE-200 quantum efficiency measurement station at the University of Ottawa.

trum. Another smaller peak appears around 500 nm as a shoulder to the main quantum efficiency signal, which may correspond to transitions from InGaN quantum dot hole states to extended GaN conduction band states in the intrinsic region. A further peak appears at 600-800 nm depending on the sample, which would also correspond to transitions from different quantum well states to extended GaN states. The sub-bandgap current is responsible for up to 25% of the total current produced by the device. Since the quantum efficiency measurements were performed with a monochromatic incident beam, no significant intermediate band operation is expected. Interestingly, with the addition of a broadband light bias using an incandescent light bulb, the quantum efficiency is unchanged. This could be a result of the longer wavelength photons being absorbed deeper into the nanowire structure nearer to the lower quantum dots than the shorter wavelength photons. The low mobility of holes in InGaN compounds and even GaN may make it unlikely that the holes generated at the back of the device can move towards the negatively charged *p*-type side of the nanowire so the longer-wavelength photons do not contribute to current flow. Sub-bandgap current is produced since the monochromatic light is sufficient in using two photons of the same wavelength up to even 800 nm to produce hole and electrons near the top of the nanowire. This suggests significantly long carrier lifetimes in the quantum dots. Future work could involve the comparison with a pure GaN nanowire on silicon control sample.

As a function of power, the quantum efficiency contribution from sequentially excited carriers is expected to increase as a result of the increased probability of secondary photon prior to recombination in the quantum dots. Shown in Figure 39, the quantum efficiency at

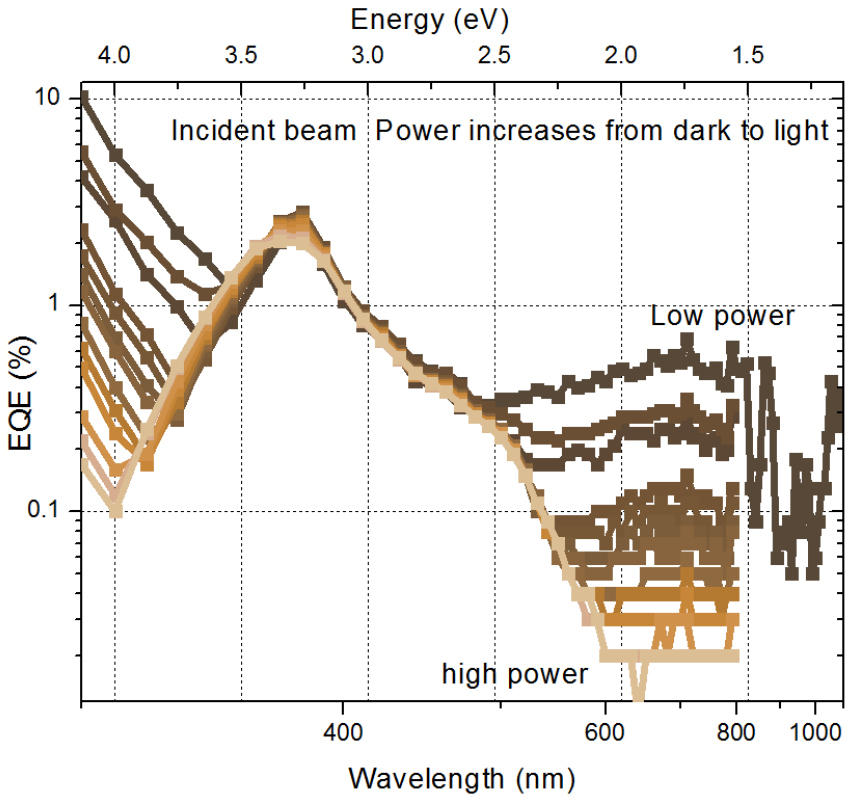

Figure 39: Quantum efficiency for sample MN797 as a function of incident beam intensity. Higher powers are indicated by lighter colours.

wavelengths shorter than 350 nm and longer than 500 nm decreases significantly with the light intensity, contrary to the expected operation of an intermediate band solar cell. A possible explanation could be that the photofilling of quantum states may be quite high, reducing the amount of sub-bandgap absorption that can occur. When the intermediate states are filled with carriers, only the intermediate state to extended GaN conduction band state transitions can occur, leading to increased optical transmission. The decrease in quantum efficiency with beam intensity below 375 nm with higher beam powers could also be an effect related to photofilling of states in quantum dots closest to the tops of the nanowires. In such a case, transport may be inhibited due filled quantum dot states affecting the transport or tunneling of additional carriers.

The quantum efficiency was used to determine the short circuit current of the solar cell and compare it to the value obtained with illuminated current-voltage characteristics. The short circuit current determined by EQE is more accurate than determined by current-voltage characteristics as the solar spectrum can be factored in directly as opposed to relying on an accurate solar simulator spectrum or using a spectral mismatch factor.

The short circuit current can be calculated with

$$Jsc = q \int_{\lambda_{min}}^{\lambda_{max}} EQE(\lambda)\Phi_{AM1.5}(\lambda)d\lambda, \tag{236}$$

where $EQE(\lambda)$ is the quantum efficiency, $\Phi_{AM1.5}(\lambda)$ is the solar spectrum, and q is the elementary charge.

In discrete steps, the equation becomes

$$Jsc = q \sum_{\lambda_{min}}^{\lambda_{max}} EQE(\lambda)\Phi_{AM1.5}(\lambda)\Delta\lambda. \tag{237}$$

The short-circuit current is calculated from the quantum efficiency in the current-voltage characteristics section.

4.6 REFLECTIVITY

The specular and diffuse reflectivities of the nanowires were measured using the same Newport® IQE 200 quantum efficiency measurement system using channels 1, 3 and 4. Both bare and fabricated samples were measured under identical conditions with the integrating sphere attached. Reflectivity results are shown in Figure 40.

The bare InGaN/GaN nanowires on silicon exhibited a relatively large diffuse reflectivity with oscillations corresponding to etalon effects in the nanowire region. The high density of nanowires allows the region to be treated as an effective index of InGaN/GaN and air. The bare nanowire region does manage to exhibit an extremely low specular reflectivity of near zero owing to virtually all light being scattered at non-normal angles upon interaction with the sub-wavelength, disordered nanowire features.

Once fabricated, the specular reflectivity increases as a result of the smoother indium tin oxide and gold contact surfaces. The oscillatory reflectivity effects are a result of the difference in refractive index of the ITO and polyimide in the fabricated cells, as opposed to simply air in bare samples. The etalon effects of the diffuse reflectivity of the fabricated cell are very weak and demonstrate a different period than the specular reflectivity. This indicates that the diffuse reflection in the fabricated cell may be mostly as result of the subwavelength scattering inside the nanowire/polyimide region in addition to the diffuse reflection off the top ITO surface.

The nanowire region is strongly absorbing up to the GaN band gap of 3.4 eV, where the etalon effects are not visible. From Crosslight APSYS simulations, absorption from the InGaN quantum dots is expected to decrease steadily until about 2 eV or 600 nm, where photons are either reflected or absorbed in the silicon substrate. Approaching 1100 nm, the specular reflection of the fabricated cell is affected by absorption in the silicon. After 1100 nm, the silicon substrate becomes transparent and the etalon effects in the overall device structure dominate.

4.7 CURRENT-VOLTAGE CHARACTERISTICS

The current-voltage characteristic of solar cells is that of a diode which is shifted upwards upon illumination. The illuminated current-

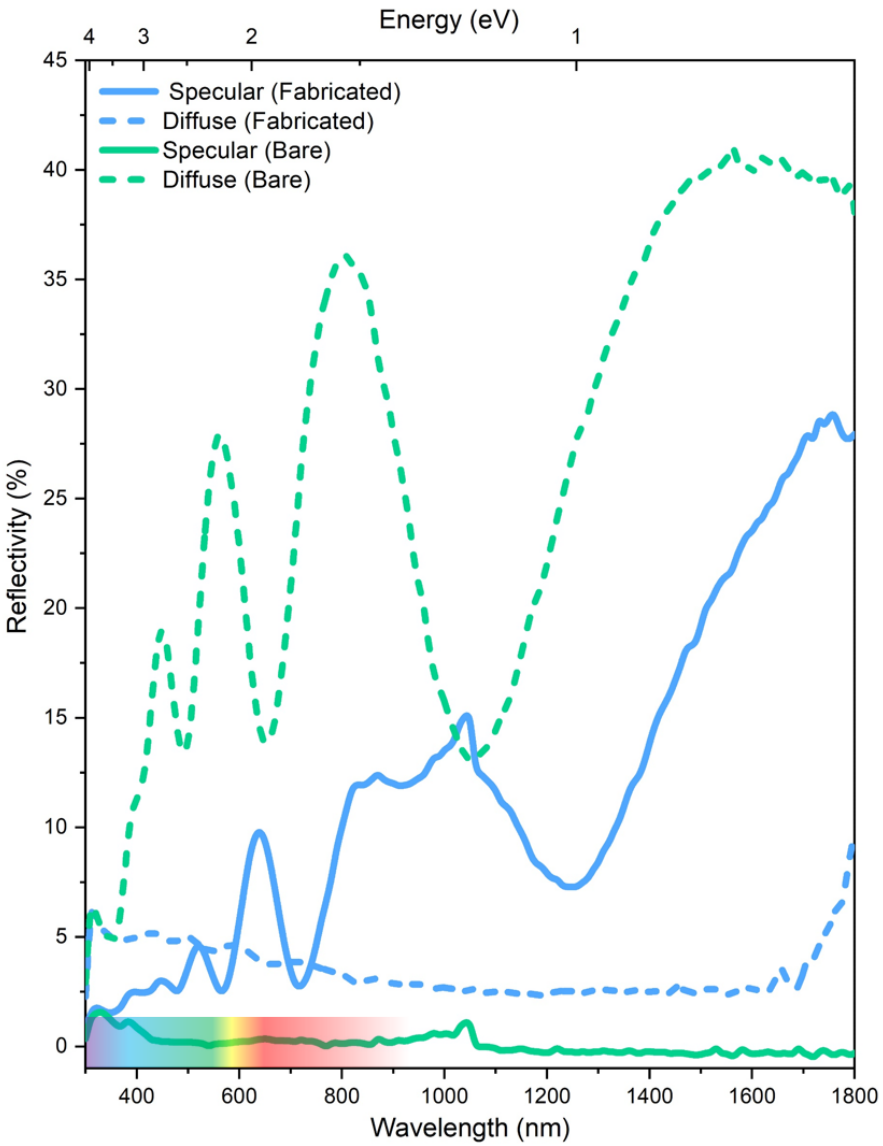

Figure 40: Specular(solid) and diffuse(dashed) reflectivity of bare(bare) and fabricated(green) nanowire samples as a function of wavelength.

voltage characteristics of the nanowire solar cells were measured as a function of illumination intensity from a solar simulator. Solar simulators are used to provide an approximate solar spectrum for consistent device testing. The light is usually generated from a high-power xenon arc lamp. The output from the lamp is collimated and filtered to best match the illumination characteristics of the sun.

Two solar simulators were used in the characterization of the illuminated current-voltage curves, each with distinct features. The primary solar simulator is the 1600 watt class AAA Newport® Sol 3A® 94123A which can provide up to 1 sun simulated AM1.5D or AM1.5G solar spectrum over a large area. The secondary solar simulator is a similar Oriel® 1600 W solar simulator which is capable of up to 20 suns of AM1.5G illumination over a smaller region. Lower concentrations of light were achieved using perforated nickel filters with varying degrees of transmittance. All measurements are performed using four probes in the Kelvin configuration to eliminate the contact resistance. Samples are mounted on gold-coated copper vacuum stages. An Olympus® stereo microscope was used to ensure proper contact between the probe tips and the contact pads of the cells.

The temperature of the stage upon which the sample was placed was measured and tuned using a PID (proportional-integral-derivative) Peltier temperature controller with a control range of 15-100°C. The temperature was maintained at 25°C +/- 2°C unless otherwise mentioned, and the current-voltage curve was acquired within five seconds of the initial illumination. The current-voltage characteristics under varying levels of AM1.5G illumination are shown in Figure 41. The solar cell revealed very low open circuit voltages that increased from 0.06 V at 0.5 suns to over 0.2 V at 16 suns in the best cells. There is a significant variation in the performance from cell to cell that is attributed to the inconsistent ITO to gold pad contact quality. The short-circuit current increased roughly linearly. The fill factor increased from about 0.25 at 0.25 suns to a maximum just under 0.3 at 16 suns. The short circuit current density increased at about 0.75-0.1 mA/cm^2 per sun depending on the cell. Significant variations in the short-circuit current per sun are attributed to the large experimental error in the illumination intensity actually experienced by the small cells. The perforated nickel foiled used to attenuate the light from the solar simulator are designed for larger solar cells where the perforation effect is averaged. This variation is especially pronounced in the lower intensities (0.25 to 1 sun). Additional measurements with another solar simulator with a variable attenuator built-in has reproduced the short-circuit current per sun. In the case of the Figure 41, the best efficiencies are found at the lower concentration intensities where the best power conversion efficiency was measured at 0.058% at 0.5 suns.

When measuring the illuminated current-voltage characteristic of solar cells, the illumination intensity is assessed through a calibrated silicon reference cell. Since the current-voltage characteristic is measured using a solar simulator which is slightly different than the AM1.5G spectrum, the reference cell does not necessarily assess the

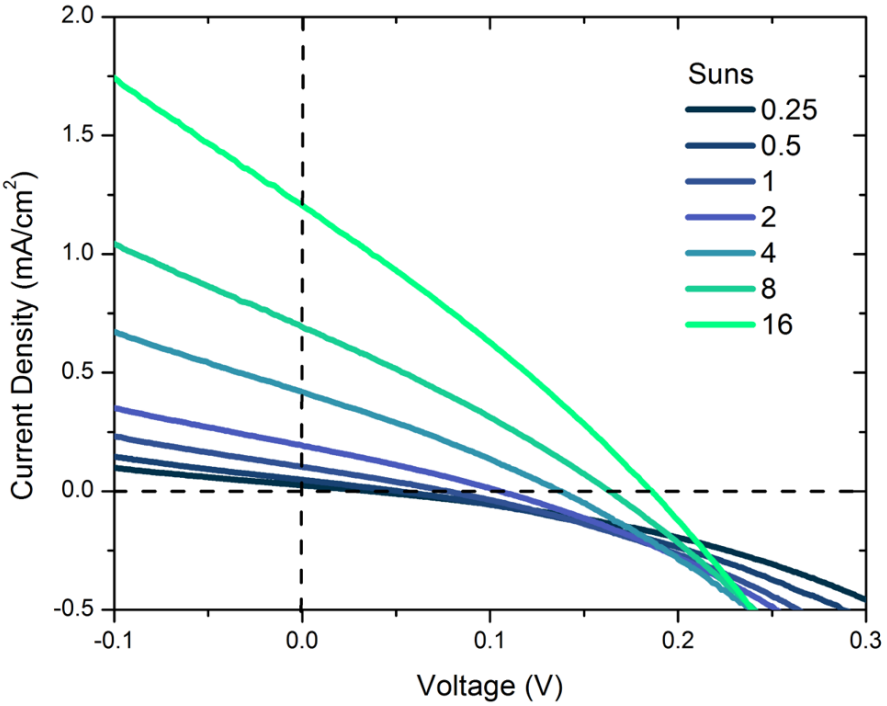

Figure 41: Illuminated current-voltage characteristics of an InGaN/GaN quantum-dot-in-nanowire solar cell.

response of the cell at all wavelengths. As a result, a spectral mismatch factor can be defined which depends on the spectral responses of the reference and test cell, as well as the spectrum of the solar simulator and a standard solar spectrum reference. The spectrum mismatch factor for the reference cell is defined in[191] and is written as

$$MMF_{spec} = \frac{\int SR_{ref}(\lambda)\Phi_{AM}(\lambda)d\lambda \int \Phi_m(\lambda)d\lambda}{\int SR_{ref}(\lambda)\Phi_m(\lambda)d\lambda \int \Phi_{AM}(\lambda)d\lambda}, \tag{238}$$

where Φ_{AM15G} is the standard solar spectrum, Φ_m is the measured spectrum of the light source used, SR is the spectral responsivity of the reference cell.

The spectrum from the Sol 3A solar simulator was measured using an ASD® FieldSpec® spectroradiometer which measures the spectrum at the sample position. The spectrum was compared to the spectrum of the AM1.5G and AM1.5D standard spectra in Figure 42 and is useful in ensuring the solar spectrum is within specification and for spectral mismatch calculations. Sharp peaks in the lamp emission spectrum are associated with xenon emission lines in the lamp.

A value of unity for MMF_{spec} would indicate that there is no spectral mismatch. From the measured spectral responsivity of the silicon reference cell, measured solar spectrum of the Sol 3A solar simulator, and the AM1.5G solar spectrum from the IEC 60904-3:2016 standard, the spectral mismatch factor was calculated from 312 to 1100 nm to be 0.94.

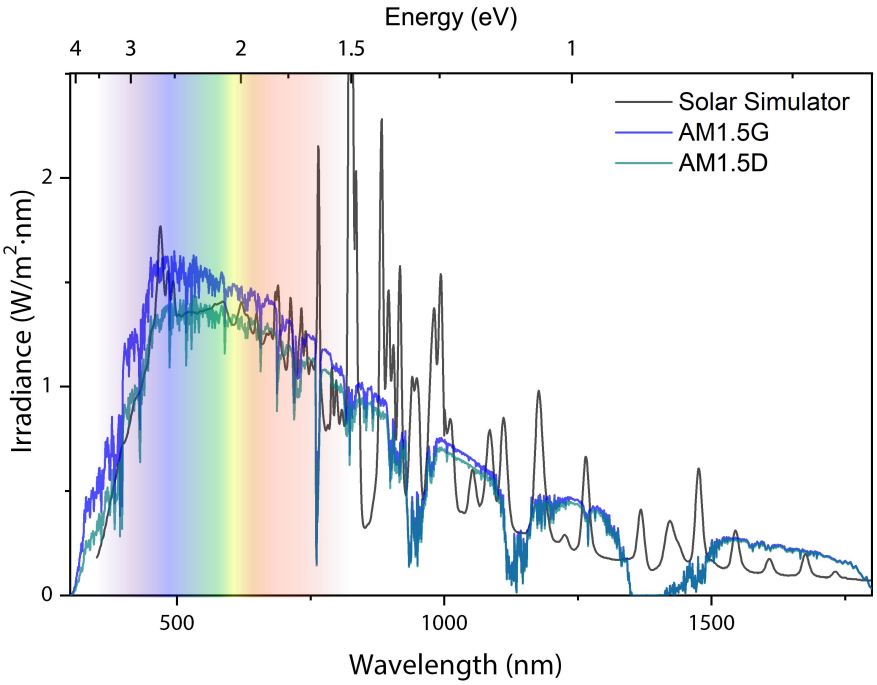

Figure 42: The AM1.5G and AM1.5D solar spectrum overlaid with the measured solar spectrum from the Sol 3A solar simulator.

The spectral mismatch factor can also be re-defined when using a reference cell, which can indicate how far off the short-circuit current is during a measurement. The discrepancy arises from the different spectral responsivities between the reference cell for illumination calibration and the cell under test. The test cell to reference cell spectral mismatch MMF_{ref} is a more stringent and is defined as

$$MMF_{ref} = \frac{\int SR_{ref}(\lambda)\Phi_{AM}(\lambda)d\lambda \int \Phi_m SR_t(\lambda)d\lambda}{\int SR_{ref}(\lambda)\Phi_m(\lambda)d\lambda \int \Phi_{AM} SR_t(\lambda)d\lambda}. \tag{239}$$

The test cell to reference cell spectral mismatch was calculated to be 0.79. We therefore expect some deviation in the short-circuit current from the true value when measuring illuminated current-voltage characteristics. Due to the difference between the spectral responsivities between bulk silicon and InGaN/GaN quantum dots, large differences in the short-circuit current are possible. Indeed, this difference can be determined by obtaining the true short-circuit current from the quantum efficiency. From equation 79 using AM1.5G as the solar reference standard spectrum, the short-circuit current was calculated as about 75 $\mu A/cm^2$. This value very close to the value of 73.5 $\mu A/cm^2$ measured using a Sol 3A solar simulator. The difference in this case is well within the spectral mismatch and other sources of error.

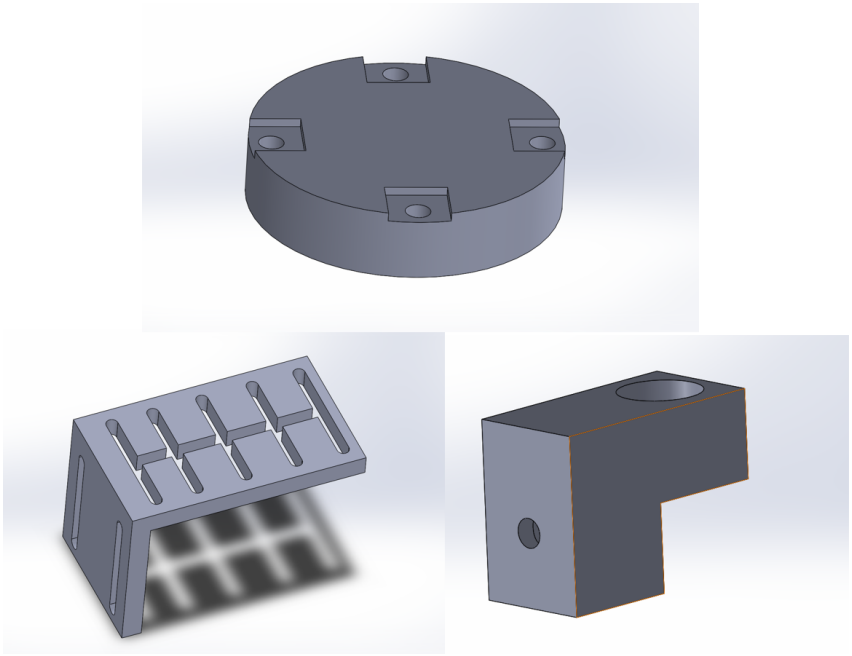

Figure 43: SolidWorks® schematics of the cryostat stage which allows for multi-probe current-voltage measurements electrical bias of nanowire solar cells.

4.7.1 *Low Temperature Current-Voltage Characteristics*

Current-voltage measurements were performed on samples mounted in a liquid nitrogen cryostat cooled to various temperatures. Samples were mounted in a liquid nitrogen cryostat on a copper stage designed for electrical connections to fabricated nanowire samples. The cryostat is equipped with electrical connections to an external port. A new stage and probe mounts were designed in SolidWorks® and machined from solid copper for optimal thermal coupling of the sample to the cold finger as shown in Figure 43. The stage consisted of a copper angle bracket which can support the mounting of a cylindrical copper plate in various positions in three dimensions. This design enabled the use a higher magnification objective lens (Olympus SLMPLN 50X with a numerical aperture of 0.35) with a shorter working distance for higher-resolution electroluminescence and photoluminescence measurements.

Four copper probe mounts were designed and machined to support metallic needle probes, as shown in Figure 43 which made contact on the gold contact pads of the individual nanowire solar cell top contacts. The probe mounts were machined with a 1 mm hole through which standard probe tips could be inserted. The electrical connections inside the cryostat were soldered to the tops of the probe mounts. Nylon spacers were used to electrically isolate the probe mounts from the copper stage. Nylon bolts were used to attach the probe mounts to the copper stage. The shared back contact of the solar cells on the bottom of the silicon wafer placed in electrical contact with the copper stage and a probe mount. A very small amount of rubber cement was used to attach the samples to the surface without

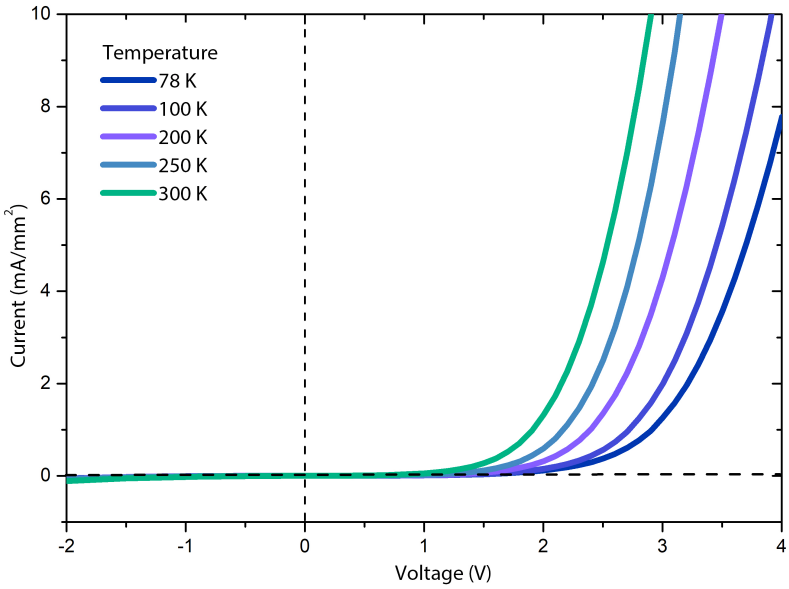

Figure 44: Current-voltages characteristics of single *p-i-n* junction nanowires as a function of temperature.

completely relying on mechanical pressure from the probe tips. The top 4-40 screws are used to push on the top of the mechanical needle probes downwards to make electrical contact with the cells. The mechanical setup is shown in Figure 50.

In this configuration, up to three cells can be independently biased simultaneously. The voltage bias is supplied by a Keithley® 2420 Sourcemeter® connected to a LabVIEW® program which performs current-voltage measurements and can supply a constant voltage bias. The back contact of the wafer is mechanically pressed against the copper stage by the probe tip which makes an electrical contact to the top bonding pad. The devices are driven by voltages ranging from 1-20 V depending on the intensity and number of junctions in the nanowire device. The temperature was controlled using a PID-controlled heating element combined with a liquid nitrogen reservoir.

The shift of the turn-on voltage for the nanowire solar cells shifts up to 1 V higher as the sample cools from 300 K to 78 K, as shown in Figure 44. An increase in the resistance of the nanowire in the forward bias regime was observed with temperatures lower than 100 K. This effect is attributed to poor dopant activation at such low temperatures since the thermal energy available for dopant ionization is less than 10 meV.

4.7.2 *Transient Current Measurements*

During electrical characterization, the nanowire cells exhibited an increase in current over time when under forward bias. This effect was taken into account by measuring the entire current-voltage characteristic over a period of less than a second and starting at two seconds

after the start of the illumination. For smaller cells, the current increase reaches an equilibrium after a significant amount of time, especially at lower forward biases. This mechanism is attributed to current crowding causing localized heating of the cell when operating as an LED. The additional heat increases the current draw through the cell which again increases the heat until the cell achieves steady state through heat dissipation with the environment. The current increase as a function of time is shown in Figure 45. The current increase is more drastic at lower bias voltages. At larger bias voltages, steady-state conditions are reached relatively quickly. At large bias voltages where the cells are emitting significant amounts of light, the change in current is negligible.

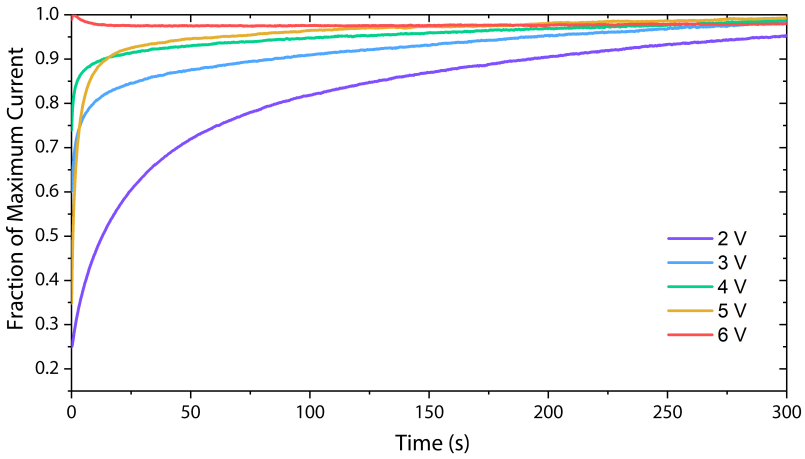

Figure 45: Current increase over the period of 300 seconds as a function of forward bias voltage.

4.8 PHOTOLUMINESCENCE

The optical properties of semiconductor nanostructures are best studied through the emission of excited carriers. The emission spectrum and intensity of emitted light are directly related to transitions between energy levels in extended or confined states. Stronger radiative recombination indicates a reduction of non-radiative recombination and thus improved performance in the case of most devices. In photoluminescence spectroscopy, carriers are usually excited using a laser beam with photon energies higher than the transition energy being studied.

The characterization of the luminescence from semiconductor nanostructures provides important information about the material composition, material quality, recombination processes, nanostructure dimensions, and the allowed optical transitions between discrete quantum states for holes and electrons. Photoluminescence of the nanowires is accomplished using a laser to excite electrons in the valence band to the conduction band states, followed by spectroscopy of the emitted photons from the subsequent radiative recombination back into lower

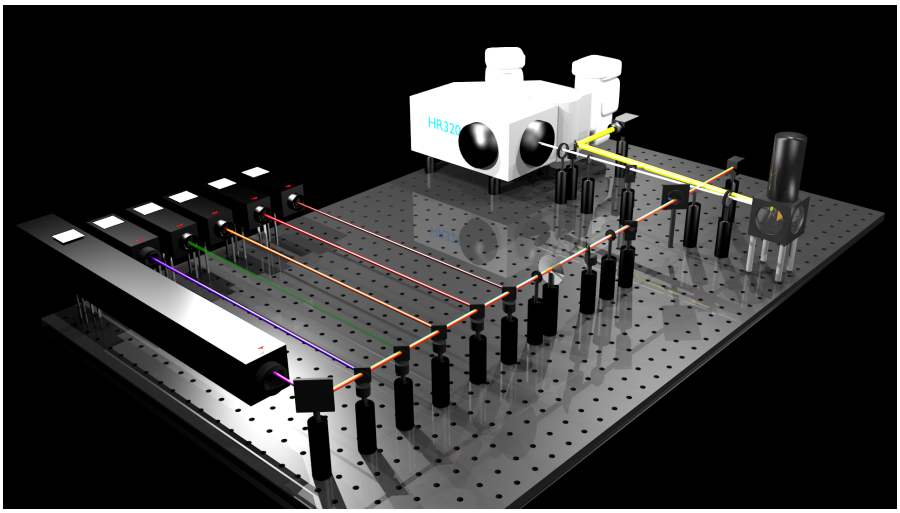

Figure 46: Photoluminescence spectroscopy system configuration. Laser beams are set up along the same optical path to enable quick switching between excitation wavelengths.

energy states. The laser wavelength is generally chosen to provide incident photons of energy greater than the intended transition(s) under study.

In the case of our nanowire samples, the radiative recombination can occur in the GaN regions, or the InGaN quantum dots. The emission from the *p*-GaN and *n*-GaN regions require photoexcitation via an ultraviolet laser, but the study of the InGaN quantum dots can proceed with a purple or blue laser since the emission produces visible photons. Photoluminescence from the quantum dot region is expected to correspond to the transition energy between the lowest occupied quantum well electron states and the highest unoccupied hole quantum well states. The molar fraction of indium in the quantum dots as well as the height of the quantum dots dictates these transition energies.

A photoluminescence setup at the University of Ottawa was constructed to use six lasers which can be selectively used for excitation using a series of mirrors on flip mounts. The setup is illustrated in Figure 46. A 200 mW InGaN diode laser of wavelength 405 nm is used as the excitation source for exciting carriers in the InGaN quantum dots. The beam is directed towards an adjustable neutral density filter and passes through two apertures to improve collimation and alignment of the beam. Light from a laser is directed towards a 45° dichroic longpass filter which reflects the laser beam towards the objective. The beam is focused onto the sample through either an f=10 cm UV-fused silica concave lens for a larger spot or a Olympus® SLMPLN 50X objective with a numerical aperture of 0.35 for microphotoluminescence. Optical power incident on the sample is measured using a Newport® 842-PE optical power meter which can selectively enter or leave the beam path through a flip mount.

A Cryo Industries of America® cryostat is used to house the sample for temperature control. The cryostat temperature is varied using liquid nitrogen and a programmable Cryocon® temperature controller.

Liquid nitrogen is poured in from the top and directly cools the copper cold finger. The sample is mounted on a copper stage connected to this cold finger. A Varian® roughing pump coupled to a Varian® turbo pump is used to provide the vacuum sufficient to eliminate the possibility of condensation within the cryostat. The sample is affixed to the stage using Elmer's® rubber cement.

The photoluminescence signal is collected and collimated back through the focusing optic, passed back through the dichroic filter, and refocused towards the slit of an iHR 320 Horiba Jobin-Yvon® spectrometer of focal length 320 mm. The light was filtered a 450 nm longpass filter to block stray laser light prior to entry in the slit. Two liquid nitrogen-cooled detectors, a Horiba® Symphony® silicon CCD detector and a Horiba® Symphony InGaAs CCD detector, are attached to the spectrometer can be used for either visible light or near-infrared spectroscopy, respectively. The diffraction grating with 1200 lines/mm blazed at 500 nm is used to diffract the photoluminescence signal. The spectrometer and CCD detectors are computer controlled using proprietary SynerJY® Symphony® Software, as well as a custom LabVIEW® application which was developed as part of this thesis to incorporate photoluminescence mapping, temperature control, and automatic measurements into a single setup.

Simultaneous microscopy of the sample is achieved through the same objective lens, where a 30:70 beamsplitter reflects a portion of the emitted light from the sample towards a Thorlabs® 1.4-megapixel CMOS camera coupled with a Thorlabs® zoom lens. During imaging and sample positioning, the sample is illuminated using a consumer grade LED lamp. The photoluminescence system is positioned atop an optical table where the lasers are encased within a box of black aluminum sheets with an opening for outputting the laser beam.

The choice of 405 nm for the excitation wavelength allows for the direct excitation of the InGaN regions since GaN remains transparent in 405 nm light. Bulk InGaN regions emit light in a very broad spectrum from 500 nm to 700 nm. The photoluminescence was measured on samples with and without InGaN quantum dots as shown in Figure 47 and those with and without core-shell structures 48. When comparing the photoluminescence of nanowires with quantum dots to those with a bulk-like InGaN region in Figure 47, the emission is broadened significantly. The broadening is accompanied by a redshift, resulting in a yellow-red appearance. The emission extends to almost 800 nm. The broadening is attributed to the indium accumulation process which forms the quantum dots structure. The integrated intensity of photoluminescence emission is greater for the nanowires with quantum dots despite a lower intensity at the centre emission wavelength.

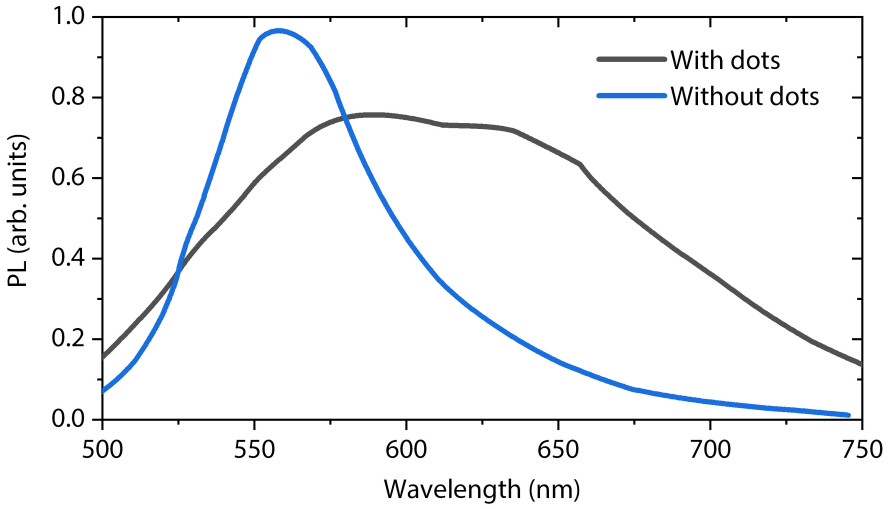

Figure 47: Photoluminescence spectra of samples MN1672 (without dots, but with a bulk-like InGaN intrinsic region) and MN1673 (with 10 InGaN dots in the intrinsic region) at 78 K. The sample without dots contains a bulk-like InGaN region. The sample with 10 quantum dots demonstrates a broader photoluminescence spectrum that extends to the edge of the visible spectrum. This is attributed to increased indium composition in a multiple quantum dot region versus a bulk-like InGaN region.

In Figure 48, the photoluminescence signal is stronger when nanowires were covered in an AlGaN passivation shell. This change is expected to reduce the surface recombination at the nanowires by introducing a larger bandgap material around the nanowires. Two broad peaks in the signal are seen at 575 nm and 675 nm which could be due to monolayer differences in dot thicknesses (centred around 3nm) predominant in the nanowires. Excited carriers are spatially isolated from the nanowire-air or nanowire-polyimide interface which contain more surface states than the passivated AlGaN/GaN interface.

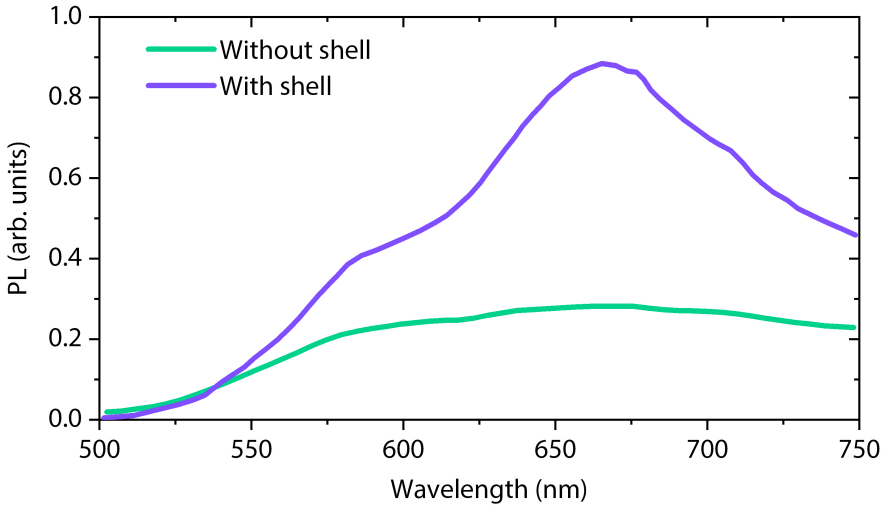

Figure 48: Photoluminescence spectra of samples MN656 (bare GaN nanowires with 10 InGaN quantum dots) and MN797 (core-shell structure around GaN nanowires with 10 InGaN quantum dots) at 78K. With the addition of an AlGaN shell, the photoluminescence signal is significantly improved due to less surface recombination of photogenerated carriers.

4.9 ELECTROLUMINESCENCE

While photoluminescence provides insight into the material properties, the transport of carriers across the multiple quantum dots to the GaN regions is critical to the operation of a solar cell. Where photoluminescence depends on the optical absorption and recombination rates at various parts of the nanowire heterostructure to provide luminescence, electroluminescence is related to the radiative recombination rates between the electron and hole quantum dot states, the carrier transport and the energy difference between these states. Electroluminescence occurs when an applied forward bias electric potential difference forces the electron and holes together in an active recombination region. This is following the operating principle of light emitting diodes (LEDs). In the case of the samples discussed in this thesis, the active region is a multiple quantum dot/quantum well region of confined energy states which support a higher radiative recombination rate.

The electroluminescence signal strength is typically several orders of magnitude above the photoluminescence in intensity so is much easier to detect than photoluminescence. In the nanostructured solar cells under investigation, the radiative recombination in the *p*-GaN and *n*-GaN regions is very small, resulting in little luminescence in the near UV. This is especially true under higher injection levels where carriers are swept into the quantum dots faster and spend less time in the quasi-neutral regions of the nanowire. Electrons and holes are injected electrically and are accelerated into the quantum dot region which consists of multiple quantum dots with slightly varying dimensions and indium compositions.

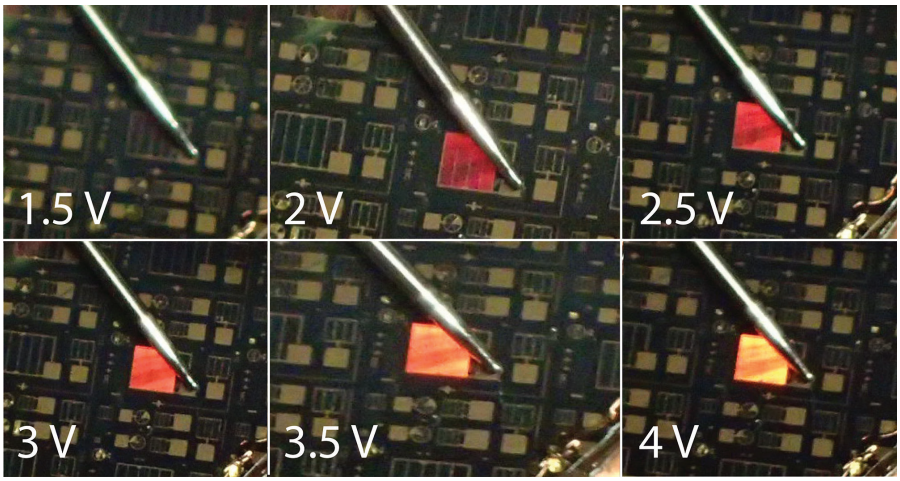

Figure 49: Photographs of electroluminescence from a single nanowire solar cell as various voltages.

4.9.1 *Single Junction LED Electroluminescence*

Electroluminescence spectroscopy was performed similarly to photoluminescence spectroscopy regarding the collection of emitted photons, but the device is electrically forward biased using an applied voltage such that carriers are injected to the device and the resulting luminescence spectrum is measured. For the fabricated *p-i-n* junction nanowires samples, the electrical connections are made with apparatus shown in Figure 43. Once a voltage is applied to the contacts, luminescence is clearly visible as shown in Figure 49.

In single junction nanowires, electroluminescence begins at approximately 1.5 V forward bias, where a faint red glow appears. With higher applied voltages, the intensity increases rapidly and blueshifts towards a white-yellow colour that can be seen in Figure 49. As the current through the device increases beyond 30 mA/mm^2 the risk of spontaneous, permanent short-circuiting of the cell increases significantly. Fortunately, this is two orders of magnitude higher than any current that would be produced under 1-sun of solar irradiance. The exact process for catastrophic cell shorting is unknown, but it is possible it is as a result of the dielectric strength of polyimide at such small thicknesses. The dielectric breakdown of the filling materials between nanowires, polyimide, has been measured to be 10-40 V for distances of 0.12-1.6 µm[192–194]. This corresponds to a 1-4 MV/cm in dielectric strength. This agrees well with the 0.7 µm tall single junction nanowires shorting at voltages over 9 V.

The nanowires can be operated beyond their equivalent open circuit voltage in photovoltaic mode, where the consumed current begins to produce light. A nanowire solar cell operating as an LED was imaged in a low magnification (4X) optical microscope as shown in Fig 51. The electroluminescence demonstrates a variety of colours with a highly non-uniform luminescence pattern resulting from either individual nanowires or clusters of nanowires despite the entire area being covered of nanowires. In order of predominance, the emission

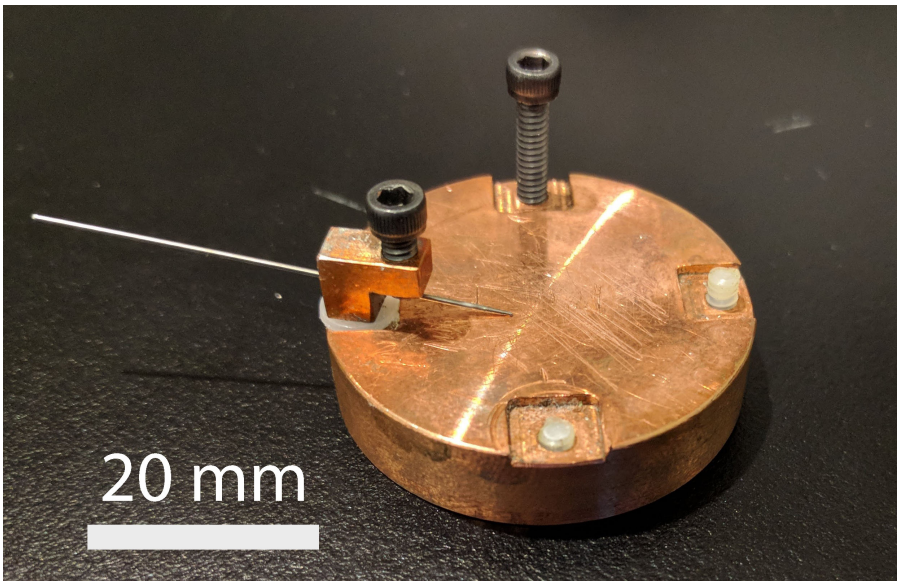

Figure 50: Copper stage and probe system designed for current-voltage measurements and electroluminescence spectroscopy inside a cryostat.

colour from localized spots are green, yellow, cyan, orange, turquoise, red and some violet. The left side of the image is clearly brighter and more yellow than the right which is likely a result of the electrical probe being placed on the left side of the cell. There are significant areas of the cell which do not electroluminesce. Despite the nanoscale diameter of the nanowires, luminescence appears to originate from half-micron scale points which would cover an area occupied by tens of nanowires. This corresponds to the diffraction limit of light. The significant differences in colour between bright spots suggest that are either many single nanowire emitters, or that bunches of nanowires emit similar colours.

4.9.2 *Six Junction LED Electroluminescence*

Monolithic six-junction nanowire LEDs were grown, fabricated and provided by Dr. Sharif Sadaf and tested as a function of forward electrical bias. The increased number of junctions in series increases the operating voltage of the device, where significant luminescence is only seen above 10 V. The luminescence was observed through a higher magnification microscope where the spatially resolved luminescence is diffraction limited as shown in Figures 52 and 53. The points of light are approximately 500 nm in diameter, corresponding roughly to the diffraction limit (Abbe limit) of visible light where the smallest feature size is approximately

$$d = \frac{\lambda}{2NA}, \tag{240}$$

where λ is the wavelength of the emitted light, and NA is the numerical aperture of the objective. As each point of light can in principle result from tens of nanowires, it is unlikely that the vast majority

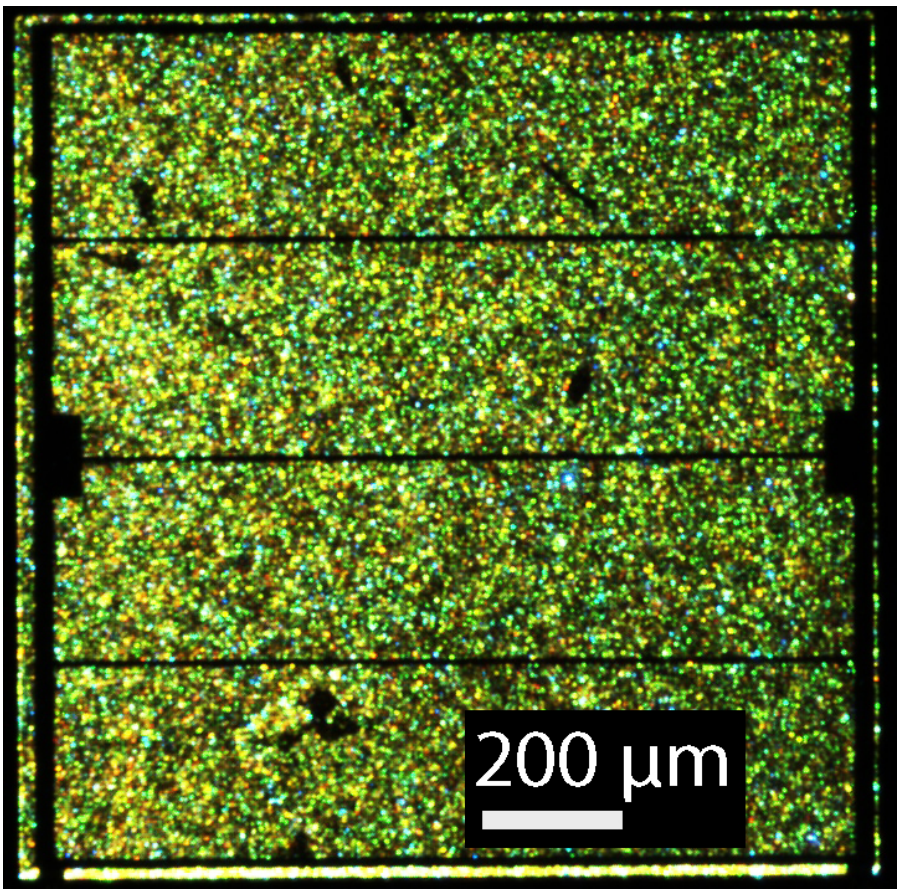

Figure 51: Electroluminescence microscopy at 4X magnification of the InGaN/GaN quantum-dot-in-nanowire solar cell with 30 mA of injected current. The straight black pattern outlines the metallic contacts of solar cell in which light cannot pass through.

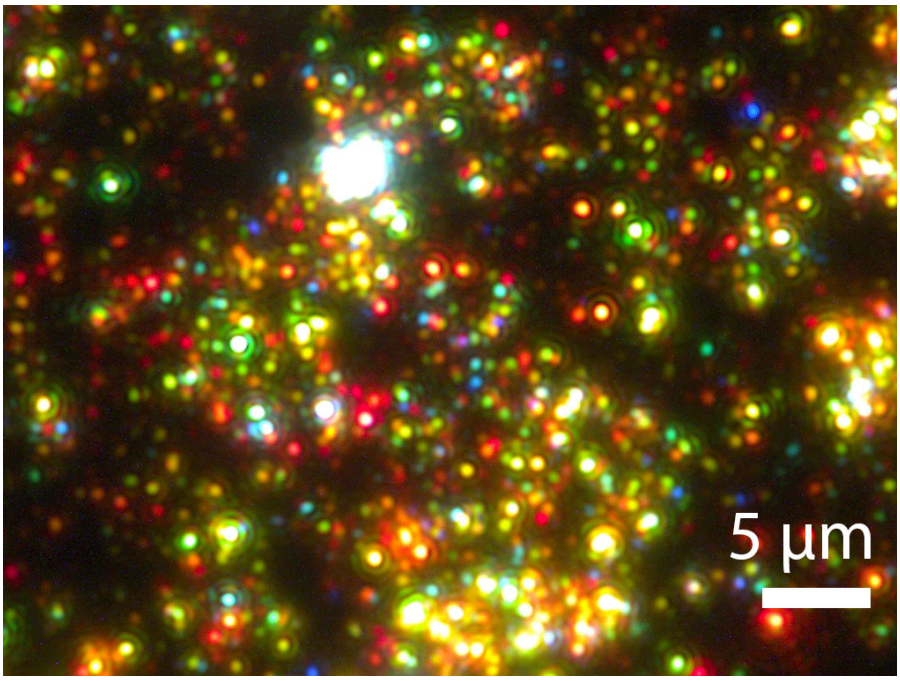

Figure 52: High resolution electroluminescence microscopy of a six junction InGaN/GaN quantum-dot-in-nanowire solar cell at 13 V forward bias.

of emission spots are a result of multiple nanowires for the following reasons. First, most spots demonstrate a consistent Airy pattern around them, which would be modified significantly if two or more nanowires were emitted very close to each other from interference effects. Second, the shape of the spots is generally circular and have a consistent size which would suggest a single location of emission. Third, it is unlikely that there is emission from multiple nanowire clusters when most of the nanowires are not emitting. Also, emission spot size is roughly a function of the emission colour. Fourth, distinct colours are observed more often in the luminescence pattern as opposed to white light that would either be the result of multiple nanowires or multiple dots with different indium compositions or thickness. Therefore, we can conclude that the luminescence pattern from microscopic electroluminescence is a result of single nanowires.

This result enables a rough estimate of the participation fraction of nanowires at a certain bias voltage, which may provide insight into the performance issues as solar cells. From electroluminescence imaging, the participation fraction reaches an average of 1% over the entire cell when nearing the maximum allowed voltage.

As a function of voltage, the six junction solar cells demonstrate luminescence beginning at around 4 V and increasing further to 16 V as shown in Figure 54. The voltage was not increased beyond 16 V to reduce the risk of a catastrophic short-circuit of the device. When the voltage is increased, the participation fraction of the nanowires increases along with a blue-shift and broadening in the emission wavelength of some nanowires. The increased participation fraction is attributed to non-uniform resistivity of each nanowire and/or contact

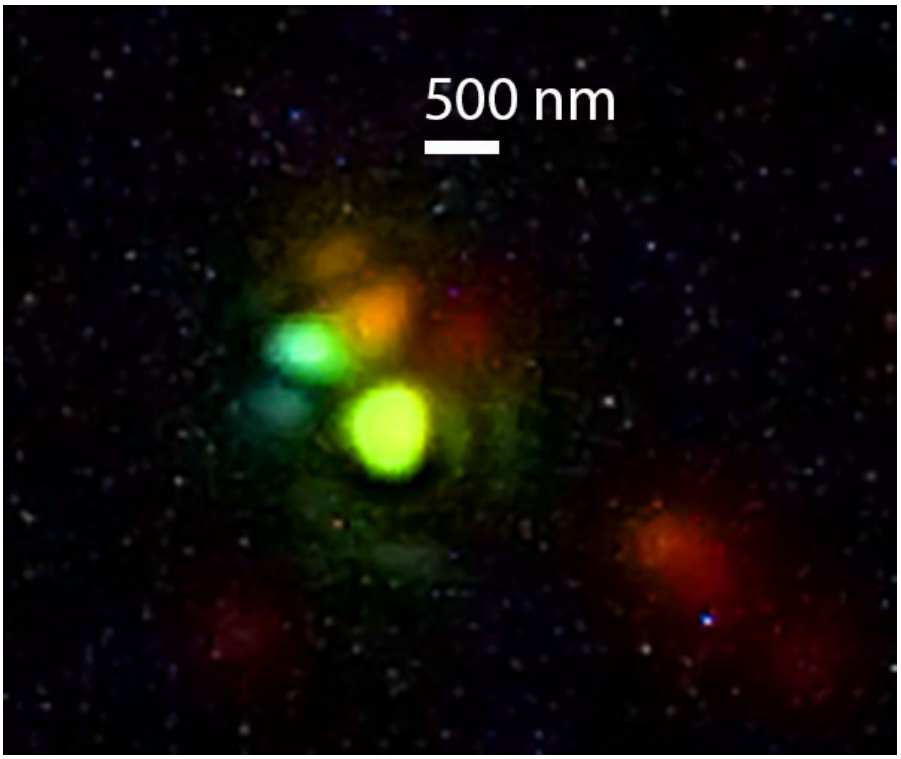

Figure 53: High resolution electroluminescence microscope image at low forward bias showing multiple nanowires in close proximity emitting very different colours.

with either the ITO or the substrate. More resistive nanowires will require more voltage to support increases current flow, which is linked to the luminescence intensity of the nanowires. The broadening is possibly from additional nanowires/quantum dots in close proximity to each other emitting different photon wavelengths.

The blueshift with increased carrier injection is likely a result of the filling of lower energy quantum dot states in certain nanowires, increasing the probability of recombination from higher energy quantum dot states. Electron-hole recombination rates are generally higher in lower energy transitions in many semiconductor systems where carriers will relax to the lowest energy state available prior to recombination. The luminescence of the nanowires is also quite dynamic, where some nanowires vary in luminescence intensity over time at a constant voltage. The time scale is on the order of 1-10 seconds. This is attributed to the interplay between the current-dependent series resistance as a function of temperature in emitting nanowires at a bias near the threshold voltage of some other nanowires. The effect is apparent in a few percent of nanowires at any given time. The increase in voltage required for multijunction nanowires is expected due the natural series connection of monolithic devices with tunnel junctions.

The electroluminescence of single junction nanowires was observed through high magnification to reveal diffraction limited emission spots similar to those found in the 6J nanowire LEDs. Emission spots are shown in Figure 55 with and without background light or electrical bias. Participation fractions were similar in the 1J and 6J devices, sug-

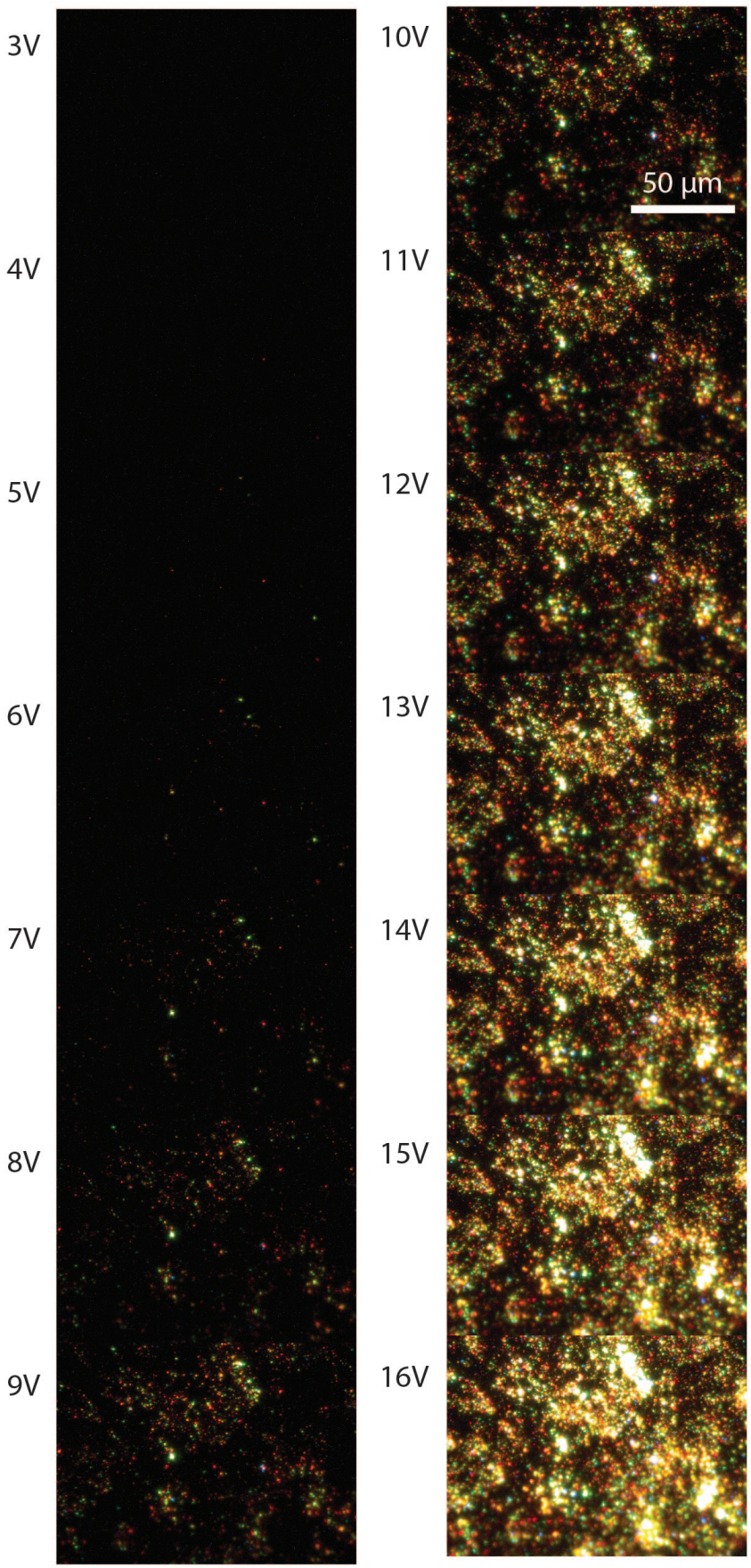

Figure 54: Electroluminescence microscopy using the 100X objective of six-junction InGaN/GaN-quantum-dot-in-nanowire LEDs up to 16V.

gesting the tunnel junctions in the 6J device are fairly reliable and that the non-uniformity in electroluminescence is likely due to the variation in nanowire contact quality with the ITO.

4.9.3 *Electroluminescence Spectroscopy*

The emission spectrum of the nanowires is similar when driven by applied voltage or incident light. For the single junction nanowires, electroluminescence spectroscopy was performed inside the cryostat. The electroluminescence was measured as a function of both temperature and wavelength. The temperature was varied from 78 K to 290 K and is shown in Figure 56. The integration time was set to 1 second with an approximate collection area of tens of microns. The integrated electroluminescence signal increases when the temperature is lowered from room temperature. Once the temperature reaches 200 K, the electroluminescence is maximized from the balance between the reduction of nonradiative recombination and the dopant activation level. The electroluminescence signal reaches a peak at about 670 nm. This matches the centre wavelength of the photoluminescence signal as well for the same sample as shown in Figure 47.

Electroluminescence at 78 K as a function of applied voltage is shown in Figure 57. At 78 K, the voltage to the nanowire cell was ramped up to 4 V from 1.5 V where the signal is barely detectable. There is a significant blueshift in the emission spectrum from about 750 nm to 650 nm when near the maximum safe current. The emission spectrum is very broad, extending further to higher and lower wavelengths as a function of voltage. Under high bias, the number of injected carriers leads to more of the lower energy states in the InGaN/GaN quantum dots becoming filled, leaving more radiative recombination events from the higher confined states in the quantum dots. On the red side of the emission (>800 nm) there is another increase in the emission spectrum which cannot be explained by filling of confined states. It is possible that additional radiative recombination past 800 nm is a result of deep trap-assisted transitions or new transitions between confined electron and hole states. At low temperatures, the usual nonradiative recombination events through such trap states are not dominant, leaving the usually longer radiative lifetimes to dominate. At 4 V, the electroluminescence signal saturates the detector pixels near the centre wavelength.

At room temperature, the luminescence is about three orders of magnitude lower than at 200 K, indicating that the device performance is being limited by nonradiative recombination. The emission spectra at room temperature from electroluminescence is shown in Figure 58. The peak wavelength blueshifts similarly at room temperature and at 78 K. The peak emission wavelength corresponds closely to the emission at 78 K. With increasing forward bias, blue and near-infrared emission does not extend as far as it would at 78 K. At transition energies less than 1.5 eV, radiative recombination from deep traps is possibly restricted with the prevalence of phonon-assisted Auger re-

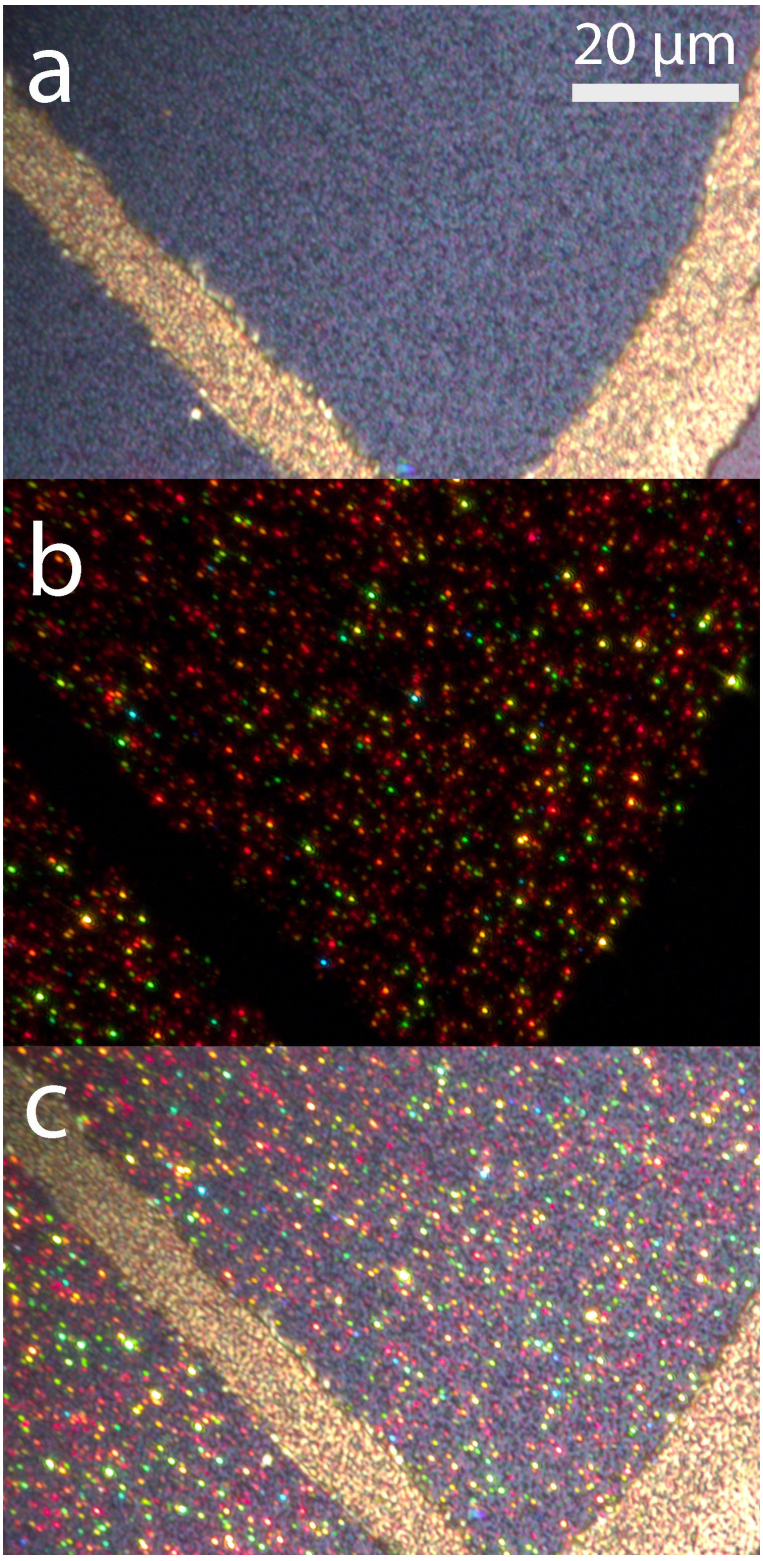

Figure 55: Electroluminescence microscopy of single junction InGaN/GaN-quantum-dot-in-nanowire LEDs under (a) no bias but with illumination, (b) 7 V bias but no illumination, (c) 7V bias with illumination.

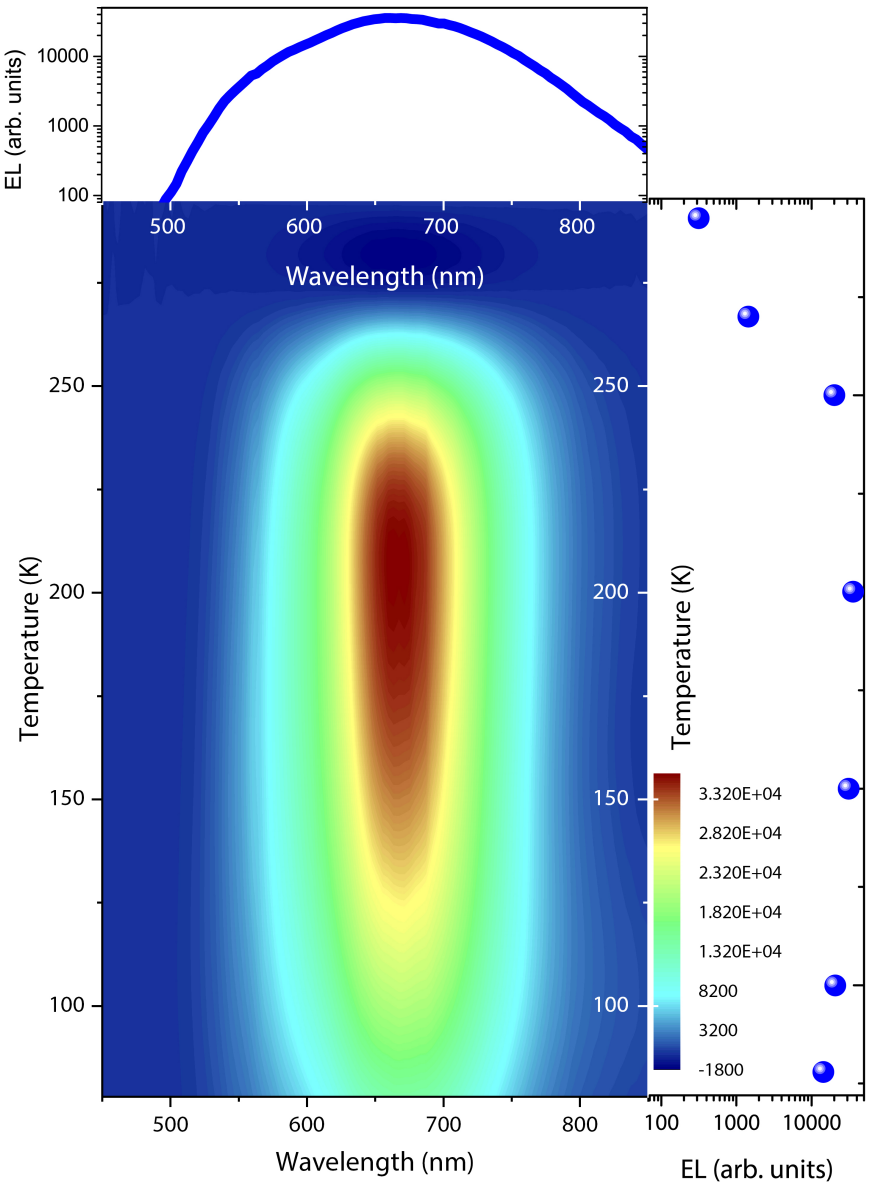

Figure 56: Electroluminescence spectra as a function of temperature. The plots to the top and right are slices through 200 K and 670 nm, respectively.

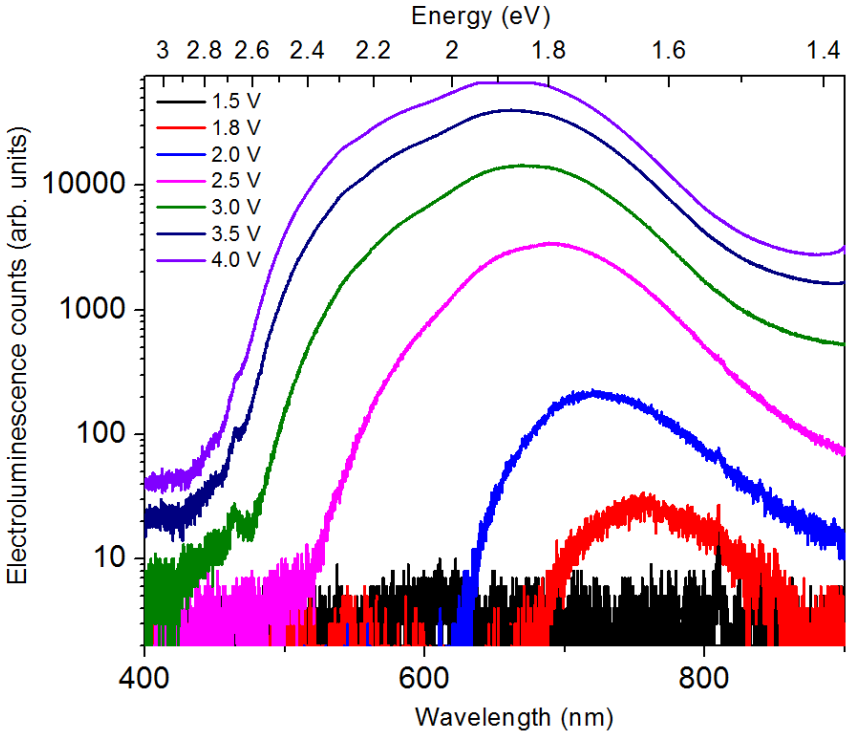

Figure 57: Single junction nanowire electroluminescence spectra at 78 K as a function of forward bias.

combination. This explanation is consistent with previous work, that has shown that Auger recombination in InGaN quantum wells that emit in the green region is highly temperature dependent[195].

4.10 SUMMARY OF EXPERIMENTAL CHARACTERIZATION

In summary, this chapter details the characterization methods and experimental results used to determine the electrical, optical and morphological properties of InGaN/GaN quantum-dot-in-nanowire solar cells and LEDs. A variety of microscopy techniques and tools was used to obtain the nanowire density, shape, diameter, growth characteristics and height. Multiple samples of varying designs were characterized. Only the *p-i-n* junction designs are viable as solar cells and were the main focus of the chapter. Designs with *n-p-n* configurations and multiple junctions were designed as light emitting diodes as were characterized by their electroluminescence and their tunnel junction functionality for future multijunction nanowire solar cell designs. The single junction nanowires were found to have an approximate diameter of 90 nm, a variation in height between 500-600 nm, and a density of approximately 10^{10} cm^{-2}. Electrical characterization of the nanowires consisted of current-voltage measurements with and without illumination from a solar simulator. Inside a cryostat, the photoluminescence and electroluminescence from the InGaN quantum dots of the GaN nanowires were measured as a function of temperature from 78 K to 295 K. Under forward voltage bias, the nanowire cells emitted a red light which shifted to yellow and green with increasing

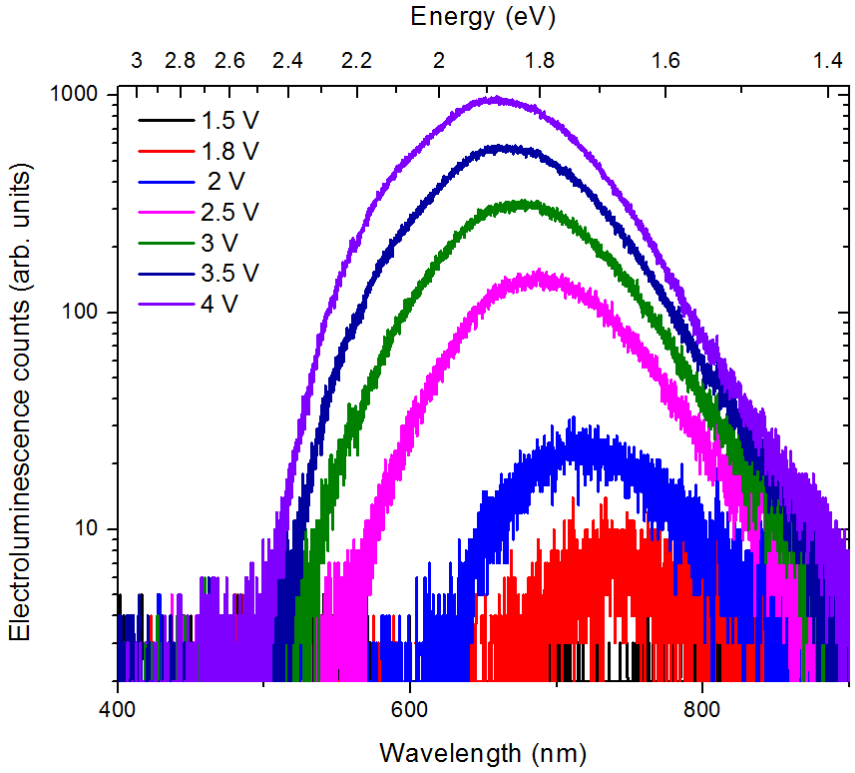

Figure 58: Single junction nanowire electroluminescence at room temperature as a function of forward bias.

current injection. The electroluminescence was imaged using a microscope as mapped down to the diffraction limit. The emission spectra from nanowires ensembles were found to be spatially sparse, fairly monochromatic per emission spot, and exhibited very consistent spot sizes and Airy patterns. The combination of these observations leads to the most likely conclusion that the micro-electroluminescence images are a result of single nanowires with emitting nanowires making up to 1% of the total nanowire count. The photoluminescence of the nanowires was measured as a function of temperature under monochromatic illumination of a 405 nm laser. An increasing photoluminescence signal was measured with decreasing temperature as expected. The addition of quantum dots and a core-shell structure provided an increase and broadening in the integrated photoluminescence signal. From quantum efficiency measurements, sub-bandgap photocurrent was detected for the first time in the axial quantum-dot-in-nanowire heterostructure devices, and at longer wavelengths than any InGaN/GaN nanowire structure to date. The performance was inversely proportional to monochromatic beam light intensity, which counterintuitively suggests intermediate band effects were inhibited by photofilling of the quantum dot states. This could be due to confined excited carriers affecting inter-dot transport and/or photofilling.

5

MODELLING AND SIMULATION OF INGAN DOT-IN-WIRE SOLAR CELLS

"Even in an era of targeted experimentation and daunting theoretical prowess enhanced by large-scale computing, many-body physics is still a humbling natural science based on discovery."

—Nathan Gemelke, 2016

5.1 INTRODUCTION

The results from the previous chapter suggest that the InGaN quantum dots play a central and complex role in the carrier transport, luminescence, and recombination across the *p-i-n* junction of InGaN/-GaN nanowires on silicon. The introduction of deep states provided by InGaN/GaN quantum wells/dots in a *p-i-n* junction not only provides a stepping stone for lower energy photons to excite electrons eventually to the conduction band of GaN, but introduces a significant and often dominant recombination pathway and trap for carriers. The realization of a functioning intermediate band solar cell necessitates high material quality to reduce non-radiative recombination as much as possible, along with high absorption and high mobility.

This chapter builds upon the theory discussed in Chapter 2 and the experimental results of Chapter 4 in order to better understand the physical processes occurring in the nanowires and provide a strategic route towards a more efficient intermediate band solar cell built from InGaN/GaN quantum-dots-in-nanowire heterostructures. This chapter includes the simulation of quantum-confined carrier wavefunctions coupled with drift diffusion device simulations to model the physics of InGaN/GaN quantum-dot-in-nanowire heterostructures. The modelling includes two different approaches to carrier transport through the InGaN multiple quantum well regions for solar cell operation: a quantum well miniband transport model as well as an inter-well tunneling model through adjacent quantum wells. The additional current generated through the InGaN quantum dots is used to determine the possible performance enhancement as an intermediate band solar cell assuming the intermediate band is isolated from the conduction and valence bands.

It is important to note that a true intermediate band is not simulated, since this necessitates distinct and correlated carrier populations between the quantum dots states, conduction band and valence band. The current enhancement from sub-bandgap processes is simulated despite this shortcoming. The nanowires are also simulated as LEDs in a more advanced coupled quantum dot framework which solves for quantum dot density of states in cylindrical dots with wetting layers, and solves the drift-diffusions in Chapter 2 to determine

the emission wavelengths and current-voltage characteristics of the nanowires.

In this chapter, the following simulations with Crosslight® APSYS are performed:

- InGaN/GaN miniband solar cell
- InGaN/GaN coupled-well solar cell
- InGaN/GaN quantum dot wavefunctions
- InGaN/GaN quantum dot LED electroluminescence
- Self-consistent quantum well polarization effects in InGaN / GaN quantum wells

5.2 MODELLING QUANTUM HETEROSTRUCTURES

The number and energies of sub-bandgap states in intermediate band solar cells are important for efficient solar power conversion. The intermediate band in our nanowires is formed by InGaN quantum dots, which have up to 40% indium. The bottom of the conduction band well is 1 eV lower in energy from the conduction band, and the top of the valence band well is 0.4 eV higher than the valence band of GaN. These values are based on approximate valence band offsets[196, 197]. The confinement effects from the quantum dots can increase the difference in energy between the lowest confined conduction band and highest confined conduction band state, and therefore do not correspond exactly to the difference in bulk bandgaps. In this section, we aim to calculate the approximate energies of the confined quantum dot states in the nanowires studied in this thesis. This will provide an idea of how the quantum dot states change with indium composition and barrier design. The modelling of the quantum dots states and confined electron wavefunctions was performed with the Crosslight® APSYS wave equation solver. A 2D mesh was constructed with a cylindrical symmetry to provide the complete mesh for the quantum dots.

A two-dimensional rectangular section of $In_xGa_{1-x}N$ dot is used to define the quantum dot. The mesh is iterated angularly to produce the cylindrical dot in three-dimensions. The surrounding material is set as pure GaN, as shown in Figure 59. The density of the mesh is increased inside the quantum dot region to better sample the wavefunction. The confined carrier wavefunctions and states are solved using multi-band $\mathbf{k} \cdot \mathbf{p}$ theory. The strained wurtzite offset model in Crosslight® APSYS was used to arrive at a more accurate bandgap configuration between InGaN and GaN due to strain. Odd and even boundary conditions were set for the confined wavefunctions due to symmetry. Electron and hole states were solved for using a single band effective-mass approximation which is usually accurate for electrons. However, any mixing between the light and heavy hole bands is not captured, rendering the energies less accurate. In addition, the ordering of the hole states and shape of the hole wavefunctions are

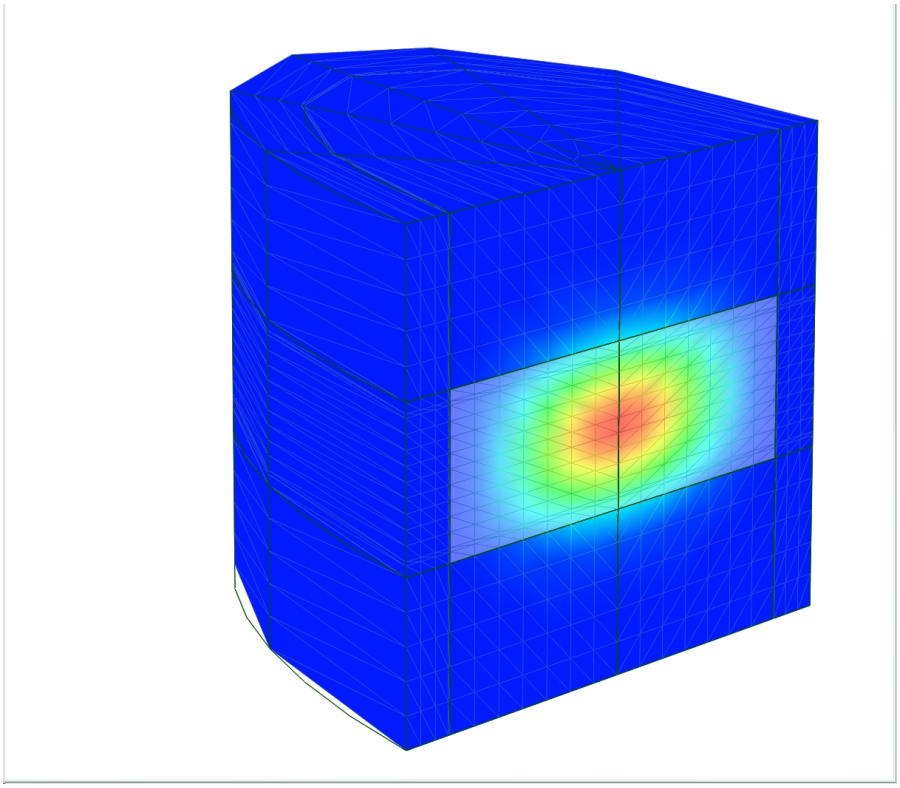

Figure 59: A cross-sectional view of the InGaN quantum dot mesh with ground state wavefunction is shown surrounded by GaN in cylindrical symmetry. The x and y axes are not to scale.

expected to be rough approximations that are acceptable for solar cell applications. The square of the single particle wavefunctions are shown in Figures 60 and are not to scale. The quantum dot dimensions were set at 3 nm in height and 20 nm in radius, corresponding to scanning transmission electron microscope images shown in Chapter 4.

The confined states for three different indium compositions inside the cylindrical dots and are shown in Figure 61. Heavy holes states appear as the ground states in the simplified model of the dots (no mixing of the valence bands). When photocarriers are generated in the InGaN quantum dots, they can be confined due to the combination of high and thick potential GaN barriers. The carrier wavefunctions provide insight into the confinement provided in the InGaN dots, and therefore the possibility of transport through tunneling between dots. The wavefunctions of confined states are shown as 2D slices from 0 to r in Figure 60 if rotated about the z axis, with even or odd parity. The hole states are found to resemble the electron states very closely since a simple effective mass model is used and a full $\vec{k} \cdot \vec{p}$ theory with mixing is not applied.

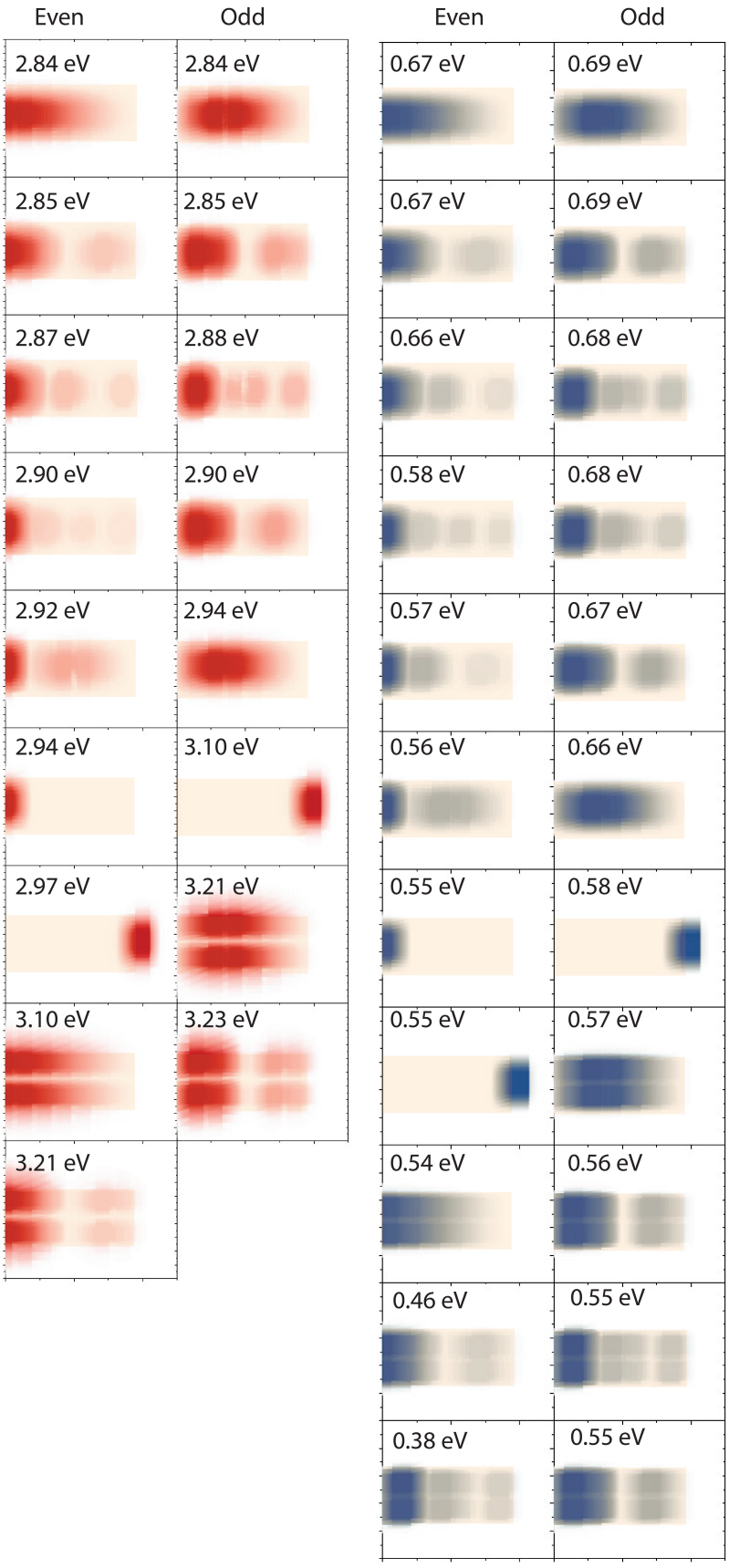

Figure 60: Square of the single particle wavefunctions of the more confined electron (red) and heavy hole (blue) states in InGaN/GaN quantum dots (translucent orange) for a 40% indium quantum dot of height 3 nm and radius of 20 nm. Wavefunctions are sorted primarily by their parity (even, odd) and by their energy difference from the bulk band edge. Energies are relative to the bulk GaN valence band.

The quantum dot states were solved for three different indium compositions of 20%, 30% and 40%, while keeping the host matrix as GaN. With decreasing indium composition, the confinement is reduced and the bandgap of InGaN increases. The split-off states could not be calculated but are expected to add to the number of states in the valence band about 0.5 eV higher in energy in the wells. In total, there are about 80 unique states in the quantum dots with 20% indium and about unique 120 states confined in the 40% indium quantum dots, each of which are doubly generate due to spin. The reference energy is set at the bottom of the conduction band energy of bulk InGaN.

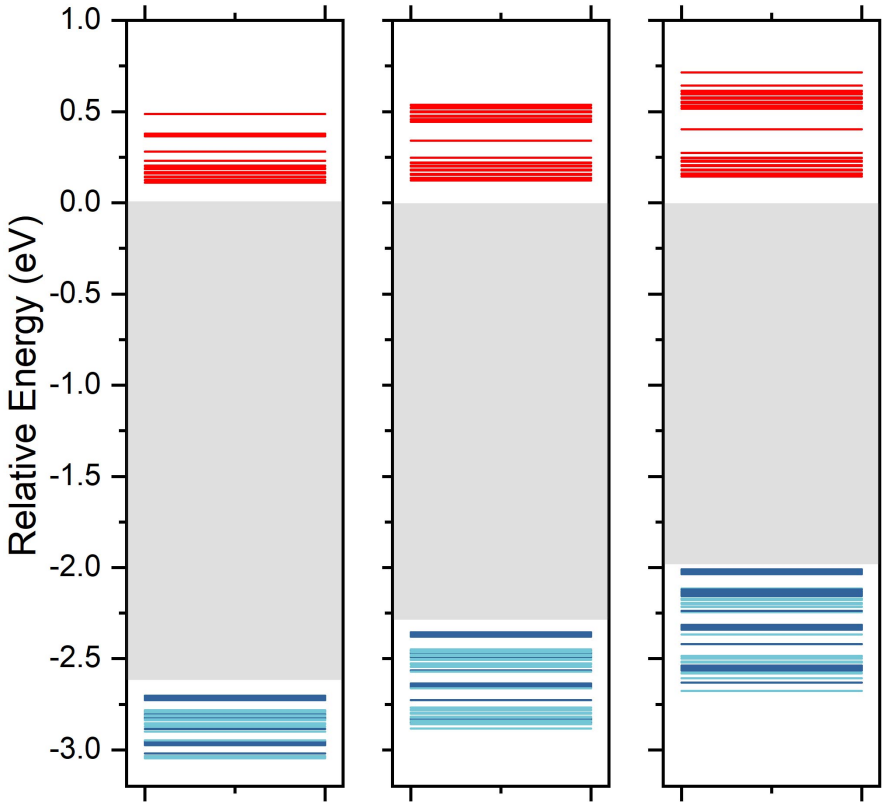

Figure 61: Single particle quantum dot confined state energies at three different indium compositions. From left to right, they are 20%, 30% and 40%. The electron states are shown in red, heavy holes in dark blue, and light hole states in light blue. Split-off states are not shown. The grey area indicates the bulk bandgap on InGaN.

The high density of states allows for rapid thermalization of excited electrons to the lowest unoccupied electron states, and similarly for holes to the top of the hole states. At high indium compositions, significant gaps over 100 meV begin to appear between the electron states which may result in longer electron relaxation lifetimes in these higher states. The highest hole states demonstrate heavy hole character with a small gap before the light hole states appear. Confinement effects are shown to shift the electron and hole states from the bulk band energies by up to 125 meV. These simulations are useful for providing a more accurate picture of the density of states for device simulation, as well as understanding the necessary steps to fulfil the

photofilling requirements of intermediate band states for maximum power conversion efficiency. In later sections in this chapter, approximations are made to treat the quantum dots as quantum wells using a full 6x6 band $\vec{\mathbf{k}} \cdot \vec{\mathbf{p}}$. This approximation is justified as the quantum dot state distribution calculated above is qualitatively similar to the quantum well states as the heavy hole states are always the lowest grouping of states, followed by a grouping of light holes. This assumption is used only to determine the approximate energy levels, their character, and their change as a function of electric field. Photofilling characteristics and of the quantum states is expected to be significantly different in quantum well and dots geometries due to the change in the density of states.

5.3 CROSSLIGHT APSYS

Drift diffusion simulations were accomplished using Crosslight® APSYS, a drift-diffusion semiconductor simulation software with a special focus on the InGaN/GaN material system and quantum wells. The simulation strategy of Crosslight makes various assumptions which serve to reduce the complexity of the simulation where negligible effects on the overall performance of the solar cell is concerned. The simulation work discussed in this thesis does relax some of these assumptions in order to illustrate their effect on the nanowire solar cell operation.

First, the model treats the nanowire solar cell as a bulk device with multiple quantum dots or wells as it assumes the confinement effects of the nanowire geometry are negligible. Second, the morphology of the surface of the solar cell is also highly irregular and densely packed with material as the tops of the nanowires coalesce as the growth proceeds. This results in the optical properties of the nanowires resembling more of rough bulk surface than a regular sub-wavelength array. Therefore, the optical characteristics of the device are modelled by using the absorption coefficient of GaN and calculated for the quantum well region using $\mathbf{k} \cdot \mathbf{p}$ theory. The reflectivity of the simulated devices was set to 0% to focus on the internal performance of the solar cell.

The simulations assume no background doping level in the intrinsic region, and abrupt interfaces and doping profiles. All simulations are run at 300 K such as to simulate expected operation in standard conditions. Illumination is simulated through a normal-incidence AM1.5G solar spectrum obtained from the National Renewable Energy Laboratory (NREL) data resource[198].

The simulations were performed in two dimensions (the growth direction z and a single lateral dimension x), with results generalized to the third dimension to provide performance metrics for real devices. Quantum dot states and wavefunctions were modelled in two dimensions (z and r), and extended to three dimensions with cylindrical symmetry. Boundary conditions where the wavefunction should be zero 3 nm above and below each dot, and 5 nm radially beyond the edge of each dot. In more complex transport modelling which

involves illumination with light, the quantum dots are approximated as quantum wells.

5.3.1 *Simulation as Light Emitting Diodes*

Under forward bias beyond the turn-on voltage, the nanowires operate as light emitting diodes, where the distribution of quantum dot sizes and indium composition create a broad spectrum of emitted light through the variety of optical transition energies. Optical transitions can be red-shifted with increases in dot diameters and thicknesses, up to the point where they approach the bulk bandgap energies. Due to the tendency for indium segregation in dots, some regions of the dots may include higher indium compositions, where even lower energy transitions can be seen. This is apparent in experimental electroluminescence spectroscopy of the nanowire solar cells in Chapter 5, where emission wavelengths up to 800 nm can be seen (1.54 eV), despite an estimated 40% average indium composition. This indicates that there are some dots with up to about 50% indium. It is also possible that some quantum dots contain relatively little indium and thus provide higher energies transitions for radiative recombination. All these effects lead to a broadening of the electroluminescence spectrum.

In quantum dots of relatively large lateral sizes (40 nm in diameter), the density of states resembles that of quantum wells, which is step-like in character. The energy separation between most states is within the thermal energy at room temperature (kT) meaning that carriers quickly relax to the lowest unoccupied state through phonon scattering. If lower confined states remain occupied, the carrier may recombine radiatively at a higher energy level, producing a higher energy photon than expected. This effect increases as the number of carriers injected into the dots increases. It is also evident in the experimental results where a blue-shift in the emission spectra is observed.

To reproduce the spectrum of the nanowire devices in forward bias through simulation, the quantum dot states are taken into account through an approach that couples the standard device drift-diffusion simulation with the quantum well and dot states. The nanowires are modelled as bulk devices with a region of weakly coupled quantum wells. The additional confinement effects from the quantum dots are captured through an initial, but separate simulation which solves the Schrödinger equation for the wavefunctions and states for each of the electron, heavy hole and light hole bands, and adds the density of states of the dot to the quantum well region. The final density of states is then used in the drift-diffusion simulation for recombination, absorption and transport physics in Crosslight. This is intended to account for additional indium segregation that creates dot-like states which increase the energy of optical transitions. This is similar to the treatment of quantum dots forming from wetting layers in the Stranski-Krastanov growth mode.

LAYER	MATERIAL	THICKNESS	DOPING
Emitter	*p*-GaN	300 nm	10^{19} cm^{-3}
Barrier	GaN	3 nm	–
QD Region	10 x (InGaN/GaN)	10 x (3 nm/3 nm)	–
Base	*n*-GaN	270 nm	10^{19} cm^{-3}

Table 6: Simulated quantum-dot-in-nanowire LED device structure parameters.

The electroluminescence of InGaN/GaN nanowires was simulated in Crosslight® APSYS. The simulation script is provided in the appendices. The simulation begins with the solving for all the electron and hole states of 4 types of InGaN quantum dots to account for varying indium compositions in real stacked quantum dots. The quantum dot heights were fixed at 3 nm, as control over the quantum dot height is more readily achieved than the indium composition. In addition, the indium composition has a greater effect on optical transition energies than fluctuations in the dot sizes. The dot diameters are set at 40 nm and assumed to be disc-shaped.

Coupling between different quantum dot states is enabled and changes the total number of states due to hybridization. Spectral broadening is modelled in two ways. The first type of broadening is intended to capture the inhomogeneous distribution of quantum dot indium compositions by solving the Schrödinger equation for a variety of dot configurations separately to obtain the density of states contribution each different dot would provide. For example, a quantum dot with a larger thickness would provide optical transitions closer to the bulk bandgap energy (redshift). The second type of broadening is achieved by introducing a broadening factor, G_B that arises from finite intraband relaxation times in the conduction and valence bands prior to radiative recombination, carrier-carrier scattering, or carrier-phonon scattering. For the purposes of this simulation, both types of broadening are treated as fitting parameters to experimental data. The device structure is described in Table 6.

The simulated spectrum was fitted to experimental electroluminescence spectra from Figure 56 in Chapter 4 to obtain a rough approximation of the indium composition, effects of quantum dot formation and shape, emission, absorption, and broadening. The fitted data is shown in Figure 62.

The quantum dot thickness did not significantly change the emission energy within the usual quantum dot thicknesses (2-5 nm) since the dots are already quite large. The most relevant fitting parameters were found to be indium composition and the broadening parameter. To achieve the fit, the indium compositions of equal numbers of four different quantum dots were found to be 35%, 40%, 45%, and 50%. This corresponds well to the energy dispersive (EDS) X-ray spectroscopy from transmission electron microscopy from the work of Nguyen *et al.* on similar nanowires[190]. The broadening parame-

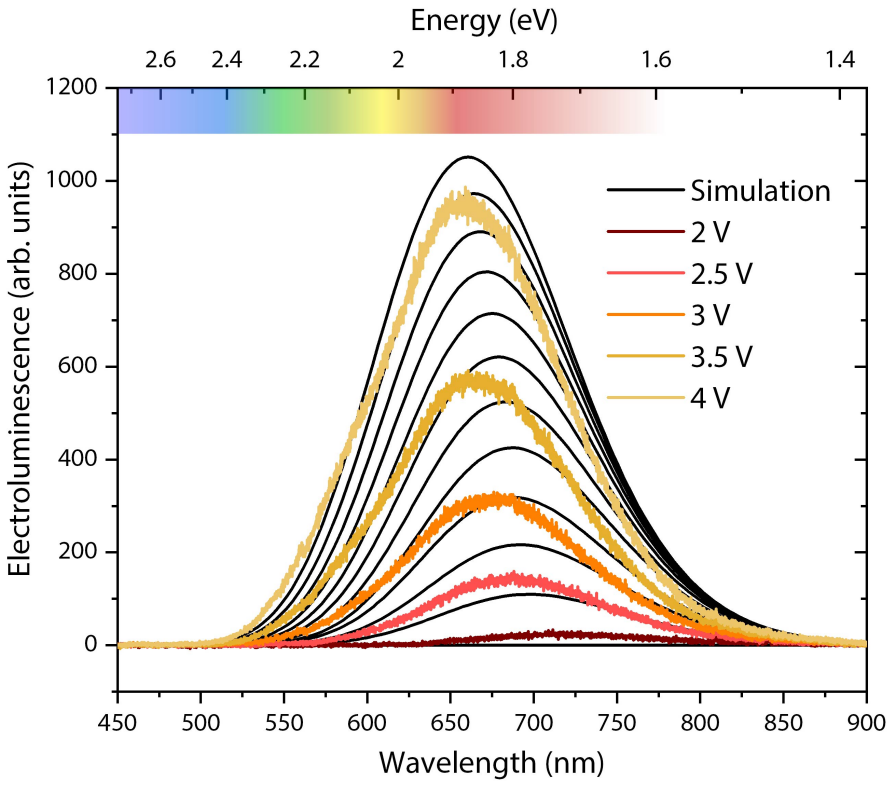

Figure 62: Fitted electroluminescence spectra of a 10InGaN/GaN quantum-dot-in-nanowire LED. Simulated results are drawn in black at multiple carrier injection rates. Coloured lines indicate experimental results.

ter (as described in Chapter 3 in Equations 192 and 193) (τ_b) was set at 5 x 10^{-15} s. This short timescale, while originating from the carrier thermalization time, is used to artificially model the large changes in indium composition and dot size. The blue-shift of the electroluminescence peak with applied voltage is reproduced in the simulation as well as the approximate centre emission wavelength. The difference in magnitude between the simulated and measured electroluminescence spectrum was not quantified as it depends on many unknown parameters and is simply scaled to illustrate the shape of the emission spectra. The shape of the measured and simulated electroluminescence spectra are similar. The simulation results produce a Gaussian-like emission spectra which would have a smaller γ coefficient and larger σ if fitting to a Voigt function. In summary, we investigated the luminescence properties of the nanowire solar cells as LEDs to determine an approximate distribution of the indium composition in the dots. The indium composition appeared to be centred around 42% with the broadening associated to dots with larger or smaller indium fractions.

5.3.2 *Miniband Transport Model*

An efficient quantum well solar cell relies on efficiency carrier transport through the barrier layers. This transport can be realized by car-

riers tunneling through barrier layers if the barriers are not too high in energy, as well as through thermally or optically assisted hopping between wells under high fields. This is usually an inefficient type of transport. In an InGaN/GaN superlattice, thermal excitation is negligible as the barrier heights are two orders of magnitude higher in energy than the thermal energy of the trapped carriers. Relying on efficient well-to-well transport requires extremely long carrier lifetimes and high mobilities such that the collection of carriers at the p and n regions occurs before any non-radiative recombination. In LEDs, this type of quantum well transport can be tolerated if carriers remain trapped prior to radiative recombination.

With very narrow quantum well barriers (<2 nm), the confined wavefunctions of each well can hybridize to form extended well states. The limit of this hybridization can create a miniband of states which span the multiple quantum well region. This allows carriers to accelerate across the quantum well region from the electric field, removing the need for tunneling through large energy barriers. This transport regime is ideal for intermediate band solar cells which may not have very long non-radiative recombination lifetimes to support many hopping and tunneling events.

Even with InGaN/GaN quantum dots and wells, the hole transport is much lower than the electron transport due to high effective mass and low mobilities and insufficient hole populations from doping. In these nanowires, it has been shown that hole transport can be improved through p-type modulation doping of the barrier layers between quantum confined structures[190]. The polarization field that occurs in InGaN/GaN interfaces does not pose as much of a barrier to miniband conduction but may introduce energy barriers for carriers to escape the miniband to the p and n regions. Polarization due to heterointerfaces is not modelled in the miniband regime but are modelled in a later section with independent quantum wells.

A *p-i-n* solar cell was modelled using Crosslight® APSYS with an InGaN/GaN quantum well superlattice structure occupying the entire intrinsic region. The quantum dots were modelled as quantum wells due to their large diameters of 40 nm, which has been determined to be the energetically favourable diameter of InGaN/GaN quantum dots[45] and corresponds to transmission electron microscopy of the dot dimensions shown in Chapter 4. The number of layers was varied from a single quantum well to 100 quantum wells. Miniband states are determined according to the theory presented in Chapter 2. The number of well is not strictly the important metric in the miniband regime, since photons are absorbed evenly throughout the region, but rather the width of the miniband region determines the number of photons absorbed. The effect of doping, mobility, carrier lifetime, indium composition, and well thicknesses are examined. The simulation file can be seen in the appendix.

The simulated structure was set to correspond to InGaN/GaN quantum dots in the samples that were characterized, of which most had 10 nominally identical wells. All quantum wells were assumed to be identical, so the energy states for a single well are the same for 100

wells. The barriers and wells were set to 3 nm thickness, for a superlattice period of 6 nm. The doping was set to the approximate values of the grown structures, which is p= 5 x 10^{18} and n= 1 x 10^{19}. Reflectivity at the front surface is fixed at zero. Transmission through the gallium nitride substrate is set at 90%, which is the expected bulk to bulk transmission as a result of the refractive index difference between silicon and gallium nitride. The thickness of the emitter was optimized at 50 nm. If the wells are too far from the top surface, ultraviolet and blue light is not absorbed in the junction, whereas if the wells are too close to the surface, red light is absorbed after the junction. Contacts were modelled as perfect, transparent contacts which cover the entire top of the surface. In practice, the typical thickness of indium tin oxide used on the nanowires has a resistance of approximately 60 Ω/□, which was about 600 Ω/□ before annealing. ITO is also only about 90% transparent for relevant wavelengths.

The quantum efficiency was calculated based on the collection probability per incident photon as a function of wavelength. It is important to note that the quantum efficiency being simulated assumes excited carrier population in the quantum wells are coupled to the GaN conduction band. This is the operation of a quantum well solar cell, and not an intermediate band solar cell. Since there are only about 80% as many photons from 600-1200 nm as from 375 nm to 600 nm, so we cannot fully rely on an abundance of near-infrared secondary absorption events nor lucky absorption of just the right photons to excite a carrier exactly the bandgap. There will be some inevitable absorption of high energy photons from intermediate band states to conduction band states that could be accomplished with longer wavelength photons. This effect is not captured in this thesis, which uses the quantum efficiency to gauge the absorption characteristics and viability of carriers in intermediate states for subsequent absorption in a true intermediate band solar cell. The maximum possible intermediate band solar cell quantum efficiency is always lower than unity in any intermediate band solar cell. The valence to intermediate band quantum efficiency is shown as a function of number of wells in Figure 63. The lower quantum efficiency for wavelengths below the bandgap of GaN (375 nm) is a result of photon absorption too close to the top contact. The low quantum efficiency at longer wavelengths is addressed with a thicker miniband region as expected. Once the miniband is longer than 500 nm, a slight decrease in the quantum efficiency is observes as the drift current becomes weaker from the lower electric field.

In this simulation, lifetimes are fixed at 1 ms and mobility is assumed to be very high in the miniband region. This provides a view into the maximum possible quantum efficiency possible given the number of quantum wells used. With up to 100 wells, the quantum efficiency approaches 97%.

The simulation results of InGaN/GaN quantum well miniband solar cells are inconsistent with measured current-voltage characteristics of the nanowires solar cells studied in this thesis for the following reasons. Firstly, the superlattice period is 6 nm, with 3 nm GaN barriers and 3 nm InGaN wells. At high indium compositions (>40%),

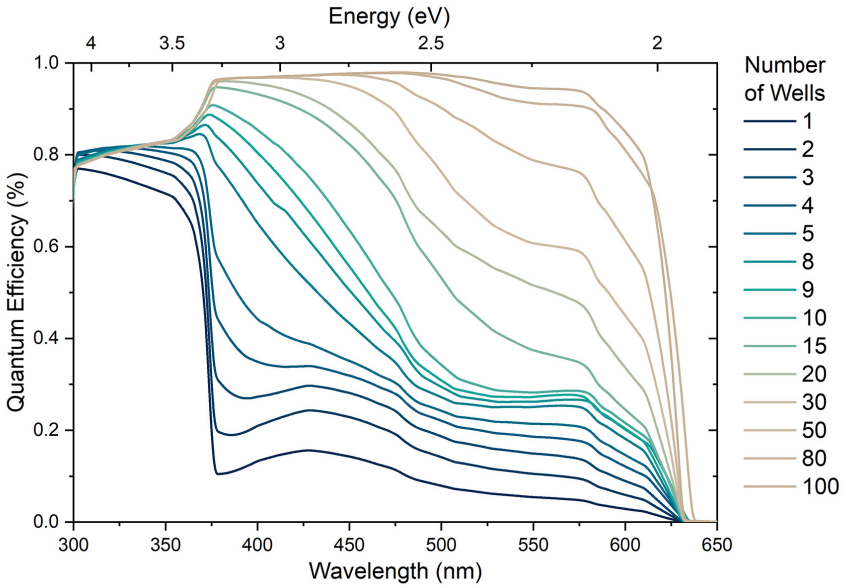

Figure 63: Valence band to intermediate band quantum efficiency as a function of quantum well number for a nearly perfect multiple quantum well miniband solar cell.

the wells are quite deep and tunneling between wells is very unlikely for confined carriers. The transport regime is fundamentally different in the grown nanowires. With the current GaN barrier thicknesses, the built in electric field is also insufficient to enable Wannier-Stark hopping between the wells. Therefore, the nanowires do not form a high mobility miniband region. Secondly, the recombination rate in the simulated miniband is much longer than what is expected in the nanowires.

Band diagrams of the InGaN/GaN miniband solar cell were calculated from the doping profile, materials and carrier concentrations for equilibrium, short-circuit, and maximum power point conditions, as shown in Figure 65. A cell with ten quantum wells was simulated with the miniband levels being calculated from the hybridization of the individual quantum well subbands. The illumination was set at 1-sun of the AM1.5G spectrum. Polarization effects were not taken into account in the miniband model as the carrier transport is unaffected by any potential barriers in an ideal miniband region.

Current-voltage characteristics were calculated up to 1.8 V as shown in Figure 64. In these simulations, the minibands are coupled directly to their respective conduction and valence bands so intermediate band physics are not captured. In a functioning intermediate band solar cell, the decoupling of the miniband and the conduction band forces only sequential absorption processes to contribute to the photocurrent to produce a higher voltage. This would make the operating voltage correspond to a pure gallium nitride junction and not of the InGaN/GaN miniband. In our simulations, tunneling between the intermediate band and the quasi-neutral regions is responsible for the current.

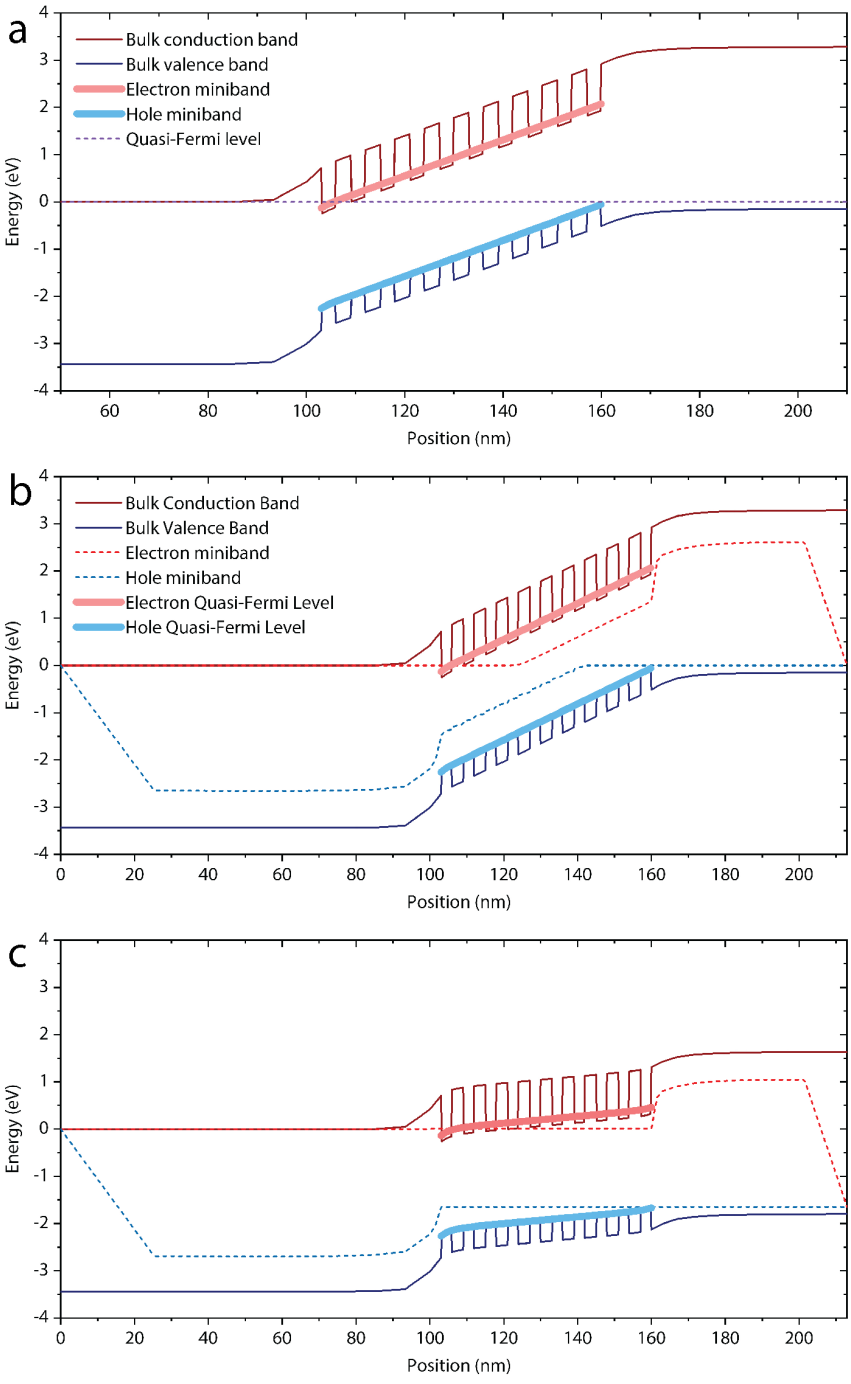

Figure 64: Band diagrams of a 10 InGaN/GaN quantum well miniband solar cell at (a) equilibrium, (b) at short circuit and (c) at the maximum power point.

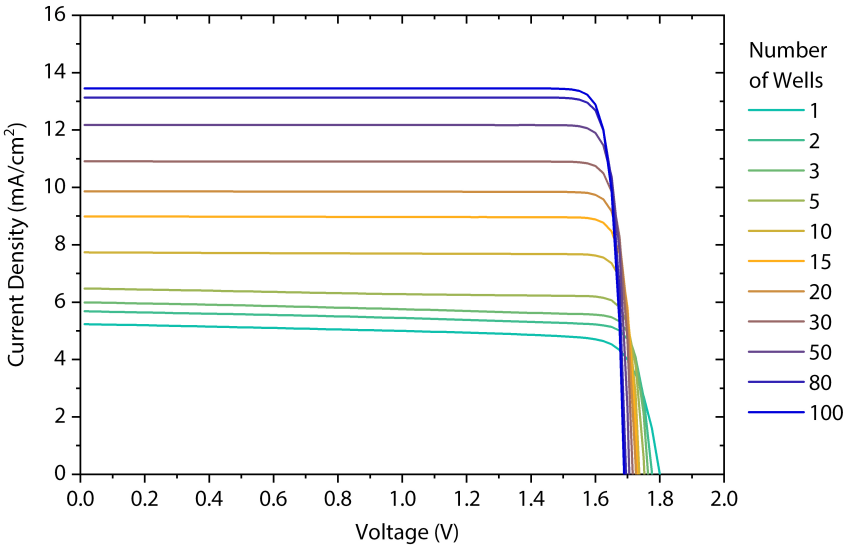

Figure 65: Current-voltage characteristics of a miniband solar cell from 1 well up to 100 wells.

The quantum well miniband solar cell produces a short-circuit current of 5 mA/cm^2 and an efficiency of 7.5% with a single quantum well (3 nm miniband). With up to 100 wells, the simulation shows a short circuit current of 20.8 mA/cm^2 and a maximum efficiency of 20.8% (600 nm miniband). The absorption from the quantum wells is approximately 10^4 cm^{-1} or greater, which is consistent with bulk InGaN/GaN superlattice structures[159–161]. The slight voltage drop observed for higher well counts is attributed to increased non-radiative recombination rates with the lower average field strength. With a few wells, a sloping current-voltage characteristic is indicative of recombination from inefficient light absorption with a single well.

5.3.3 *Coupled Quantum Well Model*

In contrast to the miniband model, which portrays consistent mobility throughout the InGaN/GaN quantum dot/well region, the high gallium nitride barriers between wells can lead to poorer transport properties. This is especially true in the case of hole transport, where hole mobilities in InGaN and GaN are less than 10 cm^2/V· s[199]. In this regime, carrier transport occurs through sequential or non-local hopping processes between the quantum wells. In such tunneling models, the superlattice period is now important since the transport characteristics of carriers depends on the wavefunction overlap between wells and the barrier heights. As excited carriers are moving across the quantum well region, they can either hop over or become trapped in the well. For trapped carriers, they can either escape optically or undergo recombination. For the coupled quantum well simulations, the *quantum transport* model in Crosslight® APSYS enables a more realistic picture of carrier transport in the current nanowire samples where

carriers can be directly excited from quantum well states to extended bulk states, hop between adjacent wells and non-adjacent wells.

Carrier transport is heavily dependent on the barrier heights and thicknesses. Using $\vec{k} \cdot \vec{p}$ calculations for the quantum well region, the state configuration can be calculated as a function of the barrier characteristics. The inter-well barrier thicknesses for a ten quantum well device were varied at equilibrium to determine the spatial overlap of adjacent quantum well subbands as shown in Figures 66 and 67. As the barriers get smaller, overlap between the quantum well subbands becomes possible. With 4 nm barriers, only the nearly de-localized states at the top of the wells are coupled to adjacent wells due to the tilting of the potential from the built-in electric field. At the maximum power point of the device, this potential is roughly flat, so the coupling is negligible between wells. Carriers will have to rely on photonic excitation to escape the well. When the barriers are 1.5 nm thick, coupling begins to be significant. The ground state wavefunctions in the well extend deep into the wells and would likely overlap at the maximum power point of the solar cell. With 1 nm or thinner barriers and, the wavefunctions are fully coupled and transport through the superlattice is driven by miniband conduction. A closer view of the quantum well subbands can be seen in Figure 67.

The nanowires are modelled again as bulk devices with multiple coupled quantum wells. The carrier concentrations and the conduction and valence bands are calculated self-consistently. The *n*-type layer thickness is set to that of the grown nanowire structures, which is 270 nm respectively. The p-type region is made thinner to improve the device performance in the UV. The device model was varied by the number of InGaN wells with 40% indium in each quantum well. The quantum dots are modelled as quantum wells again due to the large lateral dimension of the dots creating a well-like density of states that helps to simplify calculations. The simulated quantum efficiency is calculated at short-circuit as a function of wavelength up to 650 nm in Figure 68. The quantum efficiency does not extend as far into the infrared as it does in the miniband model. The sub-bandgap current generation is qualitatively similar to the experimental quantum efficiency shown in Figure 39. Lifetimes are set to very long times in the milliseconds to ensure the tunneling of carriers to the quasi-neutral regions so the increase in quantum efficiency corresponds to increased absorption. The quantum efficiency reaches up to 10% with ten quantum wells. Additional simulations with realistic carrier lifetimes of 1 µs reveal a decreasing quantum efficiency with any increase in quantum wells beyond the single well case. When simulating more than 4 quantum wells, the sub-bandgap quantum efficiency becomes negligible. Therefore, carrier transport in the nanowires must rely on secondary optical absorption events as well as some degree of non-local transport where the carriers can couple to extended states beyond the adjacent wells. Nevertheless, this provides additional support to the notion that any practical intermediate band solar cell built from InGaN quantum dots or wells should form a miniband of intermediate band of states since carrier

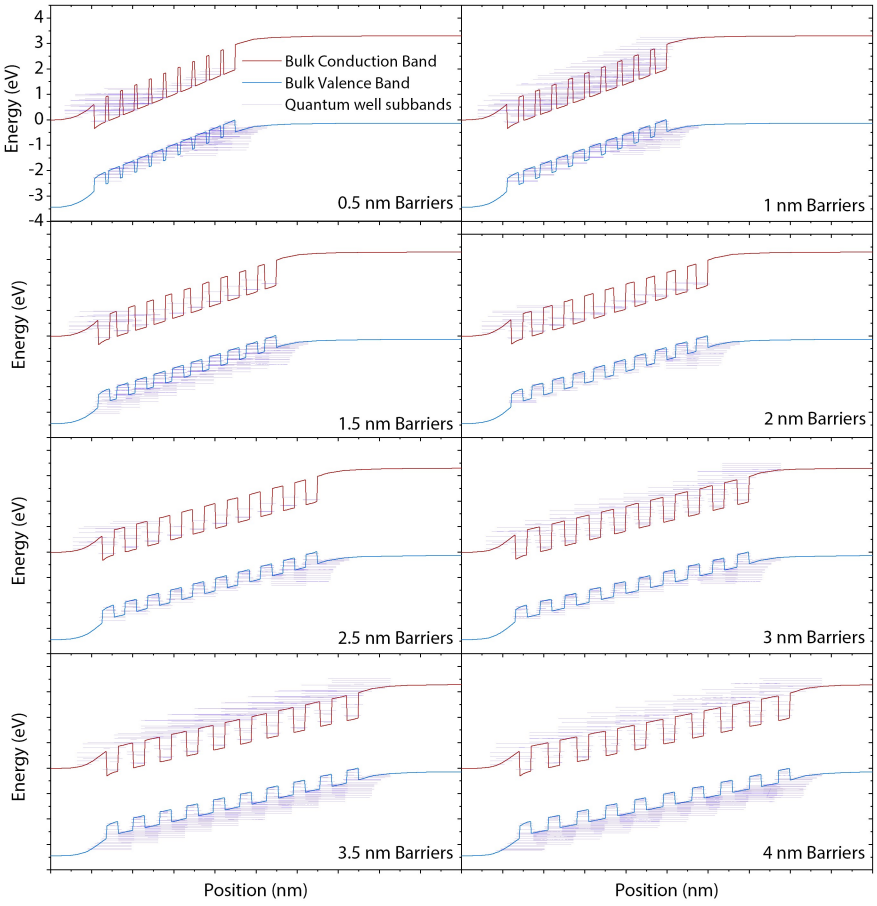

Figure 66: Simulated band diagram of a coupled quantum well solar cell at equilibrium with localized quantum well subbands for quantum well barriers of various thicknesses. Note that not all quantum states are drawn.

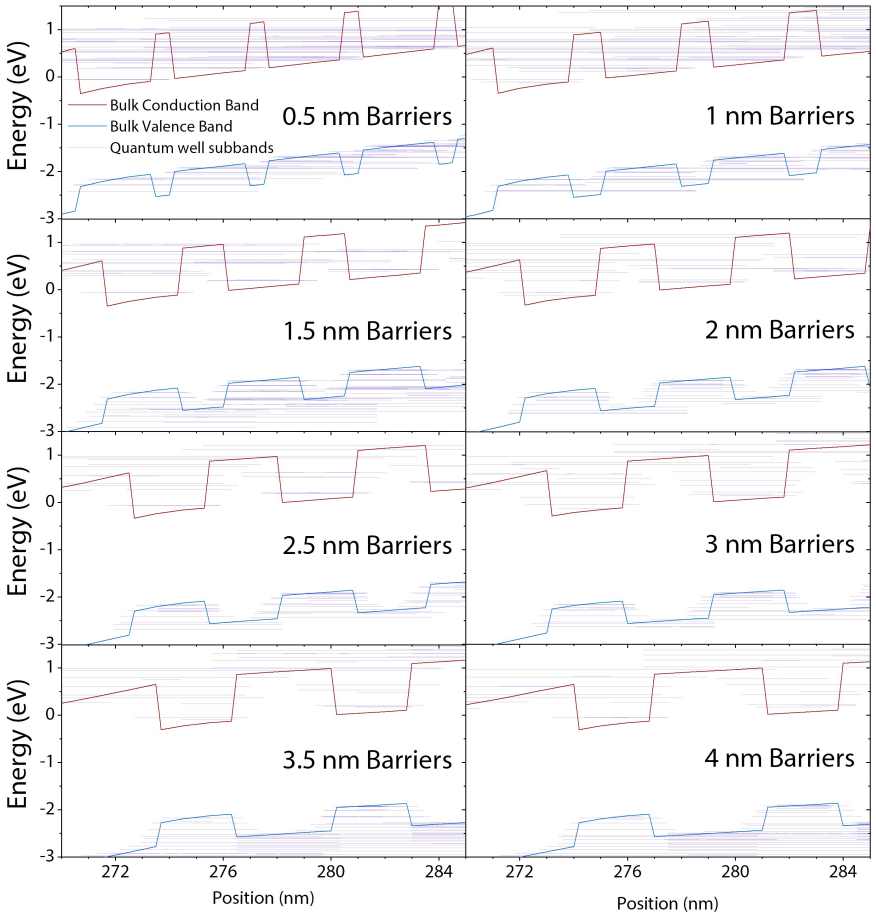

Figure 67: Close-up view of simulated localized quantum well subbands and their penetration depth to adjacent wells as a function of barrier thickness.

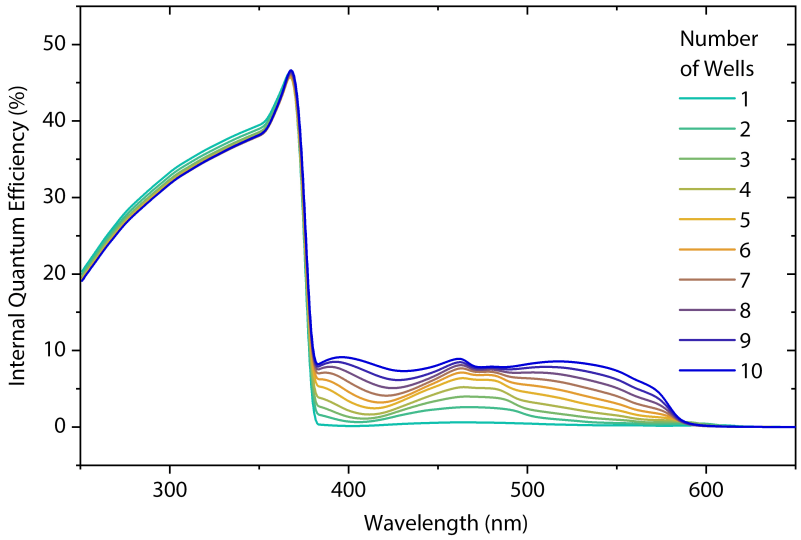

Figure 68: Internal quantum efficiency of a ten-well InGaN/GaN solar well with quantum mechanically coupled wells as a function of well number and wavelength.

re-trapping is a very common and detrimental effect. By providing the required numbers of wells for sufficient intermediate band absorption (>30), carrier re-trapping cannot be allowed to occur. Miniband conduction would allow carriers to move towards the edge of the multiple quantum well region and avoid re-trapping processes. This can be related to the figure of merit where the effective mobility in the multiple quantum well region is increased in the miniband coupled regime, and hence leads to a more efficient intermediate band device.

The simulated quantum efficiency as a function of wavelength for different indium composition is shown in Figure 69. As the indium fraction is increased, the wells become deeper allowing lower energy photons to be absorbed. The overall shape of the curves is a result of constructive and destructive interference in the thin nanowire layer.

When the well indium composition is increased, the current generation is progressively increased at longer photon wavelengths. With an indium fraction of 60%, the quantum efficiency is extended to almost 850 nm. The quantum efficiency cut-off corresponds to the energy difference between the electron and hole quantum well states. The quantum efficiency reaches a peak at approximately 11%. The lower quantum efficiency below 350 nm is a result of the 300 nm thick *p*-GaN top layer of the nanowire.

The quantum efficiencies of a quantum-dot-in-nanowire solar cell with miniband transport are higher than the equivalent device with an inter-well tunneling model that assumes localized quantum well states. The higher effective mobility of the miniband superlattice, calculated to be 32 $cm^2/V \cdot s$ for electrons and 53 $cm^2/V \cdot s$, helps to transport carriers across the quantum well region without relying on tunneling through high GaN barriers. The quantum efficiency below

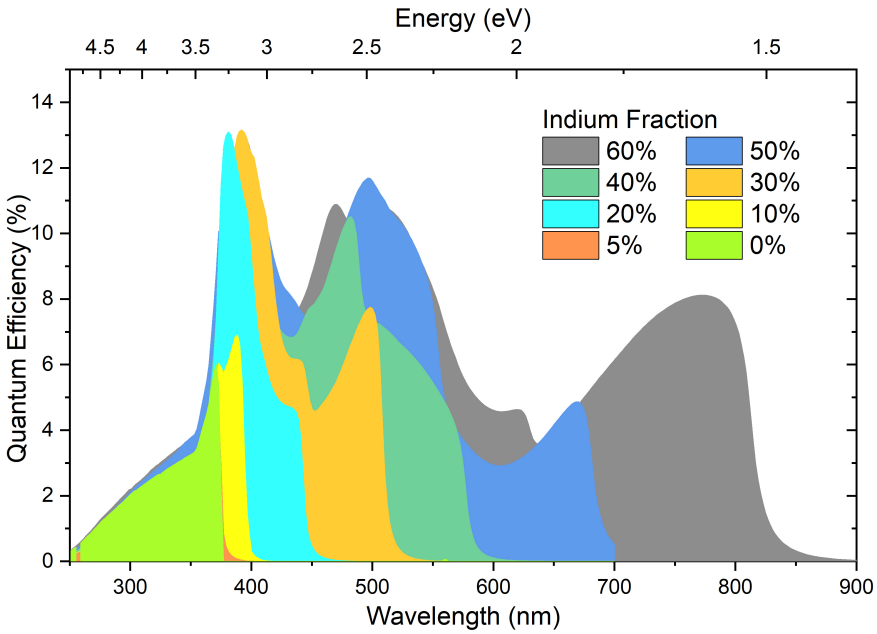

Figure 69: Quantum efficiency as a function of indium composition in a ten quantum wells InGaN/GaN quantum well solar cell.

300 nm is highly dependent on the thickness of the top *p*-GaN layer but is unimportant due to the lack of photons in this region under the AM1.5G spectrum.

The tunneling between adjacent wells depends mainly on the barrier thicknesses, carrier energy and barrier potential energy. In InGaN/GaN quantum wells/dots with high indium fractions, the barrier is quite high, making typical quantum well solar cell operation nearly impossible for typical superlattice designs. This barrier height can also help ensure intermediate band operation to prevent carriers from tunneling out of the potential well. With carriers facing barriers up to 1 eV barriers, the barriers must be very thin to approach the miniband condition. The tunneling probability can be calculated by Solving the time-dependent Schrödinger equation when a free particle encounters a rectangular barrier with the appropriate boundary conditions at the barrier interfaces to ensure a continuous function. The solution for when the particle has an energy lower than the barrier ($E < V_0$) approximated as

$$T_b = \left(\frac{1}{1 + \frac{V_0^2 \sinh^2(k_1 a_w)}{(4E(V_b - E))}} \right)^2, \tag{241}$$

where

$$k_1 = \sqrt{\frac{2m^* E}{\hbar^2}}, \tag{242}$$

and V_b is the potential energy barrier height, E is the carrier energy, and a_w is thee barrier width.

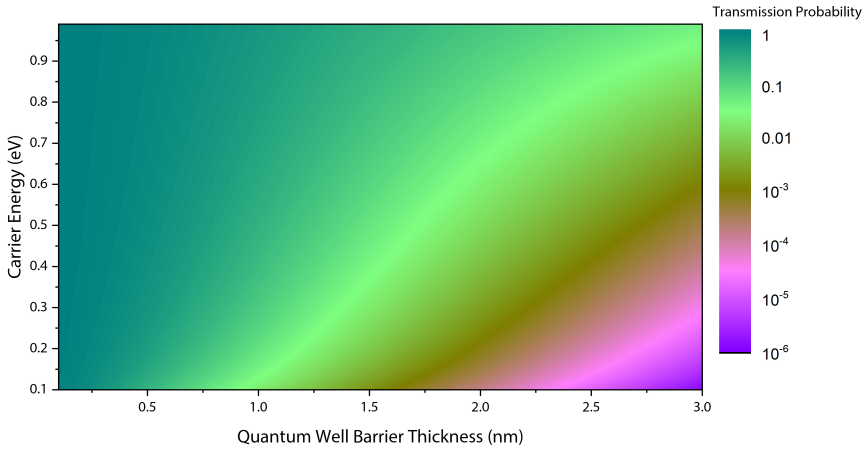

Figure 70: Tunneling probability of a carrier in a 1 eV potential barrier $In_{0.4}Ga_{0.6}N/GaN$ quantum well.

Figure 70 shows the tunneling probability according to Equation 241 for a 1 eV potential barrier for a trapped electron. The result shows that tunneling is only significant for thin barriers or carriers in higher states. With holes, which have significantly more mass but lower potential barriers, the tunneling characteristics even poorer. Despite the lower valence band barriers, the large effective masses of holes in InGaN () 1.3 m_0) prevents any appreciable tunneling unless the barriers are nearly 0.5 nm thick. From quantum dot state simulations earlier in this chapter, we can expect that most carriers will have energies from 0.1-0.2 eV from the bottom so barriers that are less than 1.5 nm are required for appreciable electron tunneling probability. Hole transport may rely more on optical transitions to move to adjacent wells.

5.3.4 *Effect of Polarization in InGaN Quantum Wells*

One of the distinguishing features of III-nitride materials is the polarization effects that arise from heterointerfaces. These effects lead to significant electric fields unrelated to doping that affect carrier transport and are discussed in more detail in Chapter 2. In quantum wells, the polarization at the InGaN/GaN interface can distort the potential carriers are subject to inside the multiple quantum well region. The effect on carrier transport depends on the polarity of the nanowire structures, which can either be N-face (or N-polar) or Ga-face (or Ga-polar). In LEDs, this effect can be quite detrimental to performance since the electron and hole can be spatially separated resulting in reduced radiative recombination. In solar cells, the effect can be desirable since the reduced recombination (even if it is radiative) can help carrier collection efficiency. In traditional quantum well solar cells, the quantum well region can be designed to screen most of the polarization charge through doping. This effect has been virtually eliminated to increase the carrier transport properties[200]. The polarization effect leads to the quantum confined stark effect which changes the absorption coefficient with the introduction of this field.

If this effect is present, the electron states are usually shifted to lower energies while the hole states are shifted higher, enabling red-shifted luminescence.

Crosslight® APSYS captures the polarization effects through a *polarization charge model* that adds a three-dimensional charge distribution within the drift-diffusion simulation. The modelling follows the formalism of Fiorentini *et al.*[201] for calculating the non-linear polarization for III-nitride materials. This provides the sheet charge that is confined to interfaces. In this case, the interface is formed by $In_{0.4}Ga_{0.6}N$ and GaN. The growth conditions of the initial GaN growth determines the polarity of the nanowires.

With increasing indium composition, the polarization effects in indium become increasingly complex. In some devices, the polarization fields can be screened by significant doping profiles in the range of 10^{19} cm^{-3}. In our nanowires, however, the quantum dot region is not intentionally doped. Modulation doping of magnesium in the barriers between quantum dots in the nanowires by Dr. Zetian Mi has been used to increase hole transport[190] and can be used in principle to counter polarization effects. Thus, it is possible that the modulation doping screens the polarization charge. Through a design similar to the AlGaN/GaN core-shell nanowires studied in this thesis, polarization effects have been shown to be drastically reduced[202]. Further evidence of polarization reduction is provided by Kim *et al.* who report on the blue-shift being indicative of polarization screening[203]. In contradiction, however, Park *et al.* have claimed that a blue-shifted in photoluminescence is evidence of the quantum confined stark effect[204].

Counterintuitively, the blue shift can be explained by both an increase and decrease in the polarization field. Electroluminescence spectra shown in Chapter 5 reveal a significant blue-shift with increasing injection current. Since the increase in current corresponds to an increase in forward bias, the change in electric field begins to reverse the tilt of the *p-i-n* junction from short-circuit current. This shifts the energy levels in the quantum dots. In both simulation and experiment in this thesis, a blue-shift is observed. The other effect occurs with high indium compositions (>40%) that create the deep wells we find in our nanowires. The piezoelectric field component of the polarization in high indium InGaN/GaN multiple quantum wells has been shown to improve hole transport for Ga-face growth polarizations[205]. This is due to the narrowing of the effective quantum well width experienced by the hole under high polarizations. Holes that encounter such a potential have a greater change of flying over the wells, lowering the hole capture rate in the wells. This results in a blue-shift of the spectrum. In any case, in a solar cell, the quantum-confined Stark effect may help to improve performance through reduced recombination from the smaller electron and hole wavefunction overlap if transport through the miniband is efficient.

To demonstrate the effect of polarization on the quantum dot states, a device with 10 quantum wells was simulated with and without polarization effects. Both Ga-face and N-face polarizations were simu-

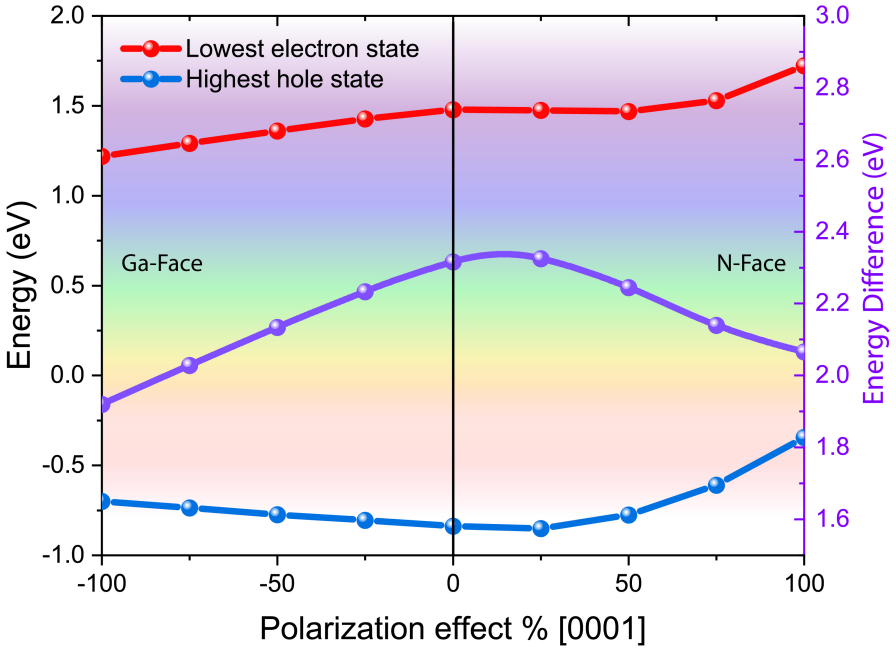

Figure 71: Simulated lowest electron state and highest hole state energies in one of ten InGaN/GaN quantum wells as a function of crystal polarization type and screening. The difference between the two levels is the expected transition energy and corresponds to the purple axis on the right.

lated. The polarization screening was varied from completely screened to completely unscreened. The indium composition in each quantum well were kept the same at 40%. The quantum states were calculated using an 6x6 $\vec{k} \cdot \vec{p}$ Luttinger-Kohn Hamiltonian model in Crosslight® APSYS which includes the mixing of heavy holes, light holes, and split-off hole subbands. The typically forbidden radiative transitions in zinc-blende III-V materials are generally allowed in III-V nitrides due to the polarization effects from the wurtzite crystal structure that break the symmetry of the conduction and valence band structure[206]. This places little importance on the optical selection rules for radiative transitions. The difference between the lowest confined electron state and highest hole state in a specific quantum well was calculated and defined as transition energy. The transition energies are shown as a function of polarization screening in Figure 71. It is worth noting that there is almost always some polarization screening in real devices, so the total polarization effect is never near 100% of the maximum value. The measured polarization strength from the literature seems to correspond about 50% in devices which demonstrate significant effects[207, 208].

With the presence of polarization, a significant red-shift of the spectrum occurs. The heavily distorted potential of the wells lowers the bulk conduction band energy on one side of the well, where electrons and holes states move closer to each other. With increased screenings of the polarization charge, the energies generally shift higher. Interestingly, the highest energy transition energies are found in the 25% Ga-face polar configuration (when 75% of the polarization effect is

screened). This maximum in transition energy is caused by the presence of the built-in electric field of the *p-i-n* junction which has relatively high doping concentrations of 0.5 x 10^{19} cm^{-3} to 1 x 10^{19} cm^{-3} in the *p* and *n* regions. The electron states are shifted higher in energy as the polarization points in the [0001] direction, increasing from 1.25 eV at maximum N-face polarization to 1.72 eV at the maximum possible Ga-face polarization, with a small dip from 25% to 50% Ga-face polarization. The hole states start at -0.70 eV with maximum N-face polarization and shift lower in energy until a minimum of -0.83 eV and increase again reaching a peak of -0.34 eV at maximum Ga-face polarization. All energies are relative to the Fermi level in equilibrium conditions.

The band diagrams of N-face and Ga-face InGaN/GaN quantum wells with 50% polarization screening in the absorber region of the *p-i-n* junctions are shown in Figure 72 and 73.

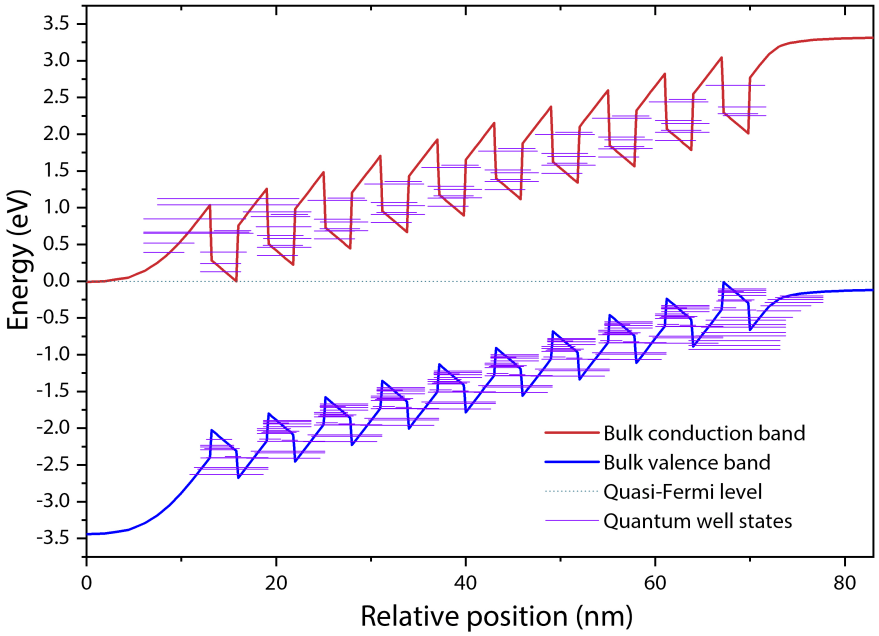

Figure 72: Band diagram of a 10 InGaN/GaN quantum well solar cell with 50% Ga-face polarization.

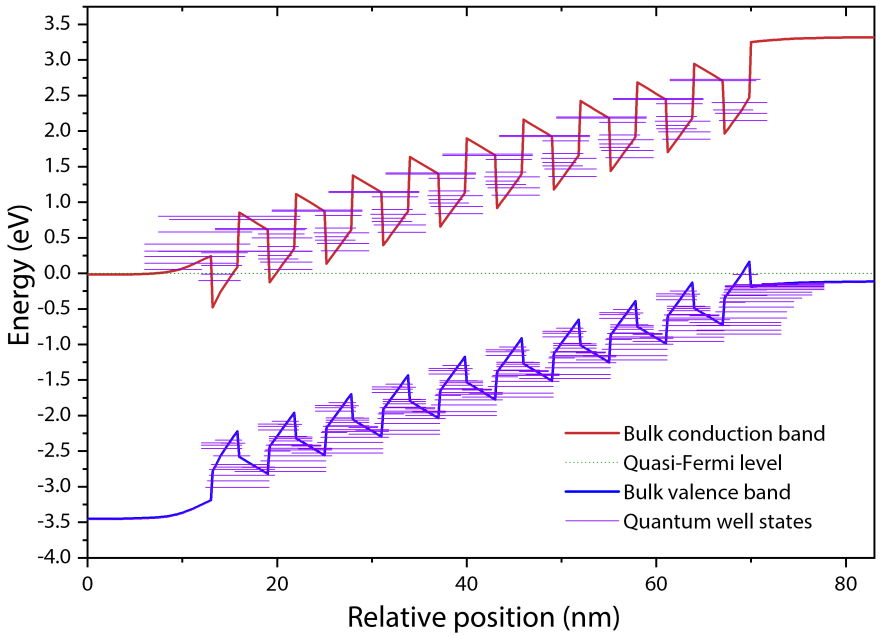

Figure 73: Band diagram of 10 InGaN/GaN quantum well solar cell with 50% N-face polarization.

The electric field caused by the polarization effects were calculated using Crosslight® APSYS and are shown in Figure 74. The polarization screening was varied from 100% to 0% for both types of polarization charge configurations. The electric field fluctuates between positive and negative values in the presence of polarization charges with a period equal to that of the quantum wells. The electric field profile of the *p-i-n* junction becomes dominated by the polarization charge once screening less than 75% (25% of maximum polarization charge effect). The electric field magnitude can reach levels higher than 3 MV/cm^{-1} without any screening. In the completely screened case, the electric field is roughly constant at about below 450 kV/cm^{-1}. Near the ends of the multiple quantum well region, the electric field increases slightly in the completely screened polarization charge case. The non-symmetric electric field profile in Figure 74 is due to the non-symmetric doping profile. The electric field drops at the two ends of the multiple quantum well region in the N-face polarization configuration. With the Ga-face polarization configuration, the large electric fields at the ends create large energy barriers for carriers to escape the multiple quantum well region. Current flow in this short-circuit condition is severely restricted since the energy barrier increases from about 0.25 eV in the N-face condition to about 1.2 eV in the Ga-face condition. Note that the results are reversed if the junction is *n-i-p* (with *n* being on top of *p*).

5.4 SUMMARY

In summary, the performance of a single junction quantum-dot-in-nanowire LED was simulated using Crosslight® APSYS. The states

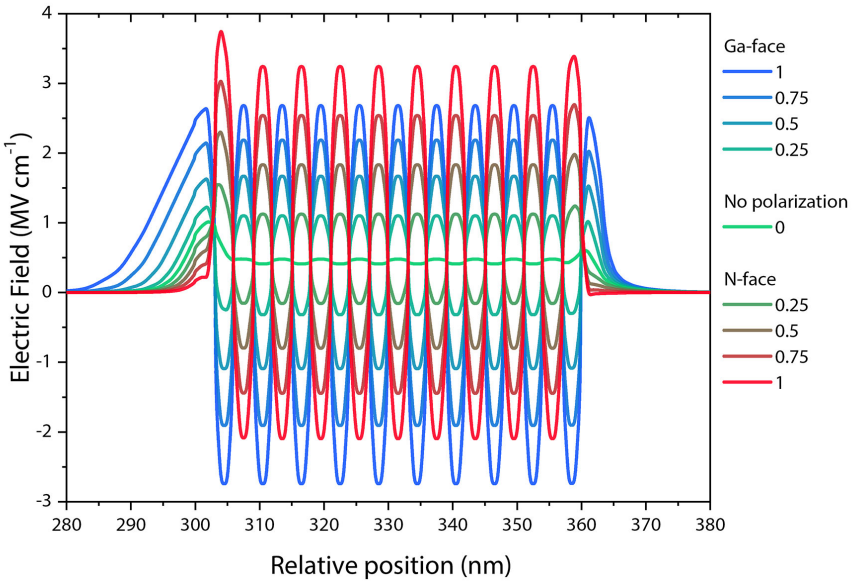

Figure 74: Electric field profile as a function of polarization direction and effect across 10 InGaN/GaN quantum wells.

and wavefunctions of four different quantum dots were solved and used in a drift-diffusion simulation in which the electroluminescence spectrum was calculated. Simulated devices were operated as LEDs which allowed for a quantum dot states and wavefunctions coupled into a drift-diffusion model with no incident illumination. The calculated emission spectrum was fitted to experimental electroluminescence spectra to verify quantum dot indium composition. The fitting parameters were used to inform subsequent solar cell models which rely on miniband and self-consistently coupled quantum well absorber regions. The current generation from sub-bandgap processes was calculated from drift-diffusion simulations coupled to various quantum well models. The first model assumed miniband transport throughout a fully coupled multiple quantum well region and has shown significant quantum efficiency in short-circuit conditions where performance is limited by the absorption in the quantum wells. The current-voltage curves of an idealized quantum well miniband solar cell were plotted in the case of the quantum well states (intermediate band) being coupled to the conduction band (lower voltage). A second model for quantum well coupling was used to calculate the solar cell performance with independent quantum well states. The coupling between the quantum wells subbands was assessed as a function of barrier thickness. Significant coupling was found to occur with wells thinner than 1.5 nm for InGaN/GaN wells with 40% indium. The final section investigates the effect of polarization on the proposed device structure. Interface charges were introduced, and the band profile and quantum states were assessed in equilibrium conditions. In a *p-i-n* configuration, it appears that a solar cell benefits from the N-face polarization due to the reduced electric fields at the edges of the multiple quantum well region that prevent electrons

and holes from reaching the quasi-neutral *p*-type and *n*-type regions, respectively.

6

MULTIJUNCTION INGAN ON SILICON

"There exists everywhere a medium in things, determined by equilibrium."

— Dmitri Mendeleev, 1880

6.1 INTRODUCTION

The wide bandgap range of InGaN compounds is the key to its use in solar cells. In the as-grown nanowire designs, the InGaN sections were designed to enable low energy photon absorption in a GaN device. By decoupling the InGaN quantum dots/wells from the GaN emitter and base of the solar cell, a higher operating voltage can be maintained in addition to the current produced from sub-bandgap absorption events. This strategy is difficult to realize since non-radiative recombination throughout the device must be very low. This requires high material quality such that carriers can undergo sequential excitation to the extended states of GaN. This problem is the primary reason for low open circuit voltage in the measured nanowire solar cells shown in Chapter 4.

An alternative approach involves multiple junctions of InGaN material in a monolithic stack connected via highly doped tunnel junctions. Some research has been done investigating the potential for InGaN solar cells on silicon with promising efficiencies with two and three-junction designs predicting efficiencies of 31% and 35% at 1-sun[209–211]. However, there are a few major issues with traditional designs of InGaN on silicon. The main issue is ensuring high InGaN material quality when grown on silicon. There has been some progress in InGaN/Si heteroepitaxy using a lower growth temperature to avoid indium segregation and desorption during growth[212]. Despite the progress, growing compounds with high indium incorporation (>40%) remains difficult to achieve. For solar cells, indium compositions up to 60% are required to produce subcells that absorb in the red portion of the spectrum. Solar cells with more than one InGaN junction require even higher indium compositions. Another issue is that InGaN with more than 60% indium fractions can accumulate charge at the interfaces and form inversion layers that restrict carrier transport[213].

Achieving sufficient *p*-type doping has long been a problem for InGaN compounds. It turns out that many wide bandgap semiconductors suffer from doping issues that are a result of the polarity of the material. Magnesium has emerged as the dopant of choice for InGaN-based devices as it has led to the highest dopant concentrations achieved in InGaN, despite the dopant ground state level being quite deep[214]. Fortunately, with annealing it has been shown that an extended shallow acceptor level is within the ionization energy

of this deep level, providing the route to functional devices we have today[215]

High doping is usually required in InGaN devices to ensure high conductivity and sufficient electric fields in the intrinsic absorber regions to sweep out carriers before recombination can occur[216]. High magnesium doping in InGaN has been challenging to achieve. The low dopant solubility makes it difficult to add more magnesium into the lattice, while passivation by hydrogen atoms leads to Mg-H complexes that interfere with the performance of the dopant[217, 218].

In the case of the nanowire growth, some of these difficulties can be alleviated. The lattice mismatch between silicon and InGaN is not an issue with nanowire growth, where strain energy can be released at the surface of the nanowire for nearly-defect free GaN material[219]. In addition, high indium incorporation can be realized with quantum wells/dots which perform the absorption while managing strain along the growth-axis through strain compensative design using AlGaN[220, 221]. In fact, it has been shown that indium compositions up to pure InN have been demonstrated in nanowires on silicon[222].

Numerical simulations of a four-junction InGaN solar cell have shown than conversion efficiencies up to 46.45% are possible under 1000X concentrated sunlight[223]. This result is achieved using an InN bottom subcell, which may not be practical due the difficulty in growing it sufficiently thick. By restricting ourselves to a silicon bottom subcell, cost-effective InGaN/Si dual-junction subcells can be fabricated with relatively high efficiency.

Since this thesis focuses on InGaN/GaN quantum dot-in-nanowires on silicon as the solar cell platform, InGaN nanowires on silicon can be grown to form the dual junction solar cell. A top nanowire junction has already been demonstrated with a pure InGaN nanowire on a silicon substrate[224], and even a pure InN nanowire cell has been shown to operate on silicon[225]. Alternatively, an InGaN/GaN superlattice can provide tunable absorption characteristics for the top subcell.

In this chapter, a bulk InGaN junction is designed to optimize the current distribution with a silicon bottom subcell. The absorption characteristics for the specific InGaN alloy are determined from interpolation of the spectral absorption coefficients obtained from experimental and theoretical parameters. The dual junction InGaN/Si solar cell is simulated using Crosslight APSYS. The extension towards a nanowire-based top subcell can be accomplished through modelling the light trapping characteristics of nanowires to absorb a similar amount of light as bulk top subcell despite being thinner. This type of modelling can be approached by finite difference time domain (FDTD) simulations or rigorous coupled wave analysis (RCWA) techniques and is outside the scope of this thesis.

6.1.0.1 *Absorption Coefficients for InGaN*

The real and complex refractive indices (n and k) for GaN are well-known as thick, high quality layers can be grown on sapphire sub-

strates. The change of the n and k values with increasing the addition of indium is less known. In the absence of experimentally determined refractive indices that drift-diffusion simulations of devices using bulk sections of InGaN require, interpolation can be used to obtain approximate values for arbitrary indium fractions. The absorption coefficients are obtained from experimental work in the literature on various InGaN alloys[85, 113, 160, 161], where the parameters are shifted by wavelength to correspond exactly to the bandgap of the alloy being used in simulation. The dispersion of n and k by the corresponding bandgap shift with additional indium. A linear interpolation for all indium compositions is used from experimentally determined n and k values for GaN and InN. The effect of the n and k values on the simulations is not crucial for nanowires without bulk InGaN regions. The nanowires that contain InGaN in the form of quantum wells/dots have absorption characteristics that are calculated from quantum mechanical methods described in Chapter 2.

6.2 SIMULATION STRATEGY

The InGaN/Si dual junction solar cell was simulated using Crosslight APSYS with the silicon substrate as the bottom junction. This value is similar to the 46% value determined by Hsu *et al.*[211], where the simulated cell does not share the same n and k or bowing parameters for InGaN used in this thesis. The n and k values used in this thesis were obtained from the interpolation of multiple experimental values. The band alignment is quite fortuitous such that silicon can form a natural tunnel junction with InGaN [211]. In the case of Crosslight simulations, the tunnel junction physics are not fully simulated but treated as very narrow regions of perfect conductivity. The indium fraction of InGaN that this occurs at is also near the ideal combination of bandgaps for the highest solar cell power conversion efficiency under the AM1.5G spectrum (1.66 eV/ 1.11 eV).

The initial step involves simulating an efficient silicon subcell. The thickness of the silicon subcell was varied between 100 μm and 350 μm to determine the optimal performance. A traditional *p-n* junction configuration was used. Highly doped cap and back surface field layers were added to reduce the surface recombination rates, resulting in improved the efficiency from about 16% to 22% for the silicon subcell alone. This increase arises from the increased operating voltage from about 0.6 V to 0.65 V. The maximum short-circuit current was approximately 38.9 mA/cm^2 under 1-sun of the AM1.5G solar spectrum, which is in line with high efficiency silicon cell designs. The ideal dual-junction solar cell based on silicon would operate on half this current to satisfy the current-matching condition in the monolithic structure. Therefore, we would expect the top InGaN subcell to produce about 18-19 mA at short-circuit conditions to balance the current production in the cell.

Multiple simulations of single junction *p-i-n* InGaN top subcells were performed with a varying indium molar fraction. The optimal

bandgap was determined when the InGaN subcell was found to produce 18-19 mA, leaving the rest of the photons for the silicon subcell. The optimal configuration was found to correspond to $In_{0.52}Ga_{0.48}N$ as the top subcell. This alloy produced about 18 mA at the maximum power point under AM1.5G illumination. From a Shockley-Read-Hall recombination rate of $1.6x10^{17}$ $cm^{-3}s^{-1}$, a thinner silicon subcell was preferable over the typical 300 μm thick silicon substrate. This also assumes a reflective back contact so a thinner silicon subcell would perform better. The simulations assumed 100% reflectivity of light at the back from the metallic back contact. This provided long-wavelength photons with an increased chance of absorption on a second pass through the silicon wafer. A schematic of the optimized InGaN/Si layer structure is shown in Figure 75.

6.3 DUAL JUNCTION INGAN ON SILICON SIMULATION RESULTS

The optimal thickness of the $In_{0.52}Ga_{0.48}N$ top subcell was determined to be 2.9 μm which was sufficient to absorb the solar spectrum at wavelengths shorter than 750 nm, yet thin enough for carriers to be swept out of the intrinsic region efficiently. This cell design provides about 20 mA of current at short circuit which drops to about 18 mA at the maximum power point. The shunt resistance is due to the low hole mobility of InGaN that is known to be significantly lower than the electron mobility. This places constraints on the junction design, where high doping must be used to increase the field strength in the intrinsic region while keeping the junction thin. Additional cap (p++) and back surface field (n++) layers were added to the $In_{0.52}Ga_{0.48}N$ subcell to increase its performance. Increased Shockley-Read-Hall recombination with additional doping is accounted for in the model from empirical data in the Crosslight material models, thus striking a balance between intrinsic region recombination and doping-related recombination is required to maximize the cell efficiency.

The InGaN subcell is fundamentally different from the silicon subcell in design and operation. The silicon subcell lifetimes are on the order of microseconds or more, where thick weakly-doped layers can result in a very efficiency subcell. High carrier mobilities in silicon allow even the smallest fields to ensure sufficient carrier separation. For silicon, the carrier separation is largely a result of the diffusion of electron and holes. In InGaN, the crystal quality is poorer due to significantly more defects when compared to the very high quality of silicon substrates. Introducing intentional doping only adds to the non-radiative recombination, especially since the electron mobilities have been known to be significantly higher than then hole mobilities[226]. This makes it difficult for photo-generated holes to be swept to the edges of the device. A *p-i-n* junction design can separate the carrier generation regions from the doping. High doping levels are then only used at the top and bottom of the device to create an electric field across the intrinsic region.

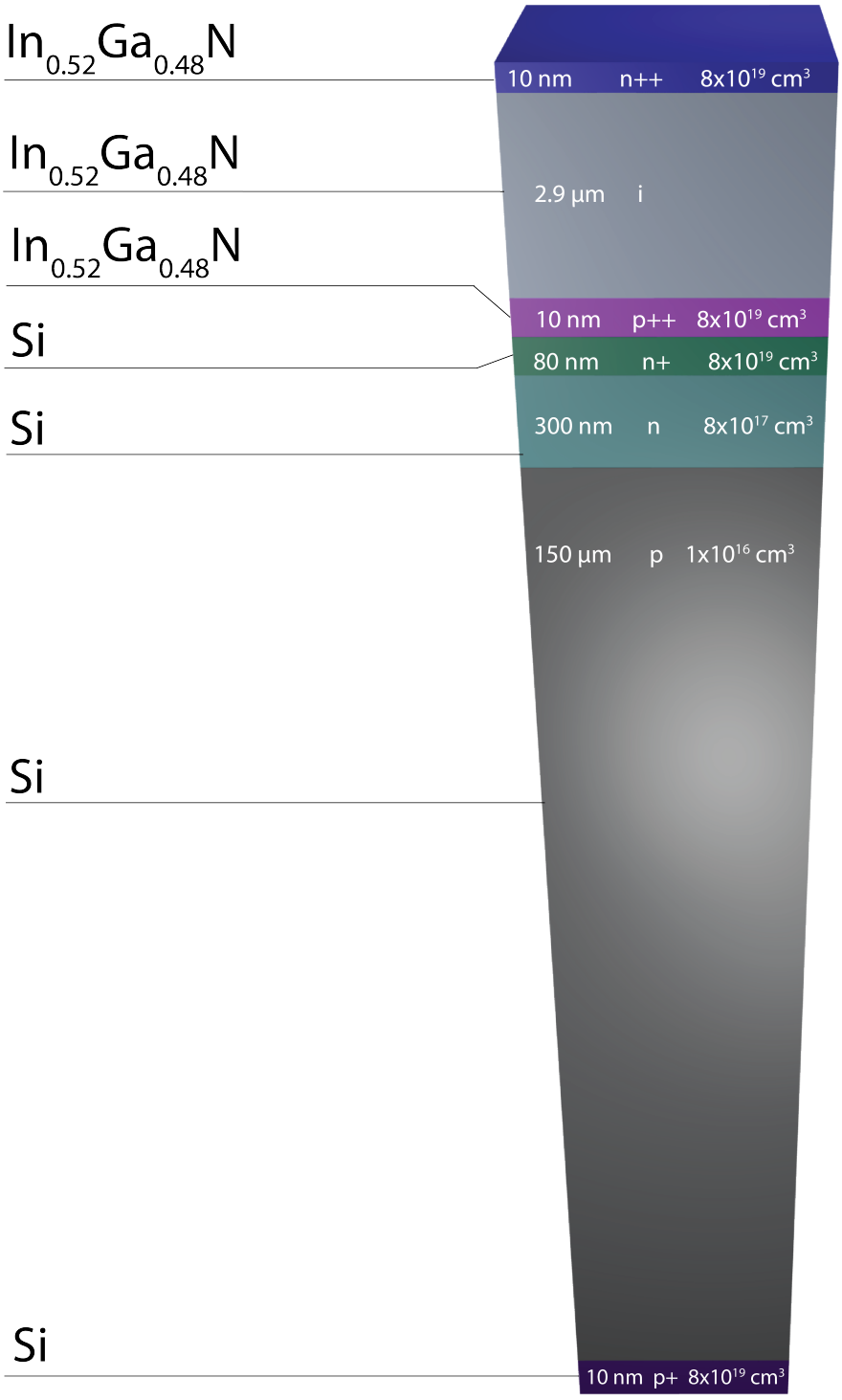

Figure 75: Schematic of the optimized InGaN/Si dual junction cell (not to scale).

Parameter	Silicon Subcell	InGaN Top Subcell	2J Cell
Voc	0.68 V	1.11 V	1.79
Jsc	20.5 mA	20 mA	18.5
Fill Factor	82.4%	81%	83.94%
Efficiency	11.5%	18%	27.8 %

Table 7: Performance characteristics of the simulated dual junction InGaN/Si solar cell.

While increasing the indium composition allows for more current production in the top subcell at the expense of the silicon subcell, the voltage decrease reduces the overall efficiency of the device. In an ideal semiconductor with high electron and hole mobility, the indium composition would be lowered so that more current would be shared with the silicon subcell. The ideal composition would be about 46-50% indium (1.5-1.6 eV bandgap), depending on the absorption characteristics of the as-grown material. The experimental absorption can vary depending on the substrate due to strain in the InGaN epilayer but may be less variable in an InGaN nanowire configuration due to less interaction with the substrate. The band diagrams of the dual-junction solar cell are shown in Figures 76.

6.4 INGAN ON SILICON CURRENT-VOLTAGE CHARACTERISTICS

The current-voltage characteristics were simulated using an AM1.5G solar spectrum set at 1000 W/m^2 and are shown in Figure 77. The dual junction cell was about 27.8% efficient at its maximum power point. This is very similar to simulated dual junction cells as modelled by Hsu *et al.*[211], who have come up with numbers up to 31% assuming all photons create electron-hole pairs and omitting resistive losses. The overall dual junction cell produces about 18.7 mA of current at J_{sc} with an open-circuit voltage of about 1.87 eV. The fill factor is about 79%. The performance characteristics are summarized in Table 7 Experimental absorption coefficients of InGaN with 54% indium were slightly shifted to lower energies to obtain the absorption coefficient for InGan with 52% indium.

6.5 DISCUSSION ON NANOWIRE TOP SUBCELLS ON SILICON

The dual junction solar cell can also be tailored to a top junction made from InGaN nanowires as opposed to bulk InGaN to remove the issues associated with lattice mismatched growth. The nanowires can provide increased absorption over bulk InGaN such that the *p-i-n* junction can be less than the nearly 3 µm thick InGaN absorber region. The height of the nanowires required to absorb a sufficient amount of light to achieve current matching with the bottom silicon subcell is highly dependent on the nanowire morphologies. Thee 600 nm height

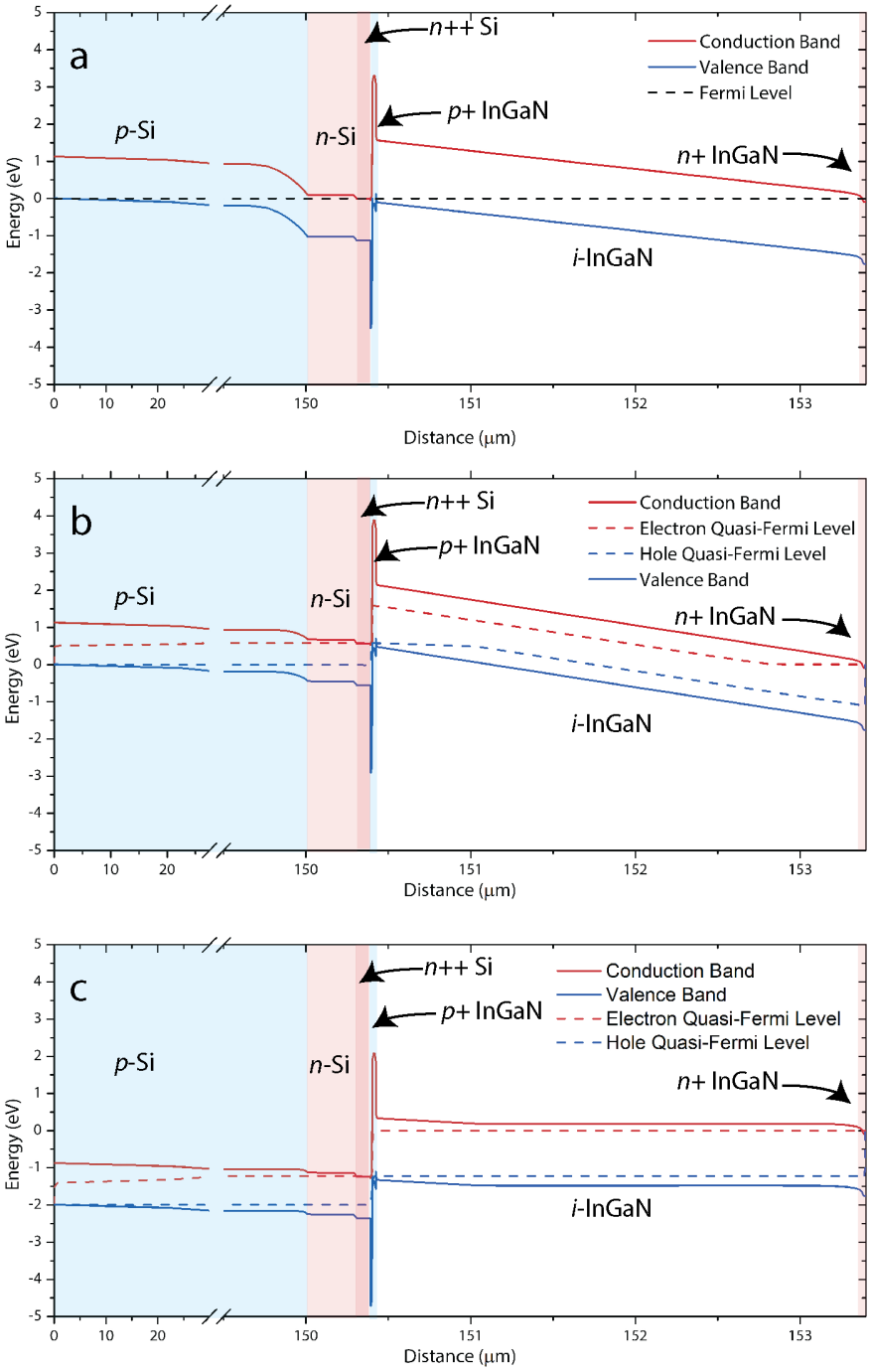

Figure 76: Band diagram for an InGaN/Si dual junction solar cell at (a) equilibrium, (b) short-circuit, and (c) at the maximum power point.

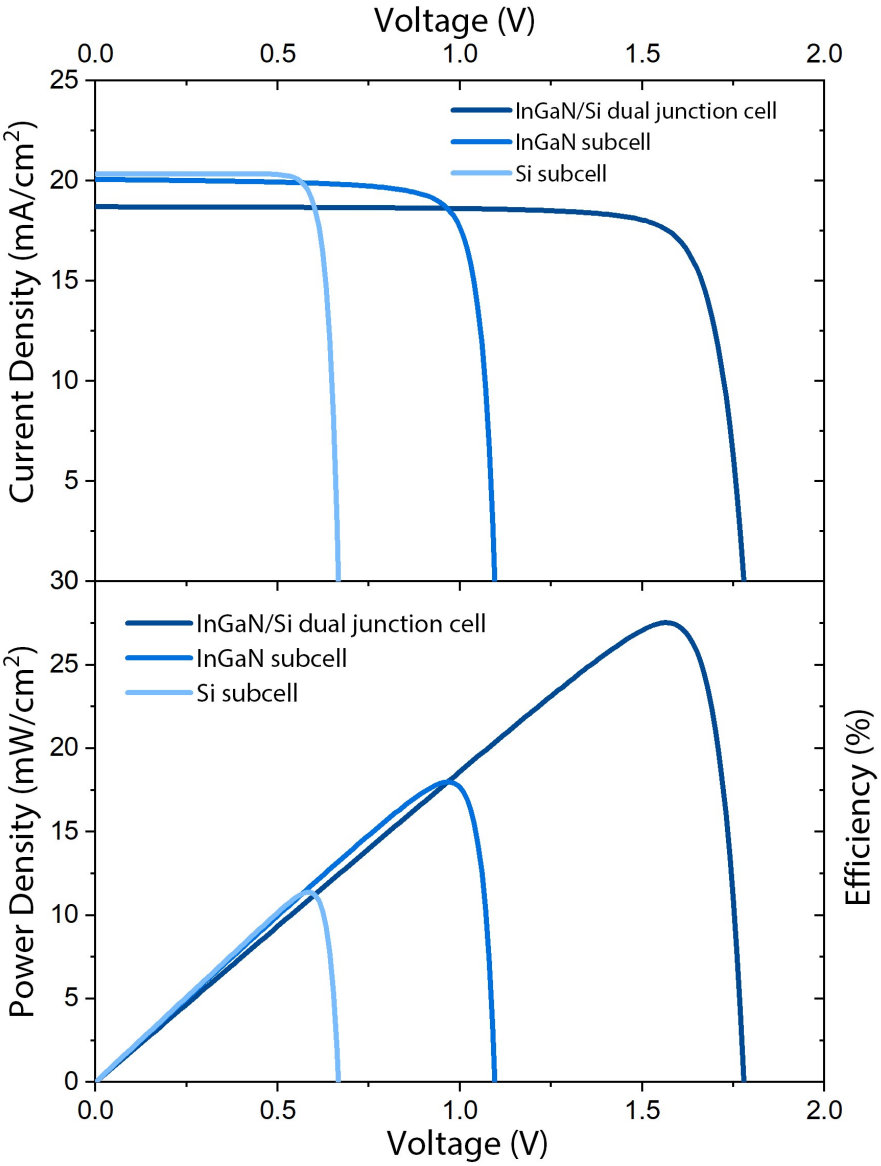

Figure 77: Simulated current density-voltage (top) and power density-voltage (bottom) curves under 1-sun illumination for individual InGaN and Si subcells (lighter colours) and complete 2J cell (darkest line).

of the nanowires grown at McGill is likely insufficient to achieve the required absorption. From reflectivity measurements, the light incident on the nanowires is significantly scattered. The large amount of scattering leads to an effective increase of the interaction path length of the incident light. The enhancement in theory can approach the limit of $4n^2$, where a 600 nm thick nanowire layer could approach the 3 μm thickness found in the bulk InGaN design. However, the index of refraction difference between polyimide and InGaN leads to a $4n^2$ enhancement factor of approximately 4 and an effective thickness of 2.4 μm. This calculation neglects any sub-wavelength type interference effects of the nanowire ensemble. Thus, a thicker nanowire layer is required.

The visible light absorption from the nanowires can be achieved using InGaN/GaN quantum wells instead of pure InGaN as it is easier to increase the indium composition in the quantum well/dot configuration when compared to bulk-like InGaN. This technique has led to promising quantum efficiencies in InGaN/GaN quantum well solar cells[227] with quantum efficiencies over 70%, and solar cells with 35% indium quantum wells for power conversion efficiencies of over 3% in concentrated sunlight[228]. Quantum well solar cells can also provide increased absorption to overcome the small losses of operating voltages[229] when compared to bulk devices. This route has additional the benefit of using GaN as the host material and hence generally improved material quality and mature growth techniques. Current quantum well solar cells unfortunately usually do not produce high quantum efficiency throughout the range of their spectral response. Polarization effects and material quality generally prevent carriers from being collected efficiently over the entire quantum well region. Further research on improving hole transport in high indium InGaN quantum wells while leveraging polarization effects is required to make such designs feasible. In addition, the use of InGaN nanowires grown on a transparent substrate like sapphire can provide a straightforward way to measure the absorption of the nanowire layer.

6.6 SUMMARY

In summary, a dual-junction solar cell was designed and simulated using Crosslight APSYS. Absorption coefficients were obtained from experimental data from similar InGaN alloy compositions. Absorption coefficients were shifted slightly in wavelength to correspond to $In_{0.52}Ga_{0.48}N$ with a corresponding bandgap of 1.66 eV. A silicon solar cell was initially designed and optimized with an efficiency of 22% using typical non-recombination rates in monocrystalline silicon. An InGaN subcell was designed to be roughly current-matched on top of the silicon subcell and the overall dual junction efficiency was optimized by varying the thicknesses of both subcells and the indium composition of the top subcell. The best dual junction cell design features a slightly overproducing silicon subcell to compensate for the

lower fill factor of the *p-i-n* InGaN top subcell. Routes to extend the model to a nanowire top subcell are discussed and rely on assessing the absorption characteristics of a dense ensemble of randomly positioned and formed InGaN nanowires. As the nanowires are strong and uniform scatters of light, the upper $4n^2$ limit of pure Lambertian scattering is used to infer that the nanowire layer should be at least 800 nm thick to demonstrate sufficient absorption.

Part III

SUMMARY AND APPENDIX

7

DISCUSSION AND CONCLUSIONS

7.1 SUMMARY

The InGaN/GaN nanowire material system is a unique approach towards high performance optoelectronic devices based on silicon. The large tunability of the InGaN alloy enables devices to operate from the ultraviolet to the infrared. For solar cells, this is a highly desirable property where high efficiency solar cells still rely on a multitude of different materials with expensive substrates. The nanowire growth mode also enables the growth of stacked quantum dots, increasing and broadening the absorption spectrum farther into the infrared and even providing a means towards realizing intermediate band solar cells with large bandgaps on inexpensive substrates. Using the cost-effectiveness of silicon and the tunability of the InGaN, the nanowire platform has multiple advantages unmatched by other material systems.

In this thesis, quantum dot-in-nanowire solar cells were grown on silicon (111). Extensive microscopy was performed on fabricated and unfabricated nanowires samples. Dense randomly positioned "forests" of nanowires were observed with some height variation and non-uniformity in diameter owing to nanowire coalescence. The nanowire composition was confirmed with energy dispersive X-ray spectroscopy using a scanning electron microscope, where indium in the middle of the nanowires was detected. Hexagonal shapes, as well as quantitative height variation of the nanowires were confirmed with atomic force microscopy.

A photoluminescence spectroscopy system was constructed for the purposes of studying the optical properties of the quantum dots inside the nanowires. The emission from the quantum dots was measured with and without an AlGaN shell demonstrating that the improved passivation at the surface improves the photoluminescence and hence reduces the non-radiative recombination in nanowires. The photoluminescence revealed a broad spectrum of emitted light from 500 nm to 750 nm with a 405 nm incident beam. The cryostat was modified to include electrical probes that can apply a voltage cross individual nanowire solar cells and LEDs. The electroluminescence was shown to increase dramatically with lower temperatures, peaking at around 200 K and then decreasing to 78 K. The quantum efficiency of the nanowires was measured as a function of wavelength and beam intensity demonstrating sub-bandgap current generation, although with poor efficiency of less than 0.1%. This corresponds to a quantum well solar cell with very deep wells. The current-voltage characteristics were measured using a solar simulator at varying intensities. Both the specular and diffuse reflectivities were measured on fabricated and unfabricated nanowire cells as a function of wave-

length, demonstrating a very low reflectivity without an explicit anti-reflection coating.

Computer-aided simulations were performed to simulate the performance of a solar cell and LED-based on the quantum dots and quantum wells and their coupling and composition inside a GaN junction. Crosslight® APSYS was used to perform the drift-diffusion simulations coupled with quantum well and dot nanostructures. Nanowires were approximated as bulk structures with no reflectivity. Quantum dots were approximated as quantum wells for the purposes of the solar cell simulations. When operating as LEDs, the emission spectrum was fitted to experimental data, suggesting the indium composition was a distribution centred around 42%. Two coupling models between quantum wells were implemented according to the carrier transport regime between InGaN quantum dots. In a miniband model that assumes very long carrier lifetimes, the quantum efficiency was calculated at over 90% extending to about 650 nm with more than 80 quantum wells. This provides an idea into how many wells are required for realizing intermediate band operation. The coupling between neighbouring quantum wells was assessed by calculating the quantum well subbands energy levels and their penetration into the barriers as a function of barrier thickness. This provided insight into the optimal barrier and well thicknesses that can enable miniband transport. This is expected to improve hole transport across the multiple quantum dot region.

7.2 TOWARDS IMPROVED INTERMEDIATE BAND OPERATION

It is clear that the nanowires studied in this thesis function well as LEDs but are not very suitable solar cells in their current design. The solar cells demonstrated efficiencies lower than 0.1%, rather than up to roughly 10% in theory based on the modelled absorption from the quantum dots. The characterization and modelling performed in this thesis has revealed that while InGaN/GaN nanowires on silicon can produce sub-bandgap current generation, the design of the nanowire and quantum dots within can be modified to greatly enhance the performance. Despite a high figure of merit for InGaN/GaN systems, the nanowire solar cells suffer from design limitations and high performance nonuniformity across the area of the nanowire device. In addition, the absorption is insufficient for a high efficiency device since the optical depth at visible wavelength is quite low.

The as-grown quantum-dot-in-nanowire devices have fairly decoupled quantum dot states, which could benefit from increased coupling to promote carrier transport. The indium composition in the dots and bulk nanowire, while high, is not enough to correspond to the optimal direct and intermediate state transition energies according to detailed balance calculations. In addition, quantum efficiency calculations show that subbandgap absorption is not nearly high enough with only 10 quantum dots. To address these issues and realize the potential of such designs, the following changes are sug-

gested for future InGaN/GaN quantum dot-in nanowire intermediate band solar cells:

- Thin quantum dots (~1 nm) to reduce carrier-retrapping and allowing for more quantum dots per nanowire
- Thin barriers between dots (~1.5 nm) to promote miniband conduction of carriers through the barriers
- Increase indium composition in entire nanowire to suit the solar spectrum
- Increase quantum dot count to increase absorption
- Optimize nanowire diameter and spacing for efficient light trapping/concentration

In addition to these design changes, the following challenges remain in the growth and fabrication of the nanowire devices:

- Improved surface passivation for improved open circuit voltage
- Consistent nanowire morphology for less resistive losses and increased nanowire participation
- More uniform quantum dot indium compositions for improved transport and less thermalization losses
- Control over polarization charge screening for recombination reduction and improved transport

There are multiple interesting avenues for future research and development of InGaN/GaN intermediate band solar cells. Such efforts can be divided into two main strategies.

7.2.1 *Growth and Fabrication challenges*

The first strategy involves addressing the growth and fabrication issues which restrict the efficient operation of high indium InGaN alloys to levels significantly below their potential. Indium segregation continues to be an issue that has been improved to some degree with InGaN/GaN quantum well/dot structures, low temperature growth conditions, and nanowire configurations. All the aforementioned techniques are employed in realizing the nanowires grown in this thesis. In the case of nanowire devices, the numerous benefits to their design tend to be hindered by the lack of uniformity in both planarity and resistivity. The large variance in the resistivity between nanowires of different geometries and proximity to the indium tin oxide and contacts leads to nanowires which demonstrate such high resistivity when compared to nearby nanowires that they are effectively inactive. Scanning electron microscopy of the nanowires themselves reveals large variations in diameter, height, and connectivity to other nanowires which can lead to difficulty in ensuring that the

p-type tops of the nanowires avoid contact to the *n*-type regions of other nanowires with polyimide while making low resistivity ohmic contacts to the ITO layer. Microelectroluminescence imaging in this thesis has shown that the nanowire solar cells are inconsistently participating in electron and hole transport in the quantum dot region. Obtaining a more uniform luminescence from nanowires is crucial in delivering large area devices which on average perform efficiently.

The very low open-circuit voltage of the fabricated cells indicates that there is significant non-radiative recombination in the nanowires. There are multiple potential causes that originate from the nanowires themselves, such as poor transport of photo-generated carriers across the quantum dot region, non-radiative recombination at the nanowire surfaces, and the silicon/GaN interface. The increased recombination from the quantum dots contributes to the poor device performance, but only as a result of the unoptimized carrier transport characteristics.

7.2.2 *Design Optimizations*

The second strategy involves modifying the design of the as-studied InGaN/GaN quantum-dot-in-nanowire solar cells to better suit the collection of electrons and holes. The current nanowire design is optimized primarily for light generation through electroluminescence where ensuring the electron and hole radiatively combine as often as possible is the priority. In LEDs, carriers are pushed towards each other with increasing forward bias that can be stronger than the built-in field required for *p-i-n* solar cell operation.

The primary modifications involve the thickness of the quantum dots and barriers. It has been shown that in thinner quantum dots or wells carrier escape is more likely[230], which is essential for an intermediate band solar cell. Ideally, the carrier escape is through optical means, but thermionic or tunneling escape is still preferable to non-radiative recombination. In addition, while lifetimes are usually higher with larger wells, the effect reverses in ultra-thin quantum wells[231]. With narrower wells the number of confined states decreases, which can affect the photofilling of the intermediate band. The barriers should also be sufficiently thin to enable miniband conduction despite the deep wells yet thick enough to prevent high trapping rates for carriers in the extended GaN states. The optimal thickness for 40% indium quantum dots seems to be about 1 nm for quantum dots, and 1.5 nm for GaN barriers to support miniband conduction of electrons. Slightly thinner barriers are required for miniband conduction of holes. More sophisticated measurements or simulations of the re-trapping rate as a function of the electric field, well/barrier dimensions and indium composition are required to determine the optimal intermediate band solar cell design.

The host material has been shown to have about 5-10% indium in some nanowires[190], which can in principle be extended to contain more indium to approach 2.1 eV for the nanowire and 0.7 eV for

the quantum dots. This bandgap leads to a higher theoretical power conversion efficiency of the AM1.5G spectrum in intermediate band solar cell operation.

Photofilling is another aspect of intermediate band solar cells that is not covered in this thesis. The theoretical study of the quantum dot nature in the nanowires and their confined states provides an estimate of the density of states available in the system. While such a solar cell operates most efficiently when the intermediate band is half full, it depends on sunlight concentration, band position, capture cross-sections for recombination events, quantum dot coupling, and carrier trapping and escape rates. Most of these parameters are still not very well known or easy to control in fabricated InGaN/GaN quantum dot systems. Future research can investigate the parameter space which can provide a consistent half-filled intermediate band in a coupled quantum dot system.

The polarization direction of the nanowires is another factor that greatly affects the potential of the InGaN/GaN platform for solar cell operation. With the *p-i-n* junction configuration, N-face GaN orientations seem to provide a much lower energy barrier and at each end of the multiple quantum well region for improved carrier transport. This energy barrier decreases with additional screening in Ga-face devices, so designs which are more-n-polar (as these nanowires are) improve the quantum efficiency.

Future work involves tailoring the InGaN/GaN quantum dot-in-nanowire on silicon material system towards improved photovoltaic operation. For intermediate band solar cells, the growth of optimized superlattice parameters is required. Since sub-bandgap current generation is substantially increased under concentrated sunlight, characterization of samples with sunlight intensities up to 1000 suns with a flash solar simulator may reveal effects related to photofilling effects of the intermediate band. The quantum efficiency change as a function of temperature would be a very insightful measurement to perform, where the nonradiative recombination rates can be inferred based on the effect of reduced temperature. With the successful demonstration of electroluminescence from six-junction nanowires, multijunction solar cells built from nanowires on silicon can be investigated as a cost-effective route towards high efficiency solar cells.

Possible computational/theoretical efforts include the detailed balance calculations of InGaN/GaN intermediate band solar cells which feature design parameters from the dot-in-nanowire material system. Models which include the finite intermediate band widths that correspond to the distribution of quantum dot states, valence band to valence band transition events, and experimentally determined carrier capture and escape transition rates will lead to more attainable performance results from simulations. An extension to the quantum efficiency calculations in Chapter 5 can be done to estimate the maximum quantum efficiency in true intermediate band solar cells by modelling the conduction band quasi-Fermi level as separate from the intermediate band. This can provide insight into the photofilling

and the additional inter-subband absorption characteristics that occur in intermediate band solar cells.

In conclusion, this thesis investigates the InGaN/GaN quantum dot-in-nanowire on silicon platform towards high efficiency solar cells. The platform demonstrates significant promise for an intermediate band solar cell or multijunction configurations on silicon. The platform introduces unparalleled flexibility in many aspects of device design. The intermediate band energy, absorption, substrate, bulk band gaps, reflectivity and transport properties can all be tuned for the most desirable properties.

The morphology of the nanowires was assessed using a variety of microscopy techniques. The current voltage characteristics were measured under a solar simulator accounting for spectral mismatch. Strong luminescence is observed from both photoluminescence and electroluminescence spectroscopy. Sub-bandgap absorption is demonstrated up to nearly 700 nm from quantum efficiency measurements. The typical light biasing condition required for sub-bandgap current generation does not seem to be required to produce current from below the band gap of GaN. This suggests a complex interaction between carrier transport and incident light that requires further study to fully understand. Simulations of quantum well solar cells were performed using Crosslight® APSYS using two types of carrier transport models for solar cell operation. The structure was also simulated as an LED with the luminescence fitted to experimental data to extract average indium compositions and transition energies. The introduction of polarization provided insight into how growth conditions can be tailored to promote charge separation and how the polarization screening affects transition energies.

APPENDIX A: SIMULATION SCRIPTS

The modelling of InGaN/GaN quantum dot and quantum well devices in this thesis uses the drift-diffusion simulations coupled with additional models that address the nanostructured active regions. This appendix lists and discusses the scripts used to produce the simulations results.

A.1 INGAN GAN QUANTUM WELL LAYER STRUCTURE: MINIBAND MODEL

Below is the Crosslight APSYS script to calculate InGaN/GaN multiple quantum well miniband solar cell quantum efficiencies and current-voltage characteristics.

Script 1: InGaN/GaN quantum well layer structure: Miniband model

```
$ ----
begin_layer
$
$independent_mqw
column column_num=1 w=10  mesh_num=3  r=1.
top_contact column_num=1 from=0.0 to=10.0 contact_num=2
bottom_contact column_num=1 from=0.0 to=10.0 contact_num=1
$
layer_mater macro_name=ingan column_num=1 var_symbol1=x var1=0
    n_doping=5.e24
layer d=0.1 n=8   r=0.8
layer_position  label=bot  location=bottom
layer_position  label=before_well delta_y_from_top=0.02
$ ----
include file=solar.bar
include file=solar40.qw
include file=solar.bar
include file=solar40.qw
include file=solar.bar
include file=solar40.qw
include file=solar.bar
include file=solar40.qw
include file=solar.bar
include file=solar40.qw
include file=solar.bar
include file=solar40.qw
include file=solar.bar
include file=solar40.qw
include file=solar.bar
include file=solar40.qw
include file=solar.bar
include file=solar40.qw
include file=solar.bar
```

```
include file=solar40.qw

$ ----
$
layer_position  label=after_well delta_y_from_top=-0.02
layer_mater macro_name=ingan column_num=1 var_symbol1=x var1=0
    p_doping=2.5e24
layer d=0.05 n=8  r=1.2
layer_position  label=top  location=top
$
end_layer
```

A.1.1 *InGaN GaN quantum well file: Miniband model*

Script 2: InGaN/GaN quantum well file (`listings` manual)

```
$
layer_mater macro_name=ingan column_num=1 &&
  active_macro=InGaN/InGaN avar1=0.4 avar2=0.0 &&
  avar_symbol1=xw avar_symbol2=xb
layer d=0.003 n=3  r=1
```

A.1.2 *InGaN GaN barrier file: Miniband model*

Script 3: InGaN/GaN barrier file (`listings` manual)

```
layer_mater macro_name=ingan column_num=1 var_symbol1=x var1=0
layer d=0.003 n=3  r=1
```

A.1.3 *InGaN GaN quantum well solution file: Miniband model*

Script 4: InGaN/GaN quantum well solution file: Miniband model

```
$file:solar.sol
$ *******
begin
$use_macrofile macro1=my.mac
load_mesh mesh_inf=solar.msh
output sol_outf=solar.out
more_output light_reflection = yes elec_mobility = yes
    hole_mobility = yes &&
elec_conc_subb=5 hole_conc_subb=5 space_charge=yes &&
trap_information=yes

$ *******
include file=solar.doping
include file=solar.mater
set_active_reg  tau_scat=0.5e-13
```

```
$import_gain_data
$band_gap value=3.4 mater=1
$band_gap value=1.97 mater=2
lifetime_n value=1e-3 mater=1
lifetime_n value=1e-3 mater=2
lifetime_p value=1e-3 mater=1
lifetime_p value=1e-3 mater=2
electron_mobility value=1e-2 mater=1
electron_mobility value=1e-2 mater=2
hole_mobility value=1e-2 mater=1
hole_mobility value=1e-2 mater=2
bandgap_optical_gen allowed=yes bandgap_gen_iqe=1

$effective_miniband_model mater1=1 mater2=2 yrange=(0.103 0.160)
    $10 wells

front_reflection power_transmission=0.99
$light_power spectrum_file=solarvisiblemr.am15g light_dir=top
$light_power incident_power=1 wavelength=1.35
$
index_spectrum spectrum_file=index_GaAs.dat mater=1
index_spectrum spectrum_file=index_In40GaN.dat mater=2
back_reflection power_transmission=0.90
$
newton_par damping_step=5. max_iter=100 print_flag=3
equilibrium
newton_par damping_step=5. print_flag=2 var_tol=1.e-1 res_tol=1.e
    -1 &&
    max_iter=100 opt_iter=15 stop_iter=80 change_variable=no &&
  turnoff_update_lightprof=yes
scan var=light value_to=1 print_step=100. &&
  init_step=1.e-10 min_step=1.e-16 max_step=10 $&&
$var2=time value2_to=100
$-------------------------------------------------$
$ EQE scan
$-------------------------------------------------$
newton_par damping_step=5 rate_damp=5e-4 var_tol=5.e-0 res_tol=5.
    e-0 &&
max_iter=80 opt_iter=20 stop_iter=70 print_flag=2 &&
change_variable=yes recover_prev_mqw=yes extrapolate= yes &&
  turnoff_update_lightprof=yes mf_solver=3
scan var=wavelength_scan value_to=0.7 &&
init_step=0.001 min_step=1e-6 max_step=0.002
light_power wavelength=0.25 incident_power=1

end
```

A.1.4 *InGaN GaN quantum well plotting file: Miniband model*

Script 5: InGaN/GaN quantum well plotting file: Miniband model

```
$file:solar.plt
begin_pstprc
```

```
plot_data plot_device=postscript
$$-----EQUILIBRIUM -------$$
get_data  main_input=solar.sol &&
  sol_inf=solar.out &&
  xy_data=[  1  1] $scan_data=[1   1]
plot_multilayer_optics variable = transmission wavelength_range =
     [0.3,0.8] &&
data_file =trans.dat1
plot_multilayer_optics variable = reflection   wavelength_range =
     [0.3,0.8] &&
data_file =reflec.dat1
plot_multilayer_optics variable = absorption  wavelength_range =
     [0.3,0.8] &&
data_file=absorp.dat1

plot_1d variable=band  y_from_label=bot y_to_label=top &&
data_file=band-in40-eq.dat1
plot_1d variable=optical_gen &&
  y_from_label=bot  y_to_label=top data_file=optgen-in40-eq.dat1

 plot_1d variable=band  y_from_label=before_well  y_to_label=
     after_well &&
 data_file=band-wells-in40-eq.dat1

 plot_1d variable=potential y_from_label=bot y_to_label=top &&
data_file=potential-in40-eq.dat

$plot_1d variable=subb_elec_conc y_from_label=bot y_to_label=top
     &&
$data_file=subb-elec-conc-eq.dat
$
$plot_1d variable=subb_hole_conc y_from_label=bot y_to_label=top
     &&
$data_file=subb-hole-conq-eq.dat
$
$plot_1d variable=tunnel_enhancement y_from_label=bot &&
$y_to_label=top  &&
$data_file=tunnel-in40-enhacement-eq.dat

$plot_1d variable=qdot_electron y_from_label=bot y_to_label=top
    &&
$data_file=qdot-electron-eq.dat
$plot_1d variable=qdot_hole y_from_label=bot y_to_label=top  &&
$data_file=qdot-hole-eq.dat

plot_1d variable=all_conc y_from_label=bot y_to_label=top  &&
data_file=carrier-in40-conc-eq.dat

plot_1d variable=field_y y_from_label=bot y_to_label=top  &&
data_file=field-in40-eq.dat

plot_1d variable=space_charge y_from_label=bot y_to_label=top  &&
data_file=space-charge-in40-eq.dat

plot_1d variable=trap_conc y_from_label=bot y_to_label=top  &&
data_file=trap-conc-in40-eq.dat
```

```
$plot_1d variable=trap_level y_from_label=bot y_to_label=top  &&
$data_file=trap-level-in40-eq.dat

$$-----AFTER LIGHT IS ON -------$$
get_data  main_input=solar.sol &&
  sol_inf=solar.out &&
  xy_data=[ 2  2] $scan_data=[2   2]
plot_1d variable=band &&
  y_from_label=bot  &&
 y_to_label=top data_file=band-in40-light.dat1

plot_1d variable=optical_gen &&
  y_from_label=bot &&
  y_to_label=top data_file=optgen-in40-light.dat1

plot_1d variable=band &&
  y_from_label=before_well y_to_label=after_well &&
  data_file=band-in40-light-wells.dat1 $cond_subband=1
      val_subband=1

  plot_1d variable=recomb_srh &&
  y_from_label=before_well   y_to_label=after_well data_file=srh.
      dat1

plot_1d variable = elec_imref y_from_label = before_well  &&
    y_to_label = after_well data_file = elec-imref-light.dat1

  plot_1d variable = hole_imref y_from_label = before_well  &&
    y_to_label = after_well data_file = hole-imref-light.dat1

plot_1d variable=recomb_rad &&
  y_from_label=before_well   y_to_label=after_well data_file=rad.
      dat1

 plot_1d variable=recomb_aug &&
  y_from_label=before_well   y_to_label=after_well data_file=
      auger.dat1

plot_1d variable=all_conc &&
  y_from_label=before_well   y_to_label=after_well  data_file=
      conc-light.dat1

plot_1d variable = linear_elec_conc y_from_label = before_well
    &&
    y_to_label = after_well data_file = elec_conc-light.dat1

plot_1d variable = linear_hole_conc y_from_label = before_well
    &&
    y_to_label = after_well data_file = hole_conc-light.dat1

    plot_1d variable = rec_elec_conc y_from_label = before_well
        &&
    y_to_label = after_well data_file = rec_elec_conc-light.dat1

plot_1d variable = rec_hole_conc y_from_label = before_well  &&
```

```
    y_to_label = after_well data_file = rec_hole_conc-light.dat1
102
plot_1d variable = trapped_elec_conc y_from_label = before_well
    &&
    y_to_label = after_well data_file = trapped_elec_conc-light.
        dat1

$plot_1d variable = trapped_hole_conc y_from_label = before_well
     &&
107 $    y_to_label = after_well data_file = trapped_hole_conc-light.
    dat1

plot_1d variable = linear_bulk_elec y_from_label = before_well
    &&
    y_to_label = after_well data_file = bulk_elec_conc-light.dat1

112 plot_1d variable = linear_bulk_hole y_from_label = before_well
    &&
    y_to_label = after_well data_file = bulk_hole_conc-light.dat1

$plot_1d variable=field_mag &&
$  y_from_label=before_well y_to_label=after_well  data_file=
    field.dat1
117
plot_1d variable=total_curr_mag &&
  y_from_label=before_well y_to_label=after_well  data_file=
      current.dat1
$
$plot_1d variable=tunnel_enhancement &&
122 $  y_from_label=before_well   y_to_label=after_well  &&
$  data_file=tunneling.dat1

plot_1d variable=elec_mobility &&
  y_from_label=bot  y_to_label=top  &&
127  data_file=elec_mobility-light.dat1

plot_1d variable=hole_mobility &&
  y_from_label=bot   y_to_label=top  &&
 data_file=hole_mobility-light.dat1
132
  plot_1d variable=elec_curr_y y_from_label=bot y_to_label=top
      &&
data_file=electron-current.dat

$plot_1d variable=elec_curr_mag y_from_label=bot y_to_label=top
    &&
137 $data_file=electron-current-mag.dat

plot_1d variable=hole_curr_y y_from_label=bot y_to_label=top  &&
data_file=hole-current.dat

142 $plot_1d variable=hole_curr_mag y_from_label=bot y_to_label=top
    &&
$data_file=hole-current-mag.dat

plot_1d variable=field_y y_from_label=bot y_to_label=top  &&
```

```
data_file=field-light.dat
147
plot_1d variable=potential y_from_label=bot y_to_label=top  &&
data_file=potential-light.dat

$plot_1d variable=subb_elec_conc y_from_label=bot y_to_label=top
     &&
152 $data_file=subb-elec-conc.dat
$
$plot_1d variable=subb_hole_conc y_from_label=bot y_to_label=top
     &&
$data_file=subb-hole-conc.dat
$
157 plot_1d variable=space_charge y_from_label=bot y_to_label=top  &&
data_file=space-charge-in40.dat

$plot_1d variable=trap_conc y_from_label=bot y_to_label=top  &&
$data_file=trap-conc-in40.dat
162
plot_1d variable=trap_level y_from_label=bot y_to_label=top  &&
data_file=trap-level-in40.dat

plot_1d variable=interband_pumping y_from_label=bot y_to_label=
    top  &&
167 data_file=interband-pumping-in40.dat


$$-----AT MAX POWER POINT-------$$
$get_data  main_input=solar.sol &&
172 $  sol_inf=solar.out &&
$  xy_data=[35 35] $scan_data=[2   2]
$plot_1d variable=band &&
$  y_from_label=bot  &&
$ y_to_label=top data_file=band-in40-vmax.dat1
177 $
$plot_1d variable=optical_gen &&
$  y_from_label=bot &&
$  y_to_label=top data_file=optgen-in40-vmax.dat1
$
182 $plot_1d variable=band &&
$  y_from_label=before_well y_to_label=after_well &&
$  data_file=band-in40-vmax-wells.dat1 $cond_subband=1
    val_subband=1
$
$  plot_1d variable=recomb_srh &&
187 $  y_from_label=before_well   y_to_label=after_well data_file=srh
    -vmax.dat1
$
$plot_1d variable = elec_imref y_from_label = before_well  &&
$    y_to_label = after_well data_file = elec-imref-vmax.dat1
$
192 $  plot_1d variable = hole_imref y_from_label = before_well  &&
$    y_to_label = after_well data_file = hole-imref-vmax.dat1
$
$plot_1d variable=recomb_rad &&
```

```
$  y_from_label=before_well   y_to_label=after_well data_file=rad
    -vmax.dat1
$
$ plot_1d variable=recomb_aug &&
$  y_from_label=before_well   y_to_label=after_well data_file=
    auger-vmax.dat1
$
$plot_1d variable=all_conc &&
$  y_from_label=before_well   y_to_label=after_well  data_file=
    conc-vmax.dat1
$
$plot_1d variable = linear_elec_conc y_from_label = before_well
    &&
$    y_to_label = after_well data_file = elec_conc-vmax.dat1
$
$plot_1d variable = linear_hole_conc y_from_label = before_well
    &&
$    y_to_label = after_well data_file = hole_conc-vmax.dat1
$
$    plot_1d variable = rec_elec_conc y_from_label = before_well
     &&
$    y_to_label = after_well data_file = rec_elec_conc-vmax.dat1
$
$plot_1d variable = rec_hole_conc y_from_label = before_well  &&
$    y_to_label = after_well data_file = rec_hole_conc-vmax.dat1
$
$plot_1d variable = trapped_elec_conc y_from_label = before_well
     &&
$    y_to_label = after_well data_file = trapped_elec_conc-vmax.
    dat1
$
$$plot_1d variable = trapped_hole_conc y_from_label = before_well
      &&
$$    y_to_label = after_well data_file = trapped_hole_conc-light
    .dat1
$
$plot_1d variable = linear_bulk_elec y_from_label = before_well
    &&
$    y_to_label = after_well data_file = bulk_elec_conc-vmax.dat1
$
$plot_1d variable = linear_bulk_hole y_from_label = before_well
    &&
$    y_to_label = after_well data_file = bulk_hole_conc-vmax.dat1
$
$$plot_1d variable=field_mag &&
$$  y_from_label=before_well y_to_label=after_well  data_file=
    field-mag-vmax.dat1
$
$plot_1d variable=total_curr_mag &&
$  y_from_label=before_well y_to_label=after_well  &&
$  data_file=current-mag-vmax.dat1
$$
$$plot_1d variable=tunnel_enhancement &&
$$  y_from_label=before_well   y_to_label=after_well  &&
$$  data_file=tunneling-vmax.dat1
$$
```

```
$plot_1d variable=elec_mobility &&
$  y_from_label=bot  y_to_label=top  &&
$ data_file=elec_mobility-vmax.dat1
$
$plot_1d variable=hole_mobility &&
$  y_from_label=bot   y_to_label=top  &&
$ data_file=hole_mobility-vmax.dat1
$
$  plot_1d variable=elec_curr_y y_from_label=bot y_to_label=top
    &&
$data_file=electron-current-vmax-vmax.dat
$
$$plot_1d variable=elec_curr_mag y_from_label=bot y_to_label=top
     &&
$$data_file=electron-current-mag-vmax.dat
$
$plot_1d variable=hole_curr_y y_from_label=bot y_to_label=top  &&
$data_file=hole-current-vmax.dat
$
$$plot_1d variable=hole_curr_mag y_from_label=bot y_to_label=top
     &&
$$data_file=hole-current-mag-vmax.dat
$$
$plot_1d variable=field_y y_from_label=bot y_to_label=top  &&
$data_file=field-vmax.dat
$
$plot_1d variable=potential y_from_label=bot y_to_label=top  &&
$data_file=potential-vmax.dat
$
$$plot_1d variable=subb_elec_conc y_from_label=bot y_to_label=top
      &&
$$data_file=subb-elec-conc-vmax.dat
$$
$$plot_1d variable=subb_hole_conc y_from_label=bot y_to_label=top
      &&
$$data_file=subb-hole-conc-vmax.dat
$
$plot_1d variable=space_charge y_from_label=bot y_to_label=top
    &&
$data_file=space-charge-in40-vmax.dat
$
$$plot_1d variable=trap_conc y_from_label=bot y_to_label=top  &&
$$data_file=trap-conc-in40-vmax.dat
$
$plot_1d variable=trap_level y_from_label=bot y_to_label=top  &&
$data_file=trap-level-in40-vmax.dat
$
$plot_1d variable=interband_pumping y_from_label=bot y_to_label=
    top  &&
$data_file=interband-pumping-in40-vmax.dat

$plot_3d variable=potential grid_sizes=100 100 &&
$  point_ll=(0. 0.) point_ur=(99. 0.422) &&
$  xrange=(0 99) yrange=(0. 0.422)
$plot_2d variable=total_curr grid_sizes=100 100 &&
$  point_ll=(0. 0.27) point_ur=(99. 0.35) &&
```

```
$  xrange=(0 99) yrange=(0.27 0.35)
$plot_2d variable=hole_curr grid_sizes=100 100 &&
$  point_ll=(0. 0.) point_ur=(99. 0.422) &&
$  xrange=(0 99) yrange=(0. 0.422)
$plot_2d variable=elec_curr grid_sizes=100 100 &&
$  point_ll=(0. 0.) point_ur=(99. 0.422) &&
$  xrange=(0 99) yrange=(0. 0.422)

$$ -------------------------------------$$
$$               Plot Voltage
$$-------------------------------------$$
$get_data  main_input=solar.sol &&
$  sol_inf=solar.out &&
$scan_data=[3  38]
$
$plot_scan scan_var=voltage_2 xrange=(0 3) user_ylabel=Current_A/
    m &&
$  variable=current_2 yrange=(0  0.0002) data_file=IV.dat1
$
$plot_scan scan_var=voltage_2 xrange=(0 3) user_ylabel=Current_A/
    m2 &&
$scale_vertical=100000 &&
$  variable=current_2 yrange=(0  20) data_file=IV-Am2.dat1
$
$plot_scan scan_var=voltage_2 xrange=(0 3)  user_ylabel=
    Current_mA/cm2 &&
$scale_vertical=10000 variable=current_2 yrange=(0 2) data_file=
    IV-mAcm2.dat1
$$ -------------------------------------$$
$$               Plot EQE
$$-------------------------------------$$
get_data main_input=solar.sol sol_inf=solar.out &&
scan_data=(3 3)
plot_scan xrange=(0.325 1.1) scan_var=wavelength_scan &&
variable=pd_efficiency user_ylabel=EQE data_file=EQE-in40.dat1
end_pstprc
```

A.2 INGAN GAN QUANTUM DOT LAYER FILE: 3D QUANTUM DOT

Script 6: Quantum dot layer file

```
begin_layer
$
$ when we have more than one columns of complex structure,
    indep_xmqw
$ is needed.
column column_num=1 w=0.02 mesh_num=8 r=1. indep_xmqw=yes
column column_num=2 w=0.005 mesh_num=4 r=1. indep_xmqw=yes
layer_mater macro_name=ingan var1=0. var_symbol1=x &&
   active_macro=cx-InGaN avar1=0. avar_symbol1=xw column_num=1
layer_mater macro_name=ingan var1=0. var_symbol1=x &&
   active_macro=cx-InGaN avar1=0. avar_symbol1=xw column_num=2
```

```
layer d=0.003 n=6 r=1
$
$ QW/WL
layer_mater macro_name=ingan var1=0.40 var_symbol1=x &&
   active_macro=cx-InGaN avar1=0.40 avar_symbol1=xw column_num=1
layer_mater macro_name=ingan var1=0.0 var_symbol1=x &&
   active_macro=cx-InGaN avar1=0.0 avar_symbol1=xw column_num=2
layer d=0.003 n=12 r=1

layer_mater macro_name=ingan column_num=1 var_symbol1=x var1=0 &&
   active_macro=cx-InGaN avar_symbol1=xw avar1=0
layer_mater macro_name=ingan column_num=2 var_symbol1=x var1=0 &&
   active_macro=cx-InGaN avar_symbol1=xw avar1=0
layer d=0.003 n=6 r=1.
end_layer
```

A.2.1 *InGaN GaN quantum dot gain file: 3D quantum dot*

Script 7: Quantum dot layer file

```
$file:gan.gain
$*****************************************
begin_gain
use_macrofile macro1=my.mac
plot_data plot_device=postscript
include file=dot.mater

set_active_reg  tau_scat=0.5e-13 qw_print=2 fd_mesh=300

sparse_eigen_solver use_mf=yes

self_consistent
band_distance data_point=300 data_file=band-dot.dat

gain_module  apply_e_field=0 tilt_imref=no
$band_distance
sp.rate_wavel wavel_range=(0.35 0.90) pn_ratio=0.5 &&
 conc_range=(1.e22 1.e25)  curve_number=8 data_point=300 &&
data_file=spon-dot.dat
gain_wavel wavel_range=(0.35 0.90) pn_ratio=0.5 &&
  conc_range=(1.e22 1.e25)  curve_number=8 data_point=300 &&
data_file=gain-dot.dat

export_gain_data
$
end_gain
```

A.2.2 *InGaN GaN quantum dot solution file: 3D quantum dot*

Script 8: Quantum dot solution file

```
begin
load_mesh  mesh_inf=dot.msh  zseg_num=1
output  sol_outf=dot.out  zseg_num=1
include  file=dot.mater
include  file=dot.doping

set_active_reg override_barrier

wurtzite_offset_model  use_strained_bandgap=yes
    partition_hydro_term=yes

cylindrical

wave_boundary point_ll=(0. 0.) point_ur=(0.025 0.009)
init_wave init_wavel=0.6
multimode mode_num=20 boundary_type1=(2 1 1 1) boundary_type2=(1
    1 1 1)
direct_eigen

solve_lateral_wave quantum_wave=yes cond_valley=1 val_valley=1 &&
  export_data=dot.qdd
$solve_lateral_wave quantum_wave=yes cond_valley=1 val_valley=2
    &&
$  export_data=dot2v2.qdd
$solve_lateral_wave quantum_wave=yes cond_valley=1 val_valley=3
    &&
$  export_data=dot3v3.qdd
$
end
```

A.2.3 *InGaN GaN quantum dot plotting file: 3D quantum dot*

Script 9: Quantum dot plotting file

```
$file:dot.plt
begin_pstprc
plot_data plot_device=postscript
get_data  main_input=dot.sol &&
  sol_inf=dot.out &&
  xy_data=[  1  1] scan_data=[1   1]

plot_1d variable=band from=(0.010 0.) to=(0.010 0.009) data_file=
    dotbandi.dat
plot_1d variable=band from=(0.023 0.) to=(0.023 0.009) data_file=
    dotbando.dat

$plot_2d variable=wave_intensity_all_modes level=20
plot_2d variable=wave_intensity mode_index=1 data_file=state1.dat
      level=30
$plot_2d variable=wave_intensity mode_index=2 data_file=state2.
    dat  level=30
```

```
$plot_2d variable=wave_intensity mode_index=3 data_file=state3.
    dat  level=30
$plot_2d variable=wave_intensity mode_index=4 data_file=state4.
    dat   level=30
$plot_2d variable=wave_intensity mode_index=5 data_file=state5.
    dat  level=30
$plot_2d variable=wave_intensity mode_index=6 data_file=state6.
    dat  level=30
$plot_2d variable=wave_intensity mode_index=7 data_file=state7.
    dat  level=30
$plot_2d variable=wave_intensity mode_index=8 data_file=state8.
    dat  level=30
$plot_2d variable=wave_intensity mode_index=9 data_file=state9.
    dat  level=30
$plot_2d variable=wave_intensity mode_index=10 data_file=state10.
    dat  level=30

extract_contour variable=wave_intensity at_fraction=0.5


end_pstprc
```

A.3 INGAN GAN QUANTUM DOT LED LAYER FILE: QUANTUM DOT LED

Script 10: InGaN/GaN quantum dot LED layer file

```
$ ----
begin_layer
$
$independent_mqw
column column_num=1 w=100.0  mesh_num=2  r=0.85
top_contact column_num=1 from=0.0 to=100.0 contact_num=2
bottom_contact column_num=1 from=0.0 to=100.0 contact_num=1
$
$
layer_mater macro_name=ingan  var1=0.0 column_num=1 var_symbol1=x
    &&
n_doping=1.e25
layer d=0.3  n=10   r=1

$ ----
layer_position  label=bot  location=bottom
layer_position  label=before_well  location=top

layer_mater macro_name=ingan var1=0.0 column_num=1 var_symbol1=x
layer d=0.003 n=4  r=1

include file=ganled.qw
include file=ganled.qw
include file=ganled.qw
include file=ganled.qw
include file=ganled.qw
```

```
27
include file=ganled.qw
include file=ganled.qw
include file=ganled.qw
include file=ganled.qw
32 include file=ganled.qw

$ ----
$
layer_position  label=after_well  location=top
37 layer_mater macro_name=ingan var1=0.0 column_num=1 var_symbol1=x
    &&
p_doping=5.e25
layer d=0.27 n=10  r=1
layer_position  label=top  location=top
$
42 end_layer
```

A.3.1 *InGaN GaN quantum well/dot layer file: Quantum dot LED*

Script 11: InGaN/GaN quantum well/dot layer file

```
$
2 layer_mater macro_name=ingan var1=0.01 column_num=1 &&
  var_symbol1=x &&
  active_macro=InGaN/InGaN  avar1=0.01 avar2=0.0 &&
  avar_symbol1=xw avar_symbol2=xb

7 qdot_layer_mater macro_name=ingan active_macro=cx-InGaN &&
  var_symbol1=x avar_symbol1=xw var1=0.300 avar1=0.300 &&
  column_num=1 height=0.003

layer d=0.003 n=4  r=1
12 $
layer_mater macro_name=ingan var1=0.0 column_num=1 var_symbol1=x
layer d=0.003 n=4  r=1
```

A.3.2 *InGaN GaN quantum dot LED solution file: Quantum dot LED*

Script 12: InGaN/GaN quantum dot LED solution file

```
$file:ganled.sol
$ *******
begin
5 load_mesh mesh_inf=ganled.msh
output sol_outf=ganled.out
more_output nonlocal_current=yes qw_states=yes  &&
hole_conc_subb=10 elec_conc_subb=10
$ *******
10 include file=ganled.doping
include file=ganled.mater
```

```
temperature temp=300

set_wavelength wavelength=0.650 backg_loss=1000
led_simple wavelength=0.650 spectrum_num=200 photon_recycle=yes
    &&
delta_wavel=0.3

$wurtzite_offset_model use_strained_bandgap=yes


$polarization_charge_model screening=0.5 vector=(0 1 0)

modify_qw tail_energy=0.03 $kp_bands=4 kp_pot_sym=no
modify_wurtzite mass_model=average

$self_consistent $wave_range=0.005
set_active_reg  tau_scat=0.5e-13 $axial_approx=yes valence_mixing
    =yes &&
$bandgap_renorm=yes

qdot_material surface_density=1e14 mater_active=2 coupled_dots=1
    &&
  tau_broaden=0.60e-14 import_dir=dot import_qdot_data=dot.qdd &&
  tau_broaden2=0.60e-14 import_dir2=dot1 import_qdot_data2=dot.
      qdd &&
  tau_broaden3=0.60e-14 import_dir3=dot2 import_qdot_data3=dot.
      qdd &&
  tau_broaden4=0.60e-14 import_dir4=dot3 import_qdot_data4=dot.
      qdd &&
  weight=100 weight2=100 weight3=100 weight4=100
$

$--------------------NON-LOCAL TRANSPORT------------------$
q_transport

$
$ MAIN SOLVER
$
newton_par damping_step=5. max_iter=100 print_flag=3 var_tol=1.e
    -5
equilibrium

newton_par damping_step=5. print_flag=2 var_tol=1 res_tol=2 &&
    max_iter=200 opt_iter=150 stop_iter=180 extrapolate=yes &&
    change_variable=yes

$--------------------TURN ON LED-------------------$
scan var=voltage_1 value_to=-2.4 print_step=0.5 &&
  init_step=0.1 min_step=1.e-10 max_step=2.5 $&&
  $var2=time value2_to=1.0

newton_par damping_step=5. print_flag=2 var_tol=1 res_tol=2 &&
    max_iter=150 opt_iter=50 stop_iter=120 extrapolate=yes &&
    change_variable=no

```

```
scan var=current_1 value_to=44.  print_step=4 &&
  init_step=0.1 min_step=1.e-5 max_step=5.


  $--------------------RAY TRACE-----------------$
$export_raytrace ray3d_convert=yes

end
```

A.3.3 *InGaN GaN quantum dot LED plotting file: Quantum dot LED*

Script 13: InGaN/GaN quantum dot LED plotting files

```
$file:ganled.plt
$ **************
begin_pstprc
plot_data plot_device=postscript


get_data  main_input=ganled.sol sol_inf=ganled.out &&
  xy_data=(1 1)
plot_1d variable=band y_from_label=before_well y_to_label=
    after_well &&
 data_file=band-wells-eq.dat
plot_1d variable=band y_from_label=bot y_to_label=top &&
data_file=band-all-eq.dat

plot_1d variable=potential y_from_label=bot y_to_label=top &&
data_file=potential-eq.dat
plot_1d variable=subb_elec_conc y_from_label=bot y_to_label=top
    &&
data_file=subb-elec-conc-eq.dat
plot_1d variable=subb_hole_conc y_from_label=bot y_to_label=top
    &&
data_file=subb-hole-conq-eq.dat
plot_1d variable=tunnel_enhancement y_from_label=bot y_to_label=
    top  &&
data_file=tunnel-enhacement-eq.dat
$plot_1d variable=qdot_electron y_from_label=bot y_to_label=top
    &&
$data_file=qdot-electron-eq.dat
$plot_1d variable=qdot_hole y_from_label=bot y_to_label=top  &&
$data_file=qdot-hole-eq.dat
plot_1d variable=all_conc y_from_label=bot y_to_label=top  &&
data_file=carrier-conc-eq.dat
plot_1d variable=field_y y_from_label=bot y_to_label=top  &&
data_file=field-eq.dat

get_data  main_input=ganled.sol sol_inf=ganled.out &&
  scan_data=(1 6)

$ convert to A
plot_scan scan_var=voltage_1 variable=current_1 &&
```

```
  data_file=with_q_transp.dat  &&
  scale_vertical=0.0003 &&
  user_ylabel=Current<A> scale_horizontal=-1

plot_scan scan_var=current_1 variable=led_effi &&
  data_file=eff_with_q_transp.dat  &&
  scale_horizontal=0.0003 &&
  user_xlabel=Current<A>

get_data  main_input=ganled.sol sol_inf=ganled.out &&
  xy_data=(6 6)

plot_1d variable=band y_from_label=before_well y_to_label=
    after_well &&
data_file=band4-wells.dat
plot_1d variable=band y_from_label=bot y_to_label=top  &&
data_file=band4-all.dat


plot_1d variable=elec_curr_y y_from_label=bot y_to_label=top  &&
data_file=electron-current.dat
plot_1d variable=elec_curr_mag y_from_label=bot y_to_label=top
    &&
data_file=electron-current-mag.dat
plot_1d variable=hole_curr_y y_from_label=bot y_to_label=top  &&
data_file=hole-current.dat
plot_1d variable=hole_curr_mag y_from_label=bot y_to_label=top
    &&
data_file=hole-current-mag.dat
plot_1d variable=field_y y_from_label=bot y_to_label=top  &&
data_file=field.dat
plot_1d variable=potential y_from_label=bot y_to_label=top  &&
data_file=potential.dat
plot_1d variable=subb_elec_conc y_from_label=bot y_to_label=top
    &&
data_file=subb-elec-conc.dat
plot_1d variable=subb_hole_conc y_from_label=bot y_to_label=top
    &&
data_file=subb-hole-conq.dat
plot_1d variable=tunnel_enhancement y_from_label=bot y_to_label=
    top  &&
data_file=tunnel-enhacement.dat
$plot_1d variable=qdot_electron y_from_label=bot y_to_label=top
    &&
$data_file=qdot-electron.dat
$plot_1d variable=qdot_hole y_from_label=bot y_to_label=top  &&
$data_file=qdot-hole.dat
plot_1d variable=all_conc y_from_label=bot y_to_label=top  &&
data_file=carrier-conc.dat
$-


plot_3d variable=potential grid_sizes=100 100 &&
  point_ll=(0. 0.) point_ur=(99. 0.422) &&
  xrange=(0 99) yrange=(0. 0.422)
plot_2d variable=total_curr grid_sizes=100 100 &&
```

```
  point_ll=(0. 0.27) point_ur=(99. 0.35) &&
  xrange=(0 99) yrange=(0.27 0.35)
plot_2d variable=hole_curr grid_sizes=100 100 &&
  point_ll=(0. 0.) point_ur=(99. 0.422) &&
  xrange=(0 99) yrange=(0. 0.422)
plot_2d variable=elec_curr grid_sizes=100 100 &&
  point_ll=(0. 0.) point_ur=(99. 0.422) &&
  xrange=(0 99) yrange=(0. 0.422)

get_data  main_input=ganled.sol sol_inf=ganled.out &&
  xy_data=(4 17)
led_spectrum scale=1 data_file=Simulated_EL.dat scale_wavelength
    =1000
end_pstprc
```

A.4 INGAN GAN QUANTUM WELL LAYER FILE: COUPLED WELL

Script 14: InGaN/GaN quantum well layer file: Coupled wells

```

$ ----
begin_layer
$
$independent_mqw
column column_num=1 w=10.0  mesh_num=2  r=1.
top_contact column_num=1 from=0.0 to=10.0 contact_num=2
bottom_contact column_num=1 from=0.0 to=10.0 contact_num=1
$
layer_mater macro_name=ingan column_num=1 var_symbol1=x var1=0 &&
n_doping=1.e+25
layer  d=0.27  n=20  r=0.8
layer_position  label=bot  location=bottom
layer_position  label=before_well  location=top
$ ---- QUANTUM WELLS-----$
$
include file=solar.bar
include file=solar40.qw
include file=solar.bar
include file=solar40.qw
include file=solar.bar
include file=solar40.qw
include file=solar.bar
include file=solar40.qw
include file=solar.bar
include file=solar40.qw
include file=solar.bar
include file=solar40.qw
include file=solar.bar
include file=solar40.qw
include file=solar.bar
include file=solar40.qw
include file=solar.bar
```

```
include file=solar40.qw
include file=solar.bar
$
layer_position  label=after_well  location=top
layer_mater macro_name=ingan column_num=1 var_symbol1=x var1=0 &&
p_doping=5.e+24
layer  d=0.2  n=30  r=-1.4
layer_position  label=top  location=top
$
end_layer
```

A.4.1 *InGaN GaN quantum well solution file: Coupled well*

Script 15: InGaN/GaN quantum well solution file: Coupled wells

```
$file:solar.sol
$ *******
begin
load_mesh mesh_inf=solar.msh
output sol_outf=solar.out
more_output light_reflection = yes qw_states=no $elec_mobility =
    yes  &&
$    hole_mobility = yes space_charge=yes
$ *******
include file=solar.doping
include file=solar.mater
$-------------------------------------------------$
$ Lifetimes
$-------------------------------------------------$
$lifetime_n value=1e-13 mater=1
$lifetime_n value=1e-13 mater=2
$lifetime_p value=1e-13 mater=1
$lifetime_p value=1e-13 mater=2
$temperature temp=300
$-------------------------------------------------$
$ Doping
$-------------------------------------------------$
$dopant_ionization_model mater = 1 mott_trans_correction = no
set_active_reg  tau_scat=0.5e-13 $valence_mixing=no axial_approx=
    yes fd_mesh=60
$modify_wurtzite
$self_consistent wave_range=0.005 impose_limit=yes
$modify_qw more_val_energy=1.3 more_cond_energy=1.3 &&
$kp_bands=4 kp88_cond_parab=yes kp_pot_sym=no use_bulkmass=no
    tail_energy=0.03
$import_gain_data
$bandgap_optical_gen allowed=yes bandgap_gen_iqe=1
$q_transport sequential_model=no n_side_down=yes
    optic_pumped_escape=no &&
$optic_pumped_fly=no q_trap_tau=1.e-11
$set_elec_mean_fp=0.01 set_hole_mean_fp=0.01
$effective_miniband_model mater1=1 mater2=3 yrange=(0.503 0.506)
$-------------------------------------------------$
```

```
$ Reflection
$-------------------------------------------------$
front_reflection power_transmission=1.00
$light_power spectrum_file=solarvisiblelr.am15g light_dir=top
$light_power incident_power=1.e4 wavelength=1.35
$
back_reflection power_transmission=0.90
$-------------------------------------------------$
$ Tunneling
$-------------------------------------------------$
$tunneling point_ll=(0., 0.276) point_ur=(10 0.279) &&
$ barrier_type=rectangle trans_broad =no &&
$ broad_width=.2
$
$ start solving
$
newton_par damping_step=5. max_iter=100 print_flag=3
equilibrium
$-------------------------------------------------$
$ Light scan
$-------------------------------------------------$
newton_par damping_step=5. print_flag=2 res_tol=5.e-1 var_tol=5.e
    -1 &&
    max_iter=60 opt_iter=10 stop_iter=40  &&
  turnoff_update_lightprof=yes extrapolate= yes &&
  change_variable=no recover_prev_mqw=no update_mqw=yes
scan var=light value_to=1 print_step=2000. &&
  init_step=1e-3 min_step=1.e-9 max_step=100 $&&
  $var2=time value2_to=100
$
$-------------------------------------------------$
$ EQE scan
$-------------------------------------------------$
newton_par damping_step=5 rate_damp=1e-4 var_tol=1.e-1 res_tol=1.
    e-1 &&
max_iter=100 opt_iter=20 stop_iter=50 print_flag=2 &&
change_variable=yes recover_prev_mqw=no extrapolate= no &&
  turnoff_update_lightprof=no mf_solver=3
scan var=wavelength_scan value_to=0.7 &&
init_step=0.001 min_step=1e-9 max_step=0.002
index_spectrum spectrum_file=index_GaAs.dat mater=1
index_spectrum spectrum_file=index_GaAs.dat mater=2
light_power wavelength=0.25 incident_power=1
$-------------------------------------------------$
$ Voltage scan
$-------------------------------------------------$
$scan var=voltage_2 value_to=2.8 print_step=4.  &&
$  init_step=0.001 min_step=1.e-5 max_step=0.02
$scan var=voltage_2 value_to=0. print_step=4.  &&
$  init_step=0.1 min_step=1.e-5 max_step=0.5
end
```

A.4.2 *InGaN GaN quantum well plotting file: Coupled well*

```
$file:solar.plt
begin_pstprc
plot_data plot_device=postscript
$$-----EQUILIBRIUM -------$$
get_data  main_input=solar.sol &&
  sol_inf=solar.out &&
  xy_data=[  1  1] $scan_data=[1   1]
plot_multilayer_optics variable = transmission wavelength_range =
      [0.3,0.8] &&
data_file =trans.dat1
plot_multilayer_optics variable = reflection   wavelength_range =
      [0.3,0.8] &&
data_file =reflec.dat1
plot_multilayer_optics variable = absorption  wavelength_range =
     [0.3,0.8] &&
data_file=absorp.dat1
plot_1d variable=band &&
  y_from_label=bot &&
 y_to_label=top data_file=band-in40-qw2.dat1
plot_1d variable=optical_gen &&
  y_from_label=bot &&
  y_to_label=top data_file=optgen-in40-qw2.dat1
 plot_1d variable=band  &&
  y_from_label=before_well &&
  y_to_label=after_well
$$-----AFTER LIGHT IS ON -------$$
get_data  main_input=solar.sol &&
  sol_inf=solar.out &&
  xy_data=[ 2  2] $scan_data=[2   2]
plot_1d variable=band &&
  y_from_label=bot  &&
 y_to_label=top data_file=band-in40-qw2-light.dat1
plot_1d variable=optical_gen &&
  y_from_label=bot &&
  y_to_label=top data_file=optgen-in40-qw2-light.dat1
plot_1d variable=band &&
  from=[5 0.24]  to =[0  0.3] &&
  data_file=band-in40-qw2-light-path.dat1 $cond_subband=1
      val_subband=1
plot_1d variable=recomb_srh &&
  y_from_label=before_well &&
  y_to_label=after_well data_file=srh.dat1
plot_1d variable=recomb_rad &&
  y_from_label=before_well &&
  y_to_label=after_well data_file=rad.dat1
 plot_1d variable=recomb_aug &&
  y_from_label=before_well &&
  y_to_label=after_well data_file=auger.dat1
plot_1d variable=all_conc &&
  y_from_label=before_well &&
  y_to_label=after_well  data_file=conc.dat1
plot_1d variable=field_mag &&
  y_from_label=before_well &&
  y_to_label=after_well  data_file=field.dat1
plot_1d variable=total_curr_mag &&
  y_from_label=before_well &&
```

```
  y_to_label=after_well  data_file=current.dat1
plot_1d variable=tunnel_enhancement &&
  y_from_label=before_well &&
  y_to_label=after_well  data_file=tunneling.dat1
$$ -------------------------------------$$
$$               Plot Voltage
$$-------------------------------------$$
$get_data  main_input=solar.sol &&
$  sol_inf=solar.out &&
$scan_data=[4   4]
$
$plot_scan scan_var=voltage_2 xrange=(0 3) user_ylabel=Current_A/
    m &&
$  variable=current_2 yrange=(0  0.0002) data_file=IV.dat1
$
$plot_scan scan_var=voltage_2 xrange=(0 3) user_ylabel=Current_A/
    m2 &&
$scale_vertical=100000 &&
$  variable=current_2 yrange=(0  20) data_file=IV-Am2.dat1
$
$plot_scan scan_var=voltage_2 xrange=(0 3)  user_ylabel=
    Current_mA/cm2 &&
$scale_vertical=10000 variable=current_2 yrange=(0  2) data_file=
    IV-mAcm2.dat1
$$ -------------------------------------$$
$$               Plot EQE
$$-------------------------------------$$
get_data main_input=solar.sol sol_inf=solar.out &&
scan_data=(3 3)
plot_scan xrange=(0.325 0.7) scan_var=wavelength_scan &&
variable=pd_efficiency user_ylabel=EQE data_file=EQE-in40-qw2.
    dat1
end_pstprc
```

A.5 ADDING INGAN GAN QUANTUM WELL POLARIZATION

To enable the polarization charge effects and control the screening, the following script is added to the InGaN/GaN quantum well LED code

Script 16: Adding InGaN/GaN quantum well polarization

```
polarization_charge_model screening=0 vector=(0 -1 0)
self_consistent wave_range=0.01
```

The self-consistent model is required to account for the highly tilted quantum wells potentials.

BIBLIOGRAPHY

[1] M. Asif and T. Muneer. "Energy supply, its demand and security issues for developed and emerging economies." In: *Renewable and Sustainable Energy Reviews* 11.7 (2007), pp. 1388–1413. ISSN: 1364-0321. DOI: https://doi.org/10.1016/j.rser.2005.12.004. URL: http://www.sciencedirect.com/science/article/pii/S1364032106000049.

[2] Susan Solomon et al. "Irreversible climate change due to carbon dioxide emissions." In: *Proceedings of the National Academy of Sciences* (2009). ISSN: 0027-8424. DOI: 10.1073/pnas.0812721106. eprint: http://www.pnas.org/content/early/2009/01/28/0812721106.full.pdf. URL: http://www.pnas.org/content/early/2009/01/28/0812721106.

[3] Marilena Kampa and Elias Castanas. "Human health effects of air pollution." In: *Environmental Pollution* 151.2 (2008). Proceedings of the 4th International Workshop on Biomonitoring of Atmospheric Pollution (With Emphasis on Trace Elements), pp. 362–367. ISSN: 0269-7491. DOI: https://doi.org/10.1016/j.envpol.2007.06.012. URL: http://www.sciencedirect.com/science/article/pii/S0269749107002849.

[4] Hajime Akimoto. "Global Air Quality and Pollution." In: *Science* 302.5651 (2003), pp. 1716–1719. ISSN: 0036-8075. DOI: 10.1126/science.1092666. eprint: http://science.sciencemag.org/content/302/5651/1716.full.pdf. URL: http://science.sciencemag.org/content/302/5651/1716.

[5] Douglas Holtz-Eakin and Thomas M. Selden. "Stoking the fires? CO2 emissions and economic growth." In: *Journal of Public Economics* 57.1 (1995), pp. 85–101. ISSN: 0047-2727. DOI: https://doi.org/10.1016/0047-2727(94)01449-X. URL: http://www.sciencedirect.com/science/article/pii/004727279401449X.

[6] Syukuro Manabe and Richard T. Wetherald. "On the Distribution of Climate Change Resulting from an Increase in CO2 Content of the Atmosphere." In: *Journal of the Atmospheric Sciences* 37.1 (1980), pp. 99–118. DOI: 10.1175/1520-0469(1980)037<0099:OTDOCC>2.0.CO;2. eprint: https://doi.org/10.1175/1520-0469(1980)037<0099:OTDOCC>2.0.CO;2. URL: https://doi.org/10.1175/1520-0469(1980)037%3C0099:OTDOCC%3E2.0.CO;2.

[7] William Shockley and Hans J. Queisser. "Detailed Balance Limit of Efficiency of p-n Junction Solar Cells." In: *Journal of Applied Physics* 32.3 (1961), pp. 510–519. DOI: 10.1063/1.1736034.

[8] Albert Polman and Harry A. Atwater. "Photonic design principles for ultrahigh-efficiency photovoltaics." In: *Nature Materials* 11 (Feb. 2012), pp. 174–177. DOI: 10.1038/nmat3263.

[9] Thomas Elsaesser et al. "Initial thermalization of photoexcited carriers in GaAs studied by femtosecond luminescence spectroscopy." In: *Phys. Rev. Lett.* 66 (13 Apr. 1991), pp. 1757–1760. DOI: 10.1103/PhysRevLett.66.1757. URL: https://link.aps.org/doi/10.1103/PhysRevLett.66.1757.

[10] Shih-Ze Sun et al. "Observation of femtosecond carrier thermalization time in indium nitride." In: *Journal of Applied Physics* 103.12 (2008), p. 123513. DOI: 10.1063/1.2940737.

[11] Marco Bernardi et al. "Ab Initio Study of Hot Carriers in the First Picosecond after Sunlight Absorption in Silicon." In: *Phys. Rev. Lett.* 112 (25 June 2014), p. 257402. DOI: 10.1103/PhysRevLett.112.257402. URL: https://link.aps.org/doi/10.1103/PhysRevLett.112.257402.

[12] A De Vos. "Detailed balance limit of the efficiency of tandem solar cells." In: *Journal of Physics D: Applied Physics* 13.5 (1980), p. 839. URL: http://stacks.iop.org/0022-3727/13/i=5/a=018.

[13] C. H. Henry. "Limiting efficiencies of ideal single and multiple energy gap terrestrial solar cells." In: *Journal of Applied Physics* 51.8 (1980), pp. 4494–4500. DOI: 10.1063/1.328272.

[14] F. Dimroth et al. "Four-Junction Wafer-Bonded Concentrator Solar Cells." In: *IEEE Journal of Photovoltaics* 6.1 (Jan. 2016), pp. 343–349. ISSN: 2156-3381. DOI: 10.1109/JPHOTOV.2015.2501729.

[15] P. T. Chiu et al. "High performance 5J and 6J direct bonded (SBT) space solar cells." In: *2015 IEEE 42nd Photovoltaic Specialist Conference (PVSC)*. June 2015, pp. 1–3. DOI: 10.1109/PVSC.2015.7355673.

[16] *Best Research-Cell Efficiencies*. 2018. URL: https://www.nrel.gov/pv/assets/images/efficiency-chart.png (visited on 03/19/2018).

[17] Elias Veinberg-Vidal et al. "Manufacturing and Characterization of III-V on Silicon Multijunction Solar Cells." In: *Energy Procedia* 92 (2016). Proceedings of the 6th International Conference on Crystalline Silicon Photovoltaics (SiliconPV 2016), pp. 242–247. ISSN: 1876-6102. DOI: https://doi.org/10.1016/j.egypro.2016.07.066. URL: http://www.sciencedirect.com/science/article/pii/S1876610216304933.

[18] J. Yang et al. "Fabrication of High-Efficiency III-V on Silicon Multijunction Solar Cells by Direct Metal Interconnect." In: *IEEE Journal of Photovoltaics* 4.4 (July 2014), pp. 1149–1155. ISSN: 2156-3381. DOI: 10.1109/JPHOTOV.2014.2313225.

[19] Matthew M. Wilkins et al. "Multijunction Solar Cell Designs Using Silicon Bottom Subcell and Porous Silicon Compliant Membrane." In: *IEEE Journal of Photovoltaics* 3 (2013), pp. 1125–1131.

[20] T. J. Grassman et al. "Development of epitaxial 2- and 3-junction III-V/Si solar cells." In: *2016 IEEE 43rd Photovoltaic Specialists Conference (PVSC)*. June 2016, pp. 2036–2039. DOI: 10.1109/PVSC.2016.7749986.

[21] V. Larrey et al. "Various GaAs to Si wafer bonding approaches for solar cells applications." In: *2017 5th International Workshop on Low Temperature Bonding for 3D Integration (LTB-3D)*. May 2017, pp. 25–25. DOI: 10.23919/LTB-3D.2017.7947421.

[22] Katsuaki Tanabe, Katsuyuki Watanabe, and Yasuhiko Arakawa. "III-V/Si hybrid photonic devices by direct fusion bonding." In: *Scientific Reports* 2.349 (2012). DOI: 10.1038/srep00349.

[23] Erwin Peiner, Andreas Guttzeit, and Hergo-Heiurich Wehmann. "The effect of threading dislocations on optical absorption and electron scattering in strongly mismatched heteroepitaxial III-V compound semiconductors on silicon." In: *Journal of Physics: Condensed Matter* 14.48 (2002), p. 13195. URL: http://stacks.iop.org/0953-8984/14/i=48/a=368.

[24] Kei May Lau. "Metamorphic Growth of III-V Devices on Silicon Toward Electronic-Photonic Monolithic Integration." In: *Asia Communications and Photonics Conference 2015*. Optical Society of America, 2015, AS3A.2. DOI: 10.1364/ACPC.2015.AS3A.2. URL: http://www.osapublishing.org/abstract.cfm?URI=ACPC-2015-AS3A.2.

[25] N. P. Blanchard et al. "Engineering Pseudosubstrates with Porous Silicon Technology." In: *Semiconductor-On-Insulator Materials for Nanoelectronics Applications*. Ed. by Alexei Nazarov et al. Berlin, Heidelberg: Springer Berlin Heidelberg, 2011, pp. 47–65. ISBN: 978-3-642-15868-1. DOI: 10.1007/978-3-642-15868-1_3.

[26] K. Derendorf et al. "Fabrication of GaInP/GaAs/Si Solar Cells by Surface Activated Direct Wafer Bonding." In: *IEEE Journal of Photovoltaics* 3.4 (Oct. 2013), pp. 1423–1428. ISSN: 2156-3381. DOI: 10.1109/JPHOTOV.2013.2273097.

[27] F. Dimroth et al. "Comparison of Direct Growth and Wafer Bonding for the Fabrication of GaInP/GaAs Dual-Junction Solar Cells on Silicon." In: *IEEE Journal of Photovoltaics* 4.2 (Mar. 2014), pp. 620–625. ISSN: 2156-3381. DOI: 10.1109/JPHOTOV.2014.2299406.

[28] J. M. Gee and G. F. Virshup. "A 31%-efficient GaAs/silicon mechanically stacked, multijunction concentrator solar cell." In: *Conference Record of the Twentieth IEEE Photovoltaic Specialists Conference*. Sept. 1988, 754–758 vol.1. DOI: 10.1109/PVSC.1988.105803.

[29] Stephanie Essig et al. "Raising the one-sun conversion efficiency of III-V/Si solar cells to 32.8% for two junctions and 35.9% for three junctions." In: *Nature Energy* 2.17144 (2017), pp. 620–625. DOI: 10.1038/nenergy.2017.144.

[30] Thomas Mårtensson et al. "Epitaxial III-V Nanowires on Silicon." In: *Nano Letters* 4.10 (2004), pp. 1987–1990. DOI: 10.1021/nl0487267.

[31] Linus C. Chuang et al. "Critical diameter for III-V nanowires grown on lattice-mismatched substrates." In: *Applied Physics Letters* 90.4 (2007), p. 043115. DOI: 10.1063/1.2436655. eprint: https://doi.org/10.1063/1.2436655. URL: https://doi.org/10.1063/1.2436655.

[32] Ningfeng Huang, Chenxi Lin, and Michelle L Povinelli. "Broadband absorption of semiconductor nanowire arrays for photovoltaic applications." In: *Journal of Optics* 14.2 (2012), p. 024004. URL: http://stacks.iop.org/2040-8986/14/i=2/a=024004.

[33] Michael D. Kelzenberg et al. "Enhanced absorption and carrier collection in Si wire arrays for photovoltaic applications." In: *Nature Materials* 9 (2010), pp. 239–244. DOI: doi:10.1038/nmat2635.

[34] J. Tatebayashi et al. "Site-controlled formation of InAs/GaAs quantum-dot-in-nanowires for single photon emitters." In: *Applied Physics Letters* 100.26 (2012), p. 263101. DOI: 10.1063/1.4731208. eprint: https://doi.org/10.1063/1.4731208. URL: https://doi.org/10.1063/1.4731208.

[35] Jiang Wu et al. "Defect-Free Self-Catalyzed GaAs/GaAsP Nanowire Quantum Dots Grown on Silicon Substrate." In: *Nano Letters* 16.1 (2016), pp. 504–511. DOI: 10.1021/acs.nanolett.5b04142. eprint: https://doi.org/10.1021/acs.nanolett.5b04142. URL: https://doi.org/10.1021/acs.nanolett.5b04142.

[36] Steffi Y. Woo et al. "Atomic Ordering in InGaN Alloys within Nanowire Heterostructures." In: *Nano Letters* 15.10 (2015), pp. 6413–6418. DOI: 10.1021/acs.nanolett.5b01628.

[37] Aleksandr V. Mazalov et al. "Research of acceptor impurity thermal activation in GaN:Mg epitaxial layers." In: *Modern Electronic Materials* 2.2 (2016), pp. 45–47. ISSN: 2452-1779. DOI: https://doi.org/10.1016/j.moem.2016.09.003. URL: http://www.sciencedirect.com/science/article/pii/S2452177916300512.

[38] U. Wahl et al. "Lattice Location of Mg in GaN: A Fresh Look at Doping Limitations." In: *Phys. Rev. Lett.* 118 (9 Mar. 2017), p. 095501. DOI: 10.1103/PhysRevLett.118.095501. URL: https://link.aps.org/doi/10.1103/PhysRevLett.118.095501.

[39] A. C. E. Chia and R. R. LaPierre. "Contact planarization of ensemble nanowires." In: *Nanotechnology* 22.24 (2011), p. 245304. URL: http://stacks.iop.org/0957-4484/22/i=24/a=245304.

[40] Antonio Luque and Antonio Martí. "Increasing the Efficiency of Ideal Solar Cells by Photon Induced Transitions at Intermediate Levels." In: *Phys. Rev. Lett.* 78 (26 June 1997), pp. 5014–5017. DOI: 10.1103/PhysRevLett.78.5014. URL: https://link.aps.org/doi/10.1103/PhysRevLett.78.5014.

[41] Tomohiro Nozawa and Yasuhiko Arakawa. "Detailed balance limit of the efficiency of multilevel intermediate band solar cells." In: *Applied Physics Letters* 98.17 (2011), p. 171108. DOI: 10.1063/1.3583587. eprint: https://doi.org/10.1063/1.3583587. URL: https://doi.org/10.1063/1.3583587.

[42] Chien-chung Lin, Wei-Ling Liu, and Ching-Yu Shih. "Detailed balance model for intermediate band solar cells with photon conservation." In: *Opt. Express* 19.18 (Aug. 2011), pp. 16927–16933. DOI: 10.1364/OE.19.016927. URL: http://www.opticsexpress.org/abstract.cfm?URI=oe-19-18-16927.

[43] A. Martí, L. Cuadra, and A. Luque. "Quantum dot intermediate band solar cell." In: *Conference Record of the Twenty-Eighth IEEE Photovoltaic Specialists Conference - 2000 (Cat. No.00CH37036)*. 2000, pp. 940–943. DOI: 10.1109/PVSC.2000.916039.

[44] Kouta Tateno et al. "VLS Growth of Alternating InAsP/InP Heterostructure Nanowires for Multiple-Quantum-Dot Structures." In: *Nano Letters* 12.6 (2012). PMID: 22594554, pp. 2888–2893. DOI: 10.1021/nl300482n. eprint: https://doi.org/10.1021/nl300482n. URL: https://doi.org/10.1021/nl300482n.

[45] Saniya Deshpande et al. "Formation and Nature of InGaN Quantum Dots in GaN Nanowires." In: *Nano Letters* 15.3 (2015). PMID: 25654749, pp. 1647–1653. DOI: 10.1021/nl5041989. eprint: https://doi.org/10.1021/nl5041989. URL: https://doi.org/10.1021/nl5041989.

[46] *Impact of surface recombination on the performance of phosphor-free InGaN/GaN nanowire white light emitting diodes*. June 2014, pp. 1–2. DOI: 10.1364/CLEO_AT.2014.AF2P.6.

[47] Hieu Pham Trung Nguyen et al. "Engineering the Carrier Dynamics of InGaN Nanowire White Light-Emitting Diodes by Distributed p-AlGaN Electron Blocking Layers." In: *Scientific Reports* 5 (2015). ISSN: 20452322. DOI: 10.1038/srep07744.

[48] Tudor Jenkins. "A brief history of ... semiconductors." In: *Physics Education* 40.5 (2005), p. 430. URL: http://stacks.iop.org/0031-9120/40/i=5/a=002.

[49] L. Łukasiak and A. Jakubowski. "History of Semiconductors." In: *Journal of Telecommunications and Information Technology* 1 (2010), pp. 3–9.

[50] Michael Faraday. "Experimental researches in electricity." In: *Philosophical transactions of the Royal Society of London* 122 (1832), pp. 125–162.

[51] Edmond Becquerel. "Mémoire sur les effets Mélectriques produits sous l'influence des rayons solaires." In: *Comptes Rendus* 9 (1839), pp. 561–567.

[52] Willoughby Smith. *Selenium, its electrical qualities, and the effect of light thereon: being a paper read before the Society of Telegraph Engineers*. Nov. 1877.

[53] F. Braun. "Ueber die Stromleitung durch Schwefelmetalle." In: *Annalen der Physik* 229 (1875), pp. 556–563. DOI: 10.1002/andp.18752291207.

[54] Charles Fritts. "On the Fritts selenium cell and batteries." In: *Van Nostrands Engineering Magazine* 32 (1885), pp. 388–395.

[55] Heinrich Rudolf Hertz. "On Electromagnetic Effects Produced by Electrical Disturbances in Insulators." In: *Electric Waves* 32 (1888), pp. 96–106.

[56] G.W. Pickard. *Rectifier.* US Patent 1,225,852. May 1917. URL: https://www.google.com/patents/US1225852.

[57] A. H. Wilson. "The theory of electronic semi-conductors." In: *Proceedings of the Royal Society of London A: Mathematical, Physical and Engineering Sciences* 133.822 (1931), pp. 458–491. ISSN: 0950-1207. DOI: 10.1098/rspa.1931.0162. eprint: http://rspa.royalsocietypublishing.org/content/133/822/458.full.pdf. URL: http://rspa.royalsocietypublishing.org/content/133/822/458.

[58] R.S. Ohl. *Light-sensitive electric device*. US Patent 2,402,662. June 1946. URL: https://www.google.com/patents/US2402662.

[59] J. H. Scaff and R. S. Ohl. "Development of silicon crystal rectifiers for microwave radar receivers." In: *The Bell System Technical Journal* 26.1 (Jan. 1947), pp. 1–30. ISSN: 0005-8580. DOI: 10.1002/j.1538-7305.1947.tb01310.x.

[60] M. Sparks. *Method of making p-n junctions*. US Patent 2,631,356. Mar. 1953. URL: https://www.google.com/patents/US2631356.

[61] W. Shockley. "The Theory of p-n Junctions in Semiconductors and p-n Junction Transistors." In: *Bell System Technical Journal* 28.3 (1949), pp. 435–489. ISSN: 1538-7305. DOI: 10.1002/j.1538-7305.1949.tb03645.x. URL: http://dx.doi.org/10.1002/j.1538-7305.1949.tb03645.x.

[62] Chih-Tang Sah, Robert N. Noyce, and William Shockley. "Carrier generation and recombination in pn junctions and pn junction characteristics." In: *Proceedings of the IRE* 45.9 (1957), pp. 1228–1243.

[63] J. Czochralski. "Ein neues Verfahren zur Messung der Kristallisationsgeschwindigkeit der Metalle." In: *Zeitschrift f´ur Physikalische Chemie* 92U.1 (1918), pp. 219–221. DOI: doi:10.1515/zpch-1918-9212.

[64] H.C. Theuerer. *Preparation of purified semiconductor material*. US Patent 3,071,444. Jan. 1963. URL: https://www.google.com/patents/US3071444.

[65] D. M. Chapin, C. S. Fuller, and G. L. Pearson. "A New Silicon p-n Junction Photocell for Converting Solar Radiation into Electrical Power." In: *Journal of Applied Physics* 25.5 (1954), pp. 676–677. DOI: 10.1063/1.1721711. eprint: https://doi.org/10.1063/1.1721711. URL: https://doi.org/10.1063/1.1721711.

[66] K. Yoshikawa et al. "Silicon heterojunction solar cell with interdigitated back contacts for a photoconversion efficiency over 26%." In: *Nature Energy* 2 (Mar. 2017), p. 17032. DOI: 10.1038/nenergy.2017.32.

[67] *Solar Frontier Achieves World Record Thin-Film Solar Cell Efficiency of 22.9%*. http://www.solar-frontier.com/eng/news/2017/1220_press.html. Accessed: 2018-01-5.

[68] Yang Bai and Lianzhou Wang. "Perovskite solar modules hit new efficiency record." In: *Science Bulletin* 62.19 (2017), pp. 1293–1294. ISSN: 2095-9273. DOI: https://doi.org/10.1016/j.scib.2017.09.021. URL: http://www.sciencedirect.com/science/article/pii/S2095927317305029.

[69] S. M. Bedair, M. F. Lamorte, and J. R. Hauser. "A two-junction cascade solar-cell structure." In: *Applied Physics Letters* 34.1 (1979), pp. 38–39. DOI: 10.1063/1.90576. eprint: https://doi.org/10.1063/1.90576. URL: https://doi.org/10.1063/1.90576.

[70] J. M. Olson et al. "A 27.3% efficient Gao.5Ino.5P/GaAs tandem solar cell." In: *Applied Physics Letters* 56.7 (1990), pp. 623–625. DOI: 10.1063/1.102717. eprint: https://doi.org/10.1063/1.102717. URL: https://doi.org/10.1063/1.102717.

[71] Nasser H. Karam et al. "Recent developments in high-efficiency Gao.5Ino.5P/GaAs/Ge dual- and triple-junction solar cells: Steps to next-generation PV cells"." In: *Solar Energy Materials and Solar Cells* 66.1-4 (Feb. 2001), pp. 453–466. ISSN: 0927-0248. DOI: 10.1016/S0927-0248(00)00207-5.

[72] *Spectrolab Hits 41.6% PV Cell Efficiency Record*. 2009. URL: http://www.renewableenergyworld.com/articles/2009/08/spectrolab-sets-solar-cell-efficiency-record-at-41-6.html (visited on 03/19/2018).

[73] Emily C. Warmann et al. "Design of photovoltaics for modules with 50% efficiency." In: *Energy Science & Engineering* 5.2 (), pp. 69–80. DOI: 10.1002/ese3.155. eprint: https://onlinelibrary.wiley.com/doi/pdf/10.1002/ese3.155. URL: https://onlinelibrary.wiley.com/doi/abs/10.1002/ese3.155.

[74] A. Ionascut-Nedelcescu et al. "Radiation hardness of gallium nitride." In: *IEEE Transactions on Nuclear Science* 49.6 (2002), pp. 2733–2738.

[75] Frank Schwierz. "An electron mobility model for wurtzite GaN." In: *Solid-State Electronics* 49.6 (2005), pp. 889–895. ISSN: 0038-1101. DOI: https://doi.org/10.1016/j.sse.2005.03.006. URL: http://www.sciencedirect.com/science/article/pii/S0038110105000870.

[76] Walid A. Hadi et al. "Transient electron transport in the III-V compound semiconductors gallium arsenide and gallium nitride." In: *Journal of Materials Science: Materials in Electronics* 24.2 (Feb. 2013), pp. 807–813. ISSN: 1573-482X. DOI: 10.1007/s10854-012-0818-2. URL: https://doi.org/10.1007/s10854-012-0818-2.

[77] Walid A. Hadi, Michael S. Shur, and Stephen K. O'Leary. "Steady-state and transient electron transport within the wide energy gap compound semiconductors gallium nitride and zinc oxide: an updated and critical review." In: *Journal of Materials Science: Materials in Electronics* 25.11 (Nov. 2014), pp. 4675–4713. ISSN: 1573-482X. DOI: 10.1007/s10854-014-2226-2. URL: https://doi.org/10.1007/s10854-014-2226-2.

[78] Hiroyuki Shibata et al. "High Thermal Conductivity of Gallium Nitride (GaN) Crystals Grown by HVPE Process." In: *Materials Transactions* 48.10 (2007), pp. 2782–2786. DOI: 10.2320/matertrans.MRP2007109.

[79] Liang Zhao, Theeradetch Detchprohm, and Christian Wetzel. "High 400 °C operation temperature blue spectrum concentration solar junction in GaInN/GaN." In: *Applied Physics Letters* 105.24 (2014), p. 243903. DOI: 10.1063/1.4904717. eprint: https://doi.org/10.1063/1.4904717. URL: https://doi.org/10.1063/1.4904717.

[80] V. Y. Davydov et al. "Absorption and emission of hexagonal InN. Evidence of narrow fundamental band gap." In: *Phys Status Solidi B* 229 (2002). URL: https://doi.org/3.0.CO;2-O.

[81] V. Y. Davydov et al. "Band gap of InN and In-rich $In_xGa_{1-x}N$ alloys ($0.36 < x < 1$)." In: *Phys Status Solidi B* 230 (2002). DOI: 3.0.CO;2-Z. URL: https://doi.org/3.0.CO;2-Z.

[82] J. Wu et al. "Unusual properties of the fundamental band gap of InN." In: *Appl Phys Lett* 80 (2002). DOI: 10.1063/1.1482786. URL: https://doi.org/10.1063/1.1482786.

[83] V. Y. Davydov et al. "Band gap of hexagonal InN and InGaN alloys." In: *Phys Status Solidi B* 234 (2002). DOI: 3.0.CO;2-H. URL: https://doi.org/3.0.CO;2-H.

[84] Takashi Matsuoka et al. "Optical bandgap energy of wurtzite InN." In: *Applied Physics Letters* 81.7 (2002), pp. 1246–1248. DOI: 10.1063/1.1499753. eprint: https://doi.org/10.1063/1.1499753. URL: https://doi.org/10.1063/1.1499753.

[85] M. Hori et al. "Optical Properties of InxGa1-xN with Entire Alloy Composition on InN Buffer Layer Grown by RF-MBE." In: *physica status solidi (b)* 234.3 (2002), pp. 750–754. ISSN: 1521-3951. DOI: 10.1002/1521-3951(200212)234:3<750::AID-PSSB750>3.0.CO;2-K. URL: http://dx.doi.org/10.1002/1521-3951(200212)234:3%3C750::AID-PSSB750%3E3.0.CO;2-K.

[86] Yasushi Nanishi, Yoshiki Saito, and Tomohiro Yamaguchi. "RF-Molecular Beam Epitaxy Growth and Properties of InN and Related Alloys." In: *Japanese Journal of Applied Physics* 42.Part 1, No. 5A (May 2003), pp. 2549–2559. ISSN: 0021-4922. DOI: 10.1143/JJAP.42.2549. URL: http://stacks.iop.org/1347-4065/42/2549.

[87] T. Miyajima et al. "Structure Analysis of InN Film Using Extended X-Ray Absorption Fine Structure Method." In: *physica status solidi (b)* 234.3 (2002), pp. 801–804. ISSN: 1521-3951. DOI: 10.1002/1521-3951(200212)234:3<801::AID-PSSB801>3.0.CO;2-W. URL: http://dx.doi.org/10.1002/1521-3951(200212)234:3%3C801::AID-PSSB801%3E3.0.CO;2-W.

[88] T. L. Tansley and C. P. Foley. "Optical band gap of indium nitride." In: *Journal of Applied Physics* 59.9 (1986), pp. 3241–3244. DOI: 10.1063/1.336906. eprint: https://doi.org/10.1063/1.336906. URL: https://doi.org/10.1063/1.336906.

[89] B.R. Natarajan et al. "Mechanisms of reactive sputtering of indium I: Growth of InN in mixed Ar-N2 discharges." In: *Thin Solid Films* 69.2 (1980), pp. 201–216. ISSN: 0040-6090. DOI: https://doi.org/10.1016/0040-6090(80)90037-1. URL: http://www.sciencedirect.com/science/article/pii/0040609080900371.

[90] M. S. Nevius et al. "Semiconducting Graphene from Highly Ordered Substrate Interactions." In: *Phys. Rev. Lett.* 115 (13 Sept. 2015), p. 136802. DOI: 10.1103/PhysRevLett.115.136802. URL: https://link.aps.org/doi/10.1103/PhysRevLett.115.136802.

[91] *New Semiconductor Materials. Biology systems. Characteristics and Properties*. http://www.matprop.ru/semicond. Accessed: 2018-06-22.

[92] *THE SEMICONDUCTORS-INFORMATION Web-Site*. http://www.semiconductors.co.uk/. Accessed: 2018-06-22.

[93] H. P. Maruska and J. J. Tietjen. "THE PREPARATION AND PROPERTIES OF VAPOR-DEPOSITED SINGLE-CRYSTAL-LINE GaN." In: *Applied Physics Letters* 15.10 (1969), pp. 327–329. DOI: 10.1063/1.1652845. eprint: https://doi.org/10.1063/1.1652845. URL: https://doi.org/10.1063/1.1652845.

[94] J.I. Pankove, E.A. Miller, and J.E. Berkeyheiser. "GaN blue light-emitting diodes." In: *Journal of Luminescence* 5.1 (1972), pp. 84–86. ISSN: 0022-2313. DOI: https://doi.org/10.1016/0022-2313(72)90038-5. URL: http://www.sciencedirect.com/science/article/pii/0022231372900385.

[95] Shuji Nakamura et al. "InGaN multi-quantum-well-structure laser diodes with cleaved mirror cavity facets." In: *Japanese Journal of Applied Physics, Part 2: Letters* 35.2 B (1996). cited By 280, pp. L217–L220. URL: https://www.scopus.com/inward/record.uri?eid=2-s2.0-0030081829&partnerID=40&md5=6fecaca5758190f94a692ae175fef1dc.

[96] Grzegorz Kamler et al. "Bulk GaN single-crystals growth." In: *Journal of Crystal Growth* 212.1 (2000), pp. 39–48. ISSN: 0022-0248. DOI: https://doi.org/10.1016/S0022-0248(99)00890-8. URL: http://www.sciencedirect.com/science/article/pii/S0022024899008908.

[97] Richter E. et al. "GaN boules grown by high rate HVPE." In: *Physica status solidi C* 8.5 (), pp. 1450–1454. DOI: 10.1002/pssc.201000901. eprint: https://onlinelibrary.wiley.com/doi/pdf/10.1002/pssc.201000901. URL: https://onlinelibrary.wiley.com/doi/abs/10.1002/pssc.201000901.

[98] M Bockowski et al. "Challenges and future perspectives in HVPE-GaN growth on ammonothermal GaN seeds." In: *Semiconductor Science and Technology* 31.9 (2016), p. 093002. URL: http://stacks.iop.org/0268-1242/31/i=9/a=093002.

[99] C. P. Foley and T. L Tansley. "Optical band gap of indium nitride." In: *Journal of Applied Physics* 59.9 (1986), pp. 3241–3244. DOI: 10.1063/1.336906. eprint: https://doi.org/10.1063/1.336906. URL: https://doi.org/10.1063/1.336906.

[100] C. P. Foley and T. L. Tansley. "Pseudopotential band structure of indium nitride." In: *Phys. Rev. B* 33 (2 Jan. 1986), pp. 1430–1433. DOI: 10.1103/PhysRevB.33.1430. URL: https://link.aps.org/doi/10.1103/PhysRevB.33.1430.

[101] C. Stampfl et al. "Native defects and impurities in InN: First-principles studies using the local-density approximation and self-interaction and relaxation-corrected pseudopotentials." In: *Phys. Rev. B* 61 (12 Mar. 2000), R7846–R7849. DOI: 10.1103/PhysRevB.61.R7846. URL: https://link.aps.org/doi/10.1103/PhysRevB.61.R7846.

[102] T. Inushima et al. "Physical properties of InN with the band gap energy of 1.1 eV." In: *Journal of crystal growth* 227 (2001), pp. 481–485.

[103] Su-Huai Wei et al. "Breakdown of the band-gap-common-cation rule: The origin of the small band gap of InN." In: *Phys. Rev. B* 67 (16 Apr. 2003), p. 165209. DOI: 10.1103/PhysRevB.67.165209. URL: https://link.aps.org/doi/10.1103/PhysRevB.67.165209.

[104] G. Orsal et al. "Bandgap energy bowing parameter of strained and relaxed InGaN layers." In: *Opt. Mater. Express* 4.5 (May 2014), pp. 1030–1041. DOI: 10.1364/OME.4.001030. URL: http://www.osapublishing.org/ome/abstract.cfm?URI=ome-4-5-1030.

[105] Min-Ho Kim et al. "Metalorganic Molecular Beam Epitaxy of InGaN Layers and Their Optical Properties." In: *physica status solidi (a)* 176.1 (1999), pp. 269–272. ISSN: 1521-396X. DOI: 10.1002/(SICI)1521-396X(199911)176:1<269::AID-PSSA269>3.0.CO;2-2. URL: http://dx.doi.org/10.1002/(SICI)1521-396X(199911)176:1%3C269::AID-PSSA269%3E3.0.CO;2-2.

[106] Shuji Nakamura. "III-V nitride based light-emitting devices." In: *Solid State Communications* 102.2 (1997). Highlights in Condensed Matter Physics and Materials Science, pp. 237–248. ISSN: 0038-1098. DOI: https://doi.org/10.1016/S0038-1098(96)00722-3. URL: http://www.sciencedirect.com/science/article/pii/S0038109896007223.

[107] K. P. O'Donnell et al. "Structural analysis of InGaN epilayers." In: *Journal of Physics: Condensed Matter* 13.32 (2001), p. 6977.

[108] S. Pereira et al. "Compositional dependence of the strain-free optical band gap in InxGa1-xN layers." In: *Applied Physics Letters* 78.15 (2001), pp. 2137–2139. DOI: 10.1063/1.1358368. eprint: https://doi.org/10.1063/1.1358368. URL: https://doi.org/10.1063/1.1358368.

[109] Ferdinand Scholz et al. "MOVPE of GaInN heterostructures and quantum wells." In: *Journal of Crystal Growth* 189-190.Supplement C (1998), pp. 8–12. ISSN: 0022-0248. DOI: https://doi.org/10.1016/S0022-0248(98)00146-8. URL: http://www.sciencedirect.com/science/article/pii/S0022024898001468.

[110] W. Shan et al. "Optical properties of InxGa1-xN alloys grown by metalorganic chemical vapor deposition." In: *Journal of Applied Physics* 84.8 (1998), pp. 4452–4458. DOI: 10.1063/1.368669. eprint: https://doi.org/10.1063/1.368669. URL: https://doi.org/10.1063/1.368669.

[111] Tetsuya Takeuchi et al. "Optical Properties of Strained AlGaN and GaInN on GaN." In: *Japanese Journal of Applied Physics* 36.2B (1997), p. L177.

[112] C. Wetzel et al. "Optical band gap in Ga1-xInxN(0<x<0.2) on GaN by photoreflection spectroscopy." In: *Applied Physics Letters* 73.14 (1998), pp. 1994–1996. DOI: 10.1063/1.122346. eprint: https://doi.org/10.1063/1.122346. URL: https://doi.org/10.1063/1.122346.

[113] J. Wu et al. "Small band gap bowing in In1-xGaxN alloys." In: *Applied Physics Letters* 80.25 (2002), pp. 4741–4743. DOI: 10.1063/1.1489481. eprint: https://doi.org/10.1063/1.1489481. URL: https://doi.org/10.1063/1.1489481.

[114] K.P O'Donnell et al. "The composition dependence of the InxGa1-xN bandgap." In: *Journal of Crystal Growth* 269.1 (2004). Proceedings of the First ONR International Indium Nitride Workshop, pp. 100–105. ISSN: 0022-0248. DOI: https://doi.org/10.1016/j.jcrysgro.2004.05.040. URL: http://www.sciencedirect.com/science/article/pii/S0022024804006165.

[115] M. D. McCluskey et al. "Effect of composition on the band gap of strained InxGa1-xN alloys." In: *Journal of Applied Physics* 93.7 (2003), pp. 4340–4342. DOI: 10.1063/1.1560563. eprint: https://doi.org/10.1063/1.1560563. URL: https://doi.org/10.1063/1.1560563.

[116] G. Orsal et al. "Bandgap energy bowing parameter of strained and relaxed InGaN layers." In: *Opt. Mater. Express* 4.5 (May 2014), pp. 1030–1041. DOI: 10.1364/OME.4.001030.

[117] Fabio Bernardini, Vincenzo Fiorentini, and David Vanderbilt. "Accurate calculation of polarization-related quantities in semiconductors." In: *Phys. Rev. B* 63 (19 Apr. 2001), p. 193201. DOI: 10.1103/PhysRevB.63.193201. URL: https://link.aps.org/doi/10.1103/PhysRevB.63.193201.

[118] Fabio Bernardini, Vincenzo Fiorentini, and David Vanderbilt. "Spontaneous polarization and piezoelectric constants of III-V nitrides." In: *Phys. Rev. B* 56 (16 Oct. 1997), R10024–R10027. DOI: 10.1103/PhysRevB.56.R10024. URL: https://link.aps.org/doi/10.1103/PhysRevB.56.R10024.

[119] Zi-Hui Zhang et al. "InGaN/GaN light-emitting diode with a polarization tunnel junction." In: *Applied Physics Letters* 102.19 (2013), p. 193508. DOI: 10.1063/1.4806978. eprint: https://doi.org/10.1063/1.4806978. URL: https://doi.org/10.1063/1.4806978.

[120] Asad J. Mughal et al. "Polarization-enhanced InGaN/GaN-based hybrid tunnel junction contacts to GaN p-i-n diodes and InGaN LEDs." In: *Applied Physics Express* 10.12 (2017), p. 121006. URL: http://stacks.iop.org/1882-0786/10/i=12/a=121006.

[121] Peter Kozodoy et al. "Polarization-enhanced Mg doping of AlGaN/GaN superlattices." In: *Applied Physics Letters* 75.16 (1999), pp. 2444–2446. DOI: 10.1063/1.125042. eprint: https://doi.org/10.1063/1.125042. URL: https://doi.org/10.1063/1.125042.

[122] *Polarization management techniques for enhanced vertical and lateral transport in III-nitride superlattices*. Vol. 7. 2006, p. 6121. DOI: 10.1117/12.657894. URL: http://dx.doi.org/10.1117/12.657894.

[123] Junjie Kang et al. "Optimal width of quantum well for reversed polarization blue InGaN light-emitting diodes." In: *AIP Advances* 3.7 (2013), p. 072121. DOI: 10.1063/1.4816716. eprint: https://doi.org/10.1063/1.4816716. URL: https://doi.org/10.1063/1.4816716.

[124] Xu Yi et al. "Polarization effect's impact on luminous efficiency in InGaN/AlGaN MQWs LED." In: *Advances in Optoelectronics and Micro/nano-optics*. Dec. 2010, pp. 1–4. DOI: 10.1109/AOM.2010.5713524.

[125] Rubén O. Nicolás and Julio C. Durán. "Theoretical maximum concentration factors for solar concentrators." In: *J. Opt. Soc. Am. A* 1.11 (Nov. 1984), pp. 1110–1113. DOI: 10.1364/JOSAA.1.001110. URL: http://josaa.osa.org/abstract.cfm?URI=josaa-1-11-1110.

[126] M. Yoshida et al. "Photon ratchet intermediate band solar cells." In: *Applied Physics Letters* 100.26 (2012), p. 263902. DOI: 10.1063/1.4731277. eprint: https://doi.org/10.1063/1.4731277. URL: https://doi.org/10.1063/1.4731277.

[127] K. Sánchez et al. "Assessment through first-principles calculations of an intermediate-band photovoltaic material based on Ti-implanted silicon: Interstitial versus substitutional origin." In: *Phys. Rev. B* 79 (16 Apr. 2009), p. 165203. DOI: 10.1103/PhysRevB.79.165203. URL: https://link.aps.org/doi/10.1103/PhysRevB.79.165203.

[128] Meng-Ju Sher and Eric Mazur. "Intermediate band conduction in femtosecond-laser hyperdoped silicon." In: *Applied Physics Letters* 105.3 (2014), p. 032103. DOI: 10.1063/1.4890618. eprint: https://doi.org/10.1063/1.4890618. URL: https://doi.org/10.1063/1.4890618.

[129] Weiming Wang, Albert Lin, and Jamie Phillips. "Intermediate-band photovoltaic solar cell based on ZnTe:O." In: 95 (July 2009), pp. 011103–011103.

[130] N. López et al. "Intermediate band solar cell: Proof of concept." In: *2011 37th IEEE Photovoltaic Specialists Conference*. June 2011, pp. 002091–002094. DOI: 10.1109/PVSC.2011.6186365.

[131] A. Luque et al. "Experimental analysis of the quasi-Fermi level split in quantum dot intermediate-band solar cells." In: *Applied Physics Letters* 87.8 (2005), p. 083505. DOI: 10.1063/1.2034090. eprint: https://doi.org/10.1063/1.2034090. URL: https://doi.org/10.1063/1.2034090.

[132] A. Martí et al. "Production of Photocurrent due to Intermediate-to-Conduction-Band Transitions: A Demonstration of a Key Operating Principle of the Intermediate-Band Solar Cell." In: *Phys. Rev. Lett.* 97 (24 Dec. 2006), p. 247701. DOI: 10.1103/PhysRevLett.97.247701. URL: https://link.aps.org/doi/10.1103/PhysRevLett.97.247701.

[133] Yoshitaka Okada et al. "Increase in photocurrent by optical transitions via intermediate quantum states in direct-doped InAs/GaNAs strain-compensated quantum dot solar cell." In: *Journal of Applied Physics* 109.2 (2011), p. 024301. DOI: 10.1063/1.3533423. eprint: https://doi.org/10.1063/1.3533423. URL: https://doi.org/10.1063/1.3533423.

[134] Feng-Wen Huang et al. "Linear photon up-conversion of 450 meV in InGaN/GaN multiple quantum wells via Mn-doped GaN intermediate band photodetection." In: *Opt. Express* 19.S6 (Nov. 2011), A1211–A1218. DOI: 10.1364/OE.19.0A1211. URL: http://www.opticsexpress.org/abstract.cfm?URI=oe-19-106-A1211.

[135] A. Martí et al. "Potential of Mn doped $In_{1-x}Ga_xN$ for implementing intermediate band solar cells." In: *Solar Energy Materials and Solar Cells* 93.5 (2009), pp. 641–644. ISSN: 0927-0248. DOI: https://doi.org/10.1016/j.solmat.2008.12.031. URL: http://www.sciencedirect.com/science/article/pii/S0927024808004960.

[136] Liwen Sang et al. "A Multilevel Intermediate-Band Solar Cell by InGaN/GaN Quantum Dots with a Strain-Modulated Structure." In: *Advanced Materials* 26.9 (2014), pp. 1414–1420. ISSN: 1521-4095. DOI: 10.1002/adma.201304335. URL: http://dx.doi.org/10.1002/adma.201304335.

[137] Nima Es'haghi Gorji et al. "The effects of recombination lifetime on efficiency and J-V characteristics of InGaN/GaN quantum dot intermediate band solar cell." In: *Physica E: Low-dimensional Systems and Nanostructures* 42.9 (2010), pp. 2353–2357. ISSN: 1386-9477. DOI: https://doi.org/10.1016/j.physe.2010.05.014. URL: http://www.sciencedirect.com/science/article/pii/S1386947710002523.

[138] Hossein Movla. "Influence of the inverse Auger process on the performance of InGaN/GaN quantum dot solar cells." In: *Optik-International Journal for Light and Electron Optics* 127.11 (2016), pp. 4799–4802. ISSN: 0030-4026. DOI: https://doi.org/10.1016/j.ijleo.2016.01.156. URL: http://www.sciencedirect.com/science/article/pii/S0030402616002059.

[139] Deng Qing-Wen et al. "Computational Investigation of InGaN/InN Quantum-Dot Intermediate-Band Solar Cell." In: *Chinese Physics Letters* 28.1 (2011), p. 018401. URL: http://stacks.iop.org/0256-307X/28/i=1/a=018401.

[140] Qiubo Zhang and Wensheng Wei. "Single intermediate-band solar cells of InGaN/InN quantum dot supracrystals." In: *Applied Physics A* 113.1 (Oct. 2013), pp. 75–82. ISSN: 1432-0630. DOI: 10.1007/s00339-013-7826-9. URL: https://doi.org/10.1007/s00339-013-7826-9.

[141] Stephen P. Bremner, Michael Y. Levy, and Christiana B. Honsberg. "Limiting efficiency of an intermediate band solar cell under a terrestrial spectrum." In: *Applied Physics Letters* 92.17 (2008), p. 171110. DOI: 10.1063/1.2907493. eprint: https://doi.org/10.1063/1.2907493. URL: https://doi.org/10.1063/1.2907493.

[142] Edes Saputra et al. "Self-Formation of In-Plane Ultrahigh-Density InAs Quantum Dots on GaAsSb/GaAs(001)." In: *Applied Physics Express* 5.12 (2012), p. 125502. URL: http://stacks.iop.org/1882-0786/5/i=12/a=125502.

[143] Kazuki Sameshima, Takuya Sano, and Koichi Yamaguchi. "Self-formation of ultrahigh-density (10^{12} cm^2) InAs quantum dots on InAsSb/GaAs(001) and their photoluminescence properties." In: *Applied Physics Express* 9.7 (2016), p. 075501. URL: http://stacks.iop.org/1882-0786/9/i=7/a=075501.

[144] Ru-Chin Tu et al. "Ultra-High-Density InGaN Quantum Dots Grown by Metalorganic Chemical Vapor Deposition." In: *Japanese Journal of Applied Physics* 43.2B (2004), p. L264. URL: http://stacks.iop.org/1347-4065/43/i=2B/a=L264.

[145] Katsuyoshi Sakamoto et al. "Quantum-dot density dependence of power conversion efficiency of intermediate-band solar cells." In: *Journal of Applied Physics* 112.12 (2012), p. 124515. DOI: 10.1063/1.4771925. eprint: https://doi.org/10.1063/1.4771925. URL: https://doi.org/10.1063/1.4771925.

[146] Yao Wu et al. "Photovoltaic Performance of a Nanowire/Quantum Dot Hybrid Nanostructure Array Solar Cell." In: *Nanoscale Research Letters* 13.1 (Feb. 2018), p. 62. ISSN: 1556-276X. DOI: 10.1186/s11671-018-2478-5. URL: https://doi.org/10.1186/s11671-018-2478-5.

[147] Peter Krogstrup et al. "Single-nanowire solar cells beyond the Shockley–Queisser limit." In: *Nature Photonics* 7 (2013), pp. 306–310. DOI: doi:10.1038/nphoton.2013.32.

[148] J. T. Sullivan et al. "Targeted Search for Effective Intermediate Band Solar Cell Materials." In: *IEEE Journal of Photovoltaics* 5.1 (Jan. 2015), pp. 212–218. ISSN: 2156-3381. DOI: 10.1109/JPHOTOV.2014.2363560.

[149] Jacob J. Krich, Bertrand I. Halperin, and Aláan Aspuru-Guzik. "Nonradiative lifetimes in intermediate band photovoltaics-Absence of lifetime recovery." In: *Journal of Applied Physics* 112.1 (2012), p. 013707. DOI: 10.1063/1.4732085. eprint: https://doi.org/10.1063/1.4732085. URL: https://doi.org/10.1063/1.4732085.

[150] Y. C. Yeo, T. C. Chong, and M. F. Li. "Electronic band structures and effective-mass parameters of wurtzite GaN and InN." In: *Journal of Applied Physics* 83.3 (1998), pp. 1429–1436. DOI: 10.1063/1.366847. eprint: https://doi.org/10.1063/1.366847. URL: https://doi.org/10.1063/1.366847.

[151] Kazuhide Kumakura, Toshiki Makimoto, and Naoki Kobayashi. "High hole concentrations in Mg-doped InGaN grown by MOVPE." In: *Journal of Crystal Growth* 221.1 (2000). Proc Tenth Int Conf Metalorganic Vapor Phase Epitaxy, pp. 267–270. ISSN: 0022-0248. DOI: https://doi.org/10.1016/S0022-0248(00)00697-7. URL: http://www.sciencedirect.com/science/article/pii/S0022024800006977.

[152] J. Piprek and S. Nakamura. "Physics of high-power InGaN/-GaN lasers." English. In: *IEE Proceedings - Optoelectronics* 149 (4 Aug. 2002), 145–151(6). ISSN: 1350-2433. URL: http://digital-library.theiet.org/content/journals/10.1049/ip-opt_20020441.

[153] Kazuhide Kumakura, Toshiki Makimoto, and Naoki Kobayashi. "High hole concentrations in Mg-doped InGaN grown by MOVPE." In: *Journal of Crystal Growth* 221.1 (2000). Proc Tenth Int Conf Metalorganic Vapor Phase Epitaxy, pp. 267–270. ISSN: 0022-0248. DOI: https://doi.org/10.1016/S0022-0248(00)00697-7. URL: http://www.sciencedirect.com/science/article/pii/S0022024800006977.

[154] C.-K. Sun et al. "Radiative recombination lifetime measurements of InGaN single quantum well." In: *Applied Physics Letters* 69.13 (1996), pp. 1936–1938. DOI: 10.1063/1.117627. eprint: https://doi.org/10.1063/1.117627. URL: https://doi.org/10.1063/1.117627.

[155] Akio Kaneta et al. "Discrimination of local radiative and nonradiative recombination processes in an InGaN/GaN single-quantum-well structure by a time-resolved multimode scanning near-field optical microscopy." In: *Applied Physics Letters* 83.17 (2003), pp. 3462–3464. DOI: 10.1063/1.1620677. eprint: https://doi.org/10.1063/1.1620677. URL: https://doi.org/10.1063/1.1620677.

[156] Yong-Hoon Cho et al. ""S-shaped" temperature-dependent emission shift and carrier dynamics in InGaN/GaN multiple quantum wells." In: *Applied Physics Letters* 73.10 (1998), pp. 1370–1372. DOI: 10.1063/1.122164. eprint: https://doi.org/10.1063/1.122164. URL: https://doi.org/10.1063/1.122164.

[157] Shuji Nakamura et al. "Optical gain and carrier lifetime of InGaN multi-quantum well structure laser diodes." In: *Applied Physics Letters* 69.11 (1996), pp. 1568–1570. DOI: 10.1063/1.117032. eprint: https://doi.org/10.1063/1.117032. URL: https://doi.org/10.1063/1.117032.

[158] T. Li et al. "Carrier localization and nonradiative recombination in yellow emitting InGaN quantum wells." In: *Applied Physics Letters* 96.3 (2010), p. 031906. DOI: 10.1063/1.3293298. eprint: https://doi.org/10.1063/1.3293298. URL: https://doi.org/10.1063/1.3293298.

[159] Giovanni Giannoccaro, Francesco De Leonardis, and Vittorio M. N. Passaro. "Modeling of the Interminiband Absorption Coefficient in InGaN Quantum Dot Superlattices." In: *Photonics* 3.1 (5 2016). ISSN: 2304-6732. DOI: 10.3390/photonics3010005. URL: http://www.mdpi.com/2304-6732/3/1/5.

[160] O. Ambacher et al. "Absorption of InGaN Single Quantum Wells Determined by Photothermal Deflection Spectroscopy." In: *Japanese Journal of Applied Physics* 37.3 (1998), p. 745.

[161] F. Renner et al. "Quantitative analysis of the polarization fields and absorption changes in InGaN/GaN quantum wells with electroabsorption spectroscopy." In: *Applied Physics Letters* 81.3 (2002), pp. 490–492. DOI: 10.1063/1.1493229. eprint: https://doi.org/10.1063/1.1493229. URL: https://doi.org/10.1063/1.1493229.

[162] K. Y. Lau, P. L. Derry, and A. Yariv. "Ultimate limit in low threshold quantum well GaAlAs semiconductor lasers." In: *Applied Physics Letters* 52.2 (1988), pp. 88–90. DOI: 10.1063/1.99042. eprint: https://doi.org/10.1063/1.99042. URL: https://doi.org/10.1063/1.99042.

[163] B. F. Levine. "Quantum-well infrared photodetectors." In: *Journal of applied physics* 74.8 (1993), R1–R81.

[164] Geert Hellings and K. D. Meyer. *High mobility and quantum well transistors*. Springer, 2013.

[165] Ivan N Stranski and Lubomir Krastanow. "Zur Theorie der orientierten Ausscheidung von Ionenkristallen aufeinander." In: *Monatshefte für Chemie und verwandte Teile anderer Wissenschaften* 71.1 (1937), pp. 351–364.

[166] Martin Volmer and A Weber. "Keimbildung in übersättigten Gebilden." In: *Zeitschrift für physikalische Chemie* 119.1 (1926), pp. 277–301.

[167] Horng-Shyang Chen et al. "Strain relaxation and quantum confinement in InGaN/GaN nanoposts." In: *Nanotechnology* 17.5 (2006), p. 1454. URL: http://stacks.iop.org/0957-4484/17/i=5/a=048.

[168] C. A. Gueymard. "The sun's total and spectral irradiance for solar energy applications and solar radiation models." In: *Solar Energy* 76 (Apr. 2004), pp. 423–453. DOI: 10.1016/j.solener.2003.08.039.

[169] B. M. Kayes et al. "27.6% Conversion efficiency, a new record for single-junction solar cells under 1 sun illumination." In: *2011 37th IEEE Photovoltaic Specialists Conference*. June 2011, pp. 000004–000008. DOI: 10.1109/PVSC.2011.6185831.

[170] Martin A. Green et al. "Solar cell efficiency tables (version 49)." In: *Progress in Photovoltaics: Research and Applications* 25.1 (2017). PIP-16-252, pp. 3–13. ISSN: 1099-159X. DOI: 10.1002/pip.2855. URL: http://dx.doi.org/10.1002/pip.2855.

[171] Siméon Denis Poisson. In: *Bulletin de la société philomatique* (1813).

[172] Siméon Denis Poisson. In: *A Treatise of Mechanics* (1842).

[173] Simon Li and colleagues. *Crosslight Device Simulation Software-General Manual*. English. Version 2016 Version. Crosslight Software Inc. 1331 pp. November 4, 2016.

[174] Chi-Kuang Sun, I-Hsing Tan, and J. E. Bowers. "Ultrafast transport dynamics of p-i-n photodetectors under high-power illumination." In: *IEEE Photonics Technology Letters* 10.1 (Jan. 1998), pp. 135–137. ISSN: 1041-1135. DOI: 10.1109/68.651137.

[175] Ross Cheriton et al. "Design optimizations of InGaAsN(Sb) subcells for concentrator photovoltaic systems." In: *Journal of Vacuum Science & Technology B, Nanotechnology and Microelectronics: Materials, Processing, Measurement, and Phenomena* 34.2 (2016), p. 02M103. DOI: 10.1116/1.4939754. eprint: https://doi.org/10.1116/1.4939754. URL: https://doi.org/10.1116/1.4939754.

[176] K. Nakamura et al. "Finite-element analysis of the miniband structures of semiconductor superlattices with arbitrary periodic potential profiles." In: *IEEE Journal of Quantum Electronics* 27.8 (Aug. 1991), pp. 2035–2041. ISSN: 0018-9197.

[177] S. Mori. "A theoretical study on the electronic structures of semiconductor heterojunctions and superlattices." PhD thesis. Tokyo, Japan: University of Tokyo, 1981.

[178] T. Ando and S. Mori. "Effective-mass theory of semiconductor heterojunctions and superlattices." In: *Surface Science* 113.1 (1982), pp. 124–130. ISSN: 0039-6028. DOI: https://doi.org/10.1016/0039-6028(82)90572-6. URL: http://www.sciencedirect.com/science/article/pii/0039602882905726.

[179] Andreas Wacker. "Semiconductor superlattices: a model system for nonlinear transport." In: *Physics Reports* 357.1 (2002), pp. 1–111. ISSN: 0370-1573. DOI: https://doi.org/10.1016/S0370-1573(01)00029-1. URL: http://www.sciencedirect.com/science/article/pii/S0370157301000291.

[180] K. Nakamura et al. "Finite-element analysis of the miniband structures of semiconductor superlattices with arbitrary periodic potential profiles." In: *IEEE Journal of Quantum Electronics* 27.8 (Aug. 1991), pp. 2035–2041. ISSN: 0018-9197. DOI: 10.1109/3.83413.

[181] S. L. Chuang. "Optical gain of strained wurtzite GaN quantum-well lasers." In: *IEEE Journal of Quantum Electronics* 32.10 (Oct. 1996), pp. 1791–1800. ISSN: 0018-9197. DOI: 10.1109/3.538786.

[182] S. L. Chuang and C. S. Chang. "k·p method for strained wurtzite semiconductors." In: *Phys. Rev. B* 54 (4 July 1996), pp. 2491–2504. DOI: 10.1103/PhysRevB.54.2491. URL: https://link.aps.org/doi/10.1103/PhysRevB.54.2491.

[183] Shun Lien Chuang. "Efficient band-structure calculations of strained quantum wells." In: *Phys. Rev. B* 43 (12 Apr. 1991), pp. 9649–9661. DOI: 10.1103/PhysRevB.43.9649. URL: https://link.aps.org/doi/10.1103/PhysRevB.43.9649.

[184] Patrick Rinke et al. "Consistent set of band parameters for the group-III nitrides AlN, GaN, and InN." In: *Phys. Rev. B* 77 (7 Feb. 2008), p. 075202. DOI: 10.1103/PhysRevB.77.075202. URL: https://link.aps.org/doi/10.1103/PhysRevB.77.075202.

[185] R. S. Varga. *Matrix Iterative Analysis*. Springer, 1962.

[186] D. L. Huffaker et al. "1.3 μm room-temperature GaAs-based quantum-dot laser." In: *Applied Physics Letters* 73.18 (1998), pp. 2564–2566. DOI: 10.1063/1.122534. eprint: https://doi.org/10.1063/1.122534. URL: https://doi.org/10.1063/1.122534.

[187] Alex W. Walker et al. "The effects of absorption and recombination on quantum dot multijunction solar cell efficiency." In: *IEEE journal of photovoltaics* 3.3 (2013), pp. 1118–1124.

[188] Simon Fafard. *Solar cell with epitaxially grown quantum dot material*. US Patent 7,863,516. Jan. 2011.

[189] Renjie Wang et al. "Color-tunable, phosphor-free InGaN nanowire light-emitting diode arrays monolithically integrated on silicon." In: *Opt. Express* 22.S7 (Dec. 2014), A1768–A1775. DOI: 10.1364/OE.22.0A1768. URL: http://www.opticsexpress.org/abstract.cfm?URI=oe-22-107-A1768.

[190] H. P. T. Nguyen et al. "p-Type Modulation Doped InGaN/-GaN Dot-in-a-Wire White-Light-Emitting Diodes Monolithically Grown on Si(111)." In: *Nano Letters* 11.5 (2011). PMID: 21517080, pp. 1919–1924. DOI: 10.1021/nl104536x. URL: http://dx.doi.org/10.1021/nl104536x.

[191] Harald Müllejans et al. "Spectral mismatch in calibration of photovoltaic reference devices by global sunlight method." In: *Measurement Science and Technology* 16.6 (2005), p. 1250. URL: http://stacks.iop.org/0957-0233/16/i=6/a=002.

[192] S. Diaham et al. "Dielectric breakdown of polyimide films: Area, thickness and temperature dependence." In: *IEEE Transactions on Dielectrics and Electrical Insulation* 17.1 (Feb. 2010), pp. 18–27. ISSN: 1070-9878. DOI: 10.1109/TDEI.2010.5411997.

[193] Y. Muramoto et al. "Self-healing breakdown and electrical conduction of polyimide thin films." In: *Proceedings of 1998 International Symposium on Electrical Insulating Materials. 1998 Asian International Conference on Dielectrics and Electrical Insulation. 30th Symposium on Electrical Insulating Ma*. Sept. 1998, pp. 173–176. DOI: 10.1109/ISEIM.1998.741713.

[194] Keiichi Miyairi. "Frequency Dependent Dielectric Breakdown of Thin Polyimide Films Prepared by Vapor Deposition Polymerization." In: *Japanese Journal of Applied Physics* 40.3R (2001), p. 1297. URL: http://stacks.iop.org/1347-4065/40/i=3R/a=1297.

[195] Felix Nippert et al. "Temperature-dependent recombination coefficients in InGaN light-emitting diodes: Hole localization, Auger processes, and the green gap." In: *Applied Physics Letters* 109.16 (2016), p. 161103. DOI: 10.1063/1.4965298. eprint: https://doi.org/10.1063/1.4965298. URL: https://doi.org/10.1063/1.4965298.

[196] Poul Georg Moses and Chris G. Van de Walle. "Band bowing and band alignment in InGaN alloys." In: *Applied Physics Letters* 96.2 (2010), p. 021908. DOI: 10.1063/1.3291055. eprint: https://doi.org/10.1063/1.3291055. URL: https://doi.org/10.1063/1.3291055.

[197] HilmiÜnlü and Asen Asenov. "Band offsets in III-nitride heterostructures." In: *Journal of Physics D: Applied Physics* 35.7 (2002), p. 591. URL: http://stacks.iop.org/0022-3727/35/i=7/a=303.

[198] *Reference Solar Spectral Irradiance: Air Mass 1.5*. http://rredc.nrel.gov/solar/spectra/am1.5/. Accessed: 2018-03-28.

[199] Yasuaki Arakawa et al. "High hole mobility p-type GaN with low residual hydrogen concentration prepared by pulsed sputtering." In: *APL Materials* 4.8 (2016), p. 086103. DOI: 10.1063/1.4960485. eprint: https://doi.org/10.1063/1.4960485. URL: https://doi.org/10.1063/1.4960485.

[200] Carl J. Neufeld et al. "Effect of doping and polarization on carrier collection in InGaN quantum well solar cells." In: *Applied Physics Letters* 98.24 (2011), p. 243507. DOI: 10.1063/1.3595487. eprint: https://doi.org/10.1063/1.3595487. URL: https://doi.org/10.1063/1.3595487.

[201] Vincenzo Fiorentini, Fabio Bernardini, and Oliver Ambacher. "Evidence for nonlinear macroscopic polarization in III–V nitride alloy heterostructures." In: *Applied Physics Letters* 80.7 (2002), pp. 1204–1206. DOI: 10.1063/1.1448668. eprint: https://doi.org/10.1063/1.1448668. URL: https://doi.org/10.1063/1.1448668.

[202] J. Renard et al. "Evidence for quantum-confined Stark effect in GaN/AlN quantum dots in nanowires." In: *Phys. Rev. B* 80 (12 Sept. 2009), p. 121305. DOI: 10.1103/PhysRevB.80.121305. URL: https://link.aps.org/doi/10.1103/PhysRevB.80.121305.

[203] Hwa-Mok Kim et al. "High-Brightness Light Emitting Diodes Using Dislocation-Free Indium Gallium Nitride/Gallium Nitride Multiquantum-Well Nanorod Arrays." In: *Nano Letters* 4.6 (2004), pp. 1059–1062. DOI: 10.1021/nl049615a. eprint: https://doi.org/10.1021/nl049615a. URL: https://doi.org/10.1021/nl049615a.

[204] Young S. Park et al. "Quantum confined Stark effect of InGaN/GaN multi-quantum disks grown on top of GaN nanorods." In: *Nanotechnology* 21.11 (2010), p. 115401. URL: http://stacks.iop.org/0957-4484/21/i=11/a=115401.

[205] Shuailong Zhang et al. "Hole transport assisted by the piezoelectric field in $In_{0.4}Ga_{0.6}N$/GaN quantum wells under electrical injection." In: *Journal of Applied Physics* 118.12 (2015), p. 125709. DOI: 10.1063/1.4931575. eprint: https://doi.org/10.1063/1.4931575. URL: https://doi.org/10.1063/1.4931575.

[206] Guoen Weng et al. "Dynamics of carrier tunneling and recombination in asymmetric coupled InGaN multiple quantum wells." In: *Optics express* 25.20 (2017), pp. 24745–24755.

[207] J. P. Ibbetson et al. "Polarization effects, surface states, and the source of electrons in AlGaN/GaN heterostructure field effect transistors." In: *Applied Physics Letters* 77.2 (2000), pp. 250–252. DOI: 10.1063/1.126940. eprint: https://doi.org/10.1063/1.126940. URL: https://doi.org/10.1063/1.126940.

[208] S. F. Chichibu et al. "Effective band gap inhomogeneity and piezoelectric field in InGaN/GaN multiquantum well structures." In: *Applied Physics Letters* 73.14 (1998), pp. 2006–2008. DOI: 10.1063/1.122350. eprint: https://doi.org/10.1063/1.122350. URL: https://doi.org/10.1063/1.122350.

[209] G.F. Brown et al. "Finite element simulations of compositionally graded InGaN solar cells." In: *Solar Energy Materials and Solar Cells* 94.3 (2010), pp. 478–483. ISSN: 0927-0248. DOI: https://doi.org/10.1016/j.solmat.2009.11.010. URL: http://www.sciencedirect.com/science/article/pii/S092702480900395X.

[210] Muhammad Nawaz and Ashfaq Ahmad. "A TCAD-based modeling of GaN/InGaN/Si solar cells." In: *Semiconductor Science and Technology* 27.3 (2012), p. 035019. URL: http://stacks.iop.org/0268-1242/27/i=3/a=035019.

[211] L. Hsu and W. Walukiewicz. "Modeling of InGaN/Si tandem solar cells." In: *Journal of Applied Physics* 104.2 (2008), p. 024507. DOI: 10.1063/1.2952031. eprint: https://doi.org/10.1063/1.2952031. URL: https://doi.org/10.1063/1.2952031.

[212] Praveen Kumar et al. "First Demonstration of Direct Growth of Planar High-In-Composition InGaN Layers on Si." In: *Applied Physics Express* 6.3 (2013), p. 035501. URL: http://stacks.iop.org/1882-0786/6/i=3/a=035501.

[213] P. D. C. King et al. "Universality of electron accumulation at wurtzite c- and a-plane and zinc-blende InN surfaces." In: *Applied Physics Letters* 91.9 (2007), p. 092101. DOI: 10.1063/1.2775807. eprint: https://doi.org/10.1063/1.2775807. URL: https://doi.org/10.1063/1.2775807.

[214] Kazuhide Kumakura, Toshiki Makimoto, and Naoki Kobayashi. "High hole concentrations in Mg-doped InGaN grown by MOVPE." In: *Journal of Crystal Growth* 221.1 (2000). Proc Tenth Int Conf Metalorganic Vapor Phase Epitaxy, pp. 267–270. ISSN: 0022-0248. DOI: https://doi.org/10.1016/S0022-0248(00)00697-7. URL: http://www.sciencedirect.com/science/article/pii/S0022024800006977.

[215] Stephan Lany and Alex Zunger. "Dual nature of acceptors in GaN and ZnO: The curious case of the shallow MgGa deep state." In: *Applied Physics Letters* 96.14 (2010), p. 142114. DOI: 10.1063/1.3383236. eprint: https://doi.org/10.1063/1.3383236. URL: https://doi.org/10.1063/1.338323.

[216] K. Kohler et al. "Control of the Mg doping profile in III-N light-emitting diodes and its effect on the electroluminescence efficiency." In: *Journal of Applied Physics* 97.10 (2005), p. 104914. DOI: 10.1063/1.1901836.

[217] B. Monemar et al. "Evidence for Two Mg Related Acceptors in GaN." In: *Phys. Rev. Lett.* 102 (23 June 2009), p. 235501. DOI: 10.1103/PhysRevLett.102.235501. URL: https://link.aps.org/doi/10.1103/PhysRevLett.102.235501.

[218] John L. Lyons, Anderson Janotti, and Chris G. Van de Walle. "Shallow versus Deep Nature of Mg Acceptors in Nitride Semiconductors." In: *Phys. Rev. Lett.* 108 (15 Apr. 2012), p. 156403. DOI: 10.1103/PhysRevLett.108.156403. URL: https://link.aps.org/doi/10.1103/PhysRevLett.108.156403.

[219] Karen L. Kavanagh. "Misfit dislocations in nanowire heterostructures." In: *Semiconductor Science and Technology* 25.2 (2010), p. 024006. URL: http://stacks.iop.org/0268-1242/25/i=2/a=024006.

[220] Syed Ahmed Al Muyeed et al. "Strain compensation in InGaN-based multiple quantum wells using AlGaN interlayers." In: *AIP Advances* 7.10 (2017), p. 105312. DOI: 10.1063/1.5000519. eprint: https://doi.org/10.1063/1.5000519. URL: https://doi.org/10.1063/1.5000519.

[221] Kazehiko Anazawa et al. "Growth of strain-compensated InGaN/AlN multiple quantum wells on GaN by MOVPE." In: *Journal of Crystal Growth* 370 (2013). 16th International Conference on Metalorganic Vapor Phase Epitaxy, pp. 82–86. ISSN: 0022-0248. DOI: https://doi.org/10.1016/j.jcrysgro.2012.08.050. URL: http://www.sciencedirect.com/science/article/pii/S0022024812006136.

[222] Tevye Kuykendall et al. "Complete composition tunability of InGaN nanowires using a combinatorial approach." In: *Nature Materials* 6 (2007), pp. 951–956. DOI: doi:10.1038/nmat2037.

[223] J. Y. Chang et al. "Numerical Investigation of High-Efficiency InGaN-Based Multijunction Solar Cell." In: *IEEE Transactions on Electron Devices* 60.12 (Dec. 2013), pp. 4140–4145. ISSN: 0018-9383. DOI: 10.1109/TED.2013.2285573.

[224] Shizhao Fan, Ishiang Shih, and Zetian Mi. "A Monolithically Integrated InGaN Nanowire/Si Tandem Photoanode Approaching the Ideal Bandgap Configuration of 1.75/1.13 eV." In: *Advanced Energy Materials* 7.2 (2017). 1600952, 1600952–n/a. ISSN: 1614-6840. DOI: 10.1002/aenm.201600952. URL: http://dx.doi.org/10.1002/aenm.201600952.

[225] H. P. T. Nguyen et al. "InN p-i-n Nanowire Solar Cells on Si." In: *IEEE Journal of Selected Topics in Quantum Electronics* 17.4 (July 2011), pp. 1062–1069. ISSN: 1077-260X. DOI: 10.1109/JSTQE.2010.2082505.

[226] B. N. Pantha et al. "Electrical and optical properties of p-type InGaN." In: *Applied Physics Letters* 95.26 (2009), p. 261904. DOI: 10.1063/1.3279149. eprint: https://doi.org/10.1063/1.3279149. URL: https://doi.org/10.1063/1.3279149.

[227] R. M. Farrell et al. "High quantum efficiency InGaN/GaN multiple quantum well solar cells with spectral response extending out to 520 nm." In: *Applied Physics Letters* 98.20 (2011), p. 201107. DOI: 10.1063/1.3591976. eprint: https://doi.org/10.1063/1.3591976. URL: https://doi.org/10.1063/1.3591976.

[228] R. Dahal et al. "InGaN/GaN multiple quantum well concentrator solar cells." In: *Applied Physics Letters* 97.7 (2010), p. 073115. DOI: 10.1063/1.3481424. eprint: https://doi.org/10.1063/1.3481424. URL: https://doi.org/10.1063/1.3481424.

[229] Keith Barnham et al. "Quantum well solar cells." In: *Applied Surface Science* 113-114 (1997). Proceedings of the Eighth International Conference on Solid Films and Surfaces, pp. 722–733. ISSN: 0169-4332. DOI: https://doi.org/10.1016/S0169-4332(96)00876-8. URL: http://www.sciencedirect.com/science/article/pii/S0169433296008768.

[230] K.W.J Barnham et al. "Quantum well solar cells." In: *Physica E: Low-dimensional Systems and Nanostructures* 14.1 (2002), pp. 27–36. ISSN: 1386-9477. DOI: https://doi.org/10.1016/S1386-9477(02)00356-9. URL: http://www.sciencedirect.com/science/article/pii/S1386947702003569.

[231] Jin Shi-Rong et al. "Well-Width Dependence of the Exciton Lifetime in GaAs/AlGaAs Quantum Wells." In: *Acta Physica Sinica (Overseas Edition)* 3.5 (1994), p. 384. URL: http://stacks.iop.org/1004-423X/3/i=5/a=009.

[232] L. Hsu and W. Walukiewicz. "Modeling of InGaN/Si tandem solar cells." In: *Journal of Applied Physics* 104.2 (2008), p. 024507. DOI: 10.1063/1.2952031. eprint: https://doi.org/10.1063/1.2952031. URL: https://doi.org/10.1063/1.2952031.

[233] M. Leszczynski et al. "Lattice parameters of gallium nitride." In: *Applied Physics Letters* 69.1 (1996), pp. 73–75. DOI: 10.1063/1.118123. eprint: https://doi.org/10.1063/1.118123. URL: https://doi.org/10.1063/1.118123.

[234] *Imec Reports Record Conversion Efficiency of 23.9 Percent on a 4cm2 Perovskite/Silicon Solar Module*. https://www.imec-int.com/en/articles/imec-reports-record-conversion-efficiency-of-23-9-percent-on-a-4cm2-perovskite-silicon-solar-module. Accessed: 2018-03-20.

[235] W. Götz et al. "Activation energies of Si donors in GaN." In: *Applied Physics Letters* 68.22 (1996), pp. 3144–3146. DOI: 10.1063/1.115805. eprint: https://doi.org/10.1063/1.115805. URL: https://doi.org/10.1063/1.115805.

[236] Michael E. Levinshtein, Sergey L. Rumyantsev, and Michael S. Shur. *Properties of Advanced Semiconductor Materials: GaN, AIN, InN, BN, SiC, SiGe*. John Wiley & Sons, 2001.

[237] O. Ambacher et al. "Two dimensional electron gases induced by spontaneous and piezoelectric polarization in undoped and doped AlGaN/GaN heterostructures." In: *Journal of Applied Physics* 87.1 (2000), pp. 334–344. DOI: 10.1063/1.371866. eprint: https://doi.org/10.1063/1.371866. URL: https://doi.org/10.1063/1.371866.

DECLARATION

I, Ross Cheriton, confirm that the presented work for the thesis entitled:

"Design and Characterizastion of InGaN/GaN Dot-in-Nanowire Heterostructures for High Efficiency Solar Cells"

was solely undertaken by myself unless explicitly mentioned. The growth and fabrication of the nanowire solar cells was exclusively done at McGill by Dr. Zetian Mi's group. All chapters and sections of this thesis that use quotes or describe concepts developed by another author are referenced to show that this material has been adopted to support the work in this thesis.

Ottawa, Ontario, Canada, July 2018

Ross Cheriton

COLOPHON

This thesis by Ross Cheriton was submitted to the Department of Physics in March 2018. The look-and-feel is based on a modified `classicthesis` developed by André Miede. The style was inspired by Robert Bringhurst's seminal book on typography "*The Elements of Typographic Style*".

Final Version as of July 19, 2018 (`classicthesis` version 1.0).